2019

Electron collision effects on radar temperature measurements of the ionosphere

BOSTON UNIVERSITY

GRADUATE SCHOOL OF ARTS AND SCIENCES

Dissertation

ELECTRON COLLISION EFFECTS ON RADAR TEMPERATURE MEASUREMENTS OF THE IONOSPHERE

by

WILLIAM J. LONGLEY

B.A., Hendrix College, 2010
M.S., Rice University, 2014

Submitted in partial fulfillment of the

requirements for the degree of

Doctor of Philosophy

2019

Approved by

First Reader _____

Meers M. Oppenheim, Ph.D.
Professor of Astronomy

Second Reader _____

Joshua L. Semeter, Ph.D.
Professor of Electrical and Computer Engineering

For Sarah. Because of Colleen.

Acknowledgements

This work was supported by NASA grants NNX14AI13G and NNX16AB80G, and NSF grants PHY-1500439 and AGS-1755350. This work used the XSEDE and TACC computational facilities, supported by NSF grant ACI-1053575. Simulation produced data and the single-particle simulation code are available on Zenodo at doi:10.5281/zenodo.2588002. The EPPIC source code used in this dissertation is available at gitlab.com/oppenheim_public. Radar observations and analysis at Millstone Hill and the Madrigal distributed database system are supported by NSF Cooperative Agreement AGS- 1762141 with the Massachusetts Institute of Technology.

The publications resulting from this research include contributions from several coauthors: Meers Oppenheim and Yakov Dimant at Boston University, Alex Fletcher at the Naval Research Laboratory (formerly Boston University), Phil Erickson and Frank Lind at MIT Haystack Observatory, and Juha Vierinen at UiT Arctic University of Norway.

Special thanks to the dissertation committee members: Meers Oppenheim, Josh Semeter, Michael Mendillo, Tereasa Brainerd, and Phil Erickson. Several members of the ISR community also contributed to this research through helpful discussions. These include but are not limited to David Hysell, Roger Varney, Koki Chau, Marco Milla, Craig Heinselman, and Anthea Coster. Also, thanks to the lecturers and organizers of the 2017 ISR Summer School at Arecibo.

ELECTRON COLLISION EFFECTS ON RADAR TEMPERATURE MEASUREMENTS OF THE IONOSPHERE

WILLIAM J. LONGLEY

Boston University, Graduate School of Arts and Sciences, 2019

Major Professor: Meers M. Oppenheim, Professor of Astronomy

ABSTRACT

Most plasmas in astrophysics are hot, tenuous gases where macroscopic electric and magnetic fields dominate the plasma dynamics. In the Earth's ionosphere the plasma is cold and dense, and the small-scale Coulomb force between charged particles becomes important. In this dissertation I implement a grid-based Coulomb collision algorithm in the Electrostatic Parallel Particle-in-Cell (EPPIC) simulator to model spectra observed by incoherent scatter radars (ISR). The modeled spectra are then compared to observations from Millstone Hill to show that current radar techniques can systematically underestimate plasma temperatures in the ionosphere.

ISRs transmit radio waves that are Thomson scattered by electrons in the ionosphere, and then measure the Doppler shift spectra off the ion-acoustic wave. The measured spectra are then fit to a forward model in order to estimate altitude profiles of plasma density, electron temperature, ion temperature, and ion drift speed. For radars looking at aspect angles within 5° of perpendicular to the Earth's magnetic field, the magnetic field constrains electron movement and Coulomb collisions add an additional source of damping that narrows the spectral width. Fitting the collisionally narrowed

spectra to collisionless theories leads to underestimates of plasma temperatures by as much as 25%.

Using EPPIC, I present the first fully kinetic, self-consistent, particle-in-cell simulations of ISR spectra with electron-ion and electron-electron Coulomb collisions. For intermediate aspect angles between 0.5° and 2° off perpendicular, the damping effects of electron-ion and electron-electron collisions are the same and the resulting spectra are narrower than what current theories predict. For aspect angles larger than 3° away from perpendicular, the simulations with electron-ion collisions match collisionless ISR theory well, but spectra with electron-electron collisions are narrower than theory predicts at aspect angles as large as 5° away from perpendicular. I use the Millstone Hill radar to measure spectra at small aspect angles and show that current theories produce incorrect temperature measurements at aspect angles of 4.6° or less. The EPPIC simulations show that a nonlinear interaction between electron-electron collisions and Landau damping causes the errors in temperature measurement, which is not accounted for in current theories.

Contents

List of Tables

List of Figures

List of Abbreviations

ACF	Autocorrelation Function
EPPIC	Electrostatic Parallel Particle-in-Cell simulator
ISR	Incoherent Scatter Radar
IRI	International Reference Ionosphere, 2016 version
LFM	Lyon-Fedder-Mobarry global MHD magnetospheric simulation
MHD	Magnetohydrodynamics
MSIS	Naval Research Laboratory Mass Spectrometer Incoherent Scatter radar model
NGP	Nearest Grid Point
SNR	Signal to Noise Ratio
PIC	Particle-in-Cell
UV	Ultraviolet

Standard Notation and Constants

α	Magnetic aspect angle. Defined as 0 when $\vec{k}_{radar} \perp \vec{B}$.
B	Magnetic field
K_B	Boltzmann's constant. Sometimes also K.
g	Surface gravity on Earth
Λ or $\log\Lambda$	Coulomb logarithm
R_E	Earth's radius

Chapter 1

Introduction

Incoherent Scatter Radars (ISR) are large research facilities that measure a wide range of plasma parameters in the Earth's upper atmosphere. For decades these radars have provided researchers with extremely valuable data sets over a wide range of altitudes, local times, latitudes, seasons, and solar conditions. While ISR can measure or derive many useful parameters, the technique focuses heavily on obtaining accurate measurements of the plasma density and temperature. When a radar looks within 5° of perpendicular to the Earth's magnetic field, current ISR techniques systematically underestimate the plasma temperature by 20-30%.

To understand and correct the systematic errors in ISR temperature measurements this dissertation will answer the following questions:

1) Under what conditions do Coulomb collisions effect temperature and density measurements of the Earth's ionosphere?
2) Do electron-electron collisions damp a plasma wave differently than electron-ion collisions?
3) Do particle-in-cell simulations provide a more accurate forward model than current theories for ISR temperature estimates, and why?

This dissertation focuses on simulating and measuring ISR spectra when the radar looks nearly perpendicular to the magnetic field. The organization of this dissertation is as follows: Chapter 1 provides background on the ionosphere, collisional physics, and plasma simulation methods. Chapter 2 reviews current ISR theory and experimental methods. Chapters 3 and 4 simulate the effects of electron-ion and electron-electron collisions on ISR spectra, respectively. In Chapter 5 these simulations are compared to measured spectra from the Millstone Hill radar. Chapter 6 summarizes the results of this dissertation and discusses future directions for ISR theory.

1.1 The Geospace Environment

The geospace environment is roughly defined as the region of space near Earth. This region starts at 80 km above the Earth's surface, which is coincidentally the altitude required to earn a U.S. Astronaut Badge, and extends out past the moon's orbit at a distance of 60 Earth radii (R_E). This large region of space is strongly influenced by the Sun and is further subdivided based on how the Sun influences a specific region. At 10-60 R_E the Sun's magnetic field and ejected plasma, known as the solar wind, directly interact with the Earth's magnetic field and create a bubble in the solar wind known as the magnetosphere. At distances less than 5 R_E, the inner magnetosphere is less affected by the Sun's magnetic field, but plasma from the solar wind is driven into this region and creates the radiation belts. At altitudes below 1,000 km, the solar wind has little direct effect, but the Sun's UV and x-ray radiation photoionizes the upper reaches of Earth's neutral atmosphere, creating a plasma environment called the ionosphere between 80-1,000 km above the Earth's surface. The incoherent scatter radars (ISR) examined in this

dissertation measure the temperature, density, and velocity of the plasma in the ionosphere. The measurements from these radars are assimilated into MSIS and IRI, which are global empirical models of the neutral atmosphere and ionosphere. These models, and ISR data sets in general, are used heavily in long term solar cycle studies of the ionosphere's response to changing solar activity.

The geospace environment is highly dynamic and varies based on solar activity. Increases in the solar wind speed, density, or magnetic field strength cause the coupled magnetosphere-ionosphere system to respond dynamically and in a way that can cause economic damage. These solar storms drive more plasma into the radiation belts, increasing the radiation hazard to Earth orbiting spacecraft. The increased electric fields in the polar regions can induce electric currents in power lines and pipelines, potentially damaging those systems. During solar storms, electric fields can also penetrate to lower latitudes, which, combined with the typical recombination and motion of the ionosphere at sunset, leads to an instability that degrades radio communications and GPS signals (*Abdu,* 2012). This *Equatorial Spread F* instability can also occur due to disturbances in the neutral atmosphere below 100 km. Separating the different causes for the same space weather effect requires good measurements of the ionosphere in order to understand the conditions before the onset of equatorial spread F. This dissertation seeks to improve the accuracy of ionosphere measurements by ISR facilities so that researchers can better study equatorial spread F, assimilate ISR data into the MSIS and IRI model, and better understand the complex magnetosphere-ionosphere system.

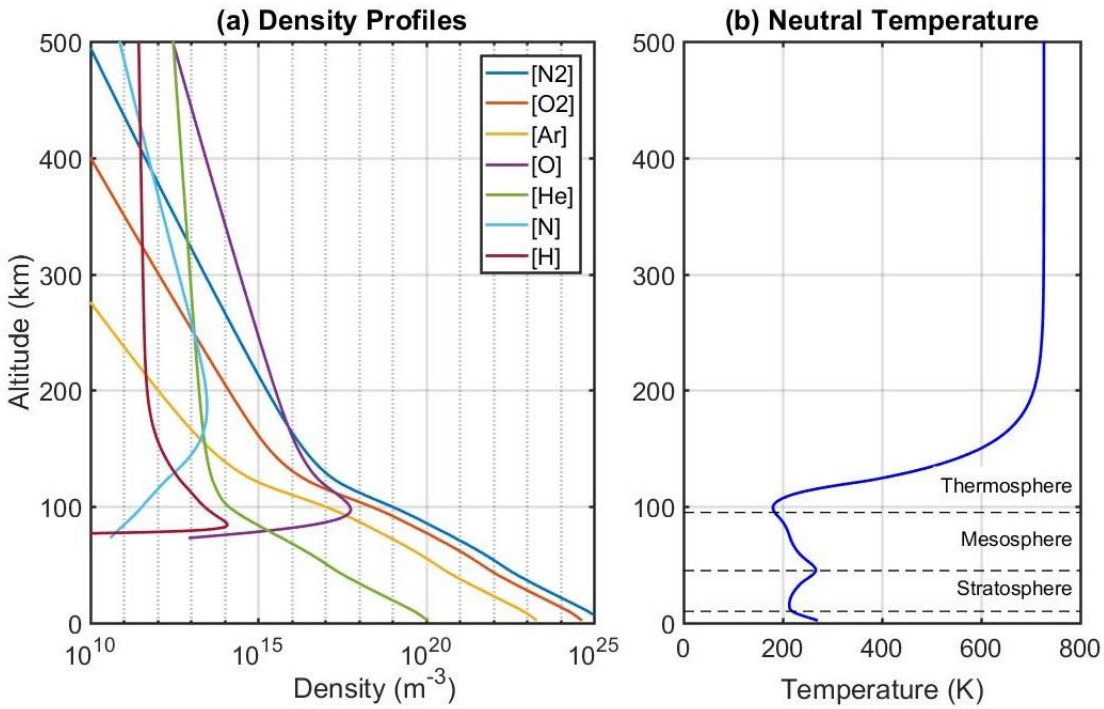

Figure 1.1 (Left) Altitude dependence of the density for the main neutral species in the Earth's atmosphere. The neutral species are molecular Nitrogen (N_2) and Oxygen (O_2), and atomic Argon (Ar), Oxygen (O), Helium (He), Nitrogen (N), and Hydrogen (H). (Right) The altitude profile of the neutral temperature. The different regions of Earth's neutral atmosphere are defined by where the neutral temperature is either increasing or decreasing with altitude.

1.1.1 Earth's Atmosphere

The Earth's ionosphere is embedded in the neutral atmosphere and is mostly created by solar radiation ionizing neutral molecules. Figure 1.1 shows the temperature and density of different neutral species for normal daytime conditions near Boston, Massachusetts. The altitude profiles plotted in Figure 1.1 are generated using the NRLMSISE-00 model (MSIS), which is an empirical model that assimilates temperature and density measurements from many instruments, including ISR (*Hedin*, 1991). At the Earth's surface the atmosphere is composed of 78% molecular Nitrogen, 21% molecular

Oxygen, and trace amounts of Argon and Helium. At altitudes of 100 km and below the neutral gases are well mixed by turbulence. Below around 100 km the composition ratios do not vary with altitude, and the overall density decreases exponentially with height. Above the turbopause at ~100 km the different gases are not mixed by turbulence, and the density of each species decreases at a different exponential rate. This changes the atmospheric composition, with heavier neutral species settling at lower altitudes than lighter species.

A neutral gas in equilibrium is structured such that the gravitational force is balanced exactly by a pressure gradient, and the density varies with altitude as

$$n(z) = n_0 \exp\left(-\frac{z}{H_s}\right), \tag{1.1}$$

where n_0 is the density at sea level. The scale height, H_s, for the exponential decay in equation (1.1) is

$$H_s = \frac{K_B T_s}{m_s g}. \tag{1.2}$$

The scale height relations in equations (1.1) – (1.2) explain most of the density structure in Figure 1.1. Below the turbopause at 100 km the atmosphere is effectively a single, turbulently mixed species. The density in this region follows a scale height relation with a temperature around 200-300 K, and a mass that is the average of all the species being turbulently mixed. Above the turbopause the temperature rapidly increases due to photoionization, which increases the scale height. Additionally, without turbulent mixing the scale height is different for each neutral species. Heavier species will have a

smaller scale height and will be confined to lower altitudes, and lighter species will have a larger scale height and will be denser at higher altitudes compared to heavier species. Some atomic species such as Oxygen, Nitrogen, and Hydrogen do not follow a scale height relation, and instead have density profiles that are determined by chemical reactions with other species.

The different regions of the Earth's atmosphere are determined by where the temperature is either increasing or decreasing with altitude, as shown in Figure 1.1. The atmosphere at the surface of the Earth is heated by the Sun to an average of 300 K. In the troposphere the temperature gradually decreases with altitude from 300 K at the surface to a minimum of 200 K at 10 km in altitude. The stratosphere extends from 10 km to 45 km in altitude and the region is heated back to 300 K due to UV absorption by the ozone layer, which is strongest between 20-40 km altitude. In the mesosphere from 45 km to 95 km in altitude there is no significant absorption or ionization of the Sun's radiation, so the temperature decreases with altitude until reaching a global minimum of 180 K. Above this temperature minimum is the thermosphere, where photoionization of N_2 and O_2 by solar x-rays and UV significantly heats the atmosphere to around 700 K (*Kelley*, 2009).

In the stratosphere the creation of ozone by UV radiation heats the region. The molecular oxygen is photo-dissociated by the reaction $O_2 + photon \rightarrow 2O$, and the atomic Oxygen reacts quickly with molecular Oxygen to form ozone: $O + O_2 \rightarrow O_3$. This is an example of chemistry dominating over the scale height relations in equations (1.1) - (1.2). Atomic Oxygen in the stratosphere is rapidly lost in chemical reactions with O_2 to create ozone, and also reacts with O_3 to destroy ozone and create two O_2 molecules. The

chemistry involved in the upper mesosphere and thermosphere is more complicated due to the different species being ionized. At altitudes around 100-150 km UV and x-rays photoionize molecular O_2 and N_2, which creates an atomic particle, an ion, and an electron. The sustained creation of ions and electrons by photoionization during the day creates a dynamic plasma environment known as the ionosphere.

1.1.2 Earth's Ionosphere

The photoionization of O_2 and N_2 between 100-150 km in altitude creates a plasma that eventually populates the ionosphere up to 1000 km in altitude. The governing equation for plasma density, *n*, in the ionosphere is the fluid continuity equation:

$$\frac{\partial n}{\partial t} + \nabla \cdot (\vec{u}n) = P - L. \tag{1.3}$$

Equation (1.3) states that the rate of change for the density plus the motion of the plasma moving with velocity $\vec{u}$ is equal to the production (P) of plasma minus the loss (L) of plasma. The relative importance of these terms defines several distinct regions of the ionosphere. Figures 1.2 and 1.3 show the density and temperature profiles of the daytime and nighttime ionosphere, respectively. These profiles are generated using the IRI model, which assimilates data from ISR, spacecraft, ionosondes, and other instruments to make an empirical model of the typical ionosphere (*Bilitza and Reinisch*, 2008).

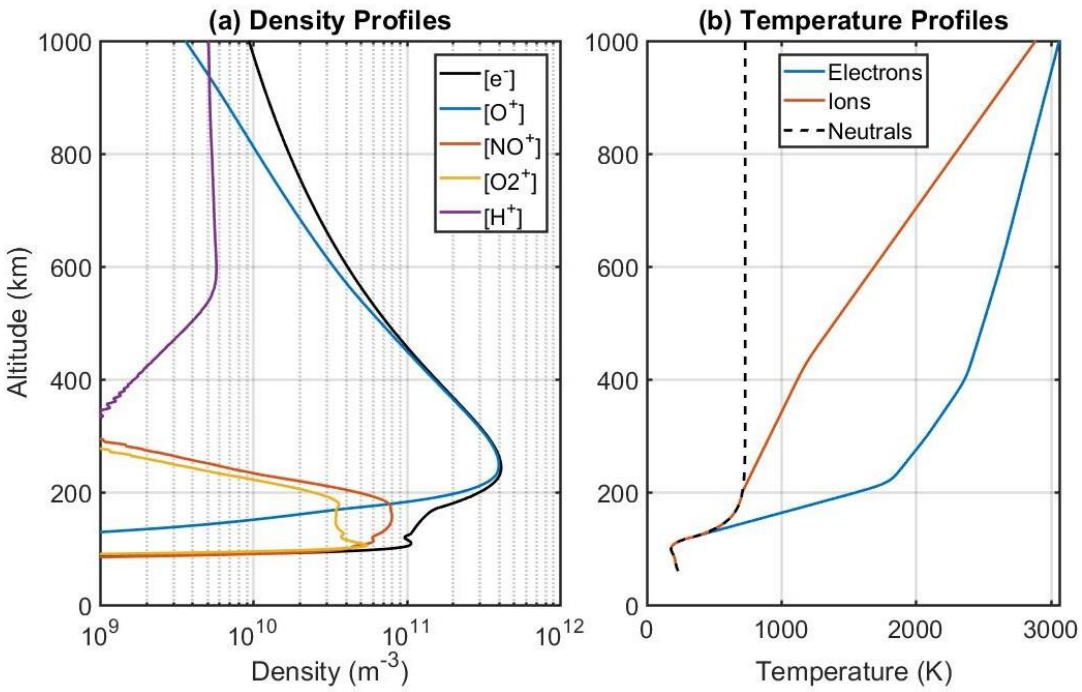

Figure 1.2 The daytime altitude profiles of density (left) and temperature (right) from IRI. The model is run at Boston's latitude for quiet conditions at noon in February.

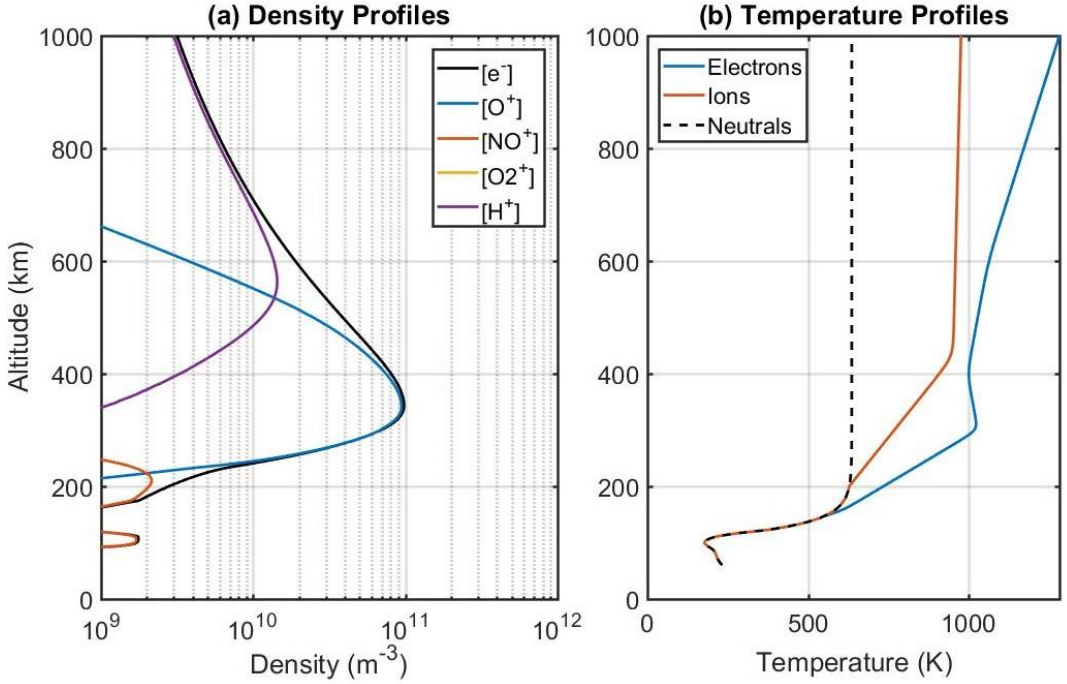

Figure 1.3 The nighttime altitude profiles of density (left) and temperature (right) from IRI. The model is run at Boston's latitude for quiet conditions at midnight in February.

The 100-150 km region where most photoionization occurs is known as the E-region. This region only exists during the day, and the dominant terms in equation (1.3) are the production and loss terms. O_2 is directly ionized to created O_2^+ and an electron, whereas N_2 is ionized to N_2^+, which rapidly undergoes one of the following reactions:

$$N_2^+ + O \rightarrow NO^+ + N$$

$$N_2^+ + O \rightarrow O^+ + N_2$$

$$N_2^+ + O_2^+ \rightarrow O_2^+ + N_2$$

In the E-region the main ion species are O_2^+ and NO^+. The O^+ created in the E-region has a longer lifetime and is able to diffuse upward through the motion term in equation (1.3). The region where O^+ settles as the main ion species is known as the F-region, which is nominally from 200-400 km in altitude. Between the E-region and F-region is the valley region, where the plasma density slightly decreases, and NO^+, O_2^+, and O^+ are all present in significant quantities. The F-region is sometimes further subdivided to the F_1 peak where NO^+ and O_2^+ are present, and the F_2 region where only O^+ is present. Above 400 km is the topside ionosphere, where H^+ and He^+ ions are minor species. Below the E-region is the low-density D-region, from 60-100 km, which is dominated by negative ions and molecular ion chemistry.

The difference between the daytime and nighttime density profiles in Figures 1.2 and 1.3 is due to how the different ions recombine at night when photoionization no longer occurs. NO^+ and O_2^+ dissociatively recombine on a time scale of a few minutes through the reactions:

$$NO^+ + e \rightarrow N + O$$

$$O_2^+ + e \rightarrow O + O$$

In contrast, O^+ recombines through a slower charge exchange process:

$$O^+ + N_2 \rightarrow NO^+ + O$$

$$O^+ + O_2 \rightarrow O_2^+ + O$$

The resulting NO^+ or O_2^+ then dissociatively recombines quickly. The time scale for O^+ recombination is ~100 hours since the charge exchange reaction is so slow. This means at night the NO^+ and O_2^+ dominated D, E, and F_1 regions all recombine and disappear within an hour. The slow time scale on O^+ recombination means the F-region persists through the night, with a slightly lower density.

The temperature profiles in the ionosphere are influenced by the neutral temperature, heat from photoionization, and heat generated in the inner magnetosphere. The ion temperature is dictated entirely by strong collisions with neutrals at low altitudes, and weak collisions with electrons at higher altitudes. During the day photoionization significantly heats the electron population throughout the E and F regions. Below 150 km the electron-neutral collision rate is high (Figure 1.4), and the heat from photoionization is effectively lost by collisions with the much denser neutral atmosphere. Above 150 km the electron-neutral collision rate is too low to cool the electron population, leading to a large increase in temperature. The electrons in the topside of the ionosphere are heated by electron precipitation or other heat fluxes coming from the inner magnetosphere (*Schunk and Nagy,* 2009).

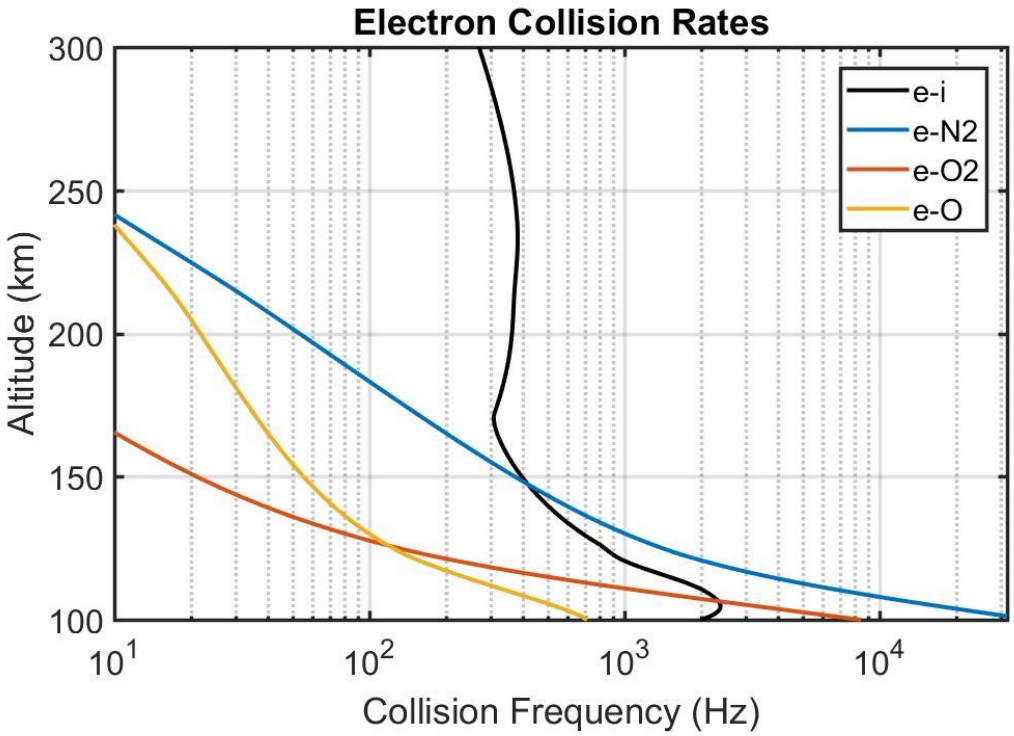

Figure 1.4 The average collision rates as a function of altitude are computed using IRI and MSIS empirical models at 14:00 local time. The electron-ion collision rate (black) is larger than any of the electron-neutral collision rates at altitudes above 180 km.

The motion of plasma in the ionosphere is complex and dynamic. In the D and E regions ion-neutral collisions are frequent, and the denser neutral atmosphere will drag the ion population with the wind pattern from the neutral atmosphere. Electrons have a high neutral collision rate as well, but their motion is constrained by the magnetic field lines which can lead to flow patterns different from ions. To a rough approximation the plasma density of each ion species follows the scale height relations in equations (1.1) – (1.2). This causes the lighter O^+ ions to diffuse upwards, creating the F_2 region 100 km higher than the altitude where photoionization is producing O^+. The temperature dependence in the scale height also means the entire ionosphere moves upwards during the day when the temperature is higher, and downwards at night.

1.1.3 Magnetosphere-Ionosphere Coupling

At high altitudes or high latitudes, the motion of the ionosphere is less affected by the neutral atmosphere, and the ionosphere needs to be considered as a part of the whole magnetosphere-ionosphere system. Figure 1.5 shows a schematic of the magnetosphere taken from an LFM simulation (*Lyons et al.*, 2004; *Merkin and Lyon,* 2010). The solar wind is a constant plasma source ejected from the Sun and traveling outward at a speed of around 400 km/s and carrying an interplanetary magnetic field (IMF) on the order of 10 nT. The simulation output in Figure 1.5 shows how the Earth's magnetosphere is influenced by this magnetic field in the solar wind. At low latitudes the Earth's magnetic field lines are closed, meaning both end points of the field line are at the Earth's surface. At high latitudes, open magnetic field lines emerge from the Earth and connect to the solar wind. The boundary between open and closed field lines is dynamic during solar storms, with southward (downward in Figure 1.5) IMF creating a larger region of open field lines around the poles. During southward IMF storms the solar wind reconnects with the oppositely directed dipole field from Earth. After reconnection the field line is driven over the pole and away from the Sun, where it reconnects into a closed field line in the tail region of the magnetosphere, and convects back to the dayside of the Earth at a lower latitude. This is known as the Dungey cycle, and the motion of magnetic field lines in the Dungey cycle drives a complex motion of the plasma in the high latitude ionosphere, both through the field line convection and through the creation of electric fields which map down field lines and into the ionosphere (*Dungey,* 1961).

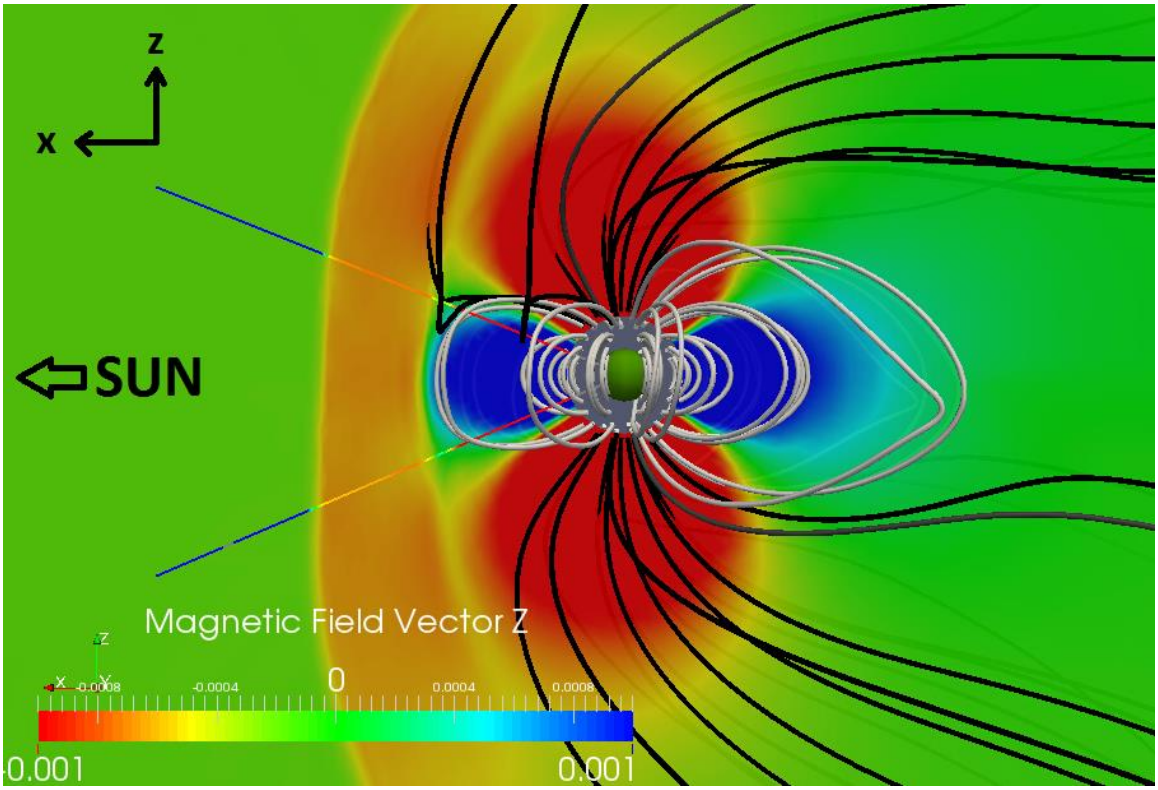

Figure 1.5 The Earth's magnetosphere from an LFM simulation. The closed field lines are shown in white, and the open field lines are shown in black. The strength of the magnetic field in the southward (downward) direction is shown in color, with the red value corresponding to -1 mG, and the blue corresponding to 1 mG (or 100 nT).

The Dungey cycle provides a path for solar wind plasma to enter the magnetosphere and eventually settle into the inner magnetosphere where the field lines are always closed. This provides the main source of H^+ and He^+ ions that create the plasmasphere from 1000 km out to 4-8 R_E depending on the solar wind conditions (*Schunk and Nagy*, 2009). Through a variety of mechanisms, the ions and electrons in the plasmasphere can be accelerated up to high energies, which creates the radiation belts (*Abel and Thorne,* 1998). The inner radiation belt extends from 2000 km in altitude up to 2 R_E and is primarily composed of high energy ions. Energetic electrons create the outer radiation belt, from 3 to 5 R_E in altitude. The energetic particles can precipitate into the

high latitude ionosphere, which heats the plasma and creates the aurora. Additionally, electrons created by photoionization can move upwards and along the magnetic field lines, interact with waves in the plasmasphere, and precipitate into the opposite hemisphere.

For decades the magnetosphere and ionosphere have been studied as separate systems, with the other region acting as a fixed boundary condition. Recently the dynamic coupling of the magnetosphere-ionosphere system has been recognized. The electric fields generated in the outer magnetosphere map down to the auroral ionosphere and can heat the E-region through either Joule heating or the Farley-Buneman instability (*Oppenheim and Dimant,* 2013). The increased E-region temperature changes the electrical conductivity of the ionosphere, which in turn changes the entire convection pattern of the magnetosphere (*Dimant and Oppenheim,* 2011a; *Dimant and Oppenheim* 2011b). Another form of magnetosphere-ionosphere coupling comes from lightning near the Earth's surface. The lightning launches electromagnetic whistler waves that propagated through the ionosphere and into the radiation belts, which cause more electrons to precipitate into the auroral region, causing heating and increasing the density through impact ionization (*Abel and Thorne*, 1998). The forefront of predictive geospace research is understanding how the ionosphere and magnetosphere couple to each other during solar storms, and ISR is one of the best tools available for both short term and long-term studies of magnetosphere-ionosphere coupling.

1.2 Collisional Plasmas

Current ISR techniques underestimate plasma temperatures when the radar line of sight looks nearly perpendicular to the Earth's magnetic field. This error occurs because current ISR theory does not correctly model the physics of electron-ion and electron-electron collisions in a magnetized plasma. Before addressing how ISR works and how collisions affect those measurements, this section will review the basics of kinetic plasma physics and the different collisions that occur in plasmas.

1.2.1 Plasma Kinetics

A single electron or ion can be represented as a point charge in phase space, with a time dependent density of (*Nicholson,* 1983)

$$N(\vec{x},\vec{v},t) = \delta\left(\vec{x} - x_p(t)\right)\delta\left(\vec{v} - \vec{v}_p(t)\right), \tag{1.4}$$

where $\vec{x}$ and $\vec{v}$ are position and velocity coordinates, while $\vec{x}_p$ and $\vec{v}_p$ are the position and velocity of the particle, and δ is the Dirac delta distribution. A plasma is composed of many charged particles of a given species *s*, so the total number density of species *s* is simply the summation of the individual particle densities in equation (1.4),

$$N_s(\vec{x},\vec{v},t) = \sum_i \delta\big(\vec{x} - x_i(t)\big)\delta\big(\vec{v} - \vec{v}_i(t)\big), \tag{1.5}$$

where again $\vec{x}$ and $\vec{v}$ are phase space coordinates, and now $\vec{x}_i$ and $\vec{v}_i$ are the position and velocity of the i^{th} particle. Equation (1.5) provides a time dependent description of each species in the plasma, which can yield the mass density (ρ_m), charge density (ρ_c), and currents (J) in the plasma by integrating N_s over all velocity space:

$$\rho_m(\vec{x},t) = \sum_s m_s \int N_s \, d^3\vec{v}\,, \tag{1.6}$$

$$\rho_c(\vec{x},t) = \sum_s q_s \int N_s \, d^3\vec{v}\,, \tag{1.7}$$

$$\vec{J}(\vec{x},t) = \sum_s q_s \int \vec{v}\, N_s \, d^3\vec{v}\,. \tag{1.8}$$

The equations presented so far are an exact, but impractical, description of a plasma. Several simplifications need to be made, including smoothing the delta distributions in equation (1.5) into a continuous function, and obtaining an equation for the time evolution of the system. The latter is easily accomplished by taking the total time derivative of N_s with respect to all 7 independent variables: t, $\vec{x}$, and $\vec{v}$. By Liouville's theorem this is

$$\begin{aligned}\frac{dN_s}{dt} = \frac{\partial N_s}{\partial t} &+ \sum_i \dot{\vec{x}}_i \cdot \nabla_x \delta\big(\vec{x} - \vec{x}_i(t)\big)\delta\big(\vec{v} - \vec{v}_i(t)\big) \\ &+ \sum_i \dot{\vec{v}}_i \cdot \nabla_v \delta\big(\vec{x} - \vec{x}_i(t)\big)\delta\big(\vec{v} - \vec{v}_i(t)\big)\,.\end{aligned} \tag{1.9}$$

where the notation is $\dot{\vec{x}} \cdot \nabla f = \frac{dx}{dt}\frac{\partial}{\partial x} f + \frac{dy}{dt}\frac{\partial}{\partial y} f + \frac{dz}{dt}\frac{\partial}{\partial z} f$, and similar for the velocity gradient in the last term. N_s represents the locations of all particles of a species in phase space, so $\frac{dN_s}{dt} \neq 0$ implies particles are either being created or destroyed. While this occurs during ionization and recombination processes in plasmas such as the ionosphere, we can assume $\frac{dN_s}{dt} = 0$ for now and add a recombination or ionization term back into equation (1.9) later. The particle positions and velocities are physically constrained by

$\dot{\vec{x}}_i = \vec{v}_i$ and $\dot{\vec{v}}_i = \vec{F}_i/m_s$. Since the particles are charged, $\vec{F}_i = q_s(\vec{E} + \vec{v}_i \times \vec{B})$ is simply the Lorentz force. The electric and magnetic fields in the Lorentz force include the self-consistent fields from solving Maxwell's equations using the charge density and current in equations (1.7) – (1.8), as well as any externally imposed fields.

Delta functions have the property $a\delta(a-b) = b\delta(b-a)$, which allows us to replace the $\dot{\vec{x}}_i$ and $\dot{\vec{v}}_i$ right before the gradients with $\dot{\vec{x}}$ and $\dot{\vec{v}}$, which can be factored out of the summations to yield

$$0 = \frac{\partial N_s}{\partial t} + \dot{\vec{x}} \cdot \nabla_x \sum_i \delta\big(\vec{x} - \vec{x}_i(t)\big)\delta\big(\vec{v} - \vec{v}_i(t)\big) + \dot{\vec{v}} \cdot \nabla_v \sum_i \delta\big(\vec{x} - \vec{x}_i(t)\big)\delta\big(\vec{v} - \vec{v}_i(t)\big). \tag{1.10}$$

The summations in equation (1.10) are the definition of N_s from equation (1.5), and upon substitution we arrive at the *Klimontovich Equation*,

$$\frac{\partial N_s}{\partial t} + \vec{v} \cdot \nabla_x N_s + \frac{q_s}{m_s}\big(\vec{E} + \vec{v} \times \vec{B}\big) \cdot \nabla_v N_s = 0. \tag{1.11}$$

The Klimontovich equation is an exact description of a plasma, but it describes the time evolution of an extremely large number of individual particles by representing them as delta distributions in phase space. In order to smooth the set of delta distributions into a continuous distribution function we assume all the variables in the Klimontovich equation can be divided into the sum of a macroscopic value that varies smoothly in phase space, and a microscopic value. For example, the particle density will be

$$N_s(\vec{x}, \vec{v}, t) = f_s(\vec{x}, \vec{v}, t) + \delta N_s(\vec{x}, \vec{v}, t), \tag{1.12}$$

where f_s is the continuous macroscopic distribution function we are interested in working with, and is defined by taking an ensemble average of many systems such that

$$\langle N_s(\vec{x},\vec{v},t)\rangle = f_s(\vec{x},\vec{v},t). \tag{1.13}$$

Using the notation where a δ prefix represents microscopic values, and a prime represents macroscopic values, the ensemble average of the Klimontovich equation separates into two parts (*Nicholson*, 1983),

$$\frac{\partial f_s}{\partial t} + \vec{v}\cdot\nabla_x f_s + \frac{q_s}{m_s}\left(\vec{E}' + \vec{v}\times\vec{B}'\right)\cdot\nabla_v f_s = \\ -\frac{q_s}{m_s}\langle\left(\delta\vec{E} + \vec{v}\times\delta\vec{B}\right)\rangle\cdot\nabla_v(f_s+\delta N_s) - \frac{q_s}{m_s}\langle\left(\vec{E}' + \vec{v}\times\vec{B}'\right)\rangle\cdot\nabla_v\delta N\,. \tag{1.14}$$

The right-hand side of equation (1.14) encompasses all of the small scale, microscopic interactions in the plasma, and is defined as the collision operator. Noting that the left-hand side of equation (1.14) is df_s/dt with Liouville's theorem applied, we write the right-hand side in shorthand as a general collision operator:

$$\frac{\partial f_s}{\partial t} + \vec{v}\cdot\nabla_x f_s + \frac{q_s}{m_s}\left(\vec{E}' + \vec{v}\times\vec{B}'\right)\cdot\nabla_v f_s = \left(\frac{\partial f_s}{\partial t}\right)_{coll}. \tag{1.15}$$

Equation (1.15) is the *Boltzmann Equation*, which is an accurate but not exact description of the plasma that is highly useful due to its simplicity. In this dissertation we will exclusively use the Boltzmann equation to describe plasmas since it accurately describes all of the important small-scale kinetic behavior in a plasma for a given collision operator. *Nicholson* (1983) more rigorously derives the Boltzmann equation from Liouville's theorem, showing how the collision operator is effectively treated as a correlation function between two particles.

1.2.2 Binary Collisions

Before evaluating the collision operators used in the Boltzmann equation it is useful to understand the physics of a collision between two particles. An elastic collision conserves the total mass, momentum, and energy of the two-particle system. Inelastic collisions such as recombination, resonant charge exchange, and impact ionization are detailed in *Schunk and Nagy* (2009) and will not be discussed here. Figure 1.6 shows the geometry of a typical elastic collision between two particles with masses m_1 and m_2. The impact parameter, b, of a binary collision is defined as the distance of closest approach if the two particles were not to collide. A fundamental task in collision physics is to find the cross section σ of a collision, which is, roughly speaking, how big of a target m_2 presents to m_1 in Figure 1.6.

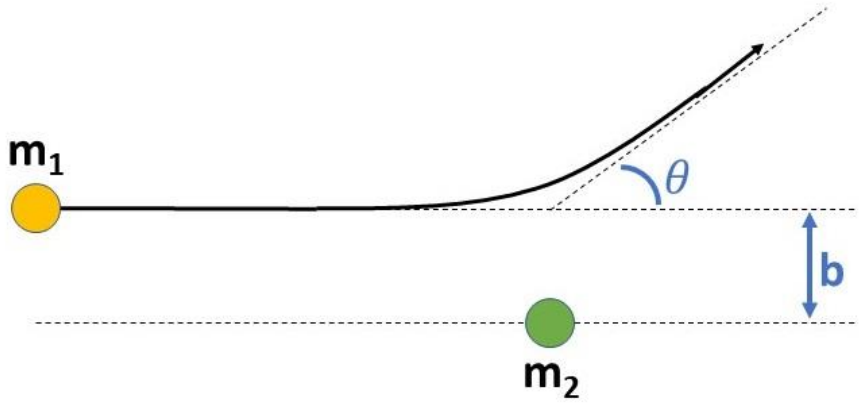

Figure 1.6 The geometry of a binary collision. In this schematic mass m_1 is moving towards and collides off a much heavier mass m_2. The angle between initial and final trajectory of m_1 defines the scattering angle θ, and the impact parameter b is the distance of closest approach if the particle did not scatter.

Consider a stream of particles with different impact parameters moving towards m_2. The number of particles that scatter off a specific area, $d\sigma$, of m_2 in a given time is

$$N = \Gamma \, d\sigma, \tag{1.16}$$

where Γ is the particle flux (dimensions of particles per area per time), and $d\sigma$ is defined as the differential cross section. Before scattering off the small target $d\sigma$, the particles must have come through a small range of impact parameters, db. Assuming a collision force that is symmetric about the $b = 0$ axis, the number of particles passing through a range of db at any angle of symmetry is

$$N = \Gamma 2\pi b \, db, \tag{1.17}$$

Since equations (1.16) and (1.17) are measuring the same number of particles per time,

$$\Gamma d\sigma = \Gamma 2\pi b \, db. \tag{1.18}$$

Equation (1.18) provides a direct relation between the impact parameter and the differential cross section (*Fetter and Walecka*, 2003). By the chain rule, equation (1.18) can be written as derivatives with respect to the final scattering solid angle $d\Omega = 2\pi \sin\theta \, d\theta$

$$\frac{d\sigma}{d\Omega} = \frac{b}{\sin\theta}\left|\frac{db}{d\theta}\right|. \tag{1.19}$$

Equation (1.19) is the differential cross section equation, which gives a relation between the target area of m_2 and the angle of deflection. The absolute value in equation (19) is therefore needed to ensure the target area is a positive, and physically meaningful

quantity. Integrating the differential cross section equation over all scattering angles yields the total collisional cross section:

$$\sigma \equiv \int_0^{\pi} \int_0^{2\pi} \left(\frac{d\sigma}{d\Omega}\right) d\Omega = \int_0^{\pi} 2\pi b \left|\frac{db}{d\theta}\right| d\theta \,. \tag{1.20}$$

The total scattering cross section is useful for defining several other collision parameters. Consider a particle m_1 moving at speed v through a gas of scattering particles with density n_s. A collision will occur if a scattering particle is within the scattering cross section, σ, of m_2 when m_1 makes its closest approach. The total number of collisions, dN_{coll}, in a given time increment, dt, is then equal to the total number of scattering particles inside a cylinder with cross section σ and length $v\ dt$, as shown in Figure 1.7. The number of collisions per unit time is then

$$dN_{coll} = n_s \sigma v\ dt. \tag{1.21}$$

This defines the *collision rate* or equivalently the *collision frequency*, f:

$$f \equiv \frac{dN_{coll}}{dt} = n_s \sigma v. \tag{1.22}$$

The collision rate is also frequently denoted by the Greek letter nu, ν, and this dissertation will use both f and ν depending on the context to avoid ambiguities with the distribution functions and velocity coordinates, often denoted by the letters f and v, with the latter typeset in equations as v. Typically, collision rates will also have a subscript for the species involved in the collision.

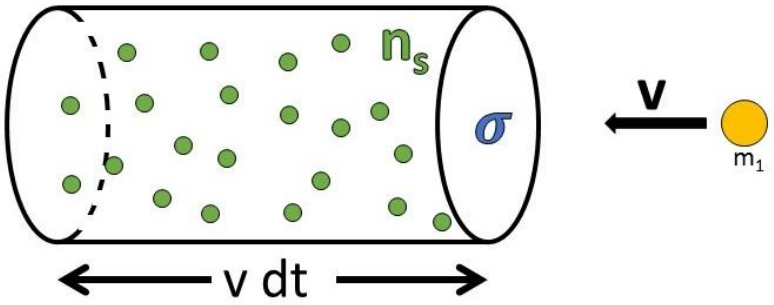

Figure 1.7. In a given time increment *dt*, an incident particle m_1 will scatter off all of the particles within a cylinder of length $v\ dt$ and cross-sectional area σ.

1.2.3 Scattering Cross Sections

To gain an understanding of the scattering cross section and collision frequency three different types of collisions will be examined:

1. Hard sphere collisions. These collisions are like two billiard balls striking each other and are a simple approximation for neutral-neutral collisions.
2. Maxwell molecule collisions. A spherically symmetric force with a $1/r^4$ potential, which is a good approximation for most charged-neutral collisions
3. Coulomb collisions. The $1/r^2$ electrostatic force describes the interaction between two charged particles.

<u>Hard Sphere Collisions</u>

The relation between the impact parameter and scattering angles is determined by the spherical geometry of the problem. For a small incoming particle colliding off a much larger sphere of radius *a*, the impact parameter is (*Fetter and Walecka*, 2003)

$$b = a\cos\left(\frac{\theta}{2}\right). \tag{1.23}$$

Taking the derivative of equation (1.23),

$$\left|\frac{db}{d\theta}\right| = \frac{a}{2}\sin\left(\frac{\theta}{2}\right). \tag{1.24}$$

From equation (1.19) the differential cross section after integrating over $d\phi$ is

$$\frac{d\sigma}{d\theta} = 2\pi b\left|\frac{db}{d\theta}\right| = \pi a^2\cos\left(\frac{\theta}{2}\right)\sin\left(\frac{\theta}{2}\right). \tag{1.25}$$

By a trig identity, $\sin(\theta/2)\cos(\theta/2) = \sin(\theta)/2$, and integrating equation (1.25) over all scattering angles yields the total scattering cross section:

$$\sigma = \int_0^{\pi}\left(\frac{d\sigma}{d\theta}\right)d\theta = \int_0^{\pi}\frac{\pi}{2}a^2\sin(\theta)\,d\theta = \pi a^2. \tag{1.26}$$

The scattering cross section is therefore the area of the target sphere, justifying the choice in terminology. Finally, the collision frequency for hard sphere collisions is

$$f = \pi a^2 n_s\, v. \tag{1.27}$$

Therefore, the hard sphere collision frequency increases linearly with the incident speed. The hard sphere collision model works for any two spherical particles that collide only by physically touching each other and is a good approximation for neutral-neutral collisions.

Maxwell Molecule Collisions

If a charged particle is approaching a neutral particle, the charge on the incident particle will push or pull the outer electrons of the neutral particle, creating a polarized electric field. The interaction between the charged particle and this polarization field is

called a Maxwell Molecule Collision, and the scattering is modeled by the potential energy function (*Schunk and Nagy*, 2009)

$$V(r) = \frac{\gamma}{r^4}, \tag{1.28}$$

where γ is a constant representing how easily the neutral particle is polarized.

To fully derive a differential cross section for a potential of the form $1/r^n$, with *n* a positive integer, the components of the final velocity must be found. For an elastic collision of a particle with an initial speed v_i in the ∥ direction, the kinematic relations are (*Nicholson*, 1983)

$$mv_\perp = \int_{-\infty}^{\infty} F_\perp(t)dt\,, \tag{1.29}$$

$$v_\parallel = \sqrt{v_i^2 - v_\perp^2}. \tag{1.30}$$

The interaction force in the perpendicular direction, $F_\perp$, is a function of the impact parameter, and the angle between the final velocities $v_\perp$ and $v_\parallel$ is the scattering angle. Deriving the relation between *b* and θ using equations (1.29) – (1.30) is exact, but cumbersome. With surprising accuracy, the same relation can be found much quicker with the following approximation for the scattering angle (*Bellan*, 2006)

$$\tan\left(\frac{\theta}{2}\right) \approx \frac{Interaction\ Energy}{Kinetic\ Energy}. \tag{1.31}$$

The initial kinetic energy of the charged particle is $m_1 v^2$, and the potential energy at closest approach is $V(b)$ using equation (1.28). Then the cross section is calculated as

$$\tan\left(\frac{\theta}{2}\right) = \frac{\gamma}{b^4 m_1 v^2}, \tag{1.32}$$

$$\left|\frac{db}{d\theta}\right| = \frac{1}{8}\left(\frac{\gamma}{mv^2}\right)^{\frac{1}{4}} \frac{\csc^2(\theta/2)}{\cot^{3/4}(\theta/2)}, \tag{1.33}$$

$$\sigma = \frac{\pi}{4v}\sqrt{\frac{\gamma}{m}} \int_0^{\pi} \frac{\sqrt{\tan(\theta/2)}}{\sin^2(\theta/2)}\, d\theta\,, \tag{1.34}$$

Evaluating the indefinite integral,

$$\sigma = \frac{\pi}{4v}\sqrt{\frac{\gamma}{m}}\left[-4\frac{\cos(\theta/2)}{\sin(\theta/2)}\right]_0^{\pi}. \tag{1.35}$$

Equation (1.35) shows an immediate problem with this approach, while the upper bound $\theta = \pi$ evaluates to 0, the lower bound of $\theta = 0$ diverges. Physically this occurs because the $1/r^4$ potential influences particles at an infinite range, leading to infinitesimal scattering angles of $\theta \approx 0$. Practically this result is useless and meaningless, any system of interest will be finite in size, or the charged particle will interact more strongly with closer particles. The integral in equation (1.35) can be saved if a practical upper bound on the impact parameter can be determined, but there is no universal bound for a charged particle streaming through a neutral gas. Instead we must ask what the useful quantity is we want from a collision. While infinitesimal deflections do add to the scattering cross section defined by equation (1.20), they do not deflect the trajectory of the charged particle in a meaningful way.

Instead of asking how often a collision with any scattering angle occurs, it is useful to ask how often collisions affect a property of the incident particles. The

momentum scattering rate is defined as the rate at which collisions deflect an incident particle by 90°, and is calculated as the first moment of the differential cross section (*Schunk and Nagy*, 2009):

$$\sigma \equiv \int_0^{\pi} \left(\frac{d\sigma}{d\theta}\right)(1-\cos\theta)d\theta = \int_0^{\pi} 2\pi b \left|\frac{db}{d\theta}\right|(1-\cos\theta)d\theta\,. \tag{1.36}$$

Similarly, the second moment integrates over $(1-\cos^2\theta)$, and is called the *energy scattering rate*, which is the rate at which a colliding particle transfers all its energy to the background scattering population. We can now reevaluate the integral in equation (1.34) to find the momentum scattering cross section of Maxwell molecules collisions:

$$\sigma = \frac{\pi}{4v}\sqrt{\frac{\gamma}{m}}\int_0^{\pi}\frac{\sqrt{\tan(\theta/2)}}{\sin^2(\theta/2)}(1-\cos\theta)d\theta\,. \tag{1.37}$$

This integral now converges as the $1-\cos\theta$ term effectively kills the contribution of infinitesimal scatterings to the total cross section. Figure 1.8 (a) compares the integrands in equations (1.34) and (1.37). Evaluating the integral yields

$$\sigma = 8.88577\ \frac{\pi}{4v}\sqrt{\frac{\gamma}{m}}. \tag{1.38}$$

The numerical constants, including the polarizability and the mass of the incident particle, can all be grouped together as a single constant α, so

$$\sigma = \frac{\alpha}{v}. \tag{1.39}$$

The momentum collision rate is then

$$f = n\sigma v = n\alpha. \tag{1.40}$$

Equation (1.40) is remarkably simple, which is why the Maxwell molecule collision model is frequently used for charged-neutral collisions. The collision rate is independent of the incident velocity, so a distribution of charged particles will all collide at the same rate. While the Maxwell molecule collision is a good approximation for most charged-neutral collisions, collisions between O^+ and H as well as collisions between an ion and its parent atom involve a resonant charge exchange, and the cross sections need to be measured by experiments (*Schunk and Nagy*, 2009).

1.2.4 Coulomb Collisions

Coulomb's Law describes the interaction between two particles with charges q_1 and q_2:

$$V(r) = -\frac{q_1 q_2}{4\pi\epsilon_0 r}. \tag{1.41}$$

Using the approximation in equation (1.31), the relation between the impact parameter and scattering angle for a Coulomb collision is (*Bellan*, 2006)

$$\tan\left(\frac{\theta}{2}\right) = \frac{q_1 q_2}{4\pi\epsilon_0 b \cdot mv^2}. \tag{1.42}$$

The scattering cross section is then derived as

$$b = \frac{q_1 q_2}{4\pi\epsilon_0 mv^2}\cot\left(\frac{\theta}{2}\right), \tag{1.43}$$

$$\left|\frac{db}{d\theta}\right| = \frac{q_1 q_2}{8\pi\epsilon_0 mv^2}\csc^2\left(\frac{\theta}{2}\right), \tag{1.44}$$

$$\sigma = \frac{q_1^2 q_2^2}{16\pi\epsilon_0^2 m^2 v^4} \int_0^{\pi} \csc^2\left(\frac{\theta}{2}\right) \cot\left(\frac{\theta}{2}\right) d\theta \,. \tag{1.45}$$

As expected for a $1/r^2$ force with infinite range, the integral in equation (1.45) diverges at $\theta = 0$, just like the integral for Maxwell molecule collisions. Unfortunately, this problem persists when calculating the momentum scattering cross section using equation (1.36). Figure 1.8 plots the integrand in equation (1.45), and the integrand of the first moment with the $1 - \cos(\theta)$ factor, alongside the same integrands for the Maxwell molecule collisions.

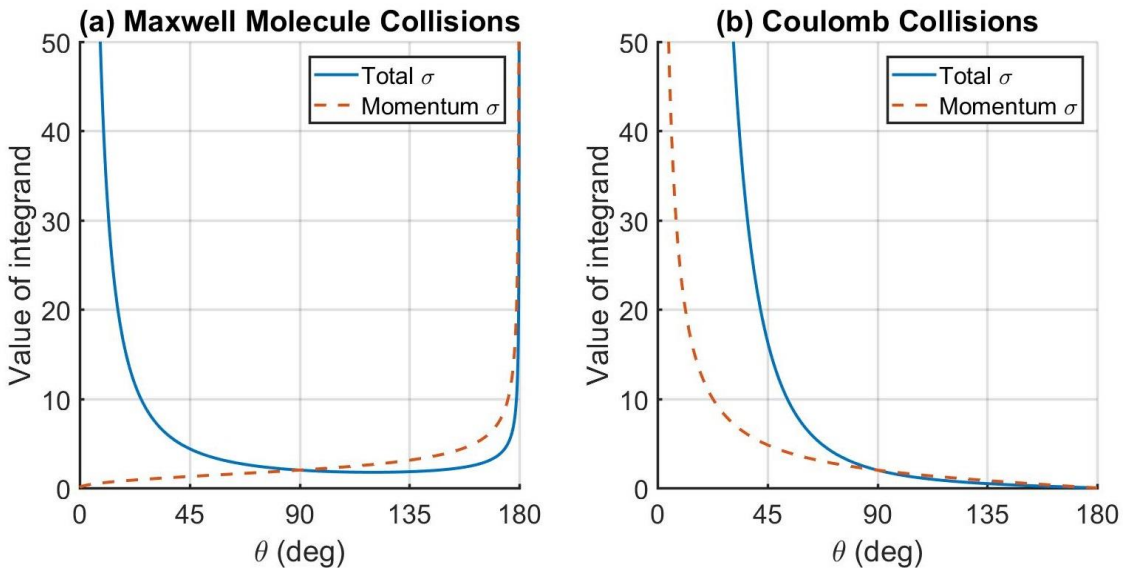

Figure 1.8 The integrands for evaluating the Maxwell molecule cross section (a) and the Coulomb collision cross section (b). The solid blue curve shows the value of the integrand for the total collision cross sections in equations (1.34) and (1.45). The dashed red line is the integrand for the momentum scattering cross section and is equal to the blue curve multiplied by $1 - \cos(\theta)$. All of the integrals converge at $\theta = 180°$, but only the momentum scattering cross section for Maxwell molecules converges at $\theta = 0°$.

Figure 1.8 shows how different the Maxwell molecule and Coulomb collision cross sections are. For the Maxwell molecules, the momentum cross section is integrable,

and shows that large angle collisions of $90° \leq \theta \leq 180°$ dominate the momentum transfer process over small angle collisions. For Coulomb collisions this is not the case, large angle collisions are a minor contribution to the cross section, and the integral does not converge as $\theta \to 0$ for either cross section. To investigate the importance of large vs. small angle Coulomb collisions we will evaluate the total scattering cross section for all large angle collisions, $90° \leq \theta \leq 180°$. From equation (1.45) this is

$$\sigma_L = \frac{q_1^2 q_2^2}{16\pi\epsilon_0^2 m^2 v^4} \int_{\frac{\pi}{2}}^{\pi} \csc^2\left(\frac{\theta}{2}\right) \cot\left(\frac{\theta}{2}\right) d\theta \,. \tag{1.46}$$

The integral evaluates to 1, so the large angle cross section for Coulomb collisions is

$$\sigma_L = \frac{q_1^2 q_2^2}{16\pi\epsilon_0^2 m^2 v^4}. \tag{1.47}$$

Recognizing from equation (1.42) that a 90° scattering has an impact parameter of

$$b_{90} = \frac{q_1 q_2}{4\pi\epsilon_0 m v^2}, \tag{1.48}$$

the large angle scattering cross section is simply

$$\sigma_L = \pi b_{90}^2. \tag{1.49}$$

The collision frequency for large angle scatterings is then

$$f_L = \frac{n q_1^2 q_2^2}{16\pi\epsilon_0^2 m^2 v^3}. \tag{1.50}$$

We now wish to see the combined effect of all small angle scatterings, which occur across a much larger range of impact parameters. For an accumulation of small

angle scatterings to matter, the cumulative effect must be the same order of magnitude as a single large angle scattering. Adding repeated deflections $\theta_1 + \theta_2 + \cdots$ will have a 0 mean, so the cumulative effect of interest is $\sum_i^N \theta_i^2$. For a large angle scattering this sum is simply θ_L^2, which we can take to be about 1 radian. Thus, we are interested in determining how many small angle collisions must occur such that (*Bellan*, 2006)

$$1 \approx \sum_i^N \theta_i^2 \,. \tag{1.51}$$

The flux of background particles past the test particle is $\Gamma = nv$. Therefore, in a given time *t*, the number of particles passing through the ring of width *db* is

$$N_{db} = \Gamma t(2\pi b db). \tag{1.52}$$

In the time *t*, the ring from *b* to *b*+*db* gives a small angle scattering contribution of

$$\theta_{db}^2 = \Gamma t(2\pi b)\theta^2(b) db. \tag{1.53}$$

The total net scattering is then found by integrating equation (1.53) over *b*,

$$1 \approx \sum_i^N \theta_i^2 = \int \Gamma t(2\pi b)\, \theta^2 db. \tag{1.54}$$

Now $\Gamma = nv$, and the collision frequency is defined as $f = n\sigma v$, so $f = \Gamma\sigma$. The collision frequency is the inverse of a relaxation time, which for our problem of interest is the time required for $\sum \theta_i^2 = 1$, thus $\Gamma\sigma = 1/t$, or $\Gamma t = 1/\sigma_s$, where σ_s is the effective scattering cross section for repeated small angle scatterings. Then we have

$$1 = \frac{2\pi}{\sigma_s} \int b\, \theta^2 db\,. \tag{1.55}$$

Since we are interested in small angle scatterings, we can simplify $\theta(b)$ in equation (1.42) by Taylor expanding $\tan(\theta/2) \approx \theta/2$ to find

$$\theta \approx \frac{q_1 q_2}{2\pi\epsilon_0 b m v^2}. \tag{1.56}$$

Substituting into equation (1.55), the small angle scattering cross section is

$$\sigma_s = 2\pi \int b \left(\frac{e^2}{2\pi\epsilon_0 b m v^2}\right) db\,, \tag{1.57}$$

$$\sigma_s = \frac{e^4}{2\pi\epsilon_0^2 m^2 v^4} \int \frac{1}{b} db\,. \tag{1.58}$$

Recognizing that the constants in front of the integral in equation (1.58) are related to the large angle cross section, we can simplify to

$$\sigma_s = 8\sigma_L \int \frac{1}{b} db\,. \tag{1.59}$$

This provides a direct relation between the total scattering cross sections of large vs. small angle scatterings, but the limits of the integral in equation (1.59) are still unspecified. At small impact parameters, $b \to 0$, the collision is a large angle scattering, so the lower integration bound is b_{90} from equation (1.48). The upper bound relates back to the problem of the Coulomb force having infinite range. Fortunately, we are only interested in Coulomb collisions in a plasma, and the $1/r^2$ force between two particles is Debye shielded, which means electrons and ions in a plasma reconfigure to shield point

charges at large distances. Debye shielding exponentially reduces the electric potential as a function of distance, resulting in the potential (*Bellan*, 2006)

$$\phi(r) = \frac{q_1 q_2}{4\pi\epsilon_0 r}\exp\left(-\frac{r}{\lambda_D}\right), \tag{1.60}$$

with the Debye length defined as

$$\lambda_D = \sqrt{\frac{\epsilon_0 K_B T}{ne^2}}. \tag{1.61}$$

Taking the Debye length as the upper bound for the integral in equation (1.59), the small angle cross section is

$$\sigma_s = 8\sigma_L \int_{b_{90}}^{\lambda_D} \frac{1}{b} db = 8\sigma_L \log\left(\frac{\lambda_D}{b_m}\right). \tag{1.62}$$

The logarithmic dependence on the integral in equation (1.62) means the small angle cross section is not very sensitive to λ_D as an approximate upper bound on the integration. This limit is further discussed in Section 1.2.6. Substituting for b_{90} in equation (1.62) defines the Coulomb logarithm,

$$\Lambda = \log\left(\frac{4\pi\epsilon_0 m v^2 \lambda_D}{q_1 q_2}\right). \tag{1.63}$$

The Coulomb logarithm (sometimes denoted $\log\Lambda$) is in the range of 10 to 15 for most plasmas of interest and is always greater than 1 for a plasma (*Chen*, 2016). Equation (1.62) shows that the effect of small angle Coulomb collisions is $8\Lambda \approx 100$ times larger

than the effect of large angle Coulomb collisions. We can therefore use the small angle collision frequency for Coulomb collisions:

$$f = n\sigma_s v = \frac{nq_1^2 q_2^2 \Lambda}{2\pi\epsilon_0^2 m^2 v^3}. \tag{1.64}$$

This strong dependence on velocity means Coulomb collisions cannot be modeled as a single process effecting the whole distribution equally. A kinetic treatment is needed to account for every particle having a different velocity, which the next section develops.

1.2.5 The Fokker-Planck Equation

In this section a Coulomb collision operator is derived for the Boltzmann equation, allowing for a kinetic treatment of Coulomb collisions. The Boltzmann equation can be written using Liouville's theorem:

$$\frac{Df}{Dt} = \left(\frac{\partial f}{\partial t}\right)_{coll}. \tag{1.65}$$

The left-hand side of equation (1.65) is the total time derivative of the distribution, so the right-hand side represents abrupt or discontinuous changes in the distribution function. Consider a particle moving with velocity $\vec{v}$. The conditional probability of the particle abruptly changing velocity to $\vec{v} + \Delta\vec{v}$ in a time increment *dt* is defined as (*Bellan*, 2006)

$$P = F(\vec{v}, \Delta\vec{v}). \tag{1.66}$$

After a collision (or lack of collision if $\Delta\vec{v} = 0$) the particle must end up at some velocity, so the integral of *F* over all possible changes in velocity $\Delta\vec{v}$ is

$$1 = \int_{-\infty}^{\infty} F(\vec{v}, \Delta\vec{v})\, d(\Delta\vec{v}). \tag{1.67}$$

Since *F* is a conditional probability, it can be used to relate how the distribution $f(\vec{v}, t)$ evolved from a previous time, $t - \Delta t$. A particle can be scattered into $f(\vec{v}, t)$ from any prior velocity $\vec{v} - \Delta\vec{v}$ according to the probability *F*. Thus, the distribution $f(\vec{v}, t)$ evolves from the previous time, by a weighted average of $f(\vec{v} - \Delta\vec{v}, t - \Delta t)$:

$$f(\vec{v}, t) = \int f(\vec{v} - \Delta\vec{v}, t - \Delta t) F(\vec{v} - \Delta\vec{v}, \Delta\vec{v}) d(\Delta\vec{v})\,. \tag{1.68}$$

Equation (1.68) is the *Boltzmann collision integral*, and is an exact statement of how the distribution evolves in time due to collisions occurring with the probability weights *F*.

As shown in the previous section, Coulomb collisions are dominated by small angle scatterings, so the integrand in the Boltzmann collision integral can be Taylor expanded for small changes in velocity, $\Delta\vec{v}$, (*Bellan*, 2006):

$$f(\vec{v}, t) = \int \left[\begin{array}{c} f(\vec{v}, t) F(\vec{v}, \Delta\vec{v}) - \Delta t \dfrac{\partial f}{\partial t}\, F(\vec{v}, \Delta\vec{v}) - \Delta\vec{v} \cdot \dfrac{\partial}{\partial \vec{v}} \left(f(\vec{v}, t) F(\vec{v}, \Delta\vec{v}) \right) \\ + \dfrac{1}{2} \Delta\vec{v}\Delta\vec{v} : \dfrac{\partial}{\partial \vec{v}} \dfrac{\partial}{\partial \vec{v}} \left(f(\vec{v}, t) F(\vec{v}, \Delta v) \right) \end{array} \right] d(\Delta\vec{v})\,. \tag{1.69}$$

In the last term the : symbol is the double dot product of two dyadic tensors. The result of a double dot product is a scalar, and explicitly this term in equation (1.69) is

$$\Delta\vec{v}\Delta\vec{v} : \frac{\partial}{\partial \vec{v}} \frac{\partial}{\partial \vec{v}} \left(f(\vec{v}, t) F(\vec{v}, \Delta v) \right) = \left(\Delta\vec{v} \cdot \frac{\partial}{\partial \vec{v}} \right) \left(\Delta\vec{v} \cdot \frac{\partial}{\partial \vec{v}} \right) \left(f(\vec{v}, t) F(\vec{v}, \Delta v) \right)$$

Rearranging equation (1.69) to pull terms independent of $\Delta\vec{v}$ out of the integral,

$$f(\vec{v},t) = f(\vec{v},t)\int F(\vec{v},\Delta\vec{v})\,d(\Delta\vec{v}) - \Delta t\frac{\partial f}{\partial t}\int F(\vec{v},\Delta\vec{v})d(\Delta\vec{v})$$
$$-\int \Delta\vec{v}\cdot\frac{\partial}{\partial\vec{v}}\big(f(\vec{v},t)F(\vec{v},\Delta\vec{v})\big)d(\Delta\vec{v}) + \frac{1}{2}\int \Delta\vec{v}\Delta\vec{v}:\frac{\partial}{\partial\vec{v}}\frac{\partial}{\partial\vec{v}}\big(f(\vec{v},t)F(\vec{v},\Delta v)\big)\,d(\Delta\vec{v})$$

The first two integrals evaluate to 1 by the definition of *F* in equation (1.67). Since $\vec{v}$ and $\Delta\vec{v}$ are independent variables, the derivatives in the last two integrals can be reordered. Equation (1.69) then simplifies to (suppressing the dependence of *f* on $\vec{v}$ and *t*)

$$\frac{\partial f}{\partial t} = -\frac{\partial}{\partial\vec{v}}\cdot\left[f\int\frac{\Delta\vec{v}}{\Delta t}F(\vec{v},\Delta\vec{v})d(\Delta\vec{v})\right] + \frac{1}{2}\frac{\partial}{\partial\vec{v}}\frac{\partial}{\partial\vec{v}}:\left[f\int\frac{\Delta\vec{v}\Delta\vec{v}}{\Delta t}F(\vec{v},\Delta\vec{v})d(\Delta\vec{v})\right]. \quad (1.70)$$

The integrals in equation (1.70) are mathematically equivalent to averaging $\Delta\vec{v}/\Delta t$ and $\Delta\vec{v}\Delta\vec{v}/\Delta t$ over the probability distribution *F*. The drag friction vector and diffusion tensors are defined respectively as

$$\vec{F}_d = \langle\frac{\Delta\vec{v}}{\Delta t}\rangle = \int\frac{\Delta\vec{v}}{\Delta t}F(\vec{v},\Delta\vec{v})d(\Delta\vec{v}), \quad (1.71)$$

$$\overline{D} = \langle\frac{\Delta\vec{v}\Delta\vec{v}}{\Delta t}\rangle = \int\frac{\Delta\vec{v}\Delta\vec{v}}{\Delta t}F(\vec{v},\Delta\vec{v})d(\Delta\vec{v}). \quad (1.72)$$

With these definitions, equation (1.70) can be written in a more compact form:

$$\frac{\partial f}{\partial t} = -\frac{\partial}{\partial\vec{v}}\cdot\left[f\vec{F}_D\right] + \frac{1}{2}\frac{\partial}{\partial\vec{v}}\frac{\partial}{\partial\vec{v}}:[f\overline{D}], \quad (1.73)$$

where *f*, $\vec{F}_D$, and $\overline{D}$ all have a time and velocity dependence. Equation (1.73) is the *Fokker-Planck collision operator*, and physically describes how small angle collisions change the distribution through a deterministic drag force and a stochastic diffusion process. After evaluating the drag and diffusion coefficients this collision operator can be

substituted into the right-hand side of the Boltzmann equation for a kinetic treatment of Coulomb collisions (*Nicholson,* 1983). While the Fokker-Planck collision operator is applied to Coulomb collisions in this dissertation, it is a robust collision operator that can be applied many other collision processes, including wave-particle scatterings in the radiation belts (*Zheng et al.*, 2014).

1.2.6 Rosenbluth Potentials

The averaging of $\Delta\vec{v}$ and $\Delta\vec{v}\Delta\vec{v}$ in equations (1.71) – (1.72) is accomplished using the scattering relation for Coulomb collisions. Generalizing $\theta(b)$ for collisions between charged particles of any mass, equation (1.56) becomes

$$\theta = \frac{q_1 q_2}{2\pi\epsilon_0 b\mu v^2}, \tag{1.74}$$

where the reduced mass, μ, accounts for the efficiency at which momentum is exchanged in a collision between two particles of arbitrary masses m_1 and m_2:

$$\mu = \frac{m_1 m_2}{m_1 + m_2}. \tag{1.75}$$

The reduced mass transforms the problem to the center of mass frame where it can be treated as one-body motion, with the relative velocity

$$\vec{v}_{rel} = \vec{v}_1 - \vec{v}_2. \tag{1.76}$$

The relative speed is unchanged in an elastic collision. For a particle initially moving in the z-direction, undergoing a collision of angle θ, the post collision velocity, $\vec{v}'_{rel}$, is (*Bellan,* 2006)

$$\vec{v}'_{rel} = v_{rel}\cos(\theta)\,\hat{z} + v_{rel}\sin(\theta)\,\hat{b}. \tag{1.77}$$

The unit vector $\hat{b}$ can lie anywhere in the x-y plane, so $\hat{b} = \hat{x}\cos\phi + \hat{y}\sin\phi$. The difference between the initial and final relative velocities is the desired $\Delta\vec{v}$:

$$\Delta\vec{v} = \vec{v}'_{rel} - \vec{v}_{rel} = v_{rel}(1-\cos\theta)\hat{z} + v_{rel}\sin\theta\,(\cos\phi\,\hat{x} + \sin\phi\,\hat{y}). \tag{1.78}$$

Since Coulomb collisions are small angle scatters, equation (1.78) Taylor expands to

$$\Delta\vec{v} = v_{rel}\left(\theta\cos\phi\,\hat{x} + \theta\sin\phi\,\hat{y} - \frac{1}{2}\theta^2\hat{z}\right). \tag{1.79}$$

Equation (1.79) was calculated in the center of mass frame. Transforming back to the lab frame to calculate $\langle\Delta\vec{v}/\Delta t\rangle$ simply requires multiplying equation (1.79) by μ/m_1.

Substituting equation (1.74) into equation (1.79) yields $\Delta\vec{v}(b,\phi)$ for Coulomb collisions. In order to calculate the drag and diffusion coefficients for the Fokker-Planck collision operator the probability function $F(\vec{v},\Delta\vec{v})$ needs to be calculated. Consider a test particle (T) with fixed speed *v* incident on a large group of field particles (F). The probability $F(\vec{v},\Delta\vec{v})$ is the conditional probability that a test particle moving at velocity $\vec{v}$ will scatter to $\vec{v}+\Delta\vec{v}$, which is precisely what the differential cross section measures. For a fixed time increment Δt, and fixed field particle velocity $\vec{v}_F$, the probability of a scattering by $\Delta\vec{v}$ is simply $\sigma\Delta t$. The total probability of scattering by $\Delta\vec{v}$ is the integral of $d\sigma/d\Omega\,\Delta t$ over all possible field particle velocities,

$$F(\vec{v},\Delta\vec{v}) = \int \frac{d\sigma}{d\Omega} f_F(\vec{v}_F)\Delta t\; d\vec{v}_F\,, \tag{1.80}$$

where the distribution f_F weights the likelihood of a field particle having a given velocity.

Substituting equation (1.80) into equation (1.71) for the drag coefficient,

$$\vec{F}_d = \langle \frac{\Delta\vec{v}}{\Delta t} \rangle = \int \int \Delta\vec{v} f_F(\vec{v}_F) \frac{d\sigma}{d\Omega}\, d\vec{v}_F d(\Delta\vec{v})\,. \tag{1.81}$$

The integration volume $d\Delta\vec{v}$ is best done in spherical coordinates. Since v_{rel} does not change in an elastic collision, the spherical volume element is just the surface element $d\Delta\vec{v} = v_{rel} \sin\theta\, d\theta d\phi$. The drag coefficient is then

$$\vec{F}_d = \int d\vec{v}_F \int f_F(\vec{v}_F) \Delta\vec{v}\, v_{rel} \frac{d\sigma}{d\Omega} \sin\theta\, d\theta d\phi\,. \tag{1.82}$$

From the definition of differential cross section in equation (1.19) the integral over θ can be rewritten as an integral over the impact parameter:

$$\vec{F}_d = \int d\vec{v}_F \int f_F(\vec{v}_F) \Delta\vec{v}\, v_{rel}\, b\, db d\phi\,. \tag{1.83}$$

Substituting equation (1.79) for $\Delta\vec{v}$, including the frame of reference change,

$$\vec{F}_d = \int d\vec{v}_F \int f_F(\vec{v}_F) \frac{\mu}{m_1} v_{rel}^2 \left(\theta \cos\phi\, \hat{x} + \theta \sin\phi\, \hat{y} - \frac{1}{2}\theta^2 \hat{z}\right) b\, db d\phi\,. \tag{1.84}$$

The azimuthal angle ϕ only appears in equation (1.84) as the sine and cosine terms, so the integral of the $\hat{x}$ and $\hat{y}$ terms over the bounds of $\phi = [0, 2\pi]$ is 0. Integrating the $\hat{z}$ term yields a factor of 2π, so equation (1.84) simplifies to

$$\vec{F}_d = -\hat{z}\, \frac{\pi\mu}{m_1} \int d\vec{v}_F \int f_F(\vec{v}_F)\, v_{rel}^2 \theta^2\, b\, db\,. \tag{1.85}$$

Substituting for $\theta(b)$,

$$\vec{F}_d = -\hat{z}\frac{q_1^2 q_2^2}{4\pi\epsilon_0^2\mu^2}\frac{\mu}{m_1}\int d\vec{v}_F \int f_F(\vec{v}_F)\frac{1}{b v_{rel}^2}\, db\,. \tag{1.86}$$

The integral of $1/b$ is a logarithm, which diverges for the bounds $b = [0, \infty]$. This is the same problem encountered in Section 1.2.4, so the upper bound is set to the Debye length, where the 1/r potential is screened by a factor of $1/e$. The Taylor expansion for $\theta(b)$ is only valid for small scatterings, so the lower bound is b_{90} from equation (1.48). Integrating equation (1.86) over *b* with these limits produces the Coulomb logarithm, so

$$\vec{F}_d = -\hat{z}\frac{q_1^2 q_2^2 \Lambda}{4\pi\epsilon_0^2\mu m_1}\int f_F(\vec{v}_F)\frac{1}{v_{rel}^2}\, d\vec{v}_F\,. \tag{1.87}$$

The integral over the field particle distribution still needs to be evaluated. By assumption $\vec{v}_{rel} = v_{rel}\hat{z}$, so equation (1.87) can be written in a general coordinate system,

$$\vec{F}_d = -\frac{q_1^2 q_2^2 \Lambda}{4\pi\epsilon_0^2\mu^2}\frac{\mu}{m_1}\int f_F(\vec{v}_F)\frac{\vec{v}_{rel}}{v_{rel}^3}\, d\vec{v}_F\,. \tag{1.88}$$

From *Bellan* (2006), the relative velocity is $\vec{v}_{rel} = \vec{v} - \vec{v}_F$, and the integrand can be rewritten in terms of the velocity gradient,

$$\vec{F}_d = \frac{q_1^2 q_2^2 \Lambda}{4\pi\epsilon_0^2\mu m_1}\frac{\partial}{\partial\vec{v}}\frac{\mu}{m_1}\int \frac{f_F(\vec{v}_F)}{|\vec{v} - \vec{v}_F|}\, d\vec{v}_F\,. \tag{1.89}$$

The drag coefficient cannot be further evaluated until the field particle distribution, f_F, is specified. For notational convenience, the integral in equation (1.89) is defined as the *H Rosenbluth potential* (*Rosenbluth et al.*, 1957):

$$H_F(\vec{v}) = \frac{\mu}{m_1}\int \frac{f_F(\vec{v}_F)}{|\vec{v} - \vec{v}_F|}\, d\vec{v}_F\,. \tag{1.90}$$

Equation (1.89) calculates the drag coefficient for Coulomb collisions between two particles of any mass or charge. The same procedure for averaging $\Delta\vec{v}\Delta\vec{v}$ can be followed to produce the diffusion coefficient. Equation (1.83) can be rewritten as the average of $\Delta\vec{v}\Delta\vec{v}$:

$$D = \langle\frac{\Delta\vec{v}\Delta\vec{v}}{\Delta t}\rangle = \int d\vec{v}_F \int f_F(\vec{v}_F)\Delta\vec{v}\Delta\vec{v}\; v_{rel}\; b\; dbd\phi\,. \tag{1.91}$$

The integrand is now over the dyadic tensor $\Delta\vec{v}\Delta\vec{v}$, which is

$$\Delta\vec{v}\Delta\vec{v} = v_{rel}^2\theta^2\begin{pmatrix} \cos^2\phi & \cos\phi\sin\phi & -\theta\cos\phi/2 \\ \cos\phi\sin\phi & \sin^2\phi & -\theta\sin\phi/2 \\ -\theta\cos\phi/2 & -\theta\sin\phi/2 & \theta^2/4 \end{pmatrix}. \tag{1.92}$$

The integration of equation (1.92) over the azimuth angle yields

$$\int_0^{2\pi}(\Delta\vec{v}\Delta\vec{v})\,d\phi = \pi v_{rel}^2\theta^2\begin{pmatrix} 1 & 0 & 0 \\ 0 & 1 & 0 \\ 0 & 0 & \theta^2/2 \end{pmatrix}. \tag{1.93}$$

Thus, the only terms that survive are the diagonal ones. Furthermore, the *zz* term scales as θ^4, and since small angle scatterings are assumed this term is negligible compared to the θ^2 terms. The resulting matrix in a coordinate independent form is (*Bellan*, 2006)

$$\begin{pmatrix} 1 & 0 & 0 \\ 0 & 1 & 0 \\ 0 & 0 & 0 \end{pmatrix} = \bar{I} - \frac{\vec{v}_{rel}\vec{v}_{rel}}{v_{rel}^2}, \tag{1.94}$$

where $\bar{I}$ is the identity matrix. The diffusion coefficient is then

$$D = \pi\int d\vec{v}_F \int f_F(\vec{v}_F)\; v_{rel}^2\theta^2\left(\bar{I} - \frac{\vec{v}_{rel}\vec{v}_{rel}}{v_{rel}^2}\right)\; b\; db\,. \tag{1.95}$$

Substituting for $\theta(b)$ and multiplying by μ^2/m_1^2 to change to the lab frame of reference,

$$D = \frac{q_1^2 q_2^2}{4\pi\epsilon_0^2 m_1^2} \int d\vec{v}_F \int f_F(\vec{v}_F) \left(\bar{I} - \frac{\vec{v}_{rel}\vec{v}_{rel}}{v_{rel}^2} \right) \frac{1}{b}\, db\,. \tag{1.96}$$

The integration over *b* once again produces the Coulomb logarithm, so

$$D = \frac{q_1^2 q_2^2 \Lambda}{4\pi\epsilon_0^2 m_1^2} \int f_F(\vec{v}_F) \left(\bar{I} - \frac{\vec{v}_{rel}\vec{v}_{rel}}{v_{rel}^2} \right) d\vec{v}_F\,. \tag{1.97}$$

With a change of integration variables, the integral is (*Bellan*, 2006)

$$D = \frac{q_1^2 q_2^2 \Lambda}{4\pi\epsilon_0^2 m_1^2} \frac{\partial}{\partial \vec{v}} \frac{\partial}{\partial \vec{v}} \int f_F(\vec{v}_F) |\vec{v} - \vec{v}_F| d\vec{v}_F\,. \tag{1.98}$$

The integration over the field distribution is defined as the *G Rosenbluth potential*:

$$G_F(\vec{v}) = \int f_F(\vec{v}_F) |\vec{v} - \vec{v}_F| d\vec{v}_F\,. \tag{1.99}$$

The definition of the Rosenbluth potentials in equations (1.90) and (1.99) allows the Fokker-Planck equation for Coulomb collisions to be written in explicit form as

$$\frac{\partial f}{\partial t} = \frac{q_1^2 q_2^2 \Lambda}{4\pi\epsilon_0^2 \mu m_1} \left(-\frac{\partial}{\partial \vec{v}} \cdot \left[f \frac{\partial H_F}{\partial \vec{v}} \right] + \frac{1}{2} \frac{\partial}{\partial \vec{v}} \frac{\partial}{\partial \vec{v}} : \left[f \frac{\partial^2 G_F}{\partial \vec{v} \partial \vec{v}} \right] \right). \tag{1.100}$$

In the form of equation (1.100) the Fokker-Planck collision operator is ready to use once the field distribution f_F is specified and the Rosenbluth potentials are calculated. It is important to note that while the Fokker-Planck collision operator has broad applications, the form of $\theta(b)$ used to derive equation (1.100) places restrictions on its use. First, the neglect of large angle scatters limits the application to low energy regimes less than 13.6 eV, at which point the scattering becomes quantum mechanical in nature (*Shkarofsky et al.*, 1966). The upper bound of $b = \lambda_D$ restricts the use of equation (1.100) to frequencies

$\omega \ll \omega_p$. At frequencies near the plasma frequency, Debye shielding cannot screen the potential fast enough and the scattering process is no longer a two-particle correlation, so the Coulomb logarithm is derived differently by considering the Bremsstrahlung radiation of an electron-ion collision in the quantum mechanical limit (*Shkarofsky et al.*, 1966).

The Fokker-Planck collision operator in equation (1.100) will be used in kinetic simulations in this dissertation. Since the Rosenbluth potentials are integrals over a particle distribution, analytic solutions of the Boltzmann equation with equation (1.100) can be difficult. A common simplification of the Fokker-Planck collision operator is the *Brownian collision operator* (also called Brownian motion operator). This collision operator is derived from the general Fokker-Planck collision operator in equation (1.73) by assuming a linear drag coefficient and a constant diffusion coefficient:

$$\vec{F}_d = -\langle \nu_{12} \rangle \vec{v}, \tag{1.101}$$

$$D = \langle \nu_{12} \rangle v_{th}^2. \tag{1.102}$$

The average collision rate in equations (1.101) and (1.102) is often taken as the Spitzer collision rate, which makes the substitution $v \to \sqrt{2KT/m} = \sqrt{2} v_{th}$ in equation (1.64):

$$\langle \nu_{12} \rangle = \frac{n q_1^2 q_2^2 \Lambda}{4\sqrt{2}\pi \epsilon_0^2 m^2 v_{th}^3}. \tag{1.103}$$

The Brownian motion collision operator is then (*Nicholson*, 1983)

$$\frac{\partial f}{\partial t} = \langle \nu_{12} \rangle \frac{\partial}{\partial \vec{v}} \cdot (f \vec{v}) + \langle \nu_{12} \rangle v_{th}^2 \frac{\partial^2}{\partial \vec{v} \partial \vec{v}} f. \tag{1.104}$$

Section 2.3 uses this Brownian collision operator to derive an analytic solution for collisional ISR spectra.

The Brownian collision operator tries to reduce the complexity of the Fokker-Planck equation by making the collision frequency independent of velocity. The resulting collision operator still has first and second order derivatives of the distribution, which are difficult to handle in linear theory. The simplest linear collision operator is the *BGK collision operator* (*Bhatnagar et al.,* 1954):

$$\frac{\partial f}{\partial t} = -\langle \nu_{12} \rangle (f - F_0). \tag{1.105}$$

The BGK collision operator represents a simple relaxation of the distribution function *f* to some assumed equilibrium distribution F_0, which is typically a Maxwellian. This collision operator is not derived from the Fokker-Planck equation, but rather proposed as is by *Bhatnagar et al.* (1954). Furthermore, the BGK operator does not assume or require small angle collisions, which were necessary to Taylor expand the Boltzmann collision integral in equation (1.68) into the Fokker-Planck collision operator. Despite the deficiencies of the BGK collision operator, Section 2.4.2 shows how the BGK collision operator is trivially included in a linear solution of ISR spectra.

1.2.7 Evaluating Fokker-Planck Coefficients

The drag and diffusion coefficients in terms of the Rosenbluth potentials are

$$\vec{F}_d = \frac{q_1^2 q_2^2 \Lambda}{4\pi\epsilon_0^2 \mu m_1} \frac{\partial}{\partial \vec{v}} H_F(\vec{v}), \tag{1.106}$$

$$D = \frac{q_1^2 q_2^2 \Lambda}{4\pi\epsilon_0^2 m_1^2} \frac{\partial}{\partial \vec{v}} \frac{\partial}{\partial \vec{v}} G_F(\vec{v}). \tag{1.107}$$

The simplest calculation of Rosenbluth potentials is for electron-ion collisions, under the assumption that $T_e \gtrsim T_i$. Under this assumption, any probable electron velocity is much larger than any ion velocity, so the ion distribution can be approximated as a delta distribution:

$$f_i(\vec{v}_i) = n_i \delta(\vec{v}_i). \tag{1.108}$$

The Rosenbluth integrals are then trivial. Noting that $\mu = m_e$, and $n_i = n_e = n$:

$$H_i(\vec{v}) = \frac{\mu}{m_e} \int \frac{n_i \delta(\vec{v}_i)}{|\vec{v} - \vec{v}_i|} d\vec{v}_i = \frac{n}{v}, \tag{1.109}$$

$$G_i(\vec{v}) = \int n_i \delta(\vec{v}_i) |\vec{v} - \vec{v}_i| d\vec{v}_i = nv. \tag{1.110}$$

To calculate the drag and diffusion coefficients, the velocity $\vec{v}$ of the colliding electron is assumed to be in the $\hat{e}_3$ direction. The velocity derivative of H_i is then

$$\frac{\partial}{\partial \vec{v}} H_i(\vec{v}) = n \frac{\partial}{\partial \vec{v}} \frac{1}{v} = -\frac{n}{v^2} \frac{\partial}{\partial \vec{v}} v = -\frac{n}{v^2} \hat{v}. \tag{1.111}$$

Therefore, the drag coefficient for electron-ion collisions is

$$\overrightarrow{F_d} = -\frac{ne^2 \Lambda}{4\pi\epsilon_0^2 m_e^2 v^2} \hat{e}_3. \tag{1.112}$$

The velocity derivatives of G_i make a dyadic tensor,

$$\frac{\partial}{\partial \vec{v}} \frac{\partial}{\partial \vec{v}} G_i(\vec{v}) = n \begin{pmatrix} \partial_1\partial_1 & \partial_1\partial_2 & \partial_1\partial_3 \\ \partial_2\partial_1 & \partial_2\partial_2 & \partial_2\partial_3 \\ \partial_3\partial_1 & \partial_3\partial_2 & \partial_3\partial_3 \end{pmatrix} v, \tag{1.113}$$

where the notation is $\partial_i = \partial/\partial v_i$. Evaluating the derivative $\partial_j \partial_i$,

$$\partial_j \partial_i v = \partial_j \partial_i \sqrt{v_1^2 + v_2^2 + v_3^2} = \partial_j \left(\frac{v_i}{v}\right),$$

$$\partial_j \partial_i v = \frac{1}{v}\partial_j v_i + v_i \partial_j \frac{1}{v} = \frac{1}{v}\delta_{ij} - \frac{v_i v_j}{v^3}. \quad (1.114)$$

The Kronecker delta is 0 except for $i = j$. Since the electron velocity is assumed to be $\vec{v} = v_3 \hat{e}_3$, the term $v_i v_j / v^3$ is 0 except for $i = j = 3$. Evaluating the terms in equation (1.114), the derivatives of G_i are

$$\frac{\partial}{\partial \vec{v}} \frac{\partial}{\partial \vec{v}} G_i(\vec{v}) = n \begin{pmatrix} 1/v & 0 & 0 \\ 0 & 1/v & 0 \\ 0 & 0 & 0 \end{pmatrix}. \quad (1.115)$$

The diffusion tensor for electron-ion collisions is then

$$D = \frac{n e^4 \Lambda}{4\pi \epsilon_0^2 m_e^2 v} \begin{pmatrix} 1 & 0 & 0 \\ 0 & 1 & 0 \\ 0 & 0 & 0 \end{pmatrix}. \quad (1.115)$$

The Fokker-Planck coefficients in equations (1.112) and (1.115) are used to simulate electron-ion collisions in Chapter 3, which also shows the rotation matrix needed to transform $\vec{v} = v_3 \hat{e}_3$ into a fixed lab coordinate system.

Assuming a delta distribution in the Rosenbluth potentials led to a trivial integral for electron-ion collisions. For electron-electron or ion collisions this assumption is not valid. Furthermore, for same species collisions the distribution in the Rosenbluth potentials is the same distribution on the right-hand side of the Boltzmann equation, leading to an intractable integro-differential equation. For same species and ion collisions

in a plasma near thermal equilibrium, the distribution in the Rosenbluth potentials can be approximated as an isotropic Maxwellian. *Manheimer et al.* (1997) shows the Rosenbluth potentials for a test mass, m_T, scattering off an isotropic Maxwellian field distribution are

$$H_F(\vec{v}) = \frac{8n}{\sqrt{\pi}b_F^3}\frac{\mu}{m_T}\left[\frac{1}{v}\int_0^v v_F^2\, e^{-\frac{v_F^2}{b_F^2}}dv_F + \int_v^\infty v_F\, e^{-\frac{v_F^2}{b_F^2}}dv_F\right], \tag{1.116}$$

$$G_F(\vec{v}) = \frac{4n}{3\sqrt{\pi}b_F^3}\left[\int_0^v \frac{v_F^2}{v}(3v^2 + v_F^2)\, e^{-\frac{v_F^2}{b_F^2}}dv_F + \int_v^\infty v_F(v^2 + 3v_F^2)e^{-\frac{v_F^2}{b_F^2}}dv_F\right]. \tag{1.117}$$

where $b_F^2 = 2KT_F/m_F$ is the thermal speed. Working out the derivatives in the coordinate system with $\vec{v} = v_3\hat{e}_3$, the drag and diffusion coefficients are

$$F_d(\vec{v}) = -\frac{ne^4\Lambda}{4\pi\epsilon_0^2\mu m_T v^2}\left[\mathrm{erf}\left(\frac{v}{b_F}\right) - \frac{2}{\sqrt{\pi}}\frac{v}{b_F}\exp\left(-\frac{v^2}{b_F^2}\right)\right], \tag{1.118}$$

$$D_{11}(\vec{v}) = D_{22}(\vec{v}) = \frac{ne^4 b_F^2\Lambda}{8\pi\epsilon_0^2 m_T^2 v^3}\left[\left(\frac{2v^2}{b_F^2} - 1\right)\mathrm{erf}\left(\frac{v}{b_F}\right) + \frac{2}{\sqrt{\pi}}\frac{v}{b_F}\exp\left(-\frac{v^2}{b_F^2}\right)\right], \tag{1.119}$$

$$D_{33}(\vec{v}) = \frac{ne^4 b_F^2\Lambda}{4\pi\epsilon_0^2 m_T^2 v^3}\left[\mathrm{erf}\left(\frac{v}{b_F}\right) - \frac{2}{\sqrt{\pi}}\frac{v}{b_F}\exp\left(-\frac{v^2}{b_F^2}\right)\right], \tag{1.120}$$

with the off-diagonal diffusion coefficients equal to 0 in this coordinate system.

Equations (1.118) – (1.120) apply to any Coulomb collisions if the background distribution can be approximated as a Maxwellian. In Chapter 4 these coefficients are used to simulate electron-electron collisions, and the validity of the isotropic Maxwellian approximation is investigated in Section 4.3. To show the validity of the electron-ion approximation in equations (1.112) and (1.115), those coefficients are plotted against the more accurate coefficients in equations (1.118) – (1.120) in Figure 1.9. The electron

distribution is overlaid in Figure 1.9 with an arbitrary scale, which shows the approximated coefficients differ from the exact solutions only for electrons with speeds less than 10% of the thermal speed. For a Maxwellian distribution this is less than 0.1% of the electron population. The ion delta distribution approximation does set the D_{33} coefficient to 0, which physically represents the ion recoil in the collision. Neglecting ion recoil in analytic work can lead to inaccurate results, such as finding electron-ion collisions reduce the total Landau + collisional damping rate of ion-acoustic waves (*Epperlein et al.*, 1992). Simulations of electron-ion collisions in this dissertation use the ion delta distribution approximation.

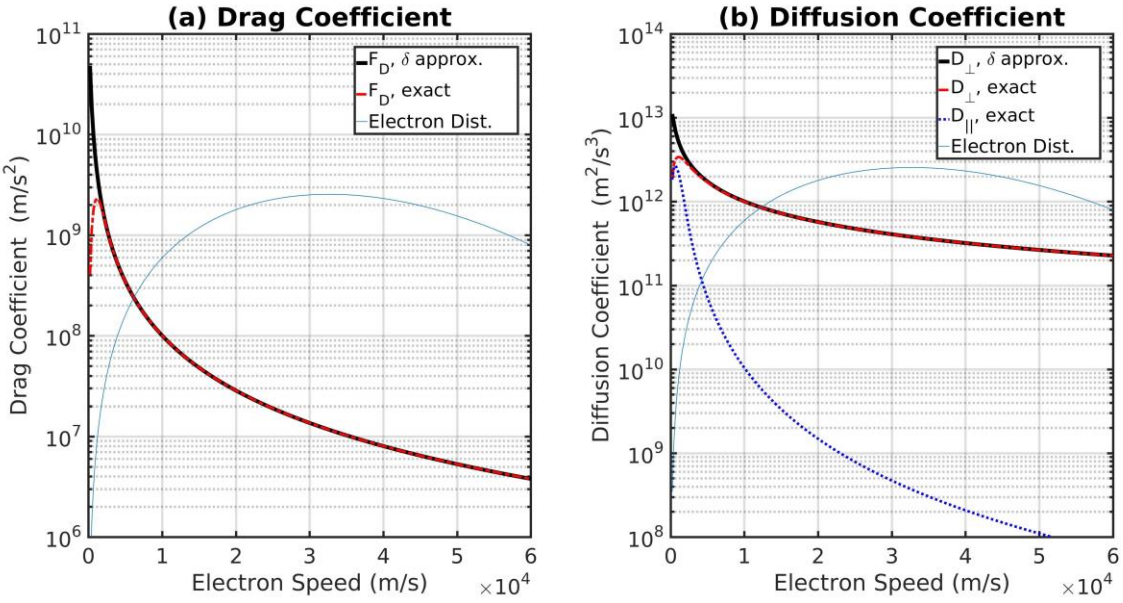

Figure 1.9 Comparison of exact electron-ion drag and diffusion coefficients (equations 1.118-1.120) to coefficients using the ion delta distribution approximation (equations 1.112 and 1.115). The electron distribution is overlaid with an arbitrary scale to show how few electrons are in the region where the two sets of coefficients disagree. The electron thermal speed is $3.26 \times 10^4\ m/s$, using a simulation electron mass of $m_e = 2.6 \times 10^{-29}\ kg$. In this figure, $D_\perp$ is equivalent to D_{11} and D_{22}, and $D_\parallel$ is equivalent to D_{33}.

1.3 Particle-in-Cell Simulations

The theory in the previous section provides an accurate description of collisional plasmas but is difficult to solve analytically. This dissertation will use the Electrostatic Parallel Particle-In-Cell simulator (EPPIC) to solve the nonlinear Bolzmann equation with the velocity dependent Fokker-Planck collision operator (*Oppenheim et al.*, 2008). PIC codes can be written in a variety of ways, but all include the same core algorithm and setup. First, a positional grid is determined, and macro-particles are placed in it. The PIC code will then loop over time, performing the following calculations during each time step:

1) Scatter macro-particles to a grid.
2) Solve for electromagnetic fields.
3) Gather the electric field at each macro-particle position.
4) Move the particles subject to fields and collisions.
5) Calculate output variables.

The initial setup of a PIC code is covered in Section 1.3.1, the scatter, field solve, and gather steps are discussed in Section 1.3.2, and the particle moving and output steps are treated in Section 1.3.3.

1.3.1 Initializing a PIC Code

As the name suggests, a PIC code places charged particles within a set of spatial grid cells. EPPIC uses a rectangular grid in 2 or 3 spatial dimensions, and techniques

exist for other coordinate systems and even unstructured meshes (*Fletcher and Close*, 2017). For any choice of grid, the discretization of space means the spatial Fourier transform of any grid variable (charge, electric field) extends through an infinite set of wavenumbers. This infinite representation leads to aliasing at wavenumbers larger than the Nyquist spatial frequency of

$$k_{Nyq} = \frac{\pi}{\Delta x}. \tag{1.121}$$

This means any quantity not resolved by the grid step will alias into smaller wavenumbers. A common result of this aliasing effect is *grid heating*, which occurs when the macroscopic electric field is aliased and produces a force at longer spatial scales than calculated. This aliasing increases the electric field in the simulation, resulting in an artificial heating. Physically, a particle should only feel the force of an electric field located within its Debye sphere, so grid heating is minimized if

$$\Delta x \leq \lambda_D. \tag{1.122}$$

The condition in equation (1.122) does not completely eliminate grid heating since the aliasing will always be present, and the next section discusses how particle shape functions are used to further reduce grid heating (*Birdsall and Langdon*, 2004). With a grid step equal to the Debye length, the Courant condition for numerical stability gives a maximum time step of

$$\Delta t = B\frac{\Delta x}{v_{th}} = B\frac{\lambda_D}{v_{th}} = \frac{B}{\omega_{pe}}, \tag{1.123}$$

where B is a constant typically between 0.1 and 1 that depends on the actual problem being simulated. From equations (1.122) and (1.123), the stability conditions of a PIC code are: spatially resolving the Debye length, and temporally resolving the electron plasma period.

The ionosphere has plasma densities of 10^5-10^6 particles per cm^{-3}, so running a PIC code with this particle density for a system around 1 meter in size results in 10^{11}-10^{12} individual particles that need to be simulated. Double precision calculations require 8 bytes per number, and the smallest realistic plasma simulations require 2 spatial and 2 velocity dimensions, meaning each particle in the simulation needs 32 bytes of memory. Thus a "small" 2D simulation at a density of 10^5 cm^{-3} requires 3 Tb of system memory to store all of the particle positions and velocities. This amount of memory is available on current Petascale supercomputers but scaling the code to 3D or larger spatial scales requires an unrealistic amount of memory. The solution to this memory scaling problem is to simulate the motion of macro-particles, which represent 10 to 10,000 real particles (called micro-particles). Figure 1.10 shows how the accuracy of nonlinear Landau damping in a 1-D Langmuir wave increases in a PIC code as the number of micro-particles per macro-particle is decreased. The next section shows how the grouping of many particles into a single macro-particle is handled during the time step.

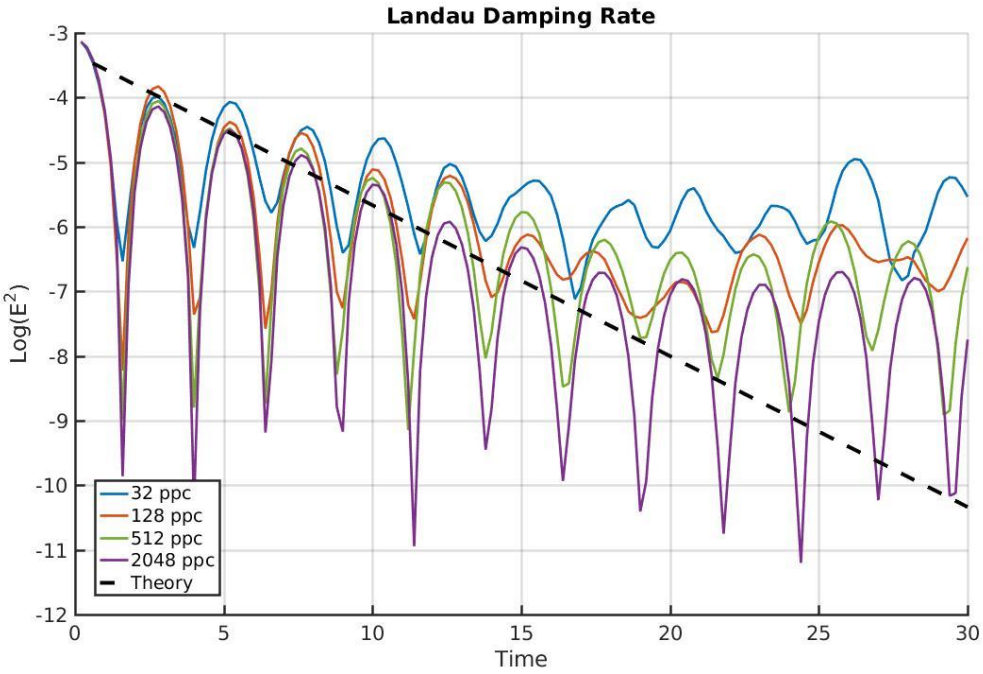

Figure 1.10 The decrease of electric field wave energy as a function of time. The dashed black line shows the linear Landau damping rate of a Langmuir wave. The colored curves show that as the number of particles per cell (ppc) increases the noise in the damping rate is decreased. The number of particles per cell is related to the inverse of the number of micro-particles per macro-particle.

PIC codes simulate a wide range of plasma waves and instabilities depending on the initial conditions. Since ISR measures the scattering off thermally driven Langmuir and ion-acoustic modes, the simulations in this dissertation rely on discrete particle noise to produce waves through the fluctuation-dissipation theorem, and do not require any driving conditions such as a background electric field or density perturbation. In a plasma the particle positions are not completely random, so an initial seeding where macro-particle positions are chosen randomly leads a larger initial total energy, and distributions that are not strictly Maxwellian on small scales. The alternative is a flat “quiet start” seeding of positions. In 1D this is equivalent to putting all of the particles at equal

intervals; for example, 10 particles in a 1-meter domain would be seeded every 0.1 m. The distributions in a quiet start are exactly Maxwellian and the initial kinetic energy is less than what it should be, which is better than initially overestimating. However, in 2D and 3D the quiet start uses a bit-reversing algorithm to match the particle position to a velocity (*Birdsall and Langdon,* 2004). The initial positions from this algorithm have a small correlation that sets an initial density perturbation, which starts an anomalous low-frequency wave. Figure 1.10 shows the initial correlation of a 2D simulation, along with the artificially enhanced wave modes produced by the spatial correlation. For this reason, ISR runs in this dissertation use a random seeding of initial particle positions, and the simulation is run for significantly longer than the time required to dissipate the extra initial energy.

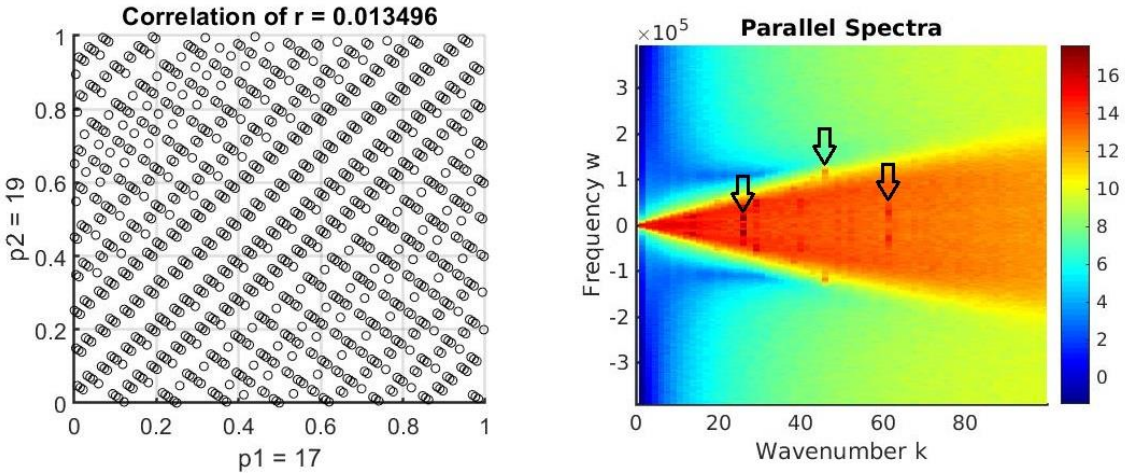

Figure 1.10 (Left) The initial particle positions using the bit-reversed quiet start with prime number seeds of 17 and 19. With higher prime numbers the particle positions start with a small correlation. (Right) The periodicity of a bit-reverse start with prime seeds of 17 and 19 leads to anomalous power (arrows) at wavelengths of 17 and 19 that persists throughout simulations, unless the system is strongly collisional or generates an instability.

1.3.2 Solving for Electric and Magnetic Fields

Once the initial conditions of the system are set the PIC code loops over time to evolve the plasma dynamics. The first operation at each time step is to scatter the particles to the grid to calculate the charge density $\rho(\vec{x})$. The position of macro-particles is a continuous variable (within machine precision), so scattering particles to the discrete grid is effectively an interpolation operation. The simplest kernel for this interpolation is the Nearest Grid Point (NGP), which places all of the macro-particle's charge on the nearest grid point. A linear interpolation (tent function) places the macro-particles charge on all of the grid points surrounding the cell the particle is in, weighted by the distance to the grid point. Cubic and Quartic splines increase the accuracy of this interpolation by weighting charge to all grid points within $2\Delta x$ and $3\Delta x$ of the macro-particle (*Chaniotis and Poulikakos*, 2004). Figure 1.11 plots the shape of the different interpolation kernels along with the spatial Fourier transform of each kernel. Since the scatter step uses the kernels to calculate charge density, which is then used to find the electric field, the periodicity shown in Fourier space is the reason why the electric field is aliased and causes grid heating if the Debye length is not sufficiently resolved.

An electromagnetic code also needs to interpolate the current ρv of each macro-particle onto the grid to find the large-scale current used in Ampere's law. For simulations of the ionosphere, the Earth's magnetic field dominates over the current driven magnetic field, and therefore we run EPPIC as an electrostatic code. The electric field is then calculated from Poisson's equation:

$$\nabla^2\phi(\vec{x}) = -\frac{\rho(\vec{x})}{\epsilon_0}\,. \tag{1.124}$$

Many different techniques exist for solving Poisson's equation on a grid. An explicit scheme discretizes the Laplacian operator and propagates the boundary conditions to the nearest grid points. This is a relaxation process, and convergence to the solution may take a long time. An implicit solution to Poisson's equation is found by simultaneously solving the linear set of discretized equations. This has the advantage of avoiding any convergence issues of an explicit solve, but the calculation of a large inverse matrix can be very slow. For a periodic system the equation can be transformed into frequency space for a fast and accurate spectral solution (*Birdsall and Langdon*, 2004). This spectral solution technique is used for ISR simulations in this dissertation since ISR probes thermally driven waves in a homogeneous plasma, which are accurately represented by periodic boundary conditions.

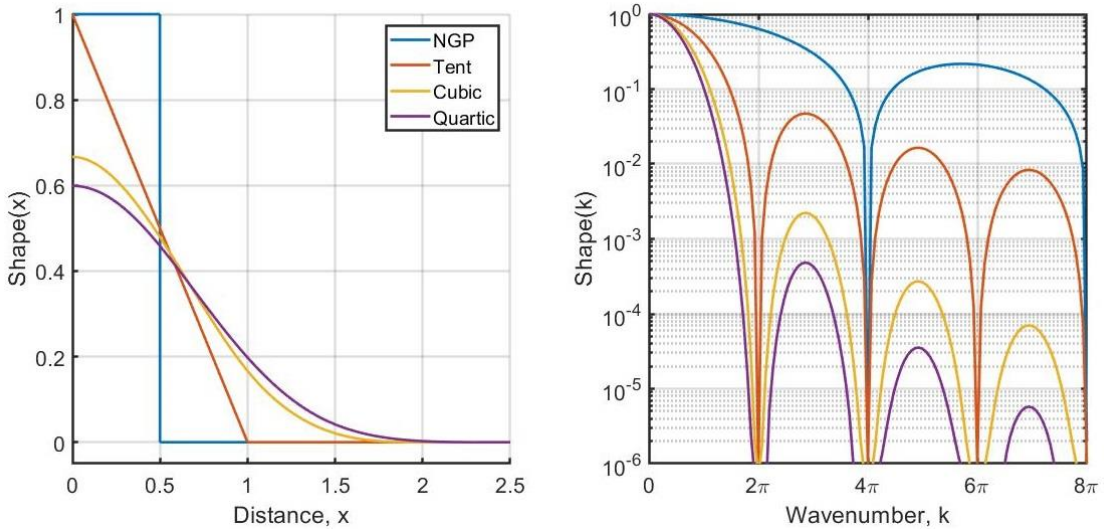

Figure 1.11 (Left) Different kernels used for interpolation during the gather and scatter steps. The distance *x* is from the center of the macro-particle and is normalized by the grid step Δx. (Right) The spatial Fourier transform of each kernel, showing how the discretization of the system aliases spatial variables such as charge density.

The electric field is calculated at every grid point, so it needs to be interpolated back to each macro-particle position (gather step) before applying the Lorentz force. This interpolation is done using the same kernels as the scatter step for finding the charge density. EPPIC uses the linear tent function for both the scatter and gather steps.

An interesting consequence of the shape functions in a PIC code is how they smooth out small scale electric fields. Figure 1.12 shows two configurations of an electron and an ion in the same grid cell. In Configuration A the particles sit exactly on the grid nodes, so a tent shape function places a charge of $\pm e$ on each grid node. The field between the two particles is then $E = e^2/8\pi\epsilon_0\Delta x^2$, which is exactly the same as Coulomb's law. In configuration B the particles are at coordinates (Δx/4, Δx/4) and (3Δx/4, 3Δx/4). The tent function then weights the charge density to be $\pm e/2$ at the grid nodes closest to each particle, so the field in the grid cell is $E = e^2/32\pi\epsilon_0\Delta x^2$. The extreme case of Configuration B is if each particle is places at the center of the cell. Then the electric field in the cell would be 0 and the particles will not interact. This shows that the interpolation step in the scatter routine will always underestimate the force between two nearby particles, and as particles get closer to each other they effectively become collisionless. While this may seem like a bad approximation to the physics of the system, it allows for different collision operators to be explicitly included in the PIC code during the particle moving step, which is done in Chapters 3 and 4.

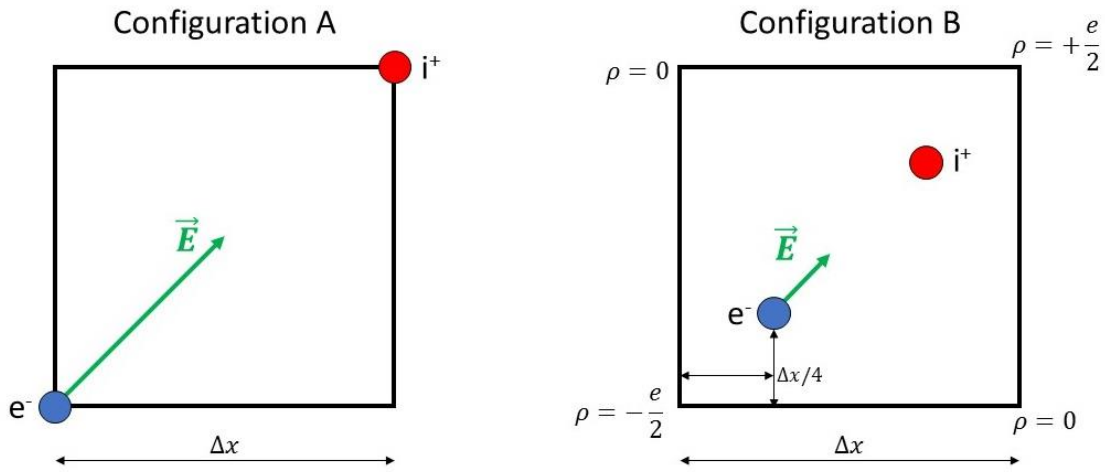

Figure 1.12 Schematic showing the electric field between two particles in a PIC code.

1.3.3 The Particle Mover

After the gather step the electric field is known at each particle position, and the Lorentz force dictates the acceleration of the particles:

$$\vec{a} = \frac{q}{m}\left(\vec{E}_0 + \vec{E}_1\right) + \frac{q}{m}\vec{v} \times \vec{B}_0, \tag{1.125}$$

where $\vec{E}_0$ and $\vec{B}_0$ are externally imposed fields and $\vec{E}_1$ is the self-consistent electric field calculated from Poisson's equation. The acceleration is a time derivative of velocity, so a simple discretization of equation (1.125) with a forward time difference is

$$\vec{v}_{t+\Delta t} = \vec{v}_t + \Delta t \frac{q}{m}\left(\vec{E} + \vec{v}_t \times \vec{B}\right), \tag{1.126}$$

where $\vec{E}$ is the total electric field. The position of the particle is then found through a leap-frog scheme as

$$\vec{x}_{t+\Delta t} = \vec{x}_t + \Delta t\, \vec{v}_{t+\Delta t}. \tag{1.127}$$

The leap-frog scheme is second order accurate in time and is often used to integrate particle trajectories. However, for particles gyrating around a magnetic field the discretization in equation (1.126) does not exactly conserve energy and close circular orbits in all cases. To address this issue, the Boris mover was developed as a phase space conserving solution to the Lorentz force (*Birdsall and Langdon*, 2004). The Boris mover effectively applies half of the electric field force, then rotates the particle around the magnetic field with the $\vec{v} \times \vec{B}$ force, then finishes by applying the remaining portion of the electric field. Schematically this updates the velocity vector in time as

$$\vec{v}^a = \vec{v}_t + \frac{q\,\Delta t}{2m}\vec{E}, \tag{1.128}$$

$$\vec{v}^b = \vec{v}^a + \vec{v}^a \times \vec{t}, \tag{1.129}$$

$$\vec{v}^c = \vec{v}^a + \vec{v}^b \times \vec{s}, \tag{1.130}$$

$$\vec{v}_{t+\Delta t} = \vec{v}^c + \frac{q\,\Delta t}{2m}\vec{E}. \tag{1.131}$$

The vectors $\vec{s}$ and $\vec{t}$ are defined by the magnetic field,

$$\vec{t} = \frac{q\,\Delta t}{2m}\vec{B}, \tag{1.132}$$

$$\vec{s} = \frac{2\vec{t}}{1+\vec{t}}. \tag{1.133}$$

Equations (1.128) – (1.133) can then be used with a leapfrog step to find the particle position with second order accuracy. A similar Boris mover scheme exists for electromagnetic codes (*Birdsall and Langdon*, 2004).

Collisions are included in a PIC code after calculating the updated particle velocity $\vec{v}_{t+\Delta t}$, but before applying the leap-frog step to obtain $\vec{x}_{t+\Delta t}$. The most direct way of including collisions is to write the collision operator in a velocity update form. Chapter 3 describes how the Fokker-Planck collision operator is equivalent to a Langevin equation of the form (*Nicholson*, 1983)

$$\vec{v}'_{t+\Delta t} = \vec{F}_D \Delta t + \vec{Q}. \tag{1.134}$$

The vector $\vec{F}_D$ is the same frictional drag vector from the Fokker-Planck equation, and the vector $\vec{Q}$ is a stochastic term related to the diffusion coefficients. Charged-neutral collisions are included by randomly sampling an initial impact parameter and azimuth angle, then calculating the post-collision velocity $\vec{v}'_{t+\Delta t}$ from the scattering relations $\theta(b)$ in Section 1.2.3.

After the velocity and position of each particle is updated the time step is complete. At this point in the code the charge density, number density, and electric fields determined in the scatter and field solve steps are output to a file. The moments of the distribution and selected particle positions and velocities are also saved to file. The time variable is then advanced, and the code starts at the scatter step again. For many problems the ions are significantly heavier and slower than electrons, so the particle mover step is often subcycled and the ions are not moved every time step. ISR simulations in this dissertation only advance ion positions every 64 time steps.

Chapter 2

Incoherent Scatter Radars (ISR)

ISR is a Cold War byproduct that has turned into an invaluable tool for studying the upper atmosphere. The first radar at Millstone Hill Observatory in Westford, Massachusetts was built in 1957 by MIT Lincoln Laboratory for the purpose of detecting and tracking satellites and ballistic missiles. The Millstone Hill radar successfully detected Sputnik 1 and tracked Sputnik 2, and the design was replicated for the Air Force's Ballistic Missile Early Warning System. At the same time, Bill Gordon at Cornell University suggested that a large and powerful radar could be used to scatter radio pulses off of electrons in the ionosphere, measuring the returned power, and deducing parameters in the ionosphere (*Gordon,* 1958). Gordon originally calculated the measured power spectrum for truly incoherent scattering off an electron gas. In truly incoherent scattering the electrons are assumed to be isolated from ions and the neutral atmosphere, and therefore the random thermal motion of electrons will Doppler broaden the transmitted pulse, with the measured spectral width determined by the electron temperature. The calculation by Gordon also showed that in contrast with other measurement techniques, ISR had no restrictions on the altitudes where it could probe the electron density and temperature in the ionosphere.

Within a year, *Bowles* (1958) tested Gordon's idea with a smaller radar and showed the measured spectral width was determined by the ion distribution. This meant the radar was not incoherently scattering off free electrons, but instead was coherently

scattering off a plasma wave that coupled the electron and ion motion together. Nonetheless, the name Incoherent Scatter Radar has stuck, and refers (incorrectly) to scatter off thermally driven waves in the ionosphere, leaving coherent scatter to describe strong scatter off of instabilities, electrojets, and other large-scale phenomena (see Figure 2.5). The rapid development of the ISR technique was quickly capitalized on as a tool for studying the ionosphere, with applications to both the space race and the detection of ballistic missile reentry signatures. Jicamarca Radio Observatory in Peru became operational in 1961, and its location at the geomagnetic equator was chosen so the radar could look perpendicular to the Earth's magnetic field and deduce ion composition ratios from ion gyroresonances (see Section 2.3). In 1963 the Arecibo Observatory in Puerto Rico became operational, with ARPA (predecessor to DARPA) funding the observatory to be built at the size originally calculated by *Gordon* (1958). In the same year an upgrade to the missile tracking radar at Millstone Hill left a spare transmitter that was repurposed for a new ISR system at the same site. Through the 1960s the theory of ISR was rapidly developed, and several more facilities in the U.S. and abroad were built. As the Cold War ended, and the era of space technology began, ISR has transitioned from a critical national defense tool to one used primarily for science, with some economic and defense applications.

2.1 ISR Overview

Currently the National Science Foundation supports a chain of radars across North and South America covering a wide range of geomagnetic latitudes. Table 2.1 lists the characteristics of the NSF radar chain, along with the DOD funded ALTAIR radar in

the Marshall Islands, and the European EISCAT radars. The choice in radar frequencies between 50 MHz and 1.3 GHz is dictated by being well above the maximum plasma frequency of 10 MHz to avoid attenuation and refraction effects, and well below the frequency where the Bragg scattering wavelength $\lambda_{\mathrm{Bragg}} = \lambda/2$ is on the order of the Debye length, and the scattering becomes truly incoherent. The L-Shell in Table 2.1 is a measure of latitude: An L-Shell of 1 is right at the equator, L-Shells between 4-6 R_E are in the auroral region, and L-Shells above 6 R_E are in the polar region.

Table 2.1 Current ISR facilities and their transmitted frequency, Bragg scattering wavelength and wavenumber, and L-shell location. NSF supported radars are denoted with an asterisk.

Radar	f (MHz)	λ_{Bragg} (m)	k_{Bragg}	L-Shell	Notes
Jicamarca*	49.9	3.006	2.0902	1.05	Always looks within 5° of perp. to **B**.
Altair (VHF) (UHF)	155.5 422	0.9646 0.3555	6.5136 17.677	1.1	Fully steerable, looks perp. to **B**.
Arecibo*	430	0.3488	18.0118	1.43	Largest aperture and highest sensitivity.
Millstone Hill*	440	0.3409	18.4307	3.12	Looks perp. to **B** in the E and F1 regions.
PFISR*	450	0.3333	18.8496	5.51	Electronically steerable AMISR system
EISCAT (VHF) (UHF) Svalbard	224 933 500	0.6696 0.1608 0.300	9.3829 39.0814 20.944	6.3 > 20	Tristatic system in UHF and VHF
Sondrestrom*	1290	0.1163	54.0354	> 15	Decommissioned 2018
RISR*	450	0.3333	18.8496	> 100	Two electronically steerable AMISR panels

Figure 2.1 shows the two radar antennas used at Millstone Hill: the fixed 68-meter Zenith antenna, and the fully steerable 46-meter MISA antenna. Both antennas can be used at the same time, allowing for two viewpoints of the ionosphere. In contrast with the dish antennas at Millstone Hill, the 300x300 meter phased array system at Jicamarca Radio Observatory is shown in Figure 2.2. Phased arrays are a collection of many crossed dipole antennas (18,432 dipoles for Jicamarca), and the relative phase difference between adjacent antennas can be adjusted to electronically steer the radar beam without moving the antennas.

The electronic steering and lack of moving parts is a big advantage of phased arrays, but the disadvantage is a phased array cannot steer in every direction. Figure 2.3 shows the radiation pattern for a circular dish antenna. This radiation pattern is symmetric around the antenna's line of sight, and as the antenna is physically steered the radiation pattern moves with the radar, keeping the same symmetry and shape apart from small deviations caused by the dish flexing when it changes elevation angle. Figure 2.4 shows the radiation pattern for a square array of 100 dipoles. The radiation sidelobes from a phased array are ordered along the symmetry axes, and as the array steers off of zenith a grating lobe of equal intensity will come into the field of view, and measurements become ambiguous. For Jicamarca the grating lobe limits the radar line of sight to within 6° of zenith. The AMISR systems operate at a different wavelength and are spaced in a different pattern, so the grating lobe limits of those radars is 25°. The faces of the AMISR systems are also tilted off zenith, which allows PFISR to look towards the auroral region, and the two panels of RISR look north and south in opposite directions.

Figure 2.1 Millstone Hill Observatory. (Photo credit: Wikimedia Commons)

Figure 2.2 Jicamarca Radio Observatory. (Photo credit: Wikimedia Commons)

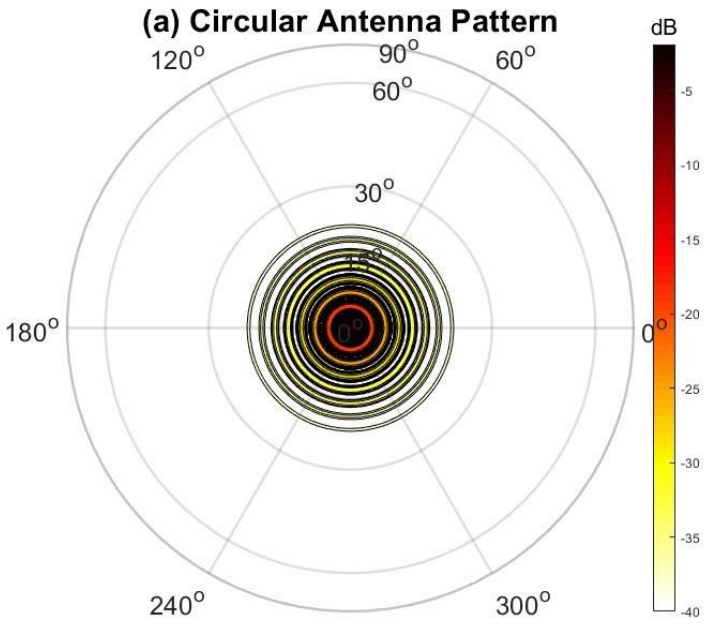

Figure 2.3 The radiation pattern of a circular dish antenna in polar coordinates. The sidelobe pattern is symmetric around the radar's line of sight, and as the antenna is physically steered the radiation pattern stays the same.

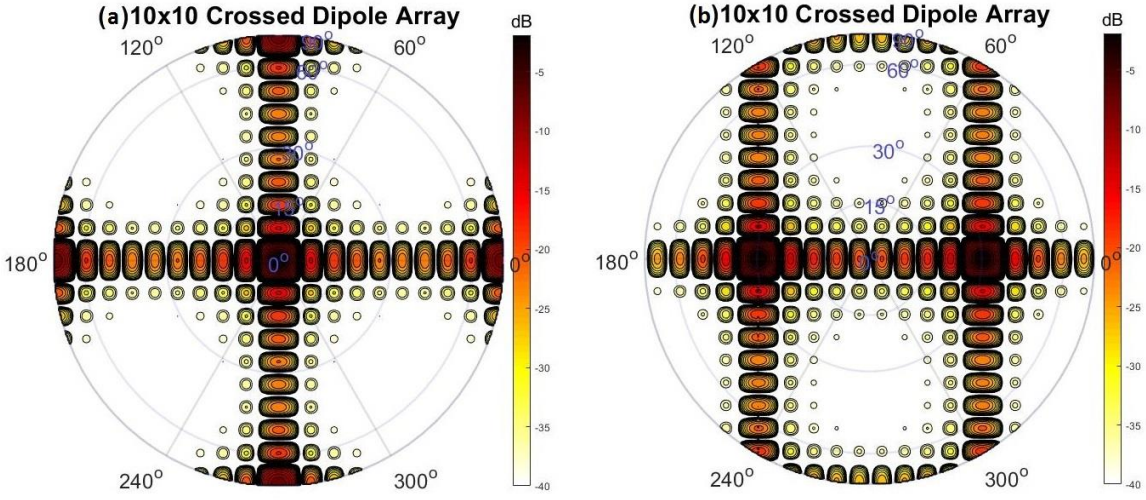

Figure 2.4 The radiation pattern for a phased array changes as the antenna is electronically steered. In plot (a) the antennas are all in phase, and the main beam is pointed upwards. In plot (b) the antenna is electronically steered 30° off zenith, and a grating lobe of equal intensity comes into the field of view.

ISR works by transmitting radio pulses that are Thomson scattered off electrons in the ionosphere (see Section 2.4.1) and measuring the Doppler shift and overall power of the returned pulse. Figure 2.5 shows the measured power at Jicamarca for a full day of operations, with several features that cause a Doppler shift pointed out. Coherent scatter is seen from Equatorial Spread-F (ESF), the equatorial electrojet (EEJ), and 150-km echoes. ESF is an instability caused by a bubble of low density plasma rising up through the F-region (*Hysell et al.*, 2014). The equatorial electrojet is a strong current system in the E-region where the neutral atmosphere drives a dynamo that produces a strong electric field at the equator (*Kelley*, 2009). The 150-km echoes are only present during the day, when photoelectrons drive a bump-on-tail instability (*Oppenheim and Dimant*, 2016).

The weak scatter between 100-400 km in Figure 2.5 is coherent scatter off thermally driven ion-acoustic and Langmuir waves. This is the scatter first detected by *Bowles* (1958) and is referred to as incoherent scatter (ISR). The spectral shape of incoherent scatter allows for radars to measure temperatures, density, and line-of-sight velocity throughout the ionosphere. The rest of this section develops the theory and methods behind this measurement process. Section 2.2 derives the basic equations for the ion-acoustic and Langmuir waves used in ISR. Section 2.3 shows the scattering spectra off of these waves. Section 2.4 more rigorously derives the exact spectral shape of the plasma waves used as a forward model in ISR. Section 2.5 shows how this forward model is used in an inversion process to estimate the plasma temperature and density from measured spectra.

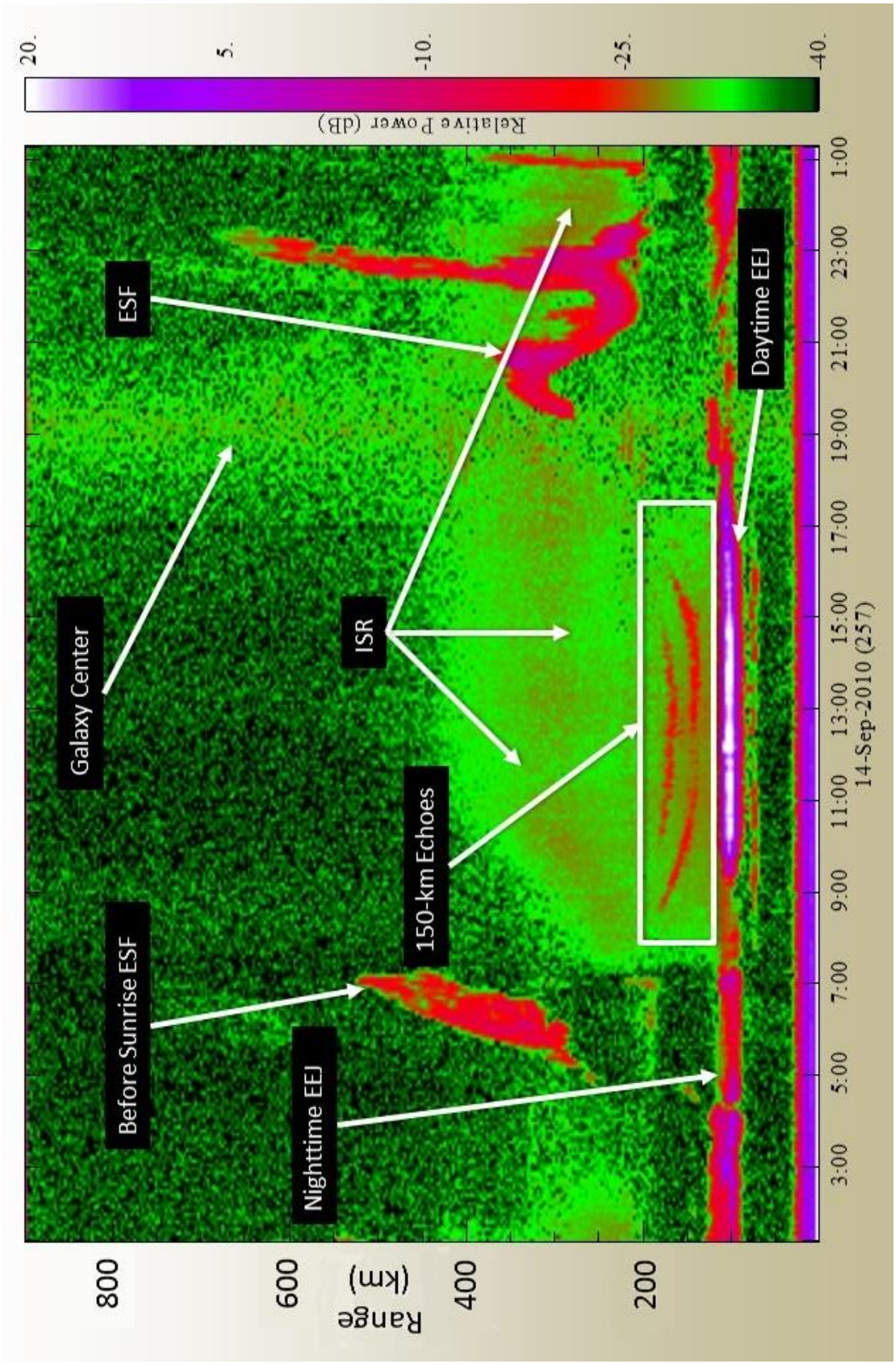

Figure 2.5 Range-time-intensity plot for a day at Jicamarca. (Photo credit: Juha Vierinen)

2.2 Waves in Plasmas

ISR measures backscatter off of three different waves during quiet conditions: the ion-acoustic mode, the Langmuir mode, and the lower hybrid/electrostatic whistler mode. Each of these waves produces a complex scattering signal that is best described with kinetic theory, which is treated in Section 2.4. In order to understand the basic physics of each wave this section will derive the dispersion relations from fluid equations, which ignore collisions and damping effects but provide a broad picture of the wave dynamics.

The fluid continuity and momentum equations are

$$\frac{\partial n}{\partial t} + \nabla \cdot (n\vec{u}) = 0, \tag{2.1}$$

$$\frac{\partial \vec{u}}{\partial t} + (\vec{u} \cdot \nabla)\vec{u} = -\frac{1}{nm}\nabla P + \frac{q}{m}\left(\vec{E} + \vec{u} \times \vec{B}\right), \tag{2.2}$$

The left-hand side of equations (2.1) and (2.2) are the convective derivatives of the number density *n* and bulk flow speed *u*, respectively. The first term on the right-hand side of equation (2.2) is the gradient of the pressure *P*, which acts to move plasma from high pressure regions to low pressure regions. The next term is the Lorentz force, and other external forces such as the Coriolis force can be added to the right-hand side of equation (2.2) if needed. The pressure is typically given by the ideal gas law,

$$P = nK_B T. \tag{2.3}$$

The system of equations is closed by assuming an energy equation for the temperature, and this section assumes a constant isothermal temperature.

2.2.1 The Langmuir Mode

The first wave of interest is electrons in an unmagnetized plasma vibrating due to thermal motion. To solve for a dispersion relation between the frequency ω and wavenumber $k = 2\pi/\lambda$, the fluid equations are linearized by assuming plane waves. This means a plasma parameter A is written as the sum of a static, 0th order component A_0, and a time varying 1st order component with a plane wave variation:

$$A(\vec{x}, t) = A_0 + A_1 \exp\left(i\vec{k} \cdot \vec{x} - \omega t\right). \tag{2.4}$$

Using equation (2.4) for the density, velocity, and electric field in equations (2.1) – (2.2) and substituting the ideal gas law yields the linearized continuity and momentum equations,

$$-i\omega n_1 + ikn_0 u_1 = 0, \tag{2.5}$$

$$-i\omega u_1 = -\frac{K_B T}{n_0 m_e} ikn_1 - \frac{e}{m_e} E_1. \tag{2.6}$$

The perturbed electric field is given by Gauss' Law

$$\nabla \cdot \vec{E} = \frac{q}{\epsilon_o}, \tag{2.7}$$

which linearizes to

$$ikE_1 = -\frac{en_1}{\epsilon_0}. \tag{2.8}$$

Putting the linearized Gauss' Law into the momentum equation yields

$$-i\omega u_1 = -\frac{K_B T}{n_0 m_e} ikn_1 - \frac{i}{k}\frac{e^2}{\epsilon_0 m_e} n_1. \quad (2.9)$$

The continuity equation is solved for u_1, which is inserted into equation (2.9) to obtain

$$\omega^2 = \frac{K_B T}{m_e} k^2 + \frac{n_0 e^2}{\epsilon_0 m_e}. \quad (2.10)$$

The first term can be simplified by noting that $v_{th} = \sqrt{K_B T/m}$ is the thermal speed of a plasma. The second term is in units of frequency, so we define the plasma frequency as

$$\omega_p^2 = \frac{n_0 e^2}{\epsilon_0 m}. \quad (2.11)$$

While this frequency was derived for electrons oscillating under thermal motion, it can define the plasma frequency for any ion or other charged species by using the density and mass of that species. Substituting the plasma frequency into equation (2.10),

$$\omega^2 = v_{th}^2 k^2 + \omega_{pe}^2. \quad (2.12)$$

Equation (2.12) is the fluid dispersion relation for the Langmuir mode. This shows a wave frequency that varies as k^2, and only electron parameters affect the frequency and propagation of the wave. The presence of the thermal velocity in the dispersion relation also shows that this wave is excited by the random thermal motion of electrons.

2.2.2 The Ion Acoustic Mode

The Langmuir mode is the high frequency natural response of electrons to small perturbations in a plasma when the magnetic field is neglected. For ions, the natural response to small perturbations is the ion-acoustic mode, which occurs at a much lower

frequency due to the higher ion mass. This wave comes from considering the linearized continuity and momentum equations for ions,

$$\omega n_{i1} = k n_0 u_{i1}, \tag{2.13}$$

$$-i\omega u_{i1} = -\frac{K_B T_i}{n_0 m_i} ikn_{i1} + \frac{e}{m_i} E_1. \tag{2.14}$$

In the Langmuir mode Poisson's equation was used to calculate the electric field due to the displacement of electrons. This works for high frequency modes, but when an ion is displaced the electrons will quickly move to maintain quasineutrality, and the balance between electrostatic and pressure gradient forces on electrons leads to the Boltzmann relation between the perturbed electron density and the electric potential, ϕ,

$$n_e = n_0 \exp\left(\frac{e\phi_1}{KT_e}\right). \tag{2.15}$$

To maintain quasineutrality the electric potential must be small, so equation (2.15) is Taylor expanded to

$$n_e = n_0 \left(1 + \frac{e\phi_1}{K_B T_e}\right). \tag{2.16}$$

The perturbed density is then

$$n_1 = n_0 \frac{e\phi_1}{K_B T_e}. \tag{2.17}$$

Noting that $E_1 = -\nabla\phi_1 = -ik\phi_1$, we can substitute equation (2.17) into the continuity equation to obtain

$$-i\omega u_{i1} = -\frac{K_B T_i}{n_0 m_i} ikn_{i1} - ik\frac{n_1}{n_0}\frac{K_B T_e}{m_i}. \tag{2.18}$$

The continuity equation provides an expression for the perturbed velocity, so substituting into equation (2.18),

$$-i\frac{\omega^2}{k}\frac{n_{i1}}{n_0} = -\frac{K_B T_i}{n_0 m_i} ikn_{i1} - ik\frac{n_1}{n_0}\frac{K_B T_e}{m_i}. \tag{2.19}$$

Simplifying, we obtain the dispersion relation for ion-acoustic waves,

$$\frac{\omega^2}{k^2} = \frac{K_B T_i}{m_i} + \frac{K_B T_e}{m_i}. \tag{2.20}$$

In deriving the dispersion relation in equation (2.20) we have assumed both ions and electrons behave isothermally. We can generalize this dispersion relation by including the adiabatic index for each species, which gives (*Chen*, 2016)

$$\omega^2 = k^2\left(\frac{\gamma_i K_B T_i + \gamma_e K_B T_e}{m_i}\right). \tag{2.21}$$

Furthermore, the sound speed c_s is defined as the quantity in parentheses in equation (2.21), so the dispersion relation for ion-acoustic waves simplifies to $\omega^2 = k^2 c_s^2$.

2.2.3 The Lower Hybrid Mode

The ion-acoustic mode is present but modified in a magnetized plasma. With a magnetic field the linearized ion momentum equation is

$$-i\omega\vec{u}_{i1} = \frac{e}{m_i}\vec{u}_{1i} \times \vec{B}_0 + \frac{e}{m_i}\vec{E}_1 - \frac{K_B T_i}{n_0 m_i} i\vec{k}n_{i1}. \tag{2.22}$$

Assuming the wave is propagating in the x-direction, and B_0 is in the z-direction, the momentum equation is broken into component form

$$-i\omega u_{i1x} = \frac{e}{m_i} u_{i1y} B_0 + \frac{e}{m_i} E_1 - \frac{K_B T_i}{n_0 m_i} ikn_{i1}, \tag{2.23}$$

$$-i\omega u_{i1y} = -\frac{e}{m_i} u_{i1x} B_0. \tag{2.24}$$

Eliminating u_{i1y} between equations (2.23) and (2.24),

$$-i\omega u_{i1x} = -\left(\frac{eB_0}{m_i}\right)^2 \frac{i}{\omega} u_{i1x} + \frac{e}{m_i} E_1 + k \frac{K_B T_i}{m_i} \frac{n_{i1}}{n_0} . \tag{2.25}$$

Recognizing the ion gyrofrequency, $\Omega_{ci} = eB_0/m_i$,

$$(\omega^2 - \Omega_{ci}^2) u_{i1x} = \frac{e}{m_i} i\omega E_1 + k\omega \frac{K_B T_i}{m_i} \frac{n_{i1}}{n_0}. \tag{2.26}$$

Rewriting the electric field as a linearized potential,

$$(\omega^2 - \Omega_{ci}^2) u_{i1x} = \frac{e}{m_i} \omega k \phi_1 + \omega k \frac{K_B T_i}{m_i} \frac{n_{i1}}{n_0}. \tag{2.27}$$

We now have to determine the electric potential for the wave. For the Langmuir mode Poisson's equation was used since the frequencies of interest were on the order of the electron plasma frequency. For the ion-acoustic mode however, the wave frequency was much lower than the electron plasma frequency, so electrons were able to rapidly respond to the wave electric field and the Boltzmann relation was valid. For low frequency waves the exact aspect angle α between the magnetic field normal vector and the wave vector matters.

For magnetic aspect angles α larger than the critical angle

$$\cos^2 \alpha_c = \frac{m_e}{m_i}, \tag{2.28}$$

the electrons can neutralize the wave and Boltzmann's relation in equation (2.17) yields

$$(\omega^2 - \Omega_{ci}^2) u_{i1x} = \frac{\omega k}{m_i} K_B T_e \frac{n_{e1}}{n_0} + \omega k \frac{K_B T_i}{m_i} \frac{n_{i1}}{n_0}. \tag{2.29}$$

The ion continuity equation relates the perturbed density to the velocity, with the wave propagation already set in the x-direction:

$$\omega n_{i1} = n_0 k \, u_{i1x}. \tag{2.30}$$

Since the Boltzmann relation applies, the plasma maintains quasi-neutrality on low frequency time scales and $n_{i1} \approx n_{e1}$. Substituting equation (2.30) into equation (2.29),

$$(\omega^2 - \Omega_{ci}^2) = k^2 \left(\frac{K_B T_e}{m_i} + \frac{K_B T_i}{m_i} \right). \tag{2.31}$$

The sound speed appears again in equation (2.31), and we see that the dispersion relation is nearly the same as the ion-acoustic mode but includes a gyrofrequency term:

$$\omega^2 = k^2 c_s^2 + \Omega_{ci}^2. \tag{2.32}$$

This is the *electrostatic ion cyclotron mode*, but this dissertation will refer to it as an ion-acoustic mode since the ion gyrofrequency term is a minor perturbation in the ionosphere. This mode shows that for aspect angles larger than α_c the ion-acoustic mode is still driven through thermal motion, though Section 2.4 shows it is heavily damped in the ionosphere at aspect angles less than ~5°.

At aspect angles smaller than α_c the electrons cannot neutralize the ion motion fast enough and the Boltzmann relation does not hold. Poisson's equation then specifies the relation between the potential and the perturbed density,

$$k^2\phi_1 = \frac{e}{\epsilon_0}(n_{i1} - n_{e1}). \tag{2.33}$$

Neglecting the pressure term and substituting Poisson's equation into equation (2.27),

$$(\omega^2 - \Omega_{ci}^2)u_{i1x} = \frac{e^2}{m_i\epsilon_0}\frac{\omega}{k}(n_{i1} - n_{e1}). \tag{2.34}$$

The inclusion of the perturbed electron density means the continuity equations are needed, and the result is

$$(\omega^2 - \Omega_{ci}^2)u_{i1x} = \frac{n_0 e^2}{m_i\epsilon_0}(u_{i1x} - u_{e1x}). \tag{2.35}$$

Recognizing the ion plasma frequency ω_{pi}, we have

$$\left(\omega^2 - \omega_{pi}^2 - \Omega_{ci}^2\right)u_{i1x} = -\omega_{pi}^2 u_{e1x}. \tag{2.36}$$

The electron velocity in equation (2.36) is found through the same derivation as the ion equation with $m_i \to m_e$ and $e \to -e$. The electron velocity equation is then

$$\left(\omega^2 - \omega_{pe}^2 - \Omega_{ce}^2\right)u_{e1x} = -\omega_{pe}^2 u_{i1x}. \tag{2.37}$$

The waves of interest are at low frequencies, $\omega \ll \Omega_{ce}$ and $\omega \ll \omega_{pe}$, so the ω^2 term can be neglected, and the electron equation becomes

$$\left(\omega_{pe}^2 + \Omega_{ce}^2\right)u_{e1x} = \omega_{pe}^2 u_{i1x}. \tag{2.38}$$

Substituting equation (2.38) into equation (2.36) and simplifying,

$$\left(\omega^2 - \omega_{pi}^2 - \Omega_{ci}^2\right)\left(\omega_{pe}^2 + \Omega_{ce}^2\right) = -\omega_{pi}^2\omega_{pe}^2, \tag{2.39}$$

$$\omega^2\left(1 + \frac{\Omega_{ce}^2}{\omega_{pe}^2}\right) - \left(\omega_{pi}^2 + \Omega_{ci}^2\right)\left(1 + \frac{\Omega_{ce}^2}{\omega_{pe}^2}\right) = -\omega_{pi}^2, \tag{2.40}$$

$$\omega^2\left(1 + \frac{\Omega_{ce}^2}{\omega_{pe}^2}\right) = \Omega_{ci}^2 + \Omega_{ce}^2\frac{\omega_{pi}^2}{\omega_{pe}^2} + \Omega_{ci}^2\frac{\Omega_{ce}^2}{\omega_{pe}^2}. \tag{2.41}$$

Explicitly writing out the gyro and plasma frequencies,

$$\omega^2\left(1 + \frac{e^2B_0^2}{m_e^2}\frac{m_e\epsilon_0}{ne^2}\right) = \frac{e^2B_0^2}{m_i^2} + \frac{e^2B_0^2}{m_e^2}\frac{m_e}{m_i} + \frac{e^4B_0^4}{m_e^2m_i^2}\frac{m_e\epsilon_0}{ne^2}, \tag{2.42}$$

$$\omega^2\left(1 + \frac{\Omega_{ci}\Omega_{ce}}{\omega_{pi}^2}\right) = \frac{e^2B_0^2}{m_im_e}\left(\frac{m_e}{m_i} + 1 + \frac{e^2B_0^2}{m_i^2}\frac{m_i\epsilon_0}{ne^2}\right). \tag{2.43}$$

Since $m_e \ll m_i$, equation (2.43) simplifies to

$$\omega^2\left(1 + \frac{\Omega_{ci}\Omega_{ce}}{\omega_{pi}^2}\right) = \Omega_{ci}\Omega_{ce}\left(1 + \frac{\Omega_{ci}^2}{\omega_{pi}^2}\right). \tag{2.44}$$

Rearranging equation (2.44) we have

$$\frac{1}{\omega^2}\left(1 + \frac{\Omega_{pi}^2}{\omega_{pi}^2}\right) = \frac{1}{\Omega_{ci}\Omega_{ce}} + \frac{1}{\omega_{pi}^2}. \tag{2.45}$$

For most plasmas, the ion plasma frequency is much larger than the ion gyrofrequency, and equation (2.45) can be approximated as

$$\frac{1}{\omega^2} = \frac{1}{\Omega_{ci}\Omega_{ce}} + \frac{1}{\omega_{pi}^2}. \tag{2.46}$$

This is the dispersion relation for the *Lower Hybrid Mode*, which couples the ion and electron gyromotion. Equation (2.46) defines the lower hybrid frequency as

$$\omega_{LH}^2 = \Omega_{ci}\Omega_{ce}. \tag{2.47}$$

Often the lower hybrid mode is treated as a very low frequency wave with $\omega < \omega_{pi}$, in which case equation (2.46) further simplifies to

$$\omega^2 = \Omega_{ci}\Omega_{ce} \equiv \omega_{LH}^2. \tag{2.48}$$

Neglecting thermal pressure for mathematical ease leads to the lower hybrid mode having no dependence on *k*. In the next section we will look at the full dispersion relation $\omega(k)$ for the lower hybrid mode, including thermal pressure and kinetic effects.

2.3 ISR Lines

The three features seen in incoherent scatter are the plasma line, the gyro line, and the ion line. These lines come from scatter off of the Langmuir mode, lower hybrid/electrostatic whistler mode, and ion-acoustic mode, respectively. The dispersion relations in Section 2.2 illuminate the physical mechanism driving each of these waves but are derived from ideal fluid equations. Figure 2.6 shows the simulated ω-k spectra of electrostatic waves propagating parallel to the magnetic field, which corresponds to a magnetic aspect angle of 90° (see Chapter 3 for simulation details). In plot(a) of Figure 2.6 the plasma line is seen at high frequencies, and mostly follows the Langmuir dispersion relation, $\omega^2 = v_{th}^2 k^2 + \omega_{pe}^2$, but has a spread in frequencies at each *k* value. Similarly, plot (b) shows the edges of the ion-acoustic mode follow the fluid dispersion

relation, $\omega = \pm c_s k$, but there is substantial structure to the wave in between the two fluid solutions. The frequency structure and broadening of the Langmuir and ion-acoustic mode comes from both collisions and a kinetic effect known as Landau damping, and in the next section the fully kinetic solution for the ion and plasma lines is derived. The gyro line is not present in spectra exactly parallel to B (*Hysell et al.*, 2017).

Figure 2.7 shows the perpendicular to B spectra, or equivalently the 0° aspect angle spectra, from the same collisional simulation. The nomenclature of plasma line and ion line only weakly holds in the perpendicular to B regime since the Langmuir mode and ion-acoustic mode do not propagate. At higher frequencies the "plasma line" comes from electron Bernstein modes, which are fully kinetic waves driven at harmonics of the electron cyclotron frequency ω_{ce} (*Chen*, 2016). Operationally, these Bernstein modes have not been observed by any radar due to their low signal to noise. At low frequencies the "ion line" is not caused by a wave but is instead the collisional diffusion of electrons across magnetic field lines, which amounts to collisional broadening of the transmitted pulse. Without collisions the perpendicular to B "ion line" would be a delta function at $\omega = 0$. The lower hybrid mode in Figure 2.6 is the gyro line, which starts at $\omega = \omega_{LH}$ for $k = 0$ and follows a k dependence determined by thermal pressure and kinetic effects.

Jicamarca was originally built at the geomagnetic equator to measure ion gyroresonances in order to estimate ion composition. The simulated spectra in Figure 2.7 includes electron-ion, electron-electron, and ion-ion Coulomb collisions. *Farley* (1964) showed that ion-ion collisions would destroy any ion gyroresonances. Since the lower hybrid mode is at $\omega_{LH} = \sqrt{\omega_{ce}\omega_{ci}}$, the ion gyroresonances would be at frequencies less

than the lower hybrid mode, and in agreement with *Farley* (1964) the simulation does not produce ion gyroresonances. *Rodrigues et al.* (2007) has shown Jicamarca can measure proton gyroresonances in the topside where Coulomb collisions are weak and obtained H^+ composition fractions with 10% uncertainty.

A radar measures the spectral power along a single cut through ω-k space at the radar's Bragg wavenumber (see Section 2.4.1). Figure 2.8 shows a sample spectrum measured by Arecibo during the day at an aspect angle of 30°, showing all three ISR lines (*Bhatt et al.,* 2006). The thermally driven plasma and gyro lines have a small SNR and are only seen at Arecibo due to its large aperture and high sensitivity (*Bhatt et al.,* 2006; *Hysell et al*., 2017). During the day photoionization can produce suprathermal electrons which can enhance the power of the plasma and gyro lines (*Malnes and Bjørna*, 1993; *Akbari et al.*, 2017). The dependence of the Langmuir frequency on density (equation 2.11) means the natural or enhanced plasma line is often used as the primary method for measuring density in the ionosphere (*Akbari et al.,* 2017).

Figure 2.8 shows that the ion line power is significantly higher than the background noise level. The high SNR and complex spectral shape of the ion line allow for its use in an inversion problem to extract density, electron temperature, ion temperature, and ion drift velocity. Obtaining temperatures and density from the ion line is colloquially referred to as *ISR*, or the *ISR technique*. The following sections develop the theory and methods used in ISR.

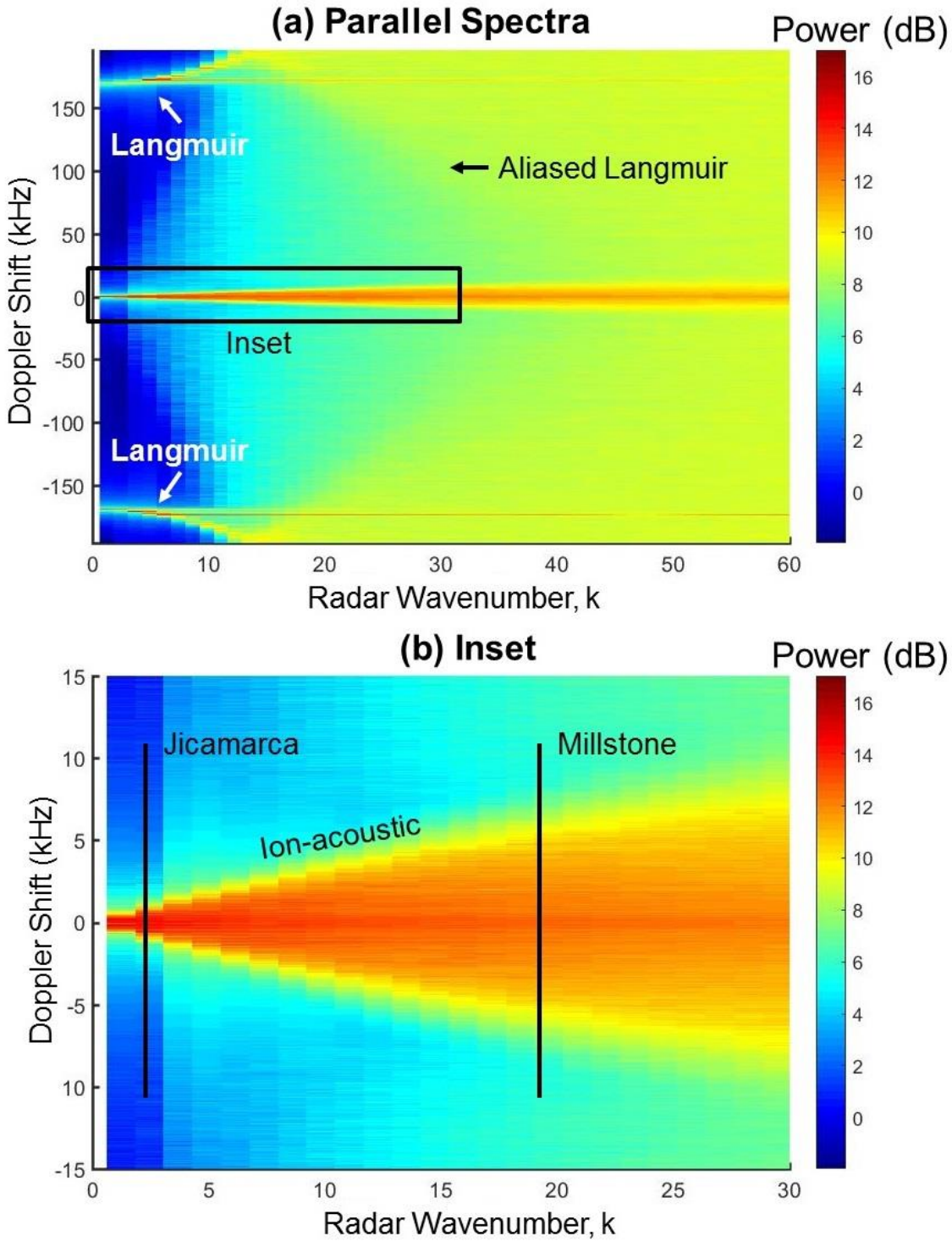

Figure 2.6 Parallel to B spectra from simulations described in Chapter 3. The Langmuir mode in (a) is the plasma line and is aliased in frequency for $k > 13$. The ion-acoustic mode in the inset of plot (b) is the ion line. Radars measure the spectra along a single k.

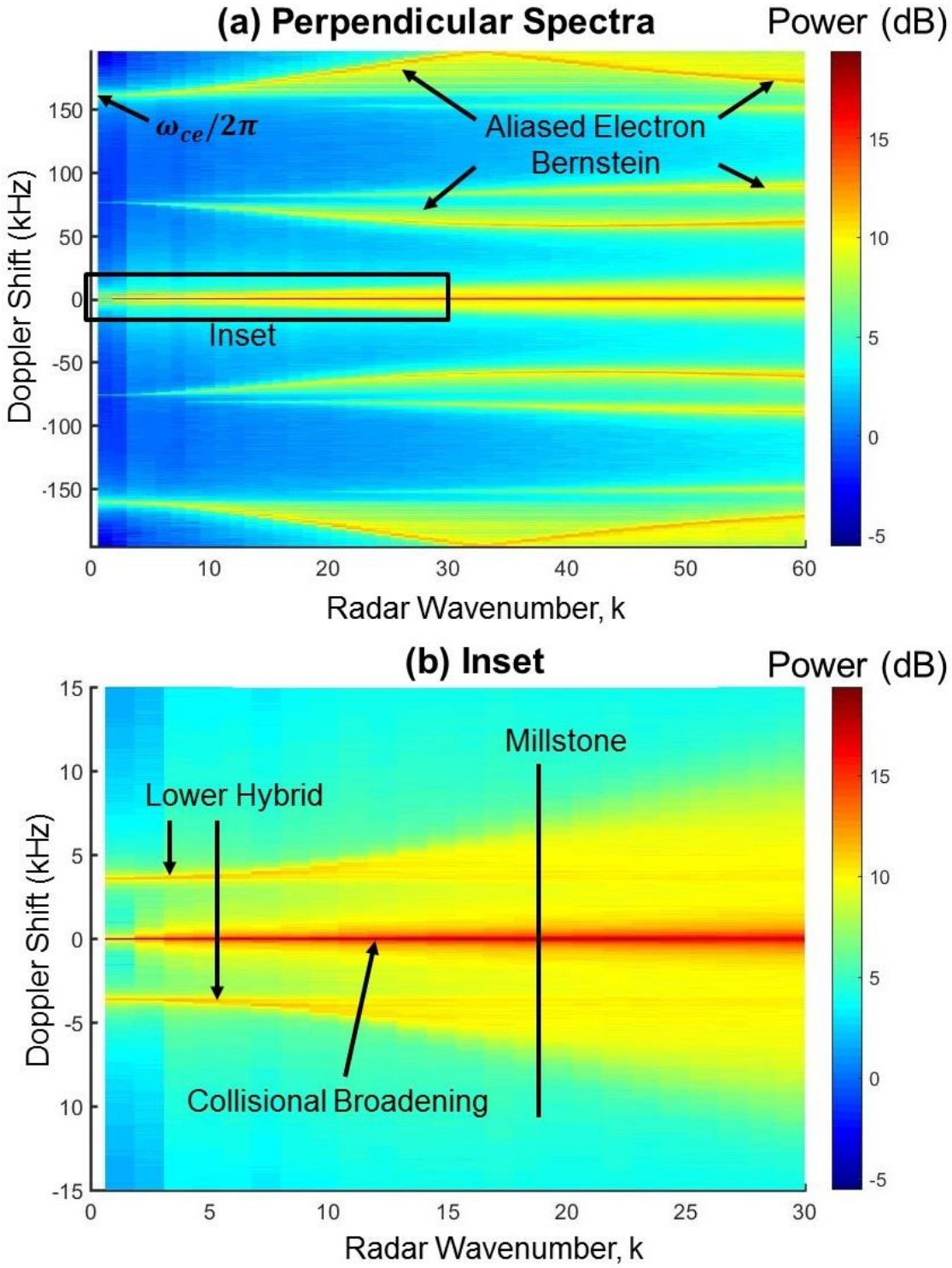

Figure 2.7 Perpendicular to B spectra from simulations described in Chapter 3. The "plasma" lines in (a) are driven by electron Bernstein modes. The inset plot (b) shows the gyro line as the lower-hybrid mode, and the ion line as collisional broadening at 0 Hz.

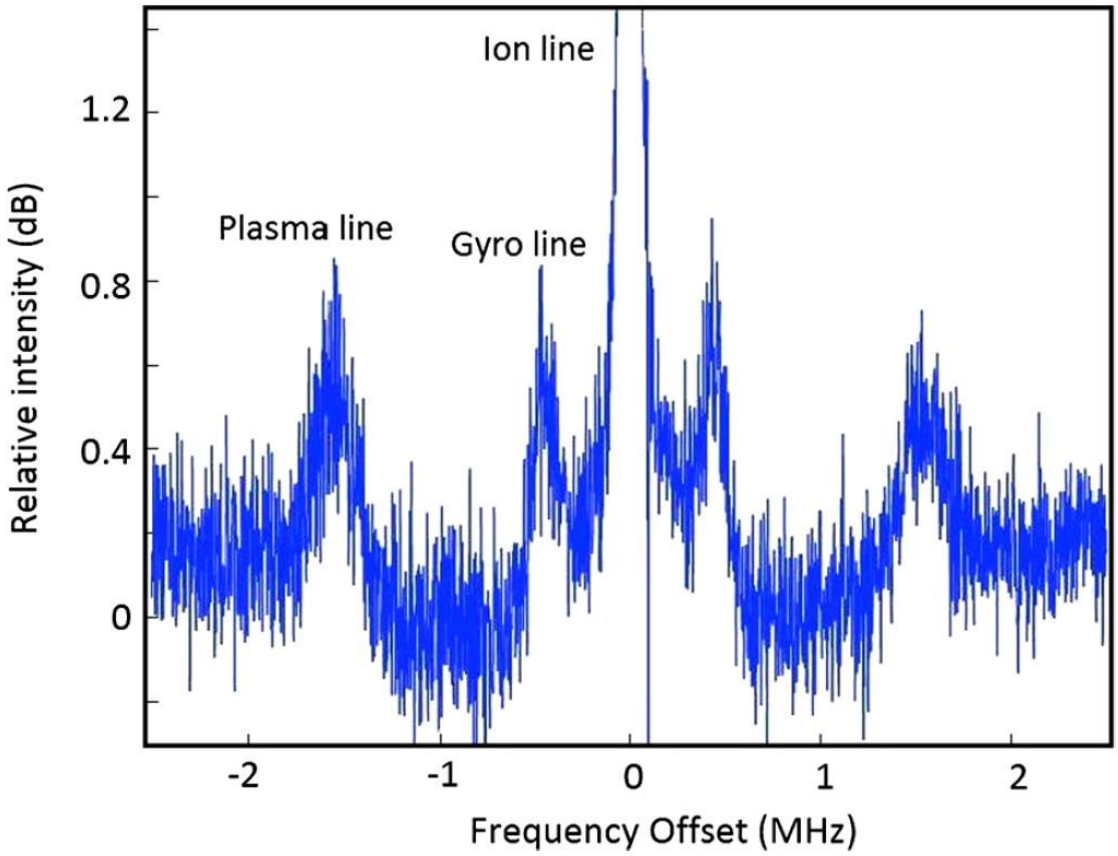

Figure 2.8 The full spectra measured by Arecibo (k = 18), showing the plasma and gyro lines at relatively low power compared to the ion line. (Figure from *Bhatt et al.*, 2006)

2.4 ISR Theory

The ISR technique measures plasma parameters in the ionosphere through an inversion process where a forward model is fit to measured ion line spectra. The inversion routine searches a multidimensional space for the electron temperature, ion temperature, density, and ion composition ratios that give the best least squares fit to the data. This section derives the analytical forwards models currently used in the inversion process, and the focus of Chapters 3 and 4 is using kinetic plasma simulations to calculate more accurate forward models.

2.4.1 Thomson Scattering for Radars

The radar pulses transmitted into the ionosphere are linearly polarized, and the electric field transmitted by the radar, E_i, can be written as *(Kudeki and Milla,* 2011)

$$\vec{E}_i(x) = E_0\, Re\left[e^{ik_0 x}\right]\hat{z}. \tag{2.49}$$

The coordinates are chosen such that the electric field is polarized in the z-direction, and the wave is propagating in the negative x-direction. This electric field will cause electrons to oscillate sinusoidally in the z-direction, which creates a dipole radiation field. This process effectively absorbs and reemits a photon and is called Thomson scattering. The dipole moment, *d*, and dipole radiation pattern for Thomson scattering is (*Rybicki and Lightman*, 1979)

$$\ddot{d} = \frac{e^2 E_i}{m_e} Re\left[e^{i\omega_0 t}\right]\hat{z}, \tag{2.50}$$

$$\vec{E}(t) = \ddot{d}(t)\frac{\sin\Theta}{c^2 R_0}, \tag{2.51}$$

where R_0 is the distance from the electron to the radar receiver. Θ is the angle between the electron's motion in the z-direction, and the receiver's line of sight in the x-direction. In this subsection cgs units are used for the Thomson scattering formulas, but the end result will be independent of unit choice and Section 2.4.2 will resume the use of SI units. Since $t = R_0/c$, equations (2.50) and (2.51) are combined, and Θ is set to 90° for backscatter, to obtain

$$\vec{E}(t) = \frac{e^2 E_i}{m_e}\frac{Re\left[e^{i(k_0 c)(R_0/c)}\right]}{c^2 R_0}\,\hat{z}. \tag{2.52}$$

Equation (2.49) provides the expression for the transmitted electric field E_i, so the backscattered electric field is

$$\vec{E}(t) = \frac{e^2}{m_e} E_0 \, Re\left[e^{ik_0 R_0}\right] \frac{Re\left[e^{ik_0 R_0}\right]}{c^2 R_0} \, \hat{z}. \tag{2.53}$$

The exponential terms can be combined, so this equation simplifies to

$$\vec{E}(t) = \frac{e^2 E_0}{c^2 R_0 m_e} \, Re\left[e^{2ik_0 R_0}\right] \hat{z}. \tag{2.54}$$

Equation (2.54) provides the expression for the scattered electric field that the radar receiver will measure. One thing to note is that equation (2.54) describes a sine wave with a wavelength that is half of the incident wavelength. This is the Bragg scattering condition, and for convenience the wave number is redefined to include the Bragg condition:

$$\vec{k} \equiv \vec{k}_{Bragg} = 2\vec{k}_0. \tag{2.55}$$

The classical electron radius is defined as $r_e = e^2/m_e c^2$, so equation (2.54) becomes

$$\vec{E}(t) = \frac{r_e}{R_0} E_0 \, Re\left[e^{ikR_0}\right] \hat{z}. \tag{2.56}$$

Equation (2.56) is the expression for the Thomson scattered electric field off a single electron in the ionosphere. If *N* is the average number density of the electrons in the ionosphere, then a large volume *V* of the plasma will contain *NV* electrons. Since electromagnetic fields obey the superposition principle, the total electric field scattered off the volume and measured by the radar receiver is

$$\vec{E}_{tot}(t) = E_0 r_e \sum_{j=1}^{NV} \frac{1}{R_{0,j}} Re\left[e^{ikR_{0,j}}\right] \hat{z}. \tag{2.57}$$

The ionosphere starts around 90 km in altitude, and the beam width of the radar is typically less than 1°, so for all electrons in the scattering volume $\vec{R}_{0,j} \cong \vec{R}_0$. Then

$$\vec{E}_{tot}(t) = \frac{E_0 r_e}{R_0} \sum_{j=1}^{NV} Re\left[e^{ikR_{0,j}}\right] \hat{z}. \tag{2.58}$$

The particle positions in the exponential cannot be approximated as R_0 though, since the resulting phase of E_{tot} is highly sensitive to the value of the exponential for each particle.

Equation (2.58) calculates the total electric field returned to the radar after Thomson scattering off of many electrons in the ionosphere. From Parseval's theorem the spectral power, *dW*, per unit area *dA*, measured by the radar is (*Rybicki and Lightman*, 1979)

$$\frac{dW}{dA\, d\omega} = c\left|\vec{E}(\omega)\right|^2, \tag{2.59}$$

where $\vec{E}(\omega)$ is the time Fourier transform of equation (2.58). The exact equation for the electron density at a given location is (see Section 1.2.1)

$$n_e(\vec{x}, t) = \sum_{j=1}^{NV} \delta\left(\vec{x} - \vec{r}_j(t)\right). \tag{2.60}$$

Where *N* is the average electron density across the volume, in comparison to the locally varying electron density n_e. Fourier transforming n_e in all three spatial dimensions yields

$$n_e(\vec{k}, t) = \int_{-\infty}^{\infty} n_e(\vec{x}, t)\, e^{i\vec{k}\cdot\vec{x}} d\vec{x}\,, \tag{2.61}$$

$$n_e(\vec{k},t) = \int_{-\infty}^{\infty} \left[\sum_{j=1}^{NV} \delta\left(\vec{x} - \vec{r}_j(t)\right) \right] e^{i\vec{k}\cdot\vec{x}} d\vec{x}\,. \tag{2.62}$$

The integration in equation (2.62) is over a summation of Dirac delta distributions, so the integral evaluates to

$$n_e(\vec{k},t) = \sum_{j=1}^{NV} e^{i\vec{k}\cdot\vec{r}_j}\,. \tag{2.63}$$

This is exactly the same summation in equation (2.58), with $\vec{k}\cdot\vec{r}_j$ as a generalization of the exponential term. Substituting equation (2.63) into equation (2.58) yields

$$\vec{E}_{tot}(t) = \frac{E_0 r_e}{R_0}\, Re\left[n_e(\vec{k},t)\right] \hat{z}. \tag{2.64}$$

As written in equation (2.64), E_{tot} is the real valued electric field measured by the radar. Since the power spectra in equation (2.59) needs $E(\omega)$, the complex electric field in the time domain is simply

$$\vec{E}_{tot}(t) = \frac{E_0 r_e}{R_0}\, n_e(\vec{k},t)\, \hat{z}. \tag{2.65}$$

Fourier transforming equation (2.65) into frequency space,

$$\vec{E}(\omega) = \frac{E_0 r_e}{R_0} \int_{-\infty}^{\infty} n_e(\vec{k},t)\, e^{i\omega t}\, dt\, \hat{z}. \tag{2.66}$$

Which is just the frequency Fourier transform of the density, so

$$\vec{E}(\omega) = \frac{E_0 r_e}{R_0}\, n_e(\vec{k},\omega)\, \hat{z}. \tag{2.67}$$

Substituting equation (2.67) into equation (2.59), the measured power spectra from Thomson scattering off a collection of electrons is

$$\left|\vec{E}(\omega)\right|^2 = \frac{E_0^2 r_e^2}{R_0^2}\left|n_e\left(\vec{k},\omega\right)\right|^2. \tag{2.68}$$

Equation (2.68) as shown is useless in operations. The electron density n_e has random thermal and wave fluctuations that make a single measurement of $|E(\omega)|^2$ meaningless. To extract macroscopic information from radar measurements of the ionosphere, an ensemble average of the system is needed. Since ensemble averages cannot be measured in a real system, the average of $|E(\omega)|^2$ over many measurements is taken. This is referred to as integration, where a single ISR measurement is obtained by averaging around 100 individual samples over a time span on the order of a minute. Thus, the averaged power spectra measured by a radar is

$$\langle\left|\vec{E}(\omega)\right|^2\rangle = \frac{E_0^2 r_e^2}{R_0^2}\langle\left|n_e\left(\vec{k},\omega\right)\right|^2\rangle. \tag{2.69}$$

This equation shows that the measured spectra depends on physical constants, fixed radar parameters E_0 and R_0, and the Fourier transform of the density, $\langle\left|n_e\left(\vec{k},\omega\right)\right|^2\rangle$. Therefore, the only parameter in the ionosphere that changes the measured spectra is the electron density, and when calculating the expected spectra in ISR theory or simulations we only need to obtain $\langle\left|n_e\left(\vec{k},\omega\right)\right|^2\rangle$.

2.4.2 Dressed Particle Theory

The most straightforward way of solving for the ISR spectra, $\langle \left|n_e(\vec{k},\omega)\right|^2 \rangle$, is to take the Boltzmann equations for electrons and ions, eliminate the perturbed electric field through Poisson's equation, and solve for the electron density. This approach is known as dressed particle theory and was originally used by *Salpeter* (1960) and further developed in *Salpeter* (1961a, b), *Hagfors* (1961), and *Dougherty* (1963). This approach is best summarized in *Froula et al.* (2011), from which this discussion follows.

The case of unmagnetized, collisionless plasmas is easy to summarize and provides a standard form for the spectra. The linearized electron and ion Boltzmann equations, and the linearized Poisson equation respectively are

$$\frac{\partial F_{1e}}{\partial t} + \vec{v}\cdot\frac{\partial F_{1e}}{\partial \vec{x}} - \frac{e}{m}\vec{E}_1\cdot\frac{\partial F_{0e}}{\partial \vec{v}} = 0, \tag{2.70}$$

$$\frac{\partial F_{1i}}{\partial t} + \vec{v}\cdot\frac{\partial F_{1i}}{\partial \vec{x}} + \frac{e}{m}\vec{E}_1\cdot\frac{\partial F_{0i}}{\partial \vec{v}} = 0, \tag{2.71}$$

$$\nabla\cdot\vec{E}_1 = \frac{e}{\epsilon_0}\int d\vec{v}\, F_{1i} - \frac{e}{\epsilon_0}\int d\vec{v} F_{1e}\,. \tag{2.72}$$

where each quantity is broken into a 0^{th} order quantity, and a small 1^{st} order perturbation. The three equations are then Fourier transformed in space and Laplace transformed in time. Substituting the electric field into the Boltzmann equations, the perturbed distributions F_1 are (*Froula et al.*, 2011)

$$F_{1s}(\omega,\vec{k},\vec{v}) = -\frac{F_{1s}(0,\vec{k},\vec{v}) - \frac{q_s}{\epsilon_0 m_s k^2}\rho_1(\omega,\vec{k})\, k\cdot\frac{\partial F_{0s}}{\partial \vec{v}}}{\omega - \vec{k}\cdot\vec{v} - i\gamma}, \tag{2.73}$$

where the total perturbed density is $\rho_1 = en_{1i} - en_{1e}$. The factor $i\gamma$ comes from the Laplace transformation in time and is the Landau damping rate, which is necessary to avoid the pole at $v = \omega/k$ when integrating F_1 over all velocity space. The Laplace transform also introduces the term $F_{1s}(0, \vec{k}, \vec{v})$, which is not present for typical Fourier analysis. Eliminating the ion density and integrating over all velocity space provides an expression for n_{1e}. Squaring and taking the ensemble average gives the final spectra (*Froula et al.*, 2011):

$$\langle \left| n_e(\omega, \vec{k}) \right|^2 \rangle = \frac{\pi}{k} \left| 1 - \frac{\chi_e}{\epsilon} \right|^2 f_{e0}\left(\frac{\omega}{k}\right) + \frac{\pi}{k} \left| \frac{\chi_e}{\epsilon} \right|^2 f_{i0}\left(\frac{\omega}{k}\right), \tag{2.74}$$

$$\epsilon = 1 + \chi_i + \chi_e, \tag{2.75}$$

$$\chi_s(\omega, \vec{k}) = \frac{\omega_{ps}^2}{k^2} \int_{-\infty}^{\infty} \frac{\vec{k} \cdot \frac{\partial f_{0s}}{\partial \vec{v}}}{\omega - \vec{k} \cdot \vec{v} - i\gamma} dv, \tag{2.76}$$

where f_{0s} is the distribution normalized to 1. The susceptibilities χ_s are just the plasma dispersion function (Z function) for each species and simplify greatly when a Maxwellian distribution is assumed and Plemelj's theorem is used to solve the integral. Note that without the Landau damping term $i\gamma$ from the Laplace transform, the integral over velocity in equation (2.76) would encounter a pole at $v = \omega/k$. Equation (2.74) gives the interpretation that the ISR spectra is a combination of 3 terms representing scattering off: 1) free electrons (proportional to $1 \cdot f_{e0}(v)$ before squaring), 2) electrons Debye shielding other electrons (proportional to $\frac{\chi_e}{\epsilon} f_{e0}(\frac{\omega}{k})$ before squaring), and 3) electrons

Debye shielding ions, which is the term $\frac{\chi_e}{\epsilon} f_{i0}\left(\frac{\omega}{k}\right)$ that dominates the spectra when the radar wavelength is longer than the Debye length, and when collisions and the magnetic field are neglected.

To solve for spectra at small magnetic aspect angles the BGK collision operator is used:

$$\left(\frac{\partial F_{1s}}{\partial t}\right)_{coll} = -\nu_{cs}\left(F_{1s} - n_{1s}F_{0s}(\vec{v})\right). \tag{2.77}$$

In contrast to the Fokker-Planck collision operator developed in Section 1.2, the BGK collision operator is linear in the perturbed distribution F_{1s} and is typically used with a velocity independent collision rate ν_{cs} that approximates all of the collisions for species *s* as a simple drag force. The second term in the BGK collision operator is included to conserve particles. For notational purposes the collision frequency will always have subscripts, and the velocity will never have subscripts. The linearized Boltzmann equations with the BGK collision operator and a static magnetic field are then

$$\frac{\partial F_{1e}}{\partial t} + \vec{v}\cdot\frac{\partial F_{1e}}{\partial \vec{x}} - \frac{e}{m}\left(\vec{E}_1 + \vec{v}\times\vec{B}_0\right)\cdot\frac{\partial F_{0e}}{\partial \vec{v}} = -\nu_{ce}\left(F_{1e} - n_{1e}F_{0e}(\vec{v})\right), \tag{2.78}$$

$$\frac{\partial F_{1i}}{\partial t} + \vec{v}\cdot\frac{\partial F_{1i}}{\partial \vec{x}} + \frac{e}{m}\left(\vec{E}_1 + \vec{v}\times\vec{B}_0\right)\cdot\frac{\partial F_{0i}}{\partial \vec{v}} = -\nu_{ci}\left(F_{1i} - n_{1i}F_{0i}(\vec{v})\right). \tag{2.79}$$

The analysis follows the same overall steps as the collisionless, unmagnetized case above, and is detailed in *Froula et al.* (2011). The magnetic term is dealt with by writing the perturbed densities as a summation of Bessel functions. The linearity of the collision operator in F_1 makes the set of equations easy to solve. After Fourier-Laplace

transforming the Boltzmann equation the term $\frac{\partial F_{1s}}{\partial t}$ goes to $i\omega F_{1s}$ and is easily combined with the $\nu_{cs}F_{1s}$ term. This yields factors of the form $(i\omega - i\vec{k}\cdot\vec{v} + \nu_{cs})$, which is treated the same as the Landau damping term in equation (2.73) with the substitution $\gamma \to \nu_{cs}$. The particle conserving term $\nu_{cs}n_{1s}F_{0s}$ is independent of F_{1s}, and acts as a constant when solving for F_{1s}. The end result for the spectra is (*Froula et al.*, 2011)

$$\langle\left|n_e(\omega,\vec{k})\right|^2\rangle = 2\left|1-\frac{L_e}{\epsilon}\right|^2 M_e + 2\left|\frac{L_e}{\epsilon}\right|^2 M_i, \tag{2.80}$$

$$\epsilon = 1 + L_e + L_i. \tag{2.81}$$

The interpretation of this result is the same as above, the first term $1 \cdot M_e$ is scattering off free electrons, the second term $L_e/\epsilon \cdot M_e$is scattering off electrons Debye shielding other electrons, and the last term is scattering off electrons Debye shielding ions. The susceptibilities L_s, and the "distributions" M_s are more complicated expressions, and for Maxwellian distributions are calculated from the equations (*Froula et al.*, 2011):

$$\bar{\rho}_s = \frac{v_{th,s}}{\sqrt{2}\,\Omega_s}, \tag{2.82}$$

$$U_s = i\sum_l e^{-k_\perp^2\bar{\rho}_s^2} I_l(k_\perp^2\bar{\rho}_s^2)\frac{\nu_{cs}}{\omega - l\Omega_s - i\nu_{cs}} Z_s\left[\frac{\omega - l\Omega_s - i\nu_{cs}}{k_\parallel v_{th,s}}\right], \tag{2.83}$$

$$L_s = \frac{\alpha^2}{1+U_s}\left(1 - \sum_l e^{-k_\perp^2\bar{\rho}_s^2} I_l(k_\perp^2\bar{\rho}_s^2)\frac{\omega - i\nu_{cs}}{\omega - l\Omega_{cs} - i\nu_{cs}} Z_s\left[\frac{\omega - l\Omega_s - i\nu_{cs}}{k_\parallel v_{th,s}}\right]\right), \tag{2.84}$$

$$M_s = \frac{1}{|1+U_s|^2}\left(-\frac{|U_s|^2}{\nu_{cs}} + \sum_l e^{-k_\perp^2\bar{\rho}_s^2} I_l(k_\perp^2\bar{\rho}_s^2)\,\mathrm{Im}\left(\frac{Z_s\left[\frac{\omega - l\Omega_s - i\nu_{cs}}{k_\parallel v_{th,s}}\right]}{\omega - l\Omega_{cs} - i\nu_{cs}}\right)\right), \tag{2.85}$$

where $v_{th,s} = \sqrt{2KT_s/m_s}$. The plasma dispersion function, Z_s, for Maxwellian distributions is

$$Z_s[x] = 2x\, e^{-x^2}\left(\int_0^x e^{s^2} ds + i\sqrt{\pi}\right). \tag{2.86}$$

The analytic solution for collisional, magnetized spectra using the Dressed Particle approach in equations (2.80) – (2.86) is relatively straightforward, but the actual calculation of the spectra is slow and prone to computational errors. The plasma dispersion function in equation (2.86) needs to be calculated from the Dawson function to avoid numerical overflow:

$$Dawson(x) = e^{-x^2}\int_0^x e^{s^2} ds\,. \tag{2.87}$$

Similarly, the modified Bessel function term $e^{-k_\perp^2\bar{\rho}_s^2} I_l(k_\perp^2\bar{\rho}_s^2)$ is prone to overflow, and most programming languages have an option to calculate the whole term. The infinite summation over the modified Bessel functions needs to be truncated, and in general this can be done at $l = \pm 500$. For solutions at smaller aspect angles or higher frequencies the summation may need to be truncated at a much higher value, which makes the computation of spectra from Dressed Particle theory very slow compared to the Fluctuation-Dissipation theory in the next section.

To summarize the dressed particle approach:

- Solves linearized electron and ion Boltzmann equations with Poisson's equation for the electric field.

- Landau damping is explicitly calculated from the plasma dispersion functions Z_s when integrating around the pole $v = \omega/k$ using Plemelj's theorem.
- Inclusion of a magnetic field is handled exactly by writing the solution as a series of Bessel functions
- BGK collision operator is used, $\left(\frac{\partial F_{1s}}{\partial t}\right)_{coll} = -\nu_{cs}F_{1s} + \nu_{cs}n_{1s}F_{0s}$. This collision operator is linear in F_{1s}, which is why it is easy to include when solving for the spectra. The Fokker-Planck collision operator can be explicitly used, but the equations may be intractable without linearizing the operator.

2.4.3 Fluctuation-Dissipation Theory

An alternative approach to solving for the ISR spectra is to look at the plasma as a circuit where thermal fluctuations give rise to Landau damping of waves (dissipation). This approach was originally developed in a series of papers by *Dougherty and Farley* (1960), *Farley et al.* (1961), and *Dougherty and Farley* (1963b), and is the approach used in *Kudeki and Milla* (2011).

Fluctuation-dissipation theory derives the spectra from Ampere's law, which in linearized, Fourier transformed form is

$$-i\vec{k} \times \vec{H} = \vec{J} + i\omega\epsilon_0\vec{E}. \tag{2.88}$$

In the direction along $\vec{k}$ the term on the left-hand side disappears, which gives the relation that all currents $\vec{J}$ in the plasma are countered by the displacement current $i\omega\epsilon_0\vec{E}$. The problem is to then determine what the currents in the plasma are. There are first

microscopic, thermally imposed currents arising from random fluctuations in the plasma. From the continuity equation these currents are

$$J_t = \frac{\omega}{k} e(n_{ti} - n_{te}), \tag{2.89}$$

where n_{ts} is the microscopic density fluctuation. The second set of currents are from macroscopic motions or waves. Assuming Ohm's law, these currents are

$$J = (\sigma_e + \sigma_i)E. \tag{2.90}$$

Putting these two types of currents into Ampere's law in the *k* direction yields

$$0 = (\sigma_e + \sigma_i)E + \frac{\omega}{k} e(n_{ti} - n_{te}) + i\omega\epsilon_0 E. \tag{2.91}$$

Using a circuit diagram, *Kudeki and Milla* 2011 shows how Kirchoff's laws yield an expression for the total electron current. This is equivalent to just defining a total electron current from the continuity equation with the overall electron density n_e:

$$-\frac{\omega}{k} e n_e = E\sigma_e - \frac{\omega}{k} e n_{te}. \tag{2.92}$$

This gives a system of equations which can be solved to find

$$n_e(\vec{k}, \omega) = \frac{(i\omega\epsilon_0 + \sigma_i) n_{te}(\omega, k) + \sigma_e n_{ti}(\omega, k)}{i\omega\epsilon_0 + \sigma_e + \sigma_i}. \tag{2.93}$$

Squaring and averaging,

$$\begin{aligned} \langle |n_e(\omega, k)|^2 \rangle = &\left| \frac{(i\omega\epsilon_0 + \sigma_e + \sigma_i) - \sigma_e}{i\omega\epsilon_0 + \sigma_e + \sigma_i} \right|^2 \langle |n_{te}(\omega, k)|^2 \rangle \\ &+ \left| \frac{\sigma_e}{i\omega\epsilon_0 + \sigma_e + \sigma_i} \right|^2 \langle |n_{ti}(\omega, k)|^2 \rangle. \end{aligned} \tag{2.94}$$

This result has the same form as equations (2.74) and (2.80) from the dressed particle theory above, with the interpretation that an overall dielectric function is $i\omega\epsilon = i\omega\epsilon_0 + \sigma_e + \sigma_i$, and that the densities n_{ts} from the thermal current terms are related to the particle distributions.

To proceed further, expressions for n_{ts} and the conductivities σ_s are needed. The thermally impressed density n_{ts} is calculated assuming the radar is scattering off a free distribution with no collective interactions (*Kudeki and Milla*, 2011):

$$\langle \left| n_{ts}\left(\omega, \vec{k}\right) \right|^2 \rangle = 2N\mathrm{Re}[J_s(\omega_s)]. \tag{2.95}$$

The conductivities σ_s are then calculated from the fluctuation-dissipation theorem and Kramers-Kronig relations (*Kudeki and Milla*, 2011),

$$\sigma_s\left(\omega, \vec{k}\right) = \frac{i\omega\epsilon_0}{k^2 h_d^2}(1 - i\omega J_s). \tag{2.96}$$

J_s is the Gordeyev integral for species *s* and its meaning is effectively defined through equation (2.95) as the scattering off species *s* in the absence of any collective effects, i.e. truly incoherent scatter. The calculation of ISR spectra then comes down to calculating the Gordeyev integral for each species, which is defined as

$$J_s(\omega) = \int_0^\infty d\tau e^{i\omega\tau} \langle e^{i\vec{k}\cdot\Delta\vec{r}} \rangle . \tag{2.97}$$

The term in angled brackets is the single particle autocorrelation function (ACF), and the Gordeyev integral is simply the one-sided Fourier transform of the ACF. For a collisionless, unmagnetized plasma, the ACF is

$$\langle e^{i\vec{k}\cdot\Delta\vec{r}}\rangle = e^{-\frac{1}{2}k^2 c_s^2 \tau^2}. \tag{2.98}$$

For a collisional, magnetized plasma, the ACF assuming a Brownian collision operator (see Section 1.2.6) is (*Woodman*, 1967)

$$\langle e^{i\vec{k}\cdot\Delta\vec{r}}\rangle = \exp\left[-k_\parallel^2 \frac{C_s^2}{\nu_{cs}^2}(\nu_{cs}\tau - 1 + e^{\nu_{cs}\tau})\right]$$
$$\times \exp\left[-k_\perp^2 \frac{c_s^2}{\nu_{cs}^2 + \Omega_s^2}(\cos(2\gamma) + \nu_{cs}\tau - e^{\nu_{cs}\tau}\cos(\Omega_s\tau - 2\gamma))\right]. \tag{2.99}$$

where ν_{cs} is the constant collision rate for the Brownian collision operator, and $\gamma \equiv \arctan(\nu_{cs}/\Omega_s)$.

Alternatively, the ACFs and thus the spectra can be calculated from simulations of a single particle moving in a magnetic field and subject to fully kinetic collisions using the Fokker-Planck collision operator. This is the approach taken in *Sulzer and Gonzalez* (1999) and *Milla and Kudeki* (2011) due to the difficulty of finding an analytic expression for the Gordeyev integral with a velocity dependent collision operator. Section 4.4 details this single particle simulation approach.

To summarize the fluctuation-dissipation theory in *Kudeki and Milla* (2011):

- Spectra is calculated from linearizing Ampere's law, and assuming thermally impressed currents $J_t = \frac{\omega}{k} e(n_{ti} - n_{te})$, and macroscopic currents from Ohm's law $\vec{J} = \sigma_s \vec{E}$.
- Gordeyev integral is calculated analytically from first principles equation of motion, or numerically from single particle simulations.

- The fluctuation-dissipation theorem provides a link between the Gordeyev integral and the real part of the conductivities, σ_s, in Ohm's law.

- The Kramers-Kronig relations determine the imaginary part of the conductivity from the real part through a Hilbert transform:

$$\mathrm{Im}[\sigma_s(\omega)] = \frac{1}{\pi}\mathcal{P}\int_{-\infty}^{\infty}\frac{\mathrm{Re}[\sigma_s(\omega)]}{W-\omega}dW\,. \tag{2.100}$$

  The Kramers-Kronig relations are calculated from a contour integral of σ_s around the complex lower half plane, and applying Plemelj's theorem to write the integral in terms of a residue (left hand side of equation 2.100), and a principal value integral (right hand side). The conductivity is then rewritten as the Hilbert transform of the Gordeyev integral, which leads to equation (2.96) for the whole conductivity. This implicit use of the Plemelj formula provides the same Landau damping term seen in the plasma dispersion function in the Dressed Particle theory. This link between the two theories is further discussed in Section 4.5.

- Magnetic fields are added exactly through the single particle ACF and Gordeyev integral.

- Analytically including velocity dependent collisions is difficult since a single, velocity independent ACF needs to be calculated. The theory can gracefully handle Brownian motion collisions, which have velocity independent drag and diffusion terms.

2.4.4 Comparison of Theories at Small Aspect Angles

The dressed particle theory and fluctuation-dissipation theory are well known to agree for unmagnetized plasmas, or for large magnetic aspect angles α when the radar looks parallel to the Earth's magnetic field. As the magnetic aspect angle decreases, and the radar looks close to perpendicular to B, the motion of electrons is constrained by the magnetic field. *Sulzer and Gonzalez* (1999) recognized that this geometric constraint means electrons have to move a much longer distance along magnetic field lines to create a measurable Doppler shift at small aspect angles (Figure 2.9). This increased transit time along the magnetic field means a collision is more likely to occur and change the electron's trajectory, and therefore damp the wave that the radar is trying to measure.

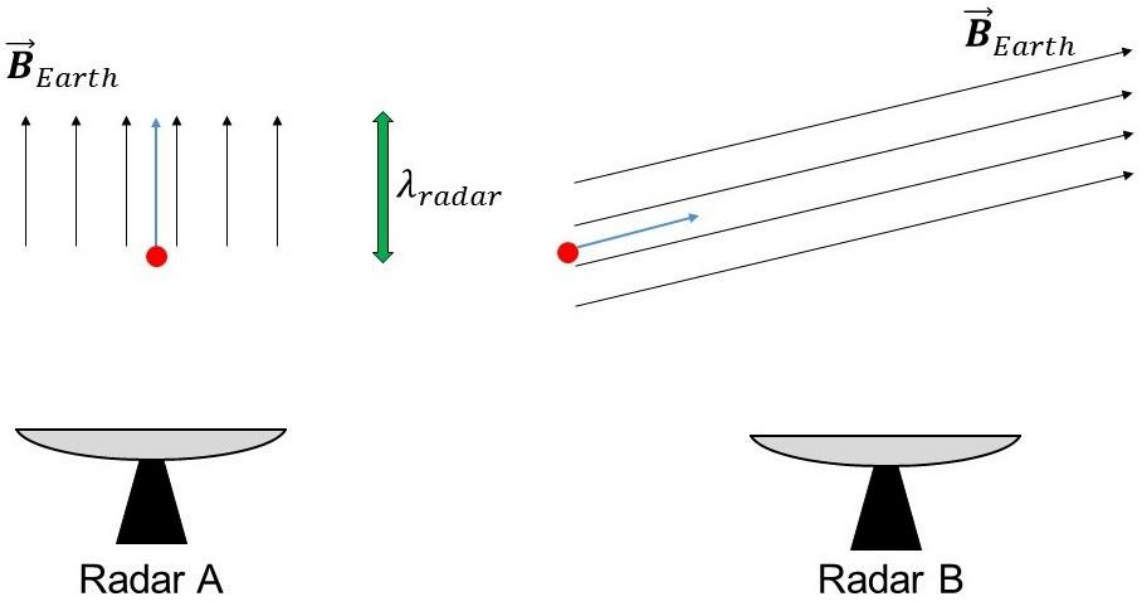

Figure 2.9 The geometry of small aspect angle ISR. Radar A (left) is measuring ISR spectra parallel to the magnetic field (black arrows). The electron (red circle) will quickly move one radar wavelength away from the radar, which will measure the resulting Doppler shift. Radar (B) is measuring small aspect angle ISR spectra. The electron motion is tied to the magnetic lines, and therefore the electron takes a significantly longer time to move one wavelength away from the radar.

The importance of collisions in small aspect angle ISR spectra is highlighted by comparing the dressed particle theory with a BGK collision operator to the fluctuation dissipation theory with a Brownian collision operator. Figure 2.10 compares these spectra to collisionless fluctuation-dissipation theory for a 50 MHz radar. For aspect angles of 4° and larger, both theories exactly match the collisionless spectra. At aspect angles of 3° and less, a substantial difference is seen between the collisional theories. The BGK collision operator describes a constant drag force, and therefore underestimates the effects of small angle ion-ion collisions which should kill off ion gyroresonances (*Farley*, 1964). While the electron collisions narrow the BGK spectra at the same rate as the Brownian spectra, the 30 Hz ion gyro-period is clearly present, showing the deficiency of the BGK collision operator. At aspect angles of 2° and less, the collisionless spectra is wider and less damped than the Brownian collisional theory. Exactly perpendicular to B the collisionless theory blows up, and the BGK theory only shows weak scatter. *Milla and Kudeki* (2011) and Chapter 4 of this dissertation show that the Brownian theory correctly models collisional diffusion across the magnetic field lines and calculates spectra perpendicular to B in exact agreement with simulations.

Figure 2.11 makes the same comparison for a 440 MHz radar. For aspect angles greater than 0.5°, both collisional theories exactly match collisionless theory. This reflects the fact that the Bragg scattering wavelength of a 440 MHz radar is 34 cm, and therefore electrons have a shorter distance to move away from the radar compared to the 3 m wavelength of a 50 MHz radar. At aspect angles of 0.33° and less the same differences between the Brownian, BGK, and collisionless theories are present.

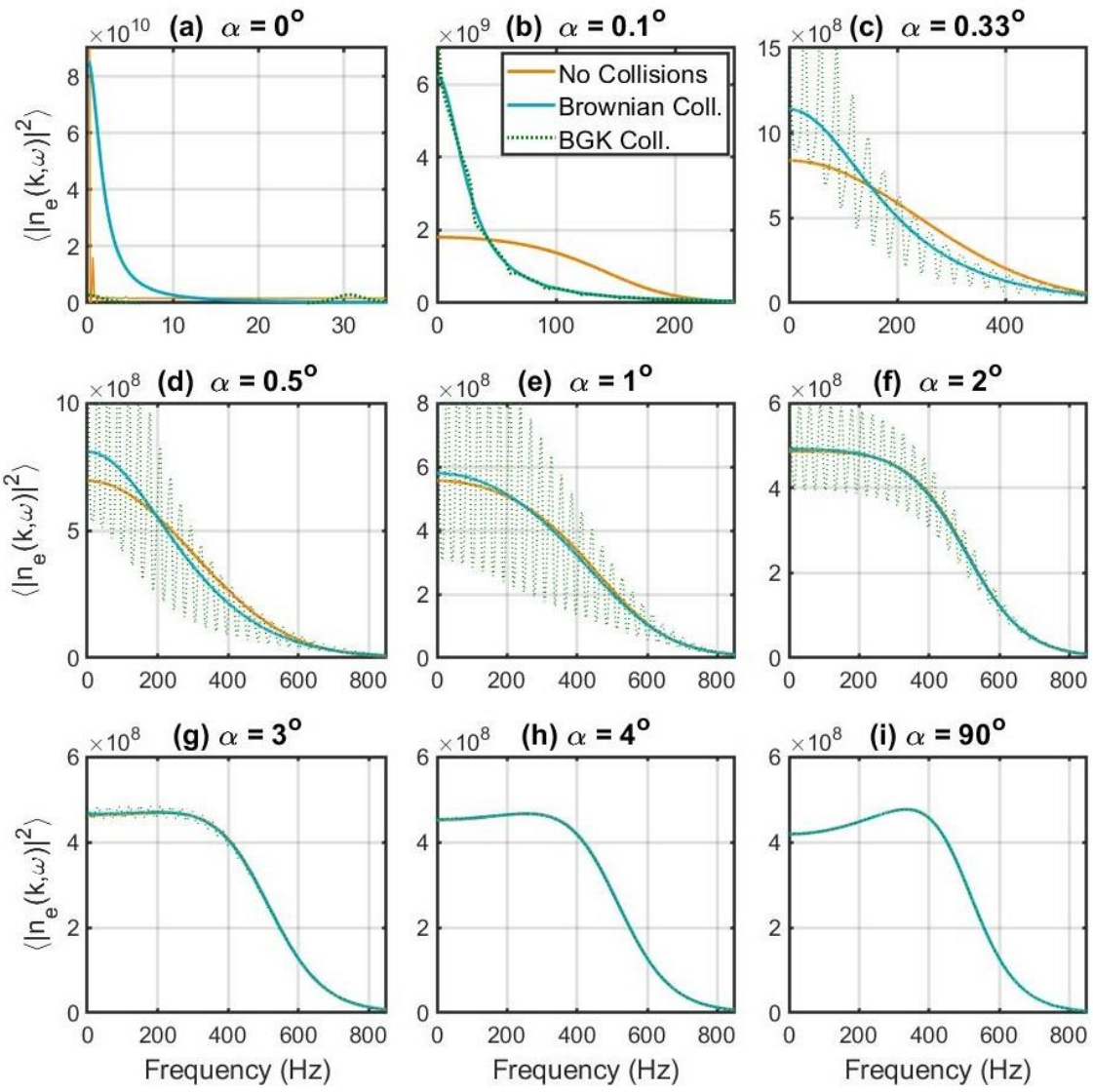

Figure 2.10 ISR spectra for a 50 MHz radar as a function of magnetic aspect angle α. The collisionless theory (orange) is calculated from the fluctuation-dissipation theory with ion collisions included to remove the ion gyroresonances. The Brownian collisional spectra (blue) is also calculated from the fluctuation dissipation theory with an electron collision rate of $\langle \nu_e \rangle = 2440\ Hz$. The same collision rate is used in the BGK dressed particle theory (dashed green), which includes ion collisions as well. All of the spectra are calculated for an O^+ plasma with $T_e = T_i = 1000\ K$, and $n = 10^{12}\ m^{-3}$.

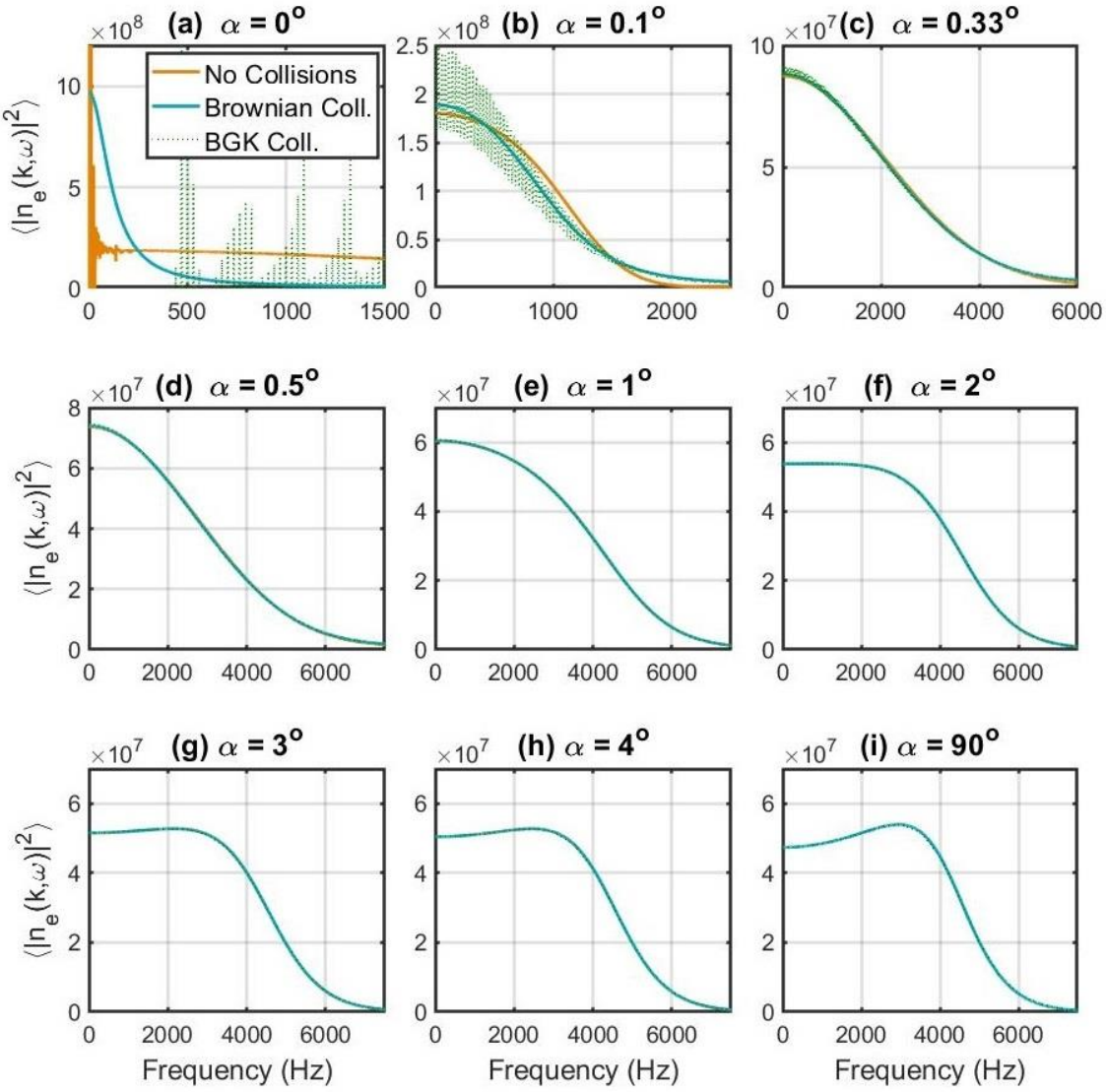

Figure 2.11 Same as Figure 2.10, but for a 440 MHz radar.

2.5 Plasma Measurements Using ISR

Radars fundamentally measure the Doppler shift of a transmitted radio wave. For an object moving at nonrelativistic speed *v*, and a transmitted frequency of f_0, the Doppler shifted frequency measured by a radar is

$$f_{Doppler} = \pm \frac{2 f_0 v}{c}. \tag{2.100}$$

The plus sign in equation (2.100) is chosen for objects moving towards from the radar (blueshift), and the minus sign is chosen for objects moving away from the radar (redshift). Incoherent scatter radars measure a Doppler shift spectrum from a large number of electrons with velocities determined by the density fluctuations $n_e(\omega, \vec{k})$ derived in Section 2.4. In this section it is shown how ISR uses the measured power versus Doppler shift to calculate the density, electron and ion temperatures, and ion composition. Trivially, the average Doppler shift of the spectrum provides a measurement of the line of sight ion velocity.

2.5.1 Pulse Codes

Before detailing how the Doppler shift spectrum is analyzed it is useful to review how ISR measurements are made. At a hardware level, the radar measures a voltage across the antenna as a function of time, computes the autocorrelation of that time series, and then Fourier transforms the autocorrelation to produce the Doppler shift spectrum. The direct measurement of a time series means a radar's output is dictated by the sampling rate of the incoming signal, and by how long the signal is measured.

If a radar transmits a continuous signal at a constant frequency, then no information is available on the distance to the target since the received signal can correspond to a transmission at any time. For this reason, and often due to hardware constraints, ISRs transmit pulses on the order of 1 ms, then measure the returned signal over a period of 10-20 ms before repeating. This period in between pulses is the inter-pulse period, or *IPP*. The IPP then dictates a maximum unambiguous range from the travel time of the radio wave:

$$R_u = \frac{c}{2} \cdot IPP. \tag{2.101}$$

Thus a 20 ms IPP yields a maximum unambiguous range of 3,000 km, and any echo coming from a distance farther than 3,000 km will be aliased in range. The IPP is chosen such that (*Hysell*, 2018)

$$\frac{\lambda}{4v_{max}} \geq IPP \geq \frac{2R_{max}}{c}. \tag{2.102}$$

The first inequality is equivalent to the Nyquist sampling criteria and shows that choosing too large of an IPP will alias the measurements in frequency space. The second inequality effectively states that the maximum range an echo can come from, R_{max}, is less than the maximum unambiguous range, R_u, from equation (2.102). If an IPP satisfies both inequalities in equation (2.102) then the target is *underspread* and a measurement from each pulse of the radar can be used to accurately construct the voltage autocorrelation function. Most ISR experiments are *overspread*, and no IPP exists that satisfies both inequalities in equation (2.102).

Measuring overspread targets requires transmitting a long pulse of length τ and oversampling the returned signal at subintervals (*Hysell,* 2018). The sampling rate of the single pulse then determines the frequencies measured in the final Doppler shift spectrum. The tradeoff for using this technique is that ISR measures backscatter off a continuum of altitudes, and the range resolution of any measurement is

$$\Delta R = \frac{c}{2}\tau. \tag{2.103}$$

Increasing the pulse length allows for more sampling of the signal and increases the power returned by scattering off a larger volume, but the tradeoff is losing sensitivity to the range at which an echo comes from. The increased return power is useful for combatting the $1/R^2$ drop off of SNR (see Section 2.5.2), or for measuring density perturbations that are typically below the noise level.

Using a coded sequence in a long pulse gains the benefit of higher SNR while mitigating the poorer range resolution. A pulse code represents a binary sequence in the transmitted waveform by inverting the phase at set intervals (baud lengths), as shown in Figure 2.12. The ideal pulse code has an autocorrelation function strongly peaked at 0 time lag, with all other time lags at minimal power. The range resolution of a pulse with baud length *t* is then

$$\Delta R = \frac{c}{2}t, \tag{2.104}$$

which is much smaller than an uncoded long pulse. Chapter 5 uses a 100-baud coded long pulse at Millstone Hill to measure ISR spectra at small magnetic aspect angles.

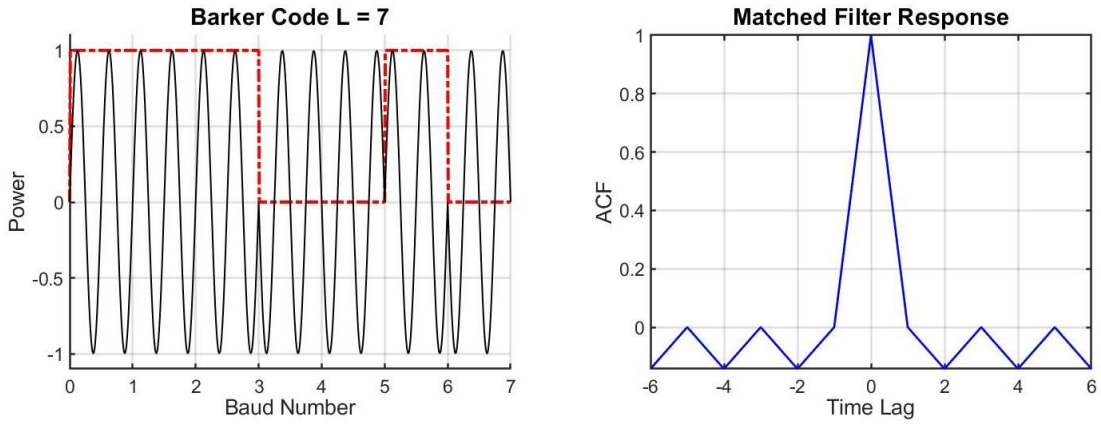

Figure 2.12 (Left) A schematic of a 7-baud Barker code. The binary coding (red) of a pulse is achieved by inverting or not inverting the phase of the transmitted signal (black) at every baud length *t*. The number of cycles per baud is greatly decreased for illustration purposes. (Right) The autocorrelation of the same Barker code is calculated, showing the matched filter response of the code.

2.5.2 Measuring Density

The thermal distribution of electron velocities leads to the radar measuring various power levels across a broad band of Doppler shifted frequencies. The received spectral power P_{rec} from a radar is calculated from the radar equation:

$$P_{rec}(\omega, \vec{k}) = \frac{P_{trans} A^2}{4\pi\lambda^2 R^4} \sigma(\omega, \vec{k}). \tag{2.105}$$

In equation (2.105) the transmitted power is P_{trans}, the effective antenna area is A, the transmitted wavelength is λ, and the distance from the radar to the target is R. The radar cross section σ in equation (2.105) is based on properties of the target and is effectively the geometric size of most objects. However, for incoherent scatter radar the target is a large volume, and the cross section is often written in terms of a cross section per scattering volume,

$$\sigma = \sigma_v \Omega R^2 \Delta R, \tag{2.106}$$

where Ω is the solid angle of the antenna beam. The volumetric cross section is related to the electron density fluctuations as (*Kudeki and Milla*, 2011)

$$\sigma_v(\omega,\vec{k}) = 4\pi r_e^2 \left|n_e(\omega,\vec{k})\right|^2. \tag{2.107}$$

The radar equation for ISR is then

$$P_{rec}(\omega,\vec{k}) = P_{trans}\frac{r_e^2}{R^2}\left(\frac{A^2\Omega\,\Delta R}{\lambda^2}\right)\left|n_e(\omega,\vec{k})\right|^2. \tag{2.108}$$

Since the power of a radio wave varies as $P \propto E^2$, we can compare equation (2.108) directly to equation (2.68) which derived the expected scattering power from Thomson scattering off a volume of electrons:

$$\left|\vec{E}(\omega)\right|^2 = \frac{E_0^2 r_e^2}{R_0^2}\left|n_e(\vec{k},\omega)\right|^2. \tag{2.68}$$

Thus, the only difference between the two equations is the term in parentheses in equation (2.108) which accounts for the gain of an antenna.

The total power measured by a radar transmitting at a fixed *k* is found by averaging equation (2.108) over multiple measurements, and then integrating over all frequencies.

$$P_{tot} = P_{trans}\frac{r_e^2}{R^2}\left(\frac{A^2\Omega\,\Delta R}{\lambda^2}\right)\int_{-\infty}^{\infty}\langle\left|n_e(\omega),\vec{k}\right|^2\rangle\,d\omega\,. \tag{2.109}$$

For aspect angles far from perpendicular to B the integral over the density fluctuation is (*Farley*, 1966)

$$P_{tot} = P_{trans}\left(\frac{A^2\Omega\,\Delta R}{4\pi R^2\lambda^2}\right)\frac{N_e}{1+T_e/T_i}. \quad (2.110)$$

This means the total power measured by the radar is directly proportional to the average electron density of the volume, N_e. If the temperature ratio T_e/T_i is known, and the antenna gain term in the parentheses is well calibrated, then the density in the ionosphere is measured directly from the total power.

In practice, the temperature ratio is not known before fitting the spectra (see Section 2.5.3), and the antenna properties that effect the gain can change over time. Often a first estimate of the density is performed using $T_e/T_i = 1$, and the antenna gain is calibrated with an independent density measurement such as an ionosonde. Density estimates can also be obtained from the frequency of the plasma line, though in most cases those measurements are restricted to daytime observations when photoelectrons enhance the Langmuir mode (*Akbari et al.*, 2017). Arecibo Observatory is the only radar sensitive enough to obtain accurate measurements of plasma line frequency at all times of day (*Vierinen et al.,* 2017). Jicamarca's low frequency allows for calibration free measurements of density through Faraday rotation (*Farley,* 1969; *Kudeki et al.,* 2003).

2.5.3 Inverting Spectra for Plasma Temperatures

The spectral shape of the unmagnetized ion line is strongly affected by the electron and ion temperatures, as well as the ion composition (Section 2.5.4). The spectral width of the ion line is determined by the ion-acoustic frequency, which from Section 2.2.1 is

$$\omega_{ia} = k\sqrt{\frac{T_i}{m_i}\left(\gamma_i K_B + \gamma_e K_B \frac{T_e}{T_i}\right)}. \tag{2.111}$$

This frequency depends primarily on the ratio T_i/m_i, and secondarily on the electron/ion temperature ratio. Figure 2.13 shows how the spectral width of the ion line increases with T_i when keeping all other parameters fixed. Similarly, Figure 2.14 shows how changing the ion mass affects the spectral width in the same way. In both figures the two peaks symmetric about $\omega = 0$ occur at the ion-acoustic frequency, ω_{ia}.

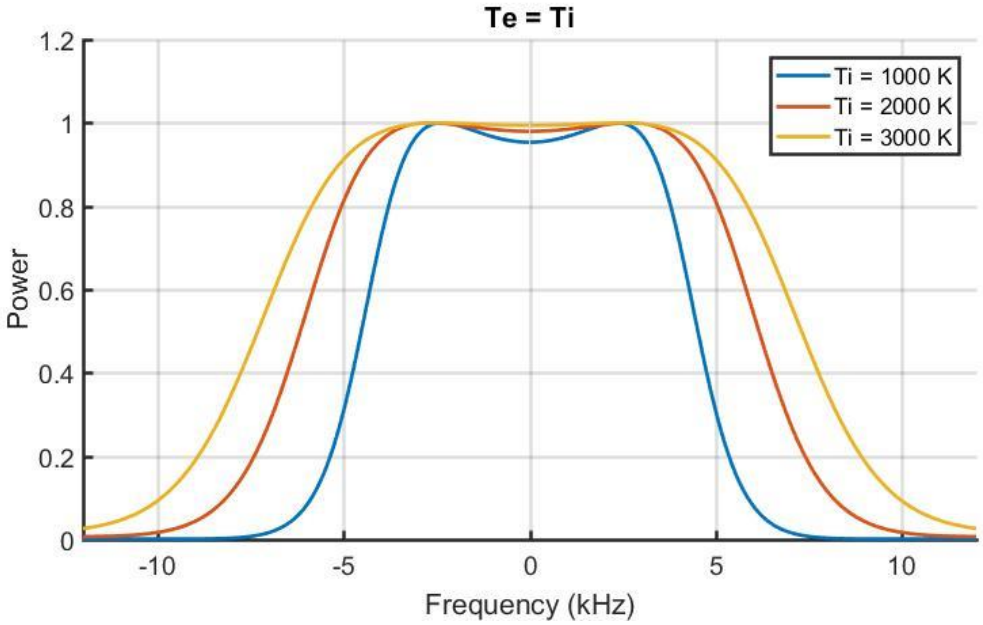

Figure 2.13 The width of the ion line increases as the ion temperature is increased. The temperature ratio is fixed at Te/Ti = 1 and an O^+ mass is used in all three curves.

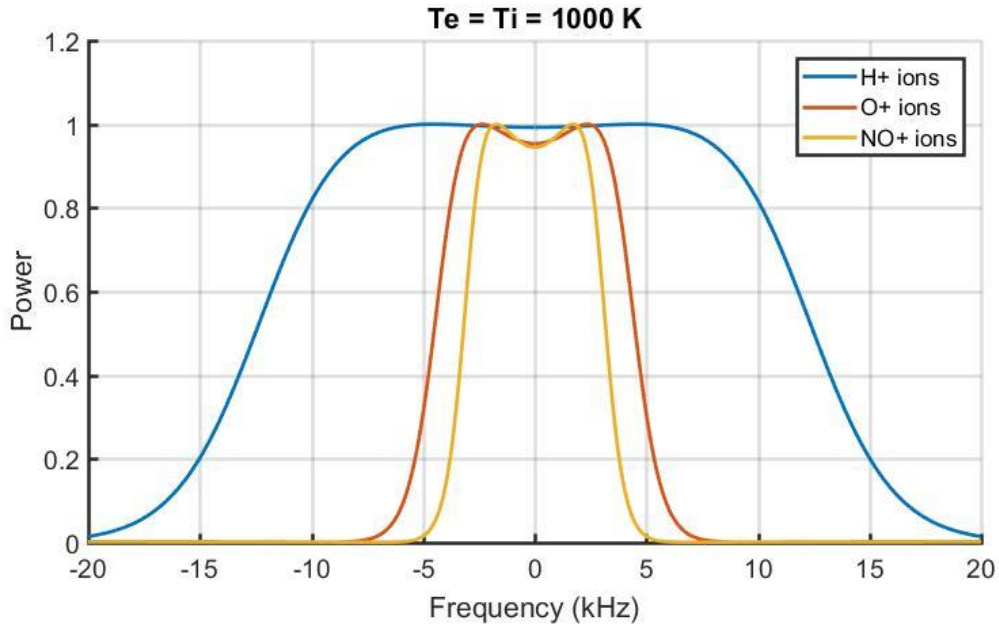

Figure 2.14 For a fixed set of temperatures, increasing the ion mass decreases the overall width of the ion line.

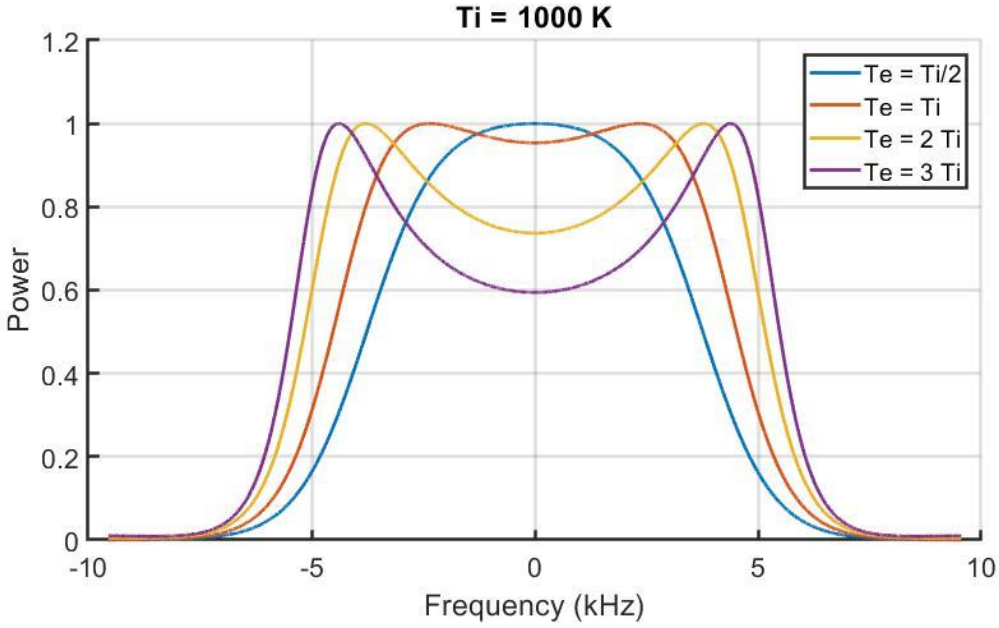

Figure 2.15 Increasing the temperature ratio, Te/Ti, has a strong effect on the Landau damping of the ion line. At large Te/Ti values the damping is decreased and the spectra tends towards the fluid solutions of $\omega \pm \omega_{ia}$. Notice that the double-hump shape is lost when Te < Ti, where Landau damping is strong.

Equation (2.111) shows that the spectral width also increases when the ratio Te/Ti increases. However, the predominant effect of the temperature ratio is in the Landau damping rate of the wave. From the dressed particle theory in Section 2.4.2 we know the damping rate of a wave varies as $\partial f_e/\partial v$, evaluated at $v_{ph} = \omega/k$. For a Maxwellian electron distribution the damping rate is then

$$\gamma \propto \frac{\partial f_e}{\partial v} = -\frac{v_{ph}}{v_{th}^2}\exp\left(-\frac{v_{ph}^2}{2v_{th}^2}\right). \tag{2.112}$$

Since $v_{th}^2 = K_B T_e/m_e$, the damping rate is inversely proportional to the electron temperature, with an adjustment to the phase velocity and proportionality constant when Ti changes. Figure 2.15 shows how Te/Ti slightly affects spectral width of the ion line while significantly changing the separation of the double-hump structure. Without any damping of the ion-acoustic mode the ion line spectra would consist of two sharp peaks at $\pm\omega_{ia}$. This means a distinct double-hump shape in the spectra indicates the wave is less damped and Te/Ti > 1, generally. Conversely, the wave is heavily damped when Te/Ti < 1, and the two humps merge together into one hump. Therefore, we can interpret an ion line with a single hump centered at $\omega = 0$ as a heavily damped wave, with increased damping corresponding to further narrowing of the spectra.

The distinct effects of ion and electron temperature on the ion line shape allow for measured spectra to be fit to a forward model through an inversion process. Using one of the forward models in Section 2.4 or the PIC simulations in Chapters 3 and 4, a least squares cost function is calculated to determine the quality of fit between the data and an initial set of temperatures. An iterative scheme such as Levenberg-Marquardt is then used

to choose a new set of temperatures, and the process is repeated until the cost function is minimized (*Swoboda*, 2017). Once the scheme converges, the final electron and ion temperatures *should* be the electron and ion temperatures in the ionosphere at the altitude where the spectra was measured. High noise values, uncertainty in ion composition, and the possibility of converging on a local but not global minimum can all lead to incorrect estimates of the electron and ion temperatures. These errors are often easy to see when visually inspecting the data and are due entirely to the fitting routine. In the next section a different error in temperature measurements is shown, where the fitting routine works optimally, but the forward model used in the inversion process is not correct.

2.5.4 The Perpendicular to B Temperature Problem

In Section 2.4.4 the ion line spectra were calculated and plotted as a function of aspect angle using the fluctuation-dissipation theory with a Brownian collision operator (referred to hereon as *Brownian theory*), and the dressed-particle theory with a BGK collision operator. As discussed in Section 2.4.4, at small aspect angles the electron Coulomb collisions add an additional source of damping to the ion-acoustic mode, which narrows the spectra. Figure 2.16 shows how using the Brownian theory for inversions at small aspect angles leads to an error in temperature measurements by ISR. The fitting routine can find the best fit to the data, even when no noise is present, but the reported temperature would be incorrect since the Brownian theory used as a forward model does not accurately describe the collisional damping of the wave, and the fitting routine compensates by calculating a higher Landau damping rate, and therefore lower Te/Ti. In this dissertation I focus on obtaining a complete, accurate description of the combined

collisional and Landau damping of the ion-acoustic mode used by ISR in order to improve the temperature fitting process at small aspect angles.

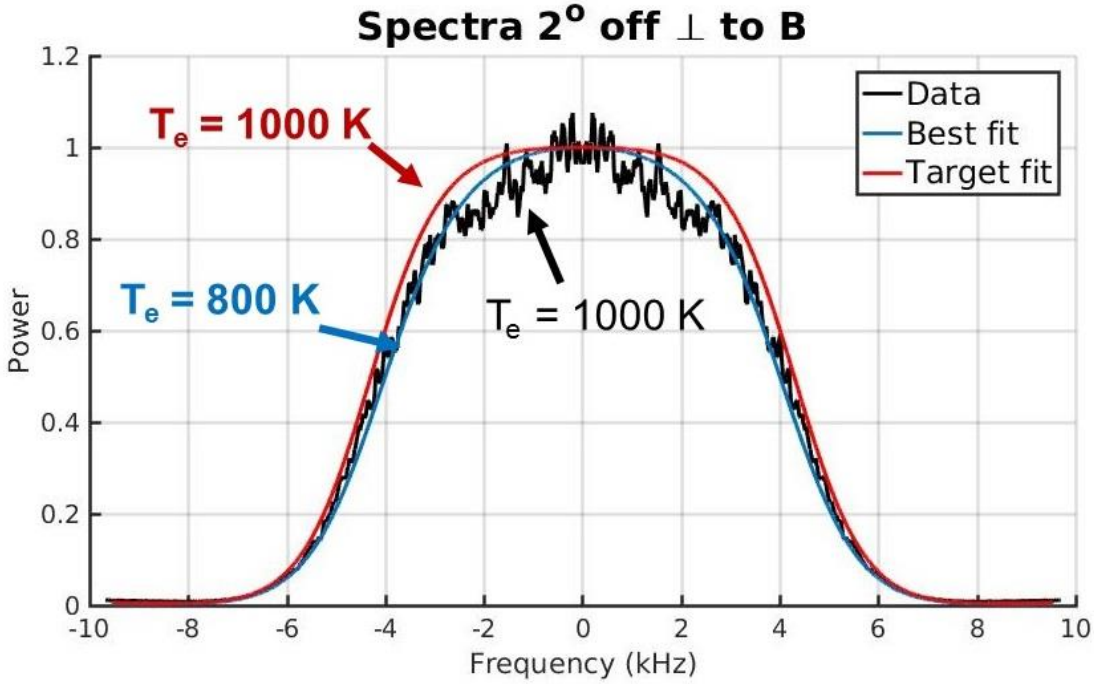

Figure 2.16 The "perpendicular to B" problem is illustrated. The synthetic data (black) is taken from PIC simulations in Chapter 3 with temperatures of Te = Ti = 1000 K. An inversion routine would report the temperature from the best fit (blue) of the Brownian theory to the synthetic data, which is Te = 800 K and Ti = 1000 K. The Brownian theory with the correct temperatures (red) is plotted to show how poorly it fits the synthetic data. This error in the fitted temperatures is due to the Brownian theory underestimating the total damping of the ion-acoustic mode by both collisions and Landau damping.

2.5.5 Ion Composition Effects

Measurements of small aspect angle spectra at Millstone have the disadvantage of looking at the valley region or F1 peak where the ions are not a single species. Since the spectral width of the ion line is proportional to T_i/m_i, errors in estimating ion composition, and thus m_i, can lead to errors in estimations of T_i for one or more ion species. ISR theory handles ion composition by including an ion line term for each

species, as well as summing over each ion species when calculating the dielectric or conductivity functions. To investigate the validity of multiple-ion ISR theory, and any temperature-composition ambiguities, a set of unmagnetized, collisionless PIC simulations is performed using the methods described in Chapter 3. The simulations consider the following cases where the composition varies between O^+ ions and a 31 amu molecular ion, which is the average mass of O_2^+ and NO^+ (hereon referred to as NO^+):

a) Baseline, O^+ only. $T_e = T_i = 1000$ K. Spectra are produced with 72 samplings.

b) 50% O^+ and 50% NO^+. $T_e = T_{O+} = T_{NO+} = 1000$ K. Spectra are produced with 72 samplings.

c) 50% O^+ and 50% NO^+. $T_e = T_{NO+} = 1000$ K, and $T_{O+} = 2000$ K. Spectra are produced with 120 samplings.

d) 50% O^+, 50% NO^+. $T_e = T_{O+} = 1000$ K, and $T_{NO+} = 2000$ K. Spectra are produced with 120 samplings.

The spectra for a 440 MHz radar in each of these cases is plotted in Figure 2.17, showing the theory agrees well with collisionless, unmagnetized PIC simulations. It is important to note that plots (b) – (d) have similar -3dB widths, which can lead to Simba ambiguities in ion temperatures if the composition is not well constrained, or if the Nala measurement has significant noise levels (*Martínez-Ledesma and Díaz Quezada*, 2019). Temperature fittings at Millstone Hill use an idealized Chapman profile for molecular ion composition (Figure 2.18), which may cause errors in temperature measurements between 160-220 km altitude. While this composition ambiguity is not ideal, the analysis

of Millstone Hill data in Chapter 5 consistently uses the same Chapman profile across all of the forward models. For radars sensitive enough to measure the ion line in the topside ionosphere, the large mass difference between O^+ and H^+ allows for accurate estimates of ion composition with far less ambiguity (*González et al.*, 2004; *Hysell et al.*, 2009).

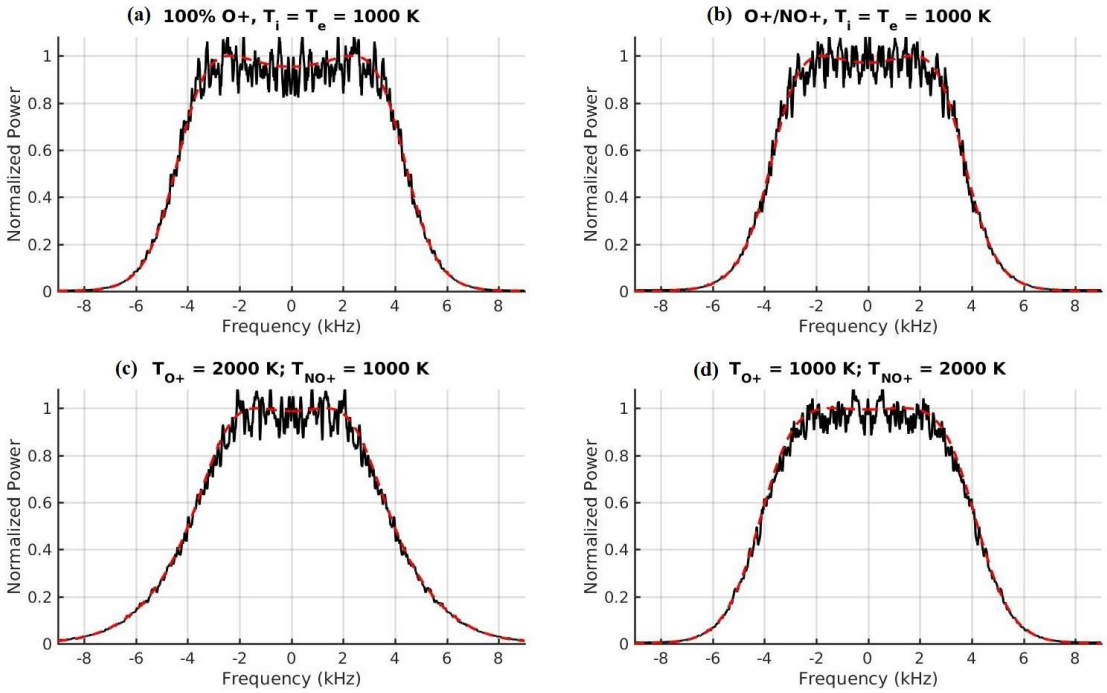

Figure 2.17 Spectra for a 440 MHz radar are simulated with different ion compositions and temperatures. The PIC simulations (black) match the unmagnetized theory (red) to within the simulation noise.

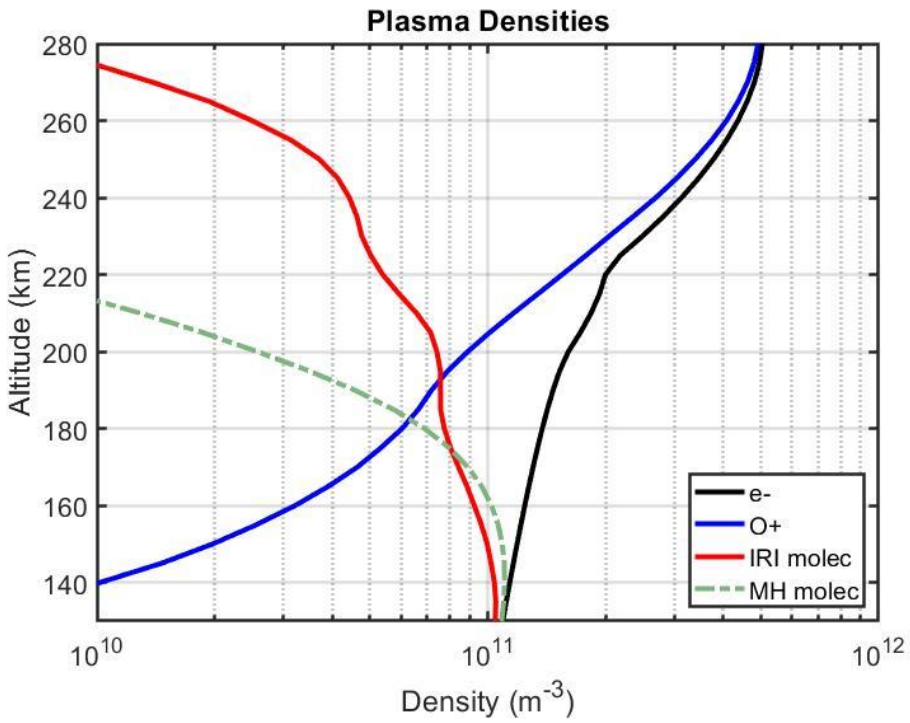

Figure 2.18 The daytime density profiles from IRI (solid lines) compared to the idealized Chapman function used by Millstone Hill (dashed green) for ion composition ratios. At altitudes above 220 km the plasma is composed primarily of O^+ ions (blue), and below 160 km the plasma is entirely O_2^+ and NO^+ molecular ions (red). The valley region between 160 km and 220 km has a mixed composition that can affect ISR temperature fittings.

Chapter 3

ISR Spectra Simulations with Electron-Ion Coulomb Collisions

This chapter has been published as

Longley, William J., Meers M. Oppenheim, Alex C. Fletcher, Yakov S. Dimant (2018), ISR Spectra Simulations with Electron-Ion Coulomb Collisions, J. Geophys. Res. Space Physics, 123. doi: 10.1002/2017JA025015.

Key points are:

- Electron-ion collisions with velocity dependent Fokker-Planck coefficients are implemented in a self-consistent particle-in-cell code.
- Particle-in-cell code simulated collisional radar spectra for all magnetic aspect angles, including perpendicular to the magnetic field.
- Simulated spectra match Brownian motion theory at angles larger than 3° away from perpendicular to the magnetic field.

3.1 Introduction

3.1.1 Collision Effects on ISR Spectra

Incoherent scatter radars (ISR) measure the returned power versus Doppler shifted frequency of radar pulses that are Thomson scattered off electrons in the ionosphere. By fitting to theoretical spectra, radio scientists calculate altitude profiles of the plasma density, electron and ion temperature, and ion drift speed (*Milla and Kudeki*, 2006; *Hysell et al.*, 2015). The theoretical spectra become difficult to calculate when the magnetic aspect angle, which is defined as 0° when the radar line of sight is perpendicular to the

magnetic field, approaches 0°. In this chapter, we simulate the ISR spectra at small aspect angles using the Electrostatic Parallel Particle-in-Cell (EPPIC) simulator (*Oppenheim et al.*, 2008), and implement a grid-based Langevin formulation of the Fokker-Planck equation.

For aspect angles greater than 5°, the plasma behavior is effectively collisionless, and the theoretical ISR spectra have been worked out in detail by *Kudeki and Milla* (2011) and others. Early calculations of temperature profiles at Jicamarca Radio Observatory modeled the plasma as collisionless for all aspect angles, which underestimated electron temperatures when compared to satellite measurements (*Carlson and Sayers*, 1970; *McClure*, 1973). *Sulzer and Gonzalez* (1999) argue that at small aspect angles the spectra narrows to the point where Coulomb collisions become an important process in an electron's motion, which in turn changes the spectra. *Sulzer and Gonzalez* (1999) also present simulations of a single electron random walking due to collisions, which show for finite aspect angles the resulting spectra are narrower than the collisionless theory suggests for the same temperature. Since Jicamarca is steering limited to aspect angles of 6° or less, the effects of Coulomb collisions are of fundamental importance to temperature measurements there.

Aponte et al. (2001) developed a numerical library from the Sulzer and Gonzalez results, and validated the collision hypothesis with data from Jicamarca. *Woodman* (2004) evaluated the velocity-independent Fokker-Planck equation to show how the effective collision frequency changes as a function of magnetic aspect angle, which gave theoretical justification for the results of Sulzer and Gonzalez. *Kudeki and Milla* (2011)

provide a general framework for ISR theory that calculates spectra from theoretical or simulated single particle autocorrelation functions. They further provide a theoretical electron autocorrelation function which approximates collisions as a velocity independent Brownian motion process. The simulations in Sulzer and Gonzalez use a guiding center approximation, which neglects diffusion across the magnetic field, and restricts their results to aspect angles larger than 0.1°. *Milla and Kudeki* (2011) address the problem of field line diffusion by simulating single particle motion in 3D, subject to the Lorentz force and velocity dependent collisions modeled by the Fokker-Planck equation. Both *Sulzer and Gonzalez* (1999) and *Milla and Kudeki* (2011) use the displacement statistics from their simulations to construct a single particle autocorrelation function that defines the ISR spectra through the general framework in *Kudeki and Milla* (2011). This approach focuses on correctly modeling the single particle motion with a collisional and magnetic force, then uses Ampere's law and the fluctuation-dissipation theorem to account for the collective behavior through electric fields. In this chapter we calculate collisional ISR spectra with a particle-in-cell (PIC) code, which directly simulates the collisional, magnetic, and electric forces simultaneously.

3.1.2 Collision Methods in PIC Codes

PIC codes apply a variety of numerical schemes and implementations (*Birdsall and Langdon*, 2004), but they all follow a few key steps. At every time step, the particles are scattered onto a fixed grid using a weighting function that considers the distance between the particle and neighboring grid nodes. This scatter step creates a charge density matrix, which allows the electric field to be computed on the grid using Poisson's

equation when using an electrostatic approximation. With the calculated electric field and an externally imposed magnetic field, the velocity and position of each particle is updated under the Lorentz force. During the scatter stage, charges in close proximity only interact through the long-range electric field computed from the charge density. Thus, it is necessary to explicitly add a model to simulate Coulomb scattering of two particles at close ranges.

The first widely used scheme for simulating Coulomb collisions is the direct binary method developed by *Takizuka and Abe* (1977). At each time step in the binary method, the particles in each grid cell are sorted into pairs and scattered off each other. The post collision velocity is calculated by sampling the scattering angle from a Gaussian distribution with zero mean and a variance derived from Coulomb's law. A further generalization of this method was developed by *Nanbu* (1997), which calculates the scattering angle for the colliding pair by assuming each particle undergoes multiple small angle collisions at the same time. No assumptions about the particle distributions need to be made using the binary method, and energy is automatically conserved in each collision pair. However, this scheme is computationally demanding because the particles need to be sorted into pairs, and a small time step must be used (*Cohen et al.*, 2010).

The grid based Langevin equation method was developed by *Jones et al*. (1996) in an effort to reduce the computational demand of simulating Coulomb collisions. The grid-based method uses the first three moments of each particle's distribution to calculate a drag coefficient and a diffusion tensor from the Fokker-Planck equation. The drag and diffusion terms are used to define a stochastic Langevin equation that is an exact

representation of the Fokker-Planck equation in the limit of infinitesimally small time steps. *Manheimer et al.* (1997) further developed this method to allow the collision cross sections to be velocity dependent. We use the algorithm developed in Manheimer to simulate Coulomb collisions in EPPIC due to its simplicity, speed, and use of velocity dependent cross sections.

3.2 Electron-Ion Collision Algorithm

The Fokker-Planck equation is a collision operator for the Boltzmann equation under the assumption of small angle Coulomb collisions (*Rosenbluth et al.*, 1957):

$$\frac{\partial f_e}{\partial t}_{coll} = \frac{\partial}{\partial \vec{v}} \cdot \left[\vec{F}_d(\vec{v}_e) f_e(\vec{v}_e)\right] + \frac{1}{2}\frac{\partial^2}{\partial \vec{v}\partial \vec{v}} : [\overline{D}(\vec{v}_e) f_e(\vec{v}_e)], \tag{3.1}$$

where F_d is a drag friction vector, D is a diffusion tensor, and f_e is the electron distribution. For electrons colliding off singly charged ions, the drag and diffusion coefficients are

$$\vec{F}_d(\vec{v}_e) = \frac{e^4}{4\pi\epsilon_0^2 m_e^2}\Lambda\frac{\partial H_i}{\partial \vec{v}}, \tag{3.2}$$

$$\overline{D}(\vec{v}_e) = \frac{e^4}{4\pi\epsilon_0^2 m_e^2}\Lambda\frac{\partial^2 G_i}{\partial \vec{v}\partial \vec{v}}. \tag{3.3}$$

Λ is the Coulomb logarithm, defined by the Debye length, h_d, and the electron speed, v_e:

$$\Lambda = \ln\left(\frac{4\pi\epsilon_0 m_e h_d v_e^2}{e^2}\right). \tag{3.4}$$

The Rosenbluth potentials, H_i and G_i, of the ion species are (*Rosenbluth et al.*, 1957):

$$H_i(\vec{v}_e) = \int d^3\vec{v}_i \frac{f_i(\vec{v}_i)}{|\vec{v}_e - \vec{v}_i|}, \tag{3.5}$$

$$G_i(\vec{v}_e) = \int d^3\vec{v}_i \, f_i(\vec{v}_i)|\vec{v}_e - \vec{v}_i| \,, \tag{3.6}$$

where f_i is the ion distribution. Typically, Rosenbluth potentials are calculated by assuming an isotropic Maxwellian distribution in the integrand. In the case of electron-ion collisions, if both species are at similar temperatures then $v_i \ll v_e$ for any given electron-ion pair. This speed difference means the ion distribution is extremely narrow compared to any electron's speed, and the calculation of equations (3.5) and (3.6) can be approximated to high accuracy by assuming the ion distribution is a delta distribution centered at $v_i = 0$. The Rosenbluth potentials under this approximation are then (*Manheimer et al.* 1997)

$$H_i(\vec{v}_e) = \frac{n_i}{v_e}, \tag{3.7}$$

$$G_i(\vec{v}_e) = n_i v_e. \tag{3.8}$$

The validity of this approximation is discussed in Appendix A.

In a coordinate system where the electron velocity is in the $\mathbf{e_3}$ direction, the diffusion tensor becomes diagonal (*Manheimer et al.*, 1997). With only one ion species present the ion density is the same as the plasma density, so the drag and diffusion coefficients for electron-ion collisions become

$$F_d(v_e) = -\frac{ne^4}{4\pi\epsilon_0^2 m_e^2 v_e^2}\Lambda, \tag{3.9}$$

$$D_{11}(v_e) = D_{22}(v_e) = \frac{ne^4}{4\pi\epsilon_0^2 m_e^2 v_e}\Lambda, \tag{3.10}$$

$$D_{33} = 0. \tag{3.11}$$

3.2.1 Langevin Equation Formulation

To implement the Fokker-Planck equation and its simplified Rosenbluth potentials into a PIC code an equivalent Langevin equation needs to be constructed. The Langevin equation is a stochastic differential equation (*Manheimer et al.,* 1997), which in velocity update form is

$$\Delta\vec{v}_{Lang} = \vec{F}_d\Delta t + \vec{Q}, \tag{3.12}$$

where F_d is the frictional drag force from the Fokker-Planck equation, and Q is a vector randomly sampled from the Gaussian distribution defined by the diffusion coefficients D_{11} and D_{33} from equations (3.9) and (3.10):

$$\phi(\vec{Q}) = \frac{1}{(2\pi\Delta t)^{3/2} D_{11} D_{33}^{1/2}} \exp\left(-\frac{Q_3^2}{2D_{33}\Delta t} - \frac{Q_1^2 + Q_2^2}{2D_{11}\Delta t}\right). \tag{3.13}$$

The Langevin equation then produces a velocity change that can be included in the velocity update step as

$$\vec{v}_{new} = \vec{v}_{old} + \vec{F}_{Lorentz}\Delta t + \vec{F}_d\Delta t + \vec{Q}. \tag{3.14}$$

The linearity of the terms in equation (3.14) allows the collision operator to be programmed into the PIC code as a separate module, which we place after the particle velocities are updated with the Lorentz force. It is important to point out that the

stochastic nature of equation (3.12) introduces small errors, and energy is not necessarily conserved globally at each time step in the simulation. A general method for correcting the full set of $\Delta \boldsymbol{v}_{Lang}$ to conserve energy at the end of the collision routine is provided by *Lemons et al.* (2009). However, since we are only simulating electron-ion collisions we will conserve energy globally by forcing each electron to conserve its energy during the collision, as described below.

3.2.2 Algorithm for Electron-Ion Collisions

The following algorithm describes how a single electron is scattered off a single ion distribution. We place this routine at the end of the velocity update step and can subcycle the collision routine by changing the time step in equation (3.15) to be the time in between collision algorithm calls. ISR runs in this chapter call the collision routine every 8 time steps in order to cut computation time in half.

Collision Algorithm

1. Calculate the Coulomb logarithm in equation (3.4) with the individual electron's velocity v_e:

$$\Lambda = \ln\left(\frac{4\pi\epsilon_0 m_e h_d v_e^2}{e^2}\right).$$

Since the ions are assumed immobile on collisional time scales, the Debye length in the plasma is the same as the electron Debye length. The simulations in this chapter are of globally homogeneous plasmas, so we can speed the simulation up by evaluating the Debye length globally.

2. Calculate the diffusion coefficient D_{11} from equation (3.10):

$$D_{11}(v_e) = D_{22}(v_e) = \frac{ne^4}{4\pi\epsilon_0^2 m_e^2 v_e}\Lambda.$$

3. For each particle, randomly sample Q in the limit as $D_{33} \to 0$ and $D_{11} = D_{22}$:

$$\phi(Q_1, Q_2) = \frac{1}{2\pi\Delta t D_{11}} \exp\left(-\frac{Q_1^2 + Q_2^2}{2D_{11}\Delta t}\right). \quad (3.15)$$

This is a Gaussian of two independent variables and therefore Q_1 and Q_2 can be sampled separately from a single variable Gaussian with a variance of $\sigma = \sqrt{\Delta t D_{11}}$ and a mean of 0. The limit $D_{33} \to 0$ also implies $Q_3 = 0$. The time step Δt should be adjusted at this step to account for any subcycling of the collision routine.

4. Calculate the rotation angles to move into a primed coordinate frame where $v_e = v_e\hat{e}_3$:

$$\phi = \text{atan2}(v_2, v_1), \quad (3.16)$$

$$\theta = \cos^{-1}\left(\frac{v_3}{v}\right). \quad (3.17)$$

5. The velocity update in the rotated prime coordinates is then

$$v_1' = Q_1, \quad (3.18)$$

$$v_2' = Q_2. \quad (3.19)$$

6. The 3rd velocity component is usually a combination of the drag coefficient and Q_3. However, in assuming that the ions are infinitely massive and stationary, we have also assumed the collision is elastic and thus the electron's speed is unchanged. The

3rd velocity component is then calculated such that energy conservation is forced in each collision (*Manheimer et al.*, 1997),

$$v_3' = \sqrt{v_{init}^2 - Q_1^2 - Q_2^2}. \tag{3.20}$$

7. Rotate back into normal, unprimed coordinates, to obtain the post-collision velocities.

$$v_1(new) = v_1' * \cos\theta \cos\phi - v_2' * \sin\phi + v_3' * \sin\theta \cos\phi\,, \tag{3.21}$$

$$v_2(new) = v_1' * \cos\theta \sin\phi + v_2' * \cos\phi + v_3' * \sin\theta \sin\phi\,, \tag{3.22}$$

$$v_3(new) = -v_1' * \sin\theta + v_3' * \cos\theta\,. \tag{3.23}$$

The above steps are repeated for each electron before continuing with the rest of the velocity update step.

3.3 Validation

EPPIC is a fully kinetic, massively parallel, domain decomposed PIC code (*Oppenheim et al.*, 2008). Since EPPIC is primarily used to simulate ionospheric plasmas, it is an electrostatic code, and the magnetic field takes on a fixed value for the duration of the run. The scatter step uses a linear shape function to aggregate charge density onto the nearest grid cells. The electric field is found by solving Poisson's equation using a spectral technique with a convolution stencil for periodic boundary conditions. A second order Boris mover is used to advance the particle velocities and positions.

The electron-ion collision routine in EPPIC is validated by looking at how collisions slow an electron beam. Table 3.1 shows the simulation parameters in units normalized to the electron thermal speed *c*. Figure 3.1 plots the simulated and theoretical

beam speed as a function of time for three different initial beam speeds. The thermal speed in the x-direction is also plotted, showing that the energy of the beam goes into heating the electrons.

The theoretical curve for a beam decelerating due to collisions is obtained by taking the first moment of the Fokker-Planck equation. For a Maxwellian distribution with bulk speed *u* and thermal speed *c*, the deceleration of the beam is

$$\frac{\partial u}{\partial t} = -\frac{e n_i c}{4\pi\epsilon_0^2 m_e^2 u^2\sqrt{2\pi}} \int_0^\infty \Lambda \left(\exp\left(\frac{-(v-u)^2}{2c^2}\right)\left[\frac{u}{c^2 v} - \frac{1}{v^2}\right] - \exp\left(\frac{-(v+u)^2}{2c^2}\right)\left[\frac{u}{c^2 v} + \frac{1}{v^2}\right]\right) dv. \quad (3.24)$$

The integration over azimuthal and polar angles has already been done, but the remaining integration over *v* is done numerically since the Coulomb logarithm varies as $\log(v^2)$. Furthermore, equation (3.24) assumes a Maxwellian distribution at all times, which is not accurate. The Coulomb collision frequency scales with velocity as $f \propto 1/v^3$, so slower moving electrons will collide more frequently, and thus the low energy tail of the beam will decelerate much faster than the high energy tail. This skews the beam away from a Maxwellian, and a full theoretical treatment of the problem would need to derive equation (3.24) using a skew-normal distribution and the 13 moment fluid equations. Such an approach is cumbersome and beyond the accuracy desired, so we account for the skew by approximating the distribution as a Maxwellian with corrected variance σ and mean *u*

$$\sigma^2 = \frac{s^2}{1 - 2\delta^2/\pi}, \tag{3.25}$$

$$u = \langle v \rangle - \sigma\delta\sqrt{2/\pi}, \tag{3.26}$$

where $\langle v \rangle$ and s are the first and second moments of the skewed distribution in our simulations. The parameter δ is calculated from the normalized third moment of the simulation, γ, as

$$\delta = \gamma \sqrt{\frac{\pi}{2\gamma^{2/3} + 2\left(2 - \frac{\pi}{2}\right)^{2/3}}}. \tag{3.27}$$

With the corrected mean and variance in equations (3.25)–(3.27), we numerically integrate equation (3.24) at every time step of the simulation to obtain the theoretical beam deceleration, which is then integrated in time to produce the theory curve in Figure 3.1. Figure 3.1 shows that the simulations match the theory well, with the remaining discrepancy resulting from the approximation of the skew-normal distribution in equation (3.24). We conclude that the collision algorithm has been correctly implemented and demonstrate that a fully kinetic PIC approach more accurately models beam decelerations than a theoretical approach that assumes invariant Maxwellian distributions.

Table 3.1. Simulation parameters used for beam validation.

Grid Size	128 x 32	Electron mass	$m_e = 1$
Grid Step	$\Delta x = \Delta y = 0.5$	Ion mass	$m_i = 1024$
Total Time Steps	10,000	Ion temperature	$T_i = T_e$
Time Step Size	$\Delta t = 0.02$	Background electron density	$n_e = 0.99\ n_i$
Particles per grid cell	1024	Beam electron density	$n_{e,beam} = 0.01\ n_i$
Initial beam speeds	$v_{in,beam} = \{0.3, 1, 2\}$	Initial thermal speeds	$v_{th,beam} = v_{th,e} = 1$

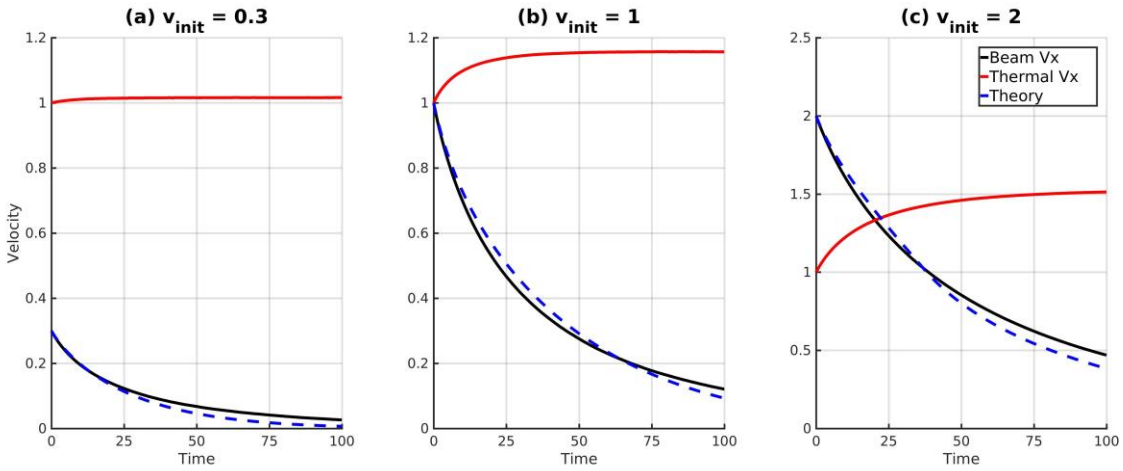

Figure 3.1. An electron beam decelerated by collisional drag against stationary ions. The electrons have initial thermal velocities of 1 in the x, y, and z direction. Three initial beam speeds are shown, with v_{beam} = 0.3, v_{beam} = 1, and v_{beam} = 2. The theoretical curve (dashed blue) is determined by equations (3.24) – (3.27). The thermal speed of the beam (red) is increased as the beam slows down (black) due to collisions.

3.4 ISR Simulations

Incoherent scatter radars transmit radio pulses at frequencies well above the maximum plasma frequency in the ionosphere. Part of the signal is returned to the receiver by Thomson scattering off electrons. *Kudeki and Milla* (2011) show that the power spectrum of the returned signal is proportional to the Fourier transform of the electron density in a subvolume ΔV:

$$\langle \left|\vec{E}(\omega)\right|^2 \rangle = \frac{r_e^2}{R^2} E_0^2 \Delta V \langle |n_e(\omega, \vec{k})|^2 \rangle, \tag{3.28}$$

R is the distance between the receiver and the scattering volume ΔV, r_e is the classical electron radius, and E_0 is the amplitude of the transmitted electric field. The Fourier transformed electron density in equation (3.28) is

$$\langle |n_e(\omega, \vec{k})|^2 \rangle = \frac{1}{\Delta V} \int d\tau \, e^{-j\omega\tau} \langle n_e^* \left(t - \frac{r}{c}, \vec{k}\right) n_e \left(t - \frac{r}{c} + \tau, \vec{k}\right) \rangle \,, \tag{3.29}$$

where $\langle n_e^* \left(t - \frac{r}{c}, \vec{k}\right) n_e \left(t - \frac{r}{c} + \tau, \vec{k}\right) \rangle$ is the normalized auto-correlation function of the electrons. *Diaz et al.* (2008) showed that unmagnetized, collisionless ISR spectra can be simulated with EPPIC by Fourier transforming the electron density output in time and space.

3.4.1 ISR Spectra Parallel to B

ISR spectra at magnetic aspect angles larger than 6° are not affected by Coulomb collisions or the magnetic field (*Aponte et al.*, 2001), which allows us to validate our PIC approach to simulating ISR spectra against the collisionless theory presented in *Kudeki and Milla* (2011). Table 3.2 shows the simulation parameters used in EPPIC. The temperatures are the same ones from *Sulzer and Gonzalez* (1999) and *Milla and Kudeki* (2011), but we use a plasma density 100 times lower in order to keep grid heating to less than 15 K, which is a non-physical increase in temperature in PIC codes when the Debye length is not well resolved by the grid. Furthermore, changes in density primarily affect the total power of the spectra and not the shape, so the results below hold for all ionospheric densities if the spectra are normalized. The grid is chosen to allow fifteen full wavelengths of a 440 MHz radar to fit in the simulation, while still resolving a Debye length of 2.18 cm. The simulation is run for 40 ms, which gives a frequency resolution of 25 Hz, and the density is zero padded to provide interpolation at 12.5 Hz. The ion movement and Coulomb collisions are calculated every 8th time step to speed up computation.

Table 3.2. Simulation parameters used for all simulations of ISR spectra in this chapter.

Grid Size	512 x 512	Electron mass	$m_e = 2.594 \times 10^{-29}$ kg
Grid Step	$\Delta x = \Delta y = 1$ cm	Ion mass (O+)	$m_i = 2.657 \times 10^{-26}$ kg
Total Time Steps	500,000	Temperature	$T_e = T_i = 1000$ K
Time Step Size	$\Delta t = 80$ ns	B field for electrons	$B_e = 1.6$ G
Particles per grid cell	128	B field for Ions	$B_i = 0.3$ G
Average density	$n_i = n_e = 10^4$ cm^{-3}	Collision density	$n_{coll} = 10^6$ cm^{-3}

To obtain the spectra we need to calculate several independent realizations of $n_e(\omega,\boldsymbol{k})$ and average the results. To do this we run 100 simulations that only differ in the initial random number seed, then Fourier transform the electron density from each run, square the result, and average the runs to form an estimate of $\langle|n_e(\omega,\vec{\boldsymbol{k}})|^2\rangle$. The spectra can then be interpolated in k space to match any desired radar line of sight with respect to the magnetic field. The electron density in equation (3.29) needs to be normalized by the variance in n_e, so to eliminate any errors in calculating the variance along different aspect angles we normalize the simulated spectra to a maximum value of 1. Due to the size of the simulation we can only read in every 64 time steps of the density output into memory for the Fourier transform, which introduces some aliasing effects. Full ω-k plots show aliased modes are only present in the 440 MHz radar spectra for aspect angles of 40° to 90°, and the aliased mode is an evanescent Langmuir mode with a constant low power across the ion line. We subtract this constant power before normalizing any parallel mode.

Simulation noise for the unmagnetized, parallel spectra is further reduced by averaging the results at magnetic aspect angles of 90°, 80°, 70°, 60°, and 50°, which

provides 500 total independent samples of the same unmagnetized spectra. Figure 3.2 shows the normalized parallel spectra from EPPIC, with and without collisions, compared to the theoretical spectra calculated from *Kudeki and Milla* (2011). The simulated spectra in Figure 3.2 agree well with the theory, validating our PIC approach to simulating ISR spectra, and showing that the collision algorithm in the PIC code has no effect on the unmagnetized spectra. Figures 3.3-3.5 show the same simulations at different aspect angles in k space and are discussed in the following sections.

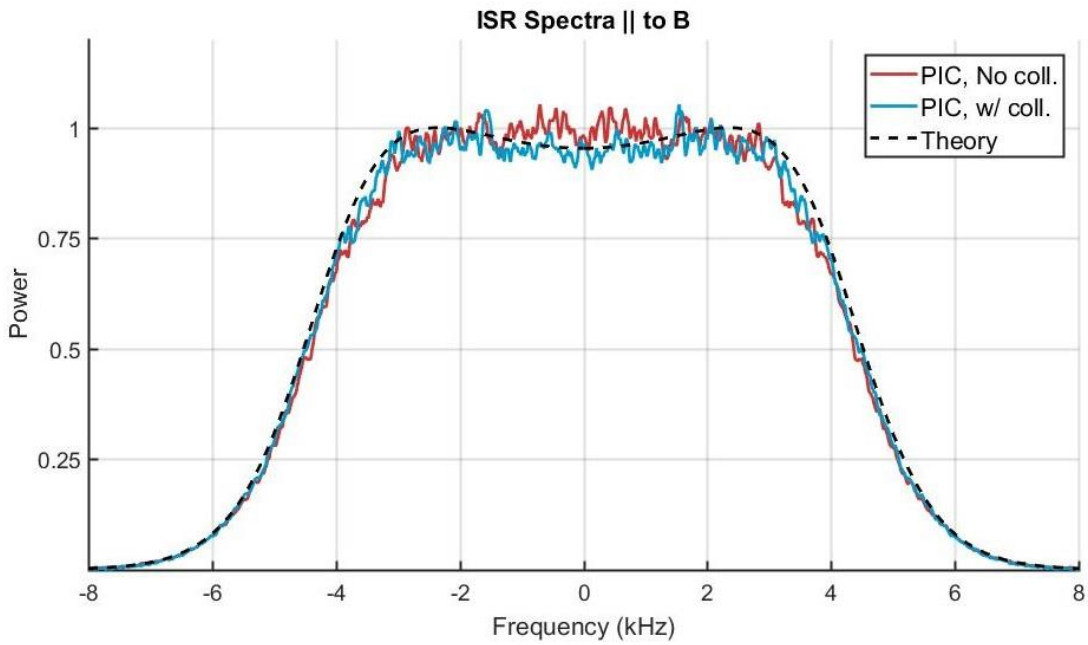

Figure 3.2. Simulated parallel spectra from the collisionless and collisional PIC runs are compared to the theory from Kudeki and Milla (2011). The spectra are for a radar frequency of 440 MHz and are normalized by their peak values. The simulated spectra at each angle are obtained by averaging 500 independent samples.

3.4.2 ISR Spectra Perpendicular to B

The spectra taken parallel to the magnetic field show that our simulations accurately reproduce the analytic theory, and that Coulomb collisions have no effect on

the spectra at large magnetic aspect angles. For magnetic aspect angles less than 5°, numerical libraries derived from single particle simulations in *Sulzer and Gonzalez* (1999) and *Milla and Kudeki* (2011) are needed for accurate spectra inversions. *Kudeki and Milla* (2011) provides an analytic theory that approximates Coulomb collisions as a Brownian motion process. Equations (62) and (63) from *Kudeki and Milla* (2011) describe the mean square displacements of magnetized electrons subject to a Brownian motion collision operator as

$$\langle \Delta l^2 \rangle = \frac{2c^2}{f^2}(f\tau - 1 + e^{-f\tau}), \tag{3.30}$$

$$\langle \Delta p^2 \rangle = \frac{2c^2}{f^2+\omega_{ce}^2}(\cos 2\gamma + f\tau - e^{-f\tau}\cos(\omega_{ce}\tau - 2\gamma)), \tag{3.31}$$

where Δl is the displacement along the magnetic field, Δp is the displacement perpendicular to B, f is the collision rate, $c^2 = KT/m$ is the thermal speed, τ is the time lag used in Fourier transforming the electron autocorrelation function, ω_{ce} is the electron gyrofrequency, and $\tan\gamma = f/\omega_{ce}$. The mean square displacements are used to calculate the electron autocorrelation function, which then defines the full ISR spectra using the general framework in *Kudeki and Milla* (2011).

The quantity $\gamma = \text{atan}(f/\omega_{ce})$ in equation (3.31) shows that the perpendicular spectra depends primarily on the ratio of the collision frequency to the gyrofrequency. The electron-ion Coulomb collision rate is (*Bellan*, 2006)

$$f(v) = \frac{n_i e^4 \Lambda}{2\pi\epsilon_0^2 m_e^2 v^3}. \tag{3.32}$$

Equations (3.30) and (3.31) require a single collision rate representative of the thermal population. Substituting $v^2 = 2KT_e/m_e$, we can obtain a velocity independent collision rate of

$$f = \frac{n_i e^4 \Lambda}{4\pi\epsilon_0^2 \sqrt{2m_e}(KT_e)^{3/2}}. \tag{3.33}$$

This collision rate varies as $f \propto m_e^{-1/2}$ when temperature is held constant, and the gyrofrequency varies as $\omega_{ce} \propto m_e^{-1}$, which means $f/\omega_{ce} \propto m_e^{1/2}$. The simulation parameters in Table 3.2 use an O^+ ion mass, but the electron mass used in the simulations is $m_e = m_i/1024$ which significantly speeds up computation time since the time step is proportional to the inverse of the electron plasma frequency. To keep the simulated spectra realistic, the ratio f/ω_{ce} in the simulation needs to match the ratio for real electrons. This is accomplished by increasing the magnetic force on the electrons such that $\omega_{ce} \propto m_e^{-1/2}$. Since the simulation electrons are 28.5 times heavier than real electrons, the gyrofrequency is modified by setting $B = 1.6$ G for the electrons in the simulations, while keeping $B = 0.3$ G for the ions. This has the added benefit of keeping the lower hybrid frequency the same, which avoids a problem of the lower hybrid mode exciting ion acoustic modes perpendicular to B. Initial runs did not use the $B = 1.6$ G correction for electrons, and the resulting spectra were heavily distorted from reality due to acoustic modes propagating perpendicular to the magnetic field.

Since density primarily affects the total power of ISR spectra, we have used $n_e = 10^4$ cm^{-3} to minimize grid heating and normalized the resulting spectra. The collision

frequency in equation (3.32) using this density is ~20 Hz, which is too low for the simulation to resolve any collisional effects on the perpendicular spectra. To solve this issue, the collision routine uses an increased density of $n_{coll} = 10^6$ cm^{-3} when calculating the Coulomb logarithm and diffusion coefficient from equations (3.4) and (3.10). The results of collisional and collisionless simulations of spectra perpendicular to B are shown in Figure 3.3, which averages 100 samples for each simulation.

The theory plotted in Figure 3.3 uses the mean square displacements for Brownian motion defined in equations (3.30) and (3.31), with a collision frequency of 370 Hz. Using equation (3.32), this collision frequency corresponds to an electron moving with speed $v^2 = 3.1\ KT/m$. *Milla and Kudeki* (2011) find a best fit collision rate of 283 Hz for their single particle simulations when using the same parameters as our simulations. The discrepancy between the best fit collision frequencies is likely due to Milla and Kudeki using the thermal speed to calculate the Coulomb logarithm in equation (3.4), while our simulations use the individual electron's speed for each collision. Figure 3.4 plots the perpendicular spectra of both simulations across a range of radar wavenumbers, showing the spectra around 0 Hz is significantly widened for all radar wavenumbers of interest.

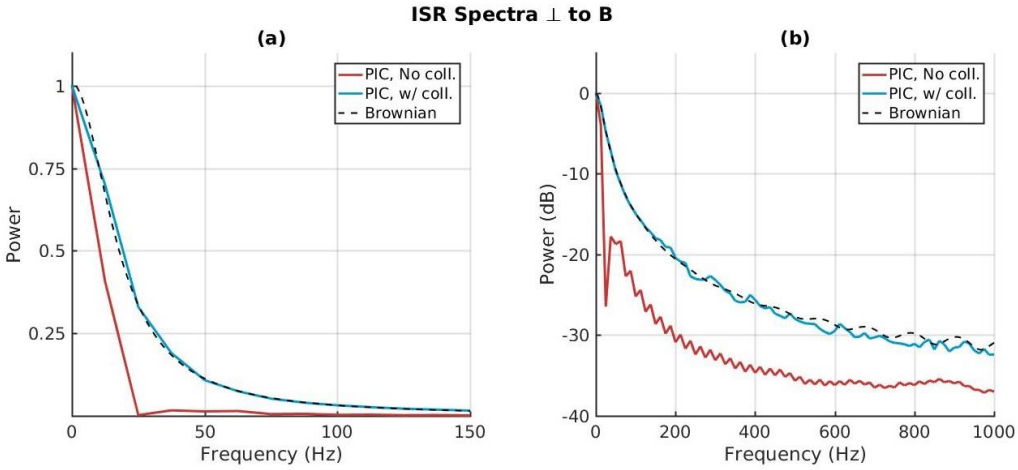

Figure 3.3. Normalized spectra for a 440 MHz radar looking perpendicular to the magnetic field. The frequency resolution of the simulations is 25 Hz, with interpolation at 12.5 Hz intervals due to zero padding the density array in time. The central peak of the collisionless simulation is narrower than this resolution indicating that without collisions the simulated spectra tends to a delta function at $f = 0$ *Hz*, as expected from collisionless ISR theory. Plot (a) shows the spectra on a linear power scale, while plot (b) shows the same spectra on a logarithmic scale across a wider frequency range. The simulated spectra at each angle are obtained by averaging 100 independent samples.

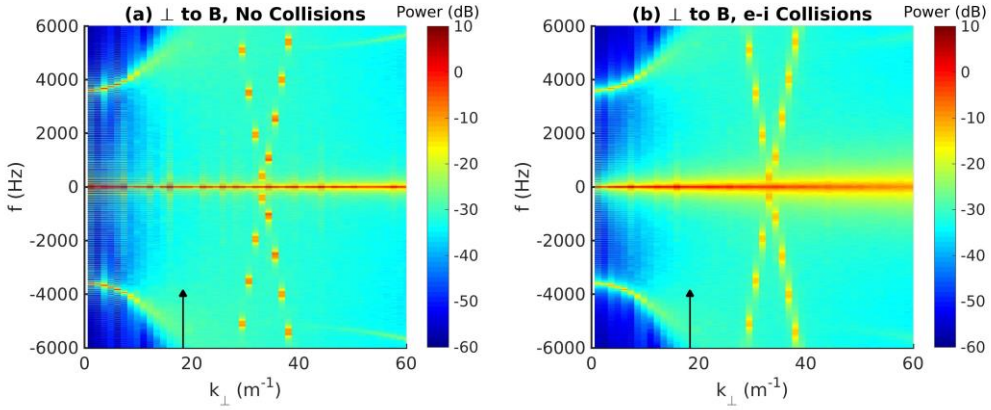

Figure 3.4. Perpendicular spectra for both simulations plotted on a logarithmic scale. The wavenumber $k_\perp$ accounts for the Bragg scattering condition, and f is the measured Doppler shift away from the carrier frequency. Each spectra is normalized to the peak value at $k_\perp = 18.4\ m^{-1}$, corresponding to a radar frequency of 440 MHz (shown by the arrow). The collisionless spectra (left) near $f = 0$ Hz is only as wide as the frequency resolution in the simulation, which is indicative of a delta function when Fourier transforming a discrete set of time samples. The simulation with collisions (right) significantly widens the low frequency spectra for all wavenumbers of interest. The lower hybrid mode is visible in both spectra in the top left and bottom left corners.

3.4.3 ISR Spectra at Small Aspect Angles

The spectra at small aspect angles is calculated from the same simulations used to obtain the spectra in Figures 3.2 and 3.3, with a bilinear interpolation of $\langle|n_e(\omega,\vec{k})|^2\rangle$ providing the spectra at any desired aspect angle. However, the use of a non-physical electron mass means the magnetic aspect angles from the simulation are not the same angles a radar would look at. The critical angle, θ_c, where the effective electron mass equals the ion mass is

$$\cos^2\theta_c = \frac{m_e}{m_i}. \tag{3.34}$$

Below this angle, the ISR spectra are controlled by electron dynamics and the ion acoustic mode is cutoff in favor of the lower hybrid mode. For an F-region plasma composed entirely of O^+ ions, the critical angle in equation (3.34) is 0.334°. Using the ion-electron mass ratio of 1024 in our simulations, this critical angle is 1.78°, and any other simulation angle, θ, can be mapped to the corresponding magnetic aspect angle, α, in an O^+ plasma as

$$\sin\alpha = \sin\theta\,\frac{\sin(1.78°)}{\sin(0.334°)}. \tag{3.35}$$

All results in this chapter are labeled with the mapped aspect angle α for an O^+ plasma.

Figure 3.5 shows the spectra from 0.75° to 5° on a linear scale, which shows that the Brownian motion theory is valid for aspect angles of 3° or more. The collisional PIC simulation in Figure 3.5 is normalized to a maximum value of 1 at each angle, and the collisionless simulation is normalized by the same amount. This shows that both

simulations have the same power for frequencies higher than ~4 kHz, and the collisionality is primarily affecting the lower frequency regime of 0-3 kHz. It is interesting to note that *Milla and Kudeki* (2011) show at angles larger than 0.5° the Brownian motion spectra is the same overall shape as theoretical spectra without collisions, albeit narrower. Figure 3.5 shows that our collisionless simulation at aspect angles between 0.75° and 2° is a completely different shape than the Brownian motion spectra, with a strong central peak at $f = 0$ Hz, and a secondary peak at $f \approx 1500$ Hz corresponding to the acoustic mode.

For a 440 MHz radar, 0.71° is the smallest angle that can be resolved by the simulation without the perpendicular mode dominating any interpolation in k space. To obtain spectra at smaller angles, we run a separate set of collisional simulations on a 1024 by 1024 grid, using the same parameters in Table 3.2, with the exception of the grid step increasing to 1.5 cm, and the total simulation time being reduced to 4 ms. The smallest resolved angle for these simulations is 0.24°, but the reduction in run time decreases the frequency resolution to 250 Hz. Figure 3.6 shows the results of this simulation at aspect angles of 0.25° and 0.5° degrees. The decrease in frequency resolution adversely impacts the accuracy of this simulation, but we can conclude that at these angles the simulated spectra are still narrower than the Brownian motion spectra.

Comparing the collisional simulations in Figures 3.5 and 3.6 to the Brownian motion spectra we see agreement between the two methods for aspect angles of 3° and larger. At angles of 2° and smaller the Brownian motion theory is wider than the collisional simulation. The width of ISR spectra is typically controlled by the ion

temperature, but at small aspect angles the electron temperature also controls the width, with higher temperatures producing wider spectra in each case. If one tried to fit a Brownian motion curve to the collisional simulation, a smaller plasma temperature would need to be used in the Brownian theory to obtain the best fit. Estimating plasma temperatures using the Brownian theory results in a 20-30% error, but the exact error in either T_i or T_e depends both on aspect angle and on the inversion routine. The spectra at smaller frequencies are controlled by electron dynamics, so an inversion method that emphasizes that region of the spectra will underestimate electron temperatures. Inversion routines that use the logarithm of the power spectra will emphasize fitting the higher frequency tail of the spectra, which will underestimate the ion temperature.

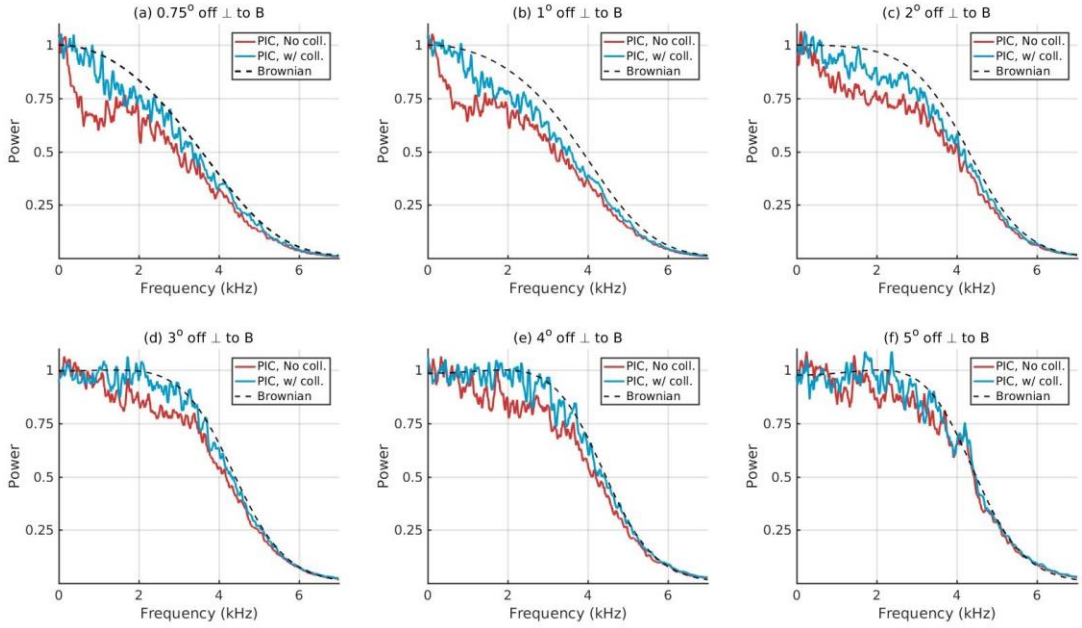

Figure 3.5. Normalized spectra of a 440 MHz radar at magnetic aspect angles of 0.75° to 5°, plotted on a linear scale. The collisionless PIC spectra (red) is normalized by the same value as the collisional PIC spectra (blue). At 3° and above the simulated collisional spectra converges on the Brownian motion theory. The simulated spectra at each angle are obtained by averaging 100 independent samples.

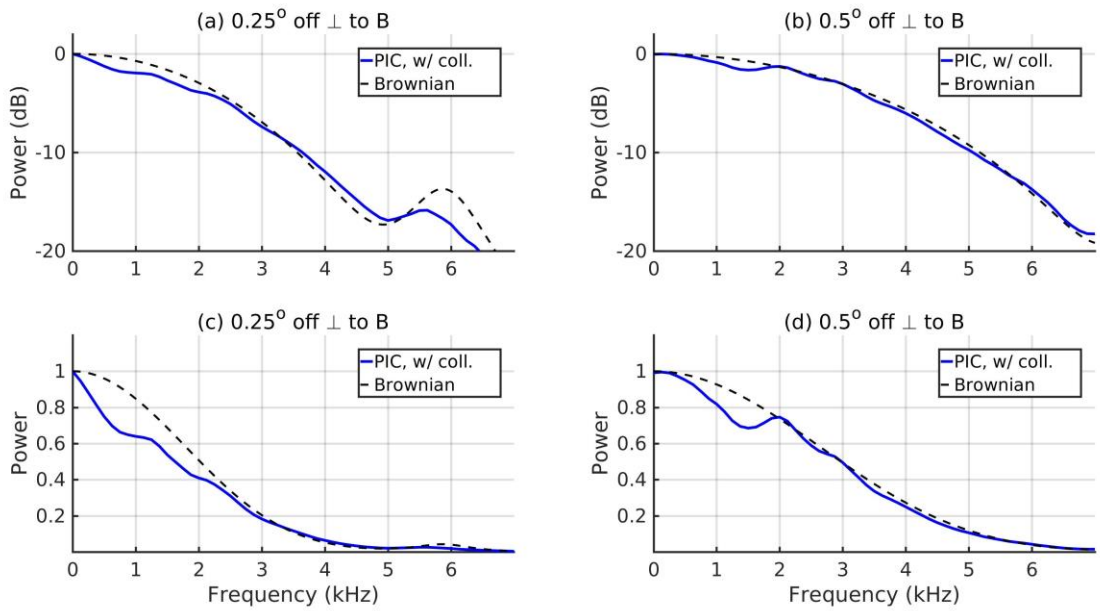

Figure 3.6. The spectra of a 440 MHz radar at 0.25° and 0.5° away from perpendicular to B. To resolve angles this small an additional set of simulations was done using the parameters in Table 3.2, with the grid size increased to 1024x1024, the grid step increased to 1.5 cm, and the simulation time reduced to 4 ms. Plots (a) and (b) are on a logarithmic scale, showing the lower hybrid mode at ~6 kHz at 0.25°, and plots (c) and (d) are the same spectra on a linear scale. The simulated spectra are obtained by averaging the results of 100 independent runs.

3.5 Discussion

The single particle simulations presented in *Sulzer and Gonzalez* (1999) and *Milla and Kudeki* (2011), as well as the Brownian motion theory, focus on calculating single particle autocorrelation functions, $\langle \exp(i\vec{k} \cdot \Delta\vec{r}_s) \rangle$, for each species *s*. The spectra are then produced using the general framework for ISR spectra described by equations 38-41 in *Kudeki and Milla* (2011). The general framework is a first principles derivation that uses fundamental relations between the autocorrelation functions, electric conductivities σ_s, and thermal noise manifesting through the fluctuation-dissipation theorem to calculate ISR spectra. For completeness, this general framework is summarized here:

$$\langle \left| n_e\left(\omega, \vec{k}\right) \right|^2 \rangle = \frac{2N_0 |i\omega\epsilon_0 + \sigma_i|^2}{|i\omega\epsilon_0 + \sigma_e + \sigma_i|^2} \mathrm{Re}[J_e(\omega)] + \frac{2N_0 |\sigma_e|^2}{|i\omega\epsilon_0 + \sigma_e + \sigma_i|^2} \mathrm{Re}[J_i(\omega)] \quad (3.36)$$

$$\sigma_s\left(\omega, \vec{k}\right) = i\omega\epsilon_0 \left(\frac{1 - i\omega J_s(\omega)}{k^2 h_s^2} \right) \quad (3.37)$$

where N_0 is the plasma density, and h_s is the Debye length. J_s is the Gordeyev integral, which is the one-sided Fourier transform of the single particle autocorrelation function of species *s*,

$$J_s(\omega) = \int_0^\infty d\tau \, e^{-i\omega\tau} \langle e^{i\vec{k}\cdot\Delta\vec{r}_s} \rangle \quad (3.38)$$

While the general framework is based on first principles derivations, this approach inherently separates the macrophysics of collective behavior from the microphysics of single particle motions. In contrast, the PIC simulations presented here directly calculate $\langle |n_e\left(\omega, \vec{k}\right)|^2 \rangle$ from a many-particle simulation that self-consistently evolves the micro and macrophysics at the same time. These two different approaches warrant a careful comparison.

3.5.1 Comparison to Brownian Motion Theory

The Coulomb collision algorithm in this chapter solves the Langevin equation

$$\Delta\vec{v}_{Lang} = \vec{F}_d \Delta t + \vec{Q},$$

with velocity dependent coefficients F_d and Q defined by the Fokker-Planck equation. The Brownian motion theory from *Kudeki and Milla* (2011) solves the same Langevin equation using coefficients F_d and Q that are averaged over the electron distribution and are independent of velocity. The resulting displacement statistics are shown in equations

(3.30) – (3.31) and are easy to use in the general framework described by equations (3.36) – (3.38). However, the single particle simulations in *Milla and Kudeki* (2011) show that the Brownian motion solution to equation (3.12) describes the effects of ion-ion collisions well, but is only accurate for electron-ion collisions for spectra exactly perpendicular to B. The collisional PIC simulations in Figure 3.3 support this conclusion, with the Brownian motion theory matching the simulations well, though the collision rate used in the theory curve is slightly higher than the best fit rates found by *Milla and Kudeki* (2011). When the spectra are normalized to a maximum power of 1, we see the collisional simulations are narrower that the Brownian motion theory for angles less than 3°. This suggests that using the Brownian motion theory to invert spectra in this range will result in an underestimation of the electron or ion temperatures. At aspect angles above 3° we do not see any significant deviations between the Brownian motion theory and our collisional simulation. At aspect angles larger than above 5° both simulations and the Brownian motion theory converge on the collisionless theory, in agreement with previous results (*Aponte et al.*, 2001).

3.5.2 Comparison to Single Particle Simulations

Milla and Kudeki (2011) calculate the electron Gordeyev integral from a set of simulations of a single electron gyrating in a magnetic field while undergoing Coulomb collisions. The Coulomb collisions are implemented through the same Langevin equation used in EPPIC,

$$\vec{v}_{new} = \vec{v}_{old} + \vec{F}_{Lorentz}\Delta t + \vec{F}_d\Delta t + \vec{Q}.$$

In the case of the single particle simulations the Lorentz force does not include an electric field, which is accounted for with the general framework in equation (3.36). The drag and diffusion coefficients come from the same Fokker-Planck equation we use, but they do not make the same assumption of a delta distribution for the ions when calculating the Rosenbluth potentials which allows for slow energy exchange in their electron-ion collisions. Additionally, the simulations in *Milla and Kudeki* (2011) include both electron-ion collisions and electron-electron collisions, making direct comparisons to their results difficult. The physics of electron-electron collisions is distinct from the physics of electron-ion collisions, but to the lowest order including both collision mechanisms will effectively double the collision frequency.

Figure 11 of *Milla and Kudeki* (2011) plots their single particle simulation results at magnetic aspect angles of 0°, 0.1°, 0.5°, and 1° against the Brownian motion theory, the single particle simulations from *Sulzer and Gonzalez* (1999), and the small angle extension of the Sulzer and Gonzalez results by *Woodman* (2004). The 0.5° results in Figure 11 of *Milla and Kudeki* (2011) show single particle simulations producing spectra that are narrower than the Brownian motion theory when normalized to the same peak value, in agreement with our simulated spectra at 0.5° in Figure 3.6. At 1°, our normalized collisional simulation is narrower than the Brownian motion theory, and the single particle simulations in Milla and Kudeki are also narrower than the Brownian motion theory. Overall, our self-consistent many particle simulations produce the same behavior at small aspect angles as the Milla and Kudeki single particle simulations.

Chapter 4 shows a quantitative comparison between the PIC simulations and the single particle simulations from *Milla and Kudeki* (2011).

3.5.3 Summary

This chapter describes the implementation of a grid-based Coulomb collision method in a massively parallel electrostatic PIC code. The collision algorithm was validated against a theoretical analysis of a beam decelerating due to collisional drag. This test showed that the theory fails to sufficiently account for the deviation of the beam's velocity distribution away from a Gaussian, but once this was accounted for in the theory it matched the simulation well. Using this collision algorithm, this chapter describes how ISR spectra can be simulated at all magnetic aspect angles, including the case of exactly perpendicular to the magnetic field where collisionless models produce singularities at harmonics of the gyrofrequency. Figures 3.3-3.6 clearly show that the simulated spectra at small magnetic aspect angles changes significantly due to electron-ion collisions.

The only analytic theory for magnetized, collisional ISR spectra is provided in *Kudeki and Milla* (2011), which approximates Coulomb collisions as a Brownian motion process with a constant collision frequency. Comparisons of our simulations to this theory show the theory is accurate exactly perpendicular to the magnetic field, and at aspect angles greater than 3°. Between 0° and 3° the theory does not agree with our simulations which means that using the Brownian motion theory to invert spectra will underestimate the plasma temperature. These results are in agreement with *Milla and Kudeki* (2011), which used single particle simulations to show the Brownian motion

theory is inaccurate for small, non-zero aspect angles. We also see that our simulations at angles less than 1° qualitatively agree with the single particle simulations, which use the same velocity dependent collision operator to produce electron autocorrelation functions that define the ISR spectra using the framework outlined in *Kudeki and Milla* (2011).

The simulations presented in this chapter were done to isolate the effects of electron-ion collisions on ISR spectra at small aspect angles. Collisions with neutrals were neglected, though *Goodwin et al.* (2018) shows that ion-neutral collisions can drastically change the shape of ISR spectra when a strong external electric field is imposed. Our simulation results are restricted to the F region where the plasma is composed of a single ion species, O^+. Multiple ion species can also be included in the PIC method should one wish to investigate collision effects in the D and E regions. However, the electron-ion collision algorithm implemented in this chapter makes no distinction between the ion species in the collision, as the Rosenbluth potentials are evaluated using a delta distribution for the ion velocities. Electron-electron collisions can be simulated in EPPIC using the same framework outlined in this chapter but have yet to be included due to the computational cost of evaluating exact Rosenbluth potentials and maintaining energy conservation. The next chapter will focus on including electron-electron collisions since they occur with a frequency similar to electron-ion collisions, and transfer energy between particles at a faster rate than electron-ion collisions.

Chapter 4

Nonlinear Effects of Electron-Electron Collisions on ISR Temperature Measurements

This chapter has been published as

Longley, William J., Meers M. Oppenheim, Yakov S. Dimant (2019), Nonlinear Effects of Electron-Electron Collisions on ISR Temperature Measurements, J. Geophys. Res. Space Physics, doi:10.1002/2019JA026753

Key points are:

- Collisional and nonlinear effects are important for incoherent scatter theory when looking close to perpendicular to Earth's magnetic field.
- Simulations show electron-electron collisions cause temperature underestimates at angles within 5° of perpendicular to the magnetic field.
- Particle-in-cell simulations show different collisional effects compared to simulations using single particle displacement statistics.

4.1 Introduction

Early incoherent scatter radar (ISR) measurements of the F-region and topside ionosphere at Jicamarca Radio Observatory systematically underestimated the electron temperature by around 20% when compared to satellite measurements (*Carlson and Sayers,* 1970; *McClure,* 1973). The disagreement between satellite and radar temperature measurements was found to be a result of the radar looking within 3° of perpendicular to

the magnetic field. Jicamarca's construction at the equator as a phased array transmitting at 50 MHz means the radar always looks within 5° of perpendicular to the magnetic field to avoid strong sidelobe echoes off the electrojet (*Aponte et al.,* 2001). Thus, the temperature discrepancy when looking nearly perpendicular to the magnetic field is a fundamental problem for operations at Jicamarca. This problem is also present at Millstone Hill, which routinely uses the 440 MHz, 46-meter steerable antenna to make azimuth scans across North America at low elevation angles. These scans are valuable due to the large number of GNSS receivers concentrated in the U.S. and Canada, which allows multi-point observations of phenomena such as SAPS, TIDs, or the 2017 eclipse (*Zhang et al.,* 2017). However, for a range of azimuth angles the radar's line of sight comes within 5° of perpendicular to the Earth's magnetic field, which causes large errors or missing values in the temperature measurements published on the CEDAR Madrigal database.

Sulzer and Gonzalez (1999) offered the first physical explanation of the perpendicular to B temperature discrepancy: Coulomb collisions dominate the shape of the measured spectra when looking at small aspect angles. Jicamarca's transmitted wavelength is significantly larger than a typical gyro-radius in the ionosphere, so the motion of electrons along the field lines is the primary mechanism for Doppler shifting the radar signal. At small aspect angles of about 0.3° to 5° away from perpendicular, the motion of the electrons at low frequencies is a result of the electrostatic ion cyclotron wave, which couples the ion acoustic mode with ion gyro motion. Coulomb collisions increase the damping of this mode as the aspect angle decreases, and the resulting

Doppler spectra measured by the radar are narrower than spectra without Coulomb collision effects. Sulzer and Gonzalez justified their physical explanation with 1D single particle simulations of electrons undergoing electron-ion and electron-electron Coulomb collisions. *Aponte et al.* (2001) confirmed the Sulzer and Gonzalez hypothesis with experiments at Jicamarca and developed a numerical library from the single particle simulations that has been in use for temperature measurements since. *Woodman* (2004) used constant velocity solutions of the Fokker-Planck equation to show how electron-ion and electron-electron collisional damping of the ion acoustic mode can vary as a function of aspect angle.

A theory for collisional spectra at small aspect angles is worked out in *Kudeki and Milla* (2011), which makes a less accurate but easy to solve approximation of all collisions being a Brownian motion process with a constant collision frequency. *Milla and Kudeki* (2011) extended the Sulzer and Gonzalez single particle simulations to 3D, which allowed them to calculate spectra at aspect angles less than 0.1°. Their single particle simulations show the Brownian motion approximation is accurate at aspect angles less than 0.01° but will still underestimate electron temperatures at larger angles. Recently, *Longley et al.* (2018) used fully kinetic particle-in-cell (PIC) simulations with electron-ion collisions to show qualitative agreement with the single particle simulations in *Milla and Kudeki* (2011) at aspect angles less than 1°. In this chapter we show that the addition of electron-electron collisions to the PIC simulations leads to different spectra than what the single particle simulations from *Milla and Kudeki* (2011) predict.

4.2 Simulating Electron-Electron Collisions

4.2.1 Theory

Under the assumption of many small angle scatterings, Coulomb collisions in a plasma are represented by the Fokker-Planck equation (*Rosenbluth et al.*, 1957):

$$\frac{\partial f_e}{\partial t}_{coll} = \frac{\partial}{\partial \vec{\boldsymbol{v}}} \cdot \left[\vec{\boldsymbol{F}}_{\boldsymbol{d}}(\vec{\boldsymbol{v}}_e) f_e(\vec{\boldsymbol{v}}_e)\right] + \frac{1}{2}\frac{\partial^2}{\partial \vec{\boldsymbol{v}} \partial \vec{\boldsymbol{v}}} : \left[\overline{\mathbf{D}}(\vec{\boldsymbol{v}}_e) f_e(\vec{\boldsymbol{v}}_e)\right], \tag{4.1}$$

where $\mathbf{F_d}$ is a drag friction vector, $\mathbf{D}$ is a diffusion tensor, and f_e is the electron distribution. Assuming the electron distribution is an isotropic Maxwellian and choosing a coordinate system where $\vec{\boldsymbol{v}}_{\boldsymbol{e}} = v\,\hat{\boldsymbol{e}}_{\boldsymbol{3}}$, the drag and diffusion coefficients for electron-electron collisions are (*Manheimer et al*, 1997)

$$F_d(v) = -\frac{ne^4\Lambda}{2\pi\epsilon_0^2 m_e^2 v^2}\left[\mathrm{erf}\left(\frac{v}{v_{th}}\right) - \frac{2}{\sqrt{\pi}}\frac{v}{v_{th}}\exp\left(-\frac{v^2}{v_{th}^2}\right)\right], \tag{4.2}$$

$$D_{11}(v) = D_{22}(v) = \frac{ne^4 v_{th}^2\Lambda}{8\pi\epsilon_0^2 m_e^2 v^3}\left[\left(\frac{2v^2}{v_{th}^2} - 1\right)\mathrm{erf}\left(\frac{v}{v_{th}}\right) + \frac{2}{\sqrt{\pi}}\frac{v}{v_{th}}\exp\left(-\frac{v^2}{v_{th}^2}\right)\right], \tag{4.3}$$

$$D_{33}(v) = \frac{ne^4 v_{th}^2\Lambda}{4\pi\epsilon_0^2 m_e^2 v^3}\left[\mathrm{erf}\left(\frac{v}{v_{th}}\right) - \frac{2}{\sqrt{\pi}}\frac{v}{v_{th}}\exp\left(-\frac{v^2}{v_{th}^2}\right)\right], \tag{4.4}$$

The thermal speed is $v_{th}^2 = 2KT/m_e$, n is the plasma density. Λ is the Coulomb logarithm, which is defined by the Debye length, h_d, and the electron speed, v:

$$\Lambda = \ln\left(\frac{4\pi\epsilon_0 m_e h_d v^2}{e^2}\right). \tag{4.5}$$

With the chosen coordinate system all off-diagonal terms in the diffusion tensor are zero. Despite the assumption of an isotropic Maxwellian distribution in the Rosenbluth potentials, we will show in Section 3 that the coefficients in equations (4.2) – (4.4) can also be used for slightly anisotropic Maxwellian plasmas.

Collisions are implemented into a PIC code using an equivalent Langevin equation. The Langevin equation describes the collision of a single particle as the combination of a deterministic drag force, $\boldsymbol{F_d}$, and a stochastic diffusion vector, $\boldsymbol{Q}$. In velocity update form the Langevin equation is (*Manheimer et al.*, 1997)

$$\Delta\vec{\boldsymbol{v}}_{Lang} = \vec{\boldsymbol{F}}_{\boldsymbol{d}}\Delta t + \vec{\boldsymbol{Q}}, \tag{4.6}$$

The components of the diffusive vector **Q** are randomly sampled from the multivariate Gaussian distribution defined by the diffusion coefficients D_{11} and D_{33} from equations (4.3) and (4.4):

$$\phi(\vec{\boldsymbol{Q}}) = \frac{1}{(2\pi\Delta t)^{3/2} D_{11} D_{33}^{1/2}} \exp\left(-\frac{Q_3^2}{2D_{33}\Delta t} - \frac{Q_1^2 + Q_2^2}{2D_{11}\Delta t}\right). \tag{4.7}$$

4.2.2 Electron-Electron Collision Algorithm

Electron-electron collisions are implemented into a PIC code in the same manner as electron-ion collisions, as described in *Manheimer et al.* (1997) and *Longley et al.* (2018). The main differences between the two algorithms are the calculation of D_{33} in equation (4.4) and subsequent random draw of Q_3 in equation (4.7), and the method for ensuring global energy conservation. Due to the stochastic nature of the diffusion term in the Langevin equation, momentum and energy are not necessarily conserved through all

of the collisions in a given time step. For electron-ion collisions *Manheimer et al.* (1997) provides a way to conserve energy for each collision on the assumption that momentum and energy is not transferred to ions during any single collision. This assumption does not work for same species collisions, where energy and momentum are freely transferred between the two colliding particles. *Lemons et al.* (2009) provides the method below for correcting the full set $\Delta\vec{v}$ to ensure total momentum and energy are conserved.

1. Calculate the coefficient

$$\vec{\beta} = \frac{1}{N}\sum_{i=1}^{N} \Delta\vec{v}_i \,, \tag{4.8}$$

   where *N* is the total number of electrons collided during the time step. The coefficient β is the average momentum imparted on each electron due to the stochastic nature of the Langevin equation. If momentum is globally conserved in a time step, then $\beta = 0$.

2. Calculate the coefficient

$$\alpha = \frac{-2\sum_{i=1}^{N} \vec{v}_i \cdot (\Delta\vec{v}_i - \vec{\beta})}{\sum_{i=1}^{N}\left(\Delta\vec{v}_i - \vec{\beta}\right)^2}, \tag{4.9}$$

   where $\vec{v}_i$ is the velocity before the collision occurs. This coefficient is related to the global energy conservation.

3. Transform the set of velocity increments to

$$\Delta\vec{v}_i' = \alpha\left(\Delta\vec{v}_i - \vec{\beta}\right). \tag{4.10}$$

4. Each electron's post-collision velocity is then

$$\vec{v}_i' = \Delta\vec{v}_i' + \vec{v}, \tag{4.11}$$

where $\vec{v}$ is the particle velocity before the collision. The set of post-collision velocities in equation (4.11) will exactly conserve energy and momentum on a global scale while accurately modeling the energy and momentum transfer of electron-electron collisions.

4.3 Validation

Electron-electron collisions are implemented into EPPIC, which is an electrostatic, fully kinetic, massively parallel, domain decomposed PIC code (*Oppenheim et al.,* 2008). The particle positions are advanced using a second order Boris mover, with the electric field determined self-consistently by solving Poisson's equation on a grid. To validate the collision algorithm, an anisotropic Maxwellian plasma is simulated, where the electron distribution is initially hotter in the *y*-direction. Theoretically the collisional relaxation of an anisotropic distribution is described by the differential equation (*Hellinger and Trávnícek*, 2009),

$$\frac{dT_y}{dt} = -2T_y \nu_{ee} \left[{}_2F_1\left(\begin{matrix}2, 1/2, \\ 5/2,\end{matrix}\ 1-\frac{T_x}{T_y}\right) - {}_2F_1\left(\begin{matrix}1, 1/2, \\ 5/2,\end{matrix}\ 1-\frac{T_x}{T_y}\right)\right], \tag{4.12}$$

where ${}_2F_1\left(\begin{matrix}a, b, \\ c,\end{matrix}\ d\right)$ is the hypergeometric function which is called in MATLAB as *hypergeom([a,b], c, d)*. The temperatures in the *x* and *z* directions are determined by conservation of energy, $T_{tot} = T_x + T_y + T_z$ where T_{tot} is constant. The collision frequency used in equation (4.12) is the thermally averaged rate, with the Coulomb logarithm evaluated using $v_{th}^2 = \frac{8}{\pi}\ KT/m$ (*Hellinger and Trávnícek*, 2009):

$$\nu_{ee} = \frac{ne^4\Lambda}{6\pi^{3/2}\epsilon_o^2 m_e^2 v_{th,y}^3}. \tag{4.13}$$

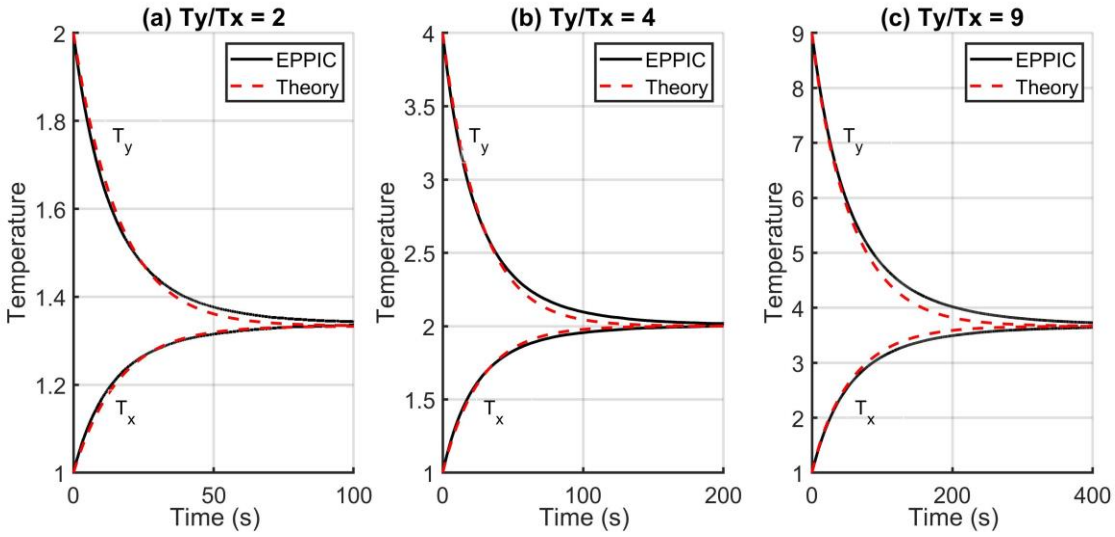

Figure 4.1 The collisional relaxation of an anisotropic electron distribution. In each plot the two curves at higher temperature correspond to T_y, which is initially hotter than $T_x = T_z$, shown by the bottom two curves in each figure. In (a) the initial anisotropy ratio is $T_y/T_x = 2$, and the maximum error between the theory and EPPIC is 1.5%. The anisotropy ratio in (b) is 4, which corresponds to $v_{th,y} = 2v_{th,x}$, but the error between the two curves is still 2.5%. The anisotropy ratio is taken to an extreme value of 9 in (c), and the error between EPPIC and the theory is 6%.

Figure 4.1 plots the theoretical solution for the plasma temperature over time compared to the temperature simulated by EPPIC. The simulations use normalized parameters where $m_i = 1024$, $m_e = 1$, $\Delta t = 0.02$, $\Delta x = 0.5$, and $v_{th,x}(t = 0) = 1$. The two solutions agree well for an initial temperature anisotropy ratio of 2, but the error between the simulated and theoretical temperatures increases as the initial anisotropy ratio increases. This is expected because the Rosenbluth potentials in equations (4.2) – (4.4) were solved using an isotropic Maxwellian distribution, which is not a good approximation for larger anisotropy ratios. The results in Figure 4.1 agree with the assertion of *Manheimer et al.* (1997) that for small anisotropies the error in calculating the Rosenbluth potentials with an isotropic Maxwellian is negligible.

4.4 ISR Simulations

Incoherent scatter radars transmit in the VHF or UHF frequency range and receive a small amount of power return from Thomson scattering off electrons in the ionosphere. The power spectrum of the returned signal is proportional to the Fourier transform of the electron density in the scattering volume ΔV (*Kudeki and Milla*, 2011),

$$P(\omega) = \frac{r_e^2}{R^2} E_0^2 \Delta V \langle |n_e(\omega, \vec{\boldsymbol{k}})|^2 \rangle, \tag{4.14}$$

where R is the distance between the radar and the scattering volume, r_e is the classical electron radius, and E_0 is the amplitude of the transmitted electric field. Thus, the only parameter that varies due to plasma motion in the ionosphere is the averaged Fourier transform of the electron density, $\langle |n_e(\omega, \vec{\boldsymbol{k}})|^2 \rangle$. *Diaz et al.* (2008) showed that unmagnetized, collisionless ISR spectra can be simulated with EPPIC by Fourier transforming the electron density output in time and space, which directly calculates the spectra, $\langle |n_e(\omega, \vec{\boldsymbol{k}})|^2 \rangle$. Recently *Longley et al.* (2018) showed that magnetized, collisional ISR spectra can also be simulated with EPPIC by taking an average of ~100 independent simulations.

4.4.1 Single Particle Simulations

Kudeki and Milla (2011) outlines a general framework for calculating ISR spectra by applying the fluctuation-dissipation theorem to single particle displacement statistics. This yields

$$\langle \left| n_e\left(\omega, \vec{\boldsymbol{k}}\right) \right|^2 \rangle = \frac{2N_0 |i\omega\epsilon_0 + \sigma_i|^2}{|i\omega\epsilon_0 + \sigma_e + \sigma_i|^2} \mathrm{Re}[J_e(\omega)] + \frac{2N_0 |\sigma_e|^2}{|i\omega\epsilon_0 + \sigma_e + \sigma_i|^2} \mathrm{Re}[J_i(\omega)], \quad (4.15)$$

$$\sigma_s\left(\omega, \vec{\boldsymbol{k}}\right) = i\omega\epsilon_0 \left(\frac{1 - i\omega J_s(\omega)}{k^2 h_s^2} \right), \quad (4.16)$$

where N_0 is the plasma density, and h_s is the Debye length. J_s is the Gordeyev integral, which is the Fourier transform of the single particle autocorrelation function (ACF) of species *s*,

$$J_s(\omega) = \int_0^\infty d\tau \, e^{-i\omega\tau} \langle e^{i\vec{\boldsymbol{k}}\cdot\Delta\vec{\boldsymbol{r}}_s} \rangle . \quad (4.17)$$

The simulations in *Milla and Kudeki* (2011) calculate the single particle ACF, $\langle e^{i\vec{\boldsymbol{k}}\cdot\Delta\vec{\boldsymbol{r}}_s} \rangle$, then use the framework in equations (4.15) – (4.17) to calculate the spectra, $\langle |n_e\left(\omega, \vec{\boldsymbol{k}}\right)|^2 \rangle$. This approach allows for a velocity dependent treatment of Coulomb collisions using the same Fokker-Planck and Langevin equations from Section 2 and requires significantly less computation time than PIC simulations. The standard analytic theory for collisional, magnetized ISR calculates the Gordeyev integral using a Gaussian ACF with constant drag and diffusion coefficients (equations 4.2-4.4) that are averaged over the electron distribution (*Kudeki and Milla*, 2011). This is equivalent to a Brownian motion collision process, and while this theory does avoid the singularities present in the Gordeyev integral when no collisions are modeled, both *Milla and Kudeki* (2011) and *Longley et al.* (2018) show the Brownian theory is not accurate for temperature estimates at small, nonzero aspect angles.

Figure 4.2 shows the results from a set of single particle simulations using the *Milla and Kudeki* (2011) method for a 50 MHz radar probing a plasma with $T_e = T_i = 1000\ K$, $n_0 = 10^{12}\ m^{-3}$, and $B = 0.25\ G$. For these simulations a single electron starts with a velocity randomly drawn from a Maxwellian distribution, and the motion of the electron is tracked over 100 ms. The ACF of a single simulation is calculated as the cross correlation of $\exp(i\vec{k} \cdot \vec{r})$, and averaging the results of 9,600 simulations that differ only in the initial velocity provides the distribution's ACF for use in equation (4.17).

Figure 4.2 shows that the effects of electron-electron collisions alone are indistinguishable from the Brownian collision theory at aspect angles larger than 0.35°, which is the angle where thermal electrons are no longer able to neutralize the ion acoustic wave, effectively cutting off the wave. While both electron-ion and electron-electron collision frequencies vary as $1/v^3$, the energy exchange in electron-ion collisions is negligible. This means that for a given electron the collision frequency is effectively constant throughout the 100 ms simulation, and the sharp peak at low frequencies in the simulations with only electron-ions is a result of slow particles colliding frequently and changing energy very slowly. Conversely, electron-electron collisions efficiently exchange energy, so after one collision the electron ends up at a different velocity, which has a different collision rate. This rapid change of energy during electron-electron collisions effectively averages the collisional motion over the distribution, which is why the simulations in Figure 4.2 with only electron-electron collisions match the Brownian theory well at aspect angles of 0.35° and larger. Simulations with both collision types average this behavior together, as slow-moving electrons still collide more frequently and

give more power at low frequencies, but the electron-electron energy exchange keeps particles from sitting at low speeds for the whole simulation. The combined effect of electron-ion and electron-electron collisions narrows the spectra at angles as large as 3°.

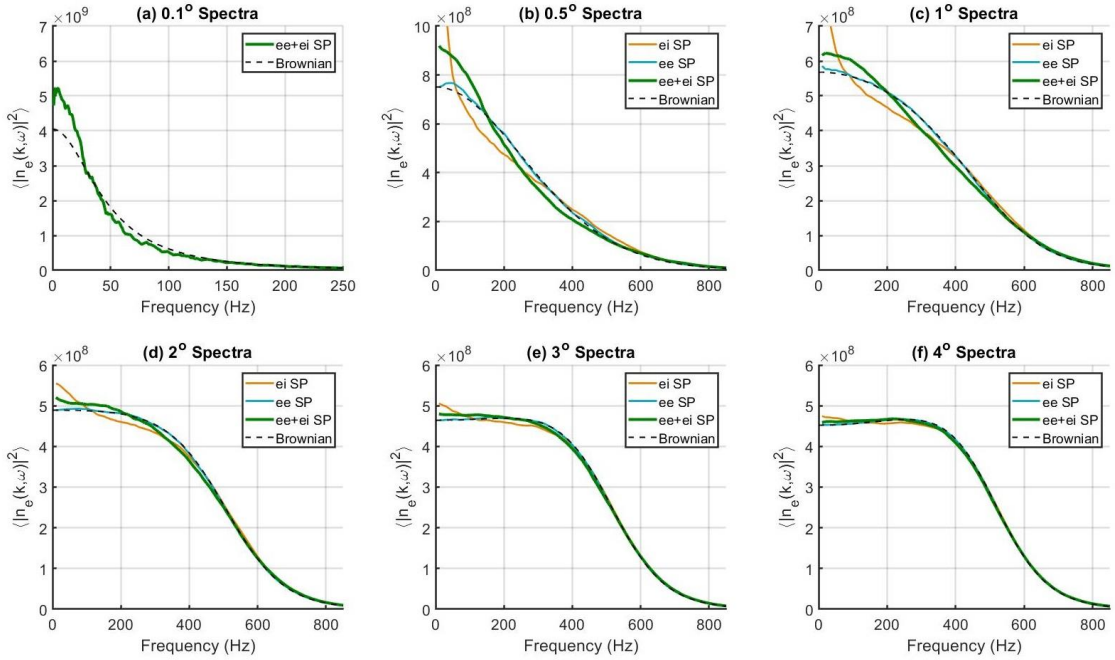

Figure 4.2 The ISR spectra for a 50 MHz radar calculated using the single-particle simulation method from *Milla and Kudeki* (2011). The electron and ion temperatures are both 1000 K, the density is 10^{12} m^{-3}, a magnetic field strength of 0.25 G is used, and the simulations use the real electron mass of $9.1x10^{-31}$ kg. The simulations with only electron-ion collisions (orange) are peaked at low frequency due to the slow energy exchange during electron-ion collisions. At aspect angles of 0.35° and higher, the simulation with only electron-electron collisions (blue) is identical to the Brownian collision theory (dashed black). The combined effect of both collision types (green) shows the spectra deviates from the Brownian theory at angles up to 3°. For plots (b)-(f), 9,600 simulations are run for 100 ms each, giving a 10 Hz resolution in the spectra. The longer correlation time of the 0.1° spectra in plot (a) required run times of 1 second. The longer runtime at 0.1° limited the computation of spectra to 4,800 simulations of only the combined collisions (green).

4.4.2 PIC Simulations

ISR spectra are simulated with the PIC code using the collision algorithm outlined in Section 4.2.2 for electron-electron collisions along with the electron-ion collision routine described in *Longley et al.* (2018). Table 1 shows the parameters for EPPIC simulations of collisional, magnetized spectra. The simulations are 2D in space with periodic boundary conditions and have 3D velocity vectors for each particle. To reduce runtime an artificial electron mass of $m_e = m_{O+}/1024$ is used, which is ~28.5 times heavier than the real electron mass. The magnetic field is increased by a factor of $\sqrt{28.5} \approx 5.4$ when applied to the electrons, which makes the simulation gyrofrequency scale as $\omega_{ce} \propto m_e^{-1/2}$. This scaling is done in order to preserve the lower-hybrid frequency, which avoids the non-physical problem of the lower-hybrid mode exciting a perpendicular to B ion-acoustic mode. See *Longley et al.* (2018) for further discussion on the use of an artificial electron mass and the scaling of electron gyrofrequency in the PIC code as $\omega_{ce} \propto m_e^{-1/2}$. The plasma density is also lowered to increase the Debye length, which avoids numerical heating over long simulations. The increased Debye length does slightly increase the Landau damping of the acoustic mode, which depends on the parameter $(k\lambda_D)^2$, and evaluates to 0.16 for a 440 MHz radar and the 2.18 cm Debye length. PIC simulations calculate the electron density, $n_e(\vec{x}, t)$, on the simulation grid at every time step in order to solve Poisson's equation for the self-consistent electric field.

The ISR spectra is then calculated by taking the discrete Fourier transform of $n_e(\vec{x}, t)$ in time and space to obtain $n_e(\vec{k}, \omega)$ for a single run of the PIC code. Since low

frequencies are of interest the time Fourier transform is unwindowed to preserve the shape of the spectra. The ISR spectra is then calculated by averaging $\left|n_e\left(\vec{k},\omega\right)\right|^2$ from 100 or 200 independent runs of the PIC code (see captions for Figures 3-5) that vary the initial particle placement and the random number seed used in the collision routines (*Diaz et al.*, 2008; *Longley et al.*, 2018). This method allows for a direct calculation of the ISR spectra, $\langle|n_e\left(\omega,\vec{\boldsymbol{k}}\right)|^2\rangle$, without needing the linear framework of *Kudeki and Milla* (2011).

Figure 4.3 shows the simulated spectra for a 440 MHz radar with only electron-ion collisions, Figure 4.4 shows the simulated spectra with only electron-electron collisions, and Figure 4.5 shows the simulated spectra with both collision types. In Figures 4.3-4.6 the Brownian theory spectra and single-particle spectra are also calculated using the same parameters as the PIC code. The 512x512 grid and 0.34 m Bragg wavelength means 0.71° is the smallest angle that can be resolved by the simulation without the perpendicular mode dominating any interpolation in k space. The effects of electron-ion and electron-electron collisions are similar at aspect angles between 0.75° and 2°, with some discrepancy at lower frequencies. However, the PIC simulations with only electron-ion collisions converge on the Brownian theory at 3°, while the electron-electron collisions create spectra narrower than the Brownian theory at angles as large as 5° away from perpendicular. This is in stark contrast to the single particle simulations in Figure 4.2, where simulations with only electron-electron collisions are identical to the Brownian theory at aspect angles of 0.35° and larger. When both electron-ion and electron-electron collisions are simulated in the PIC code the results closely match the electron-ion only simulations at aspect angles less than 2°, and

at aspect angles of 2° and larger the spectra match closely with simulations using only electron-electron collisions.

At aspect angles less than 0.35° the ion acoustic mode is cut off. Since the gyro-radius is much smaller than the radar wavelength, the radar only sees the line of sight thermal motion of electrons moving along the field lines. When the radar looks exactly perpendicular to the magnetic field it sees no line of sight thermal motion, and the collisional diffusion across magnetic field lines is the only effect seen by the radar. Figure 4.4 shows the simulated spectra exactly perpendicular to the magnetic field for PIC simulations with each collision type. The spectra with only electron-ion collisions is best fit by the Brownian theory with a collision frequency of 370 Hz, which corresponds to thermally averaging the collision rate with $v^2 = 3.1\ KT/m$. The spectra with only electron-electron collisions is best fit by the Brownian theory with a collision frequency of $370/\sqrt{2} = 262\ Hz$ as expected. The simulated spectra with both electron-ion and electron-electron collisions is well fit by the Brownian theory, but the best fit collision frequency is 500 Hz, not the expected 632 Hz that results from $\nu_{ei} + \nu_{ee}$. This discrepancy is due to the two different collision types acting as independent events in the absence of a wave.

The variance in perpendicular displacements using a Brownian collision operator with collision frequency ν is (*Woodman,* 1967; see also *Kudeki and Milla*, 2011):

$$\langle \Delta p^2 \rangle = \frac{v_{th}^2}{\nu^2 + \omega_{ce}^2}\left(\cos(2\gamma) + \nu\tau - e^{-\nu\tau}\cos(\omega_{ce}\tau - 2\gamma)\right) \qquad (4.18)$$

where $v_{th}^2 = 2KT_e/m_e$, and $\gamma = \text{atan}(\nu/\omega_{ce})$. Collisional diffusion across field lines by electron-ion and electron-electron collisions are independent events, so in this case the ACF should be evaluated by adding the variances of electron-ion and electron-electron collisions:

$$\langle \Delta p^2 \rangle_{tot} = \langle \Delta p^2 \rangle_{ei} + \langle \Delta p^2 \rangle_{ee} \tag{4.19}$$

For small time lags, τ, the variance in equation (4.18) is nonlinear in collision frequency, even in the weakly collisional limit of $\nu \ll \omega_{ce}$. Therefore, the total variance in equation (4.19) is not the same as evaluating $\langle \Delta p^2 \rangle$ with a collision frequency of $\nu_{tot} = \nu_{ei} + \nu_{ee}$. Evaluating the ACF with the total variance in equation (4.19) produces perpendicular spectra that is nearly identical to spectra with a collision rate of $\nu = 580\ Hz$, which is less than $\nu_{tot} = 632\ Hz$, but still larger than the best fit of 500 Hz shown in Figure 4.6. Thus, while a Brownian collision model fits perpendicular to B spectra, the collision rate is not strictly additive. This same effect is not present in oblique mode spectra at aspect angles of 0.35° and larger, where the spectra is shaped by the damped ion-acoustic mode. Evaluating the Brownian theory in this regime using equation (4.19) for the perpendicular variance produces spectra that are significantly wider than collisionless theory, even when the parallel variance is calculated similar to equation (4.19). It is important to note that while Figure 4.6 shows that combining electron-ion and electron-electron collisions is not trivial, Figure 4.4 shows that electron-electron collisions alone significantly damp the oblique mode spectra at a wider range of aspect angles than Brownian collision theory or single particle simulations.

Table 4.1 Simulation parameters used for all EPPIC simulations of ISR spectra.

Grid Size	512 x 512	Electron mass	$m_e = 2.594 \times 10^{-29}$ kg
Grid Step	$\Delta x = \Delta y = 1$ cm	Ion mass (O+)	$m_i = 2.657 \times 10^{-26}$ kg
Total Time Steps	500,000	Temperature	$T_e = T_i = 1000$ K
Time Step Size	$\Delta t = 80$ ns	Magnetic field for e^-	$B_e = 1.6$ G
Particles per grid cell	128	Magnetic field for Ions	$B_i = 0.3$ G
Average density	$n_i = n_e = 10^4$ cm^{-3}	Collision density	$n_{coll} = 10^6$ cm^{-3}

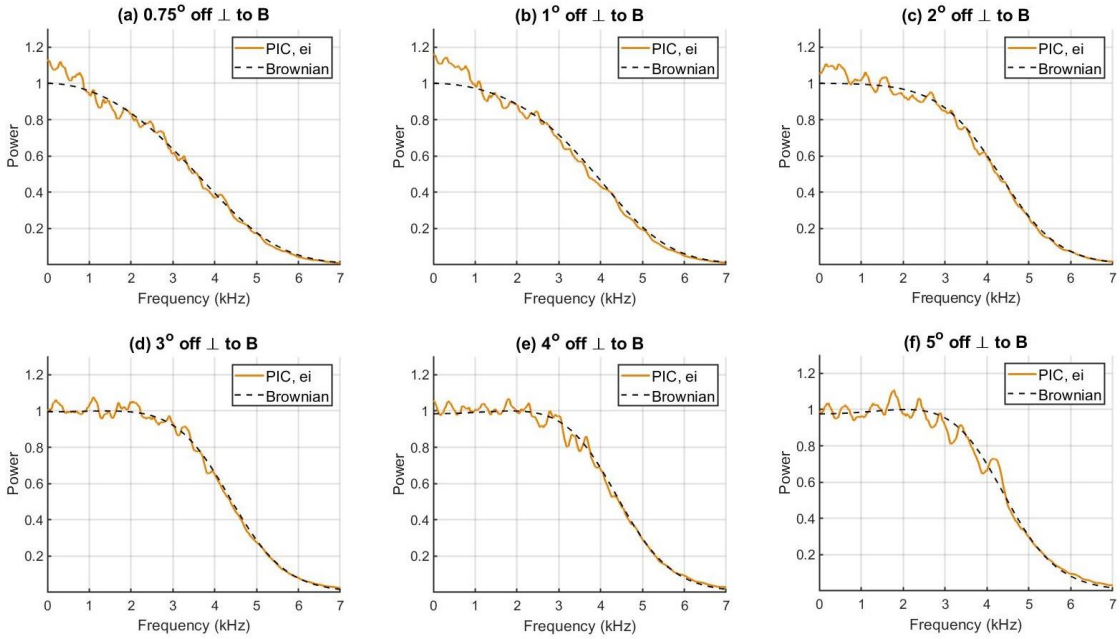

Figure 4.3 ISR spectra for a 440 MHz radar, normalized by total power. PIC simulations with only electron-ion collisions (orange) are narrower than Brownian collision theory (black) at aspect angles less than 3°. The PIC spectra are obtained by averaging 100 independent samples, and a 4th order Savitzky-Golay filter with a 21-bin span is used to smooth the simulated spectra.

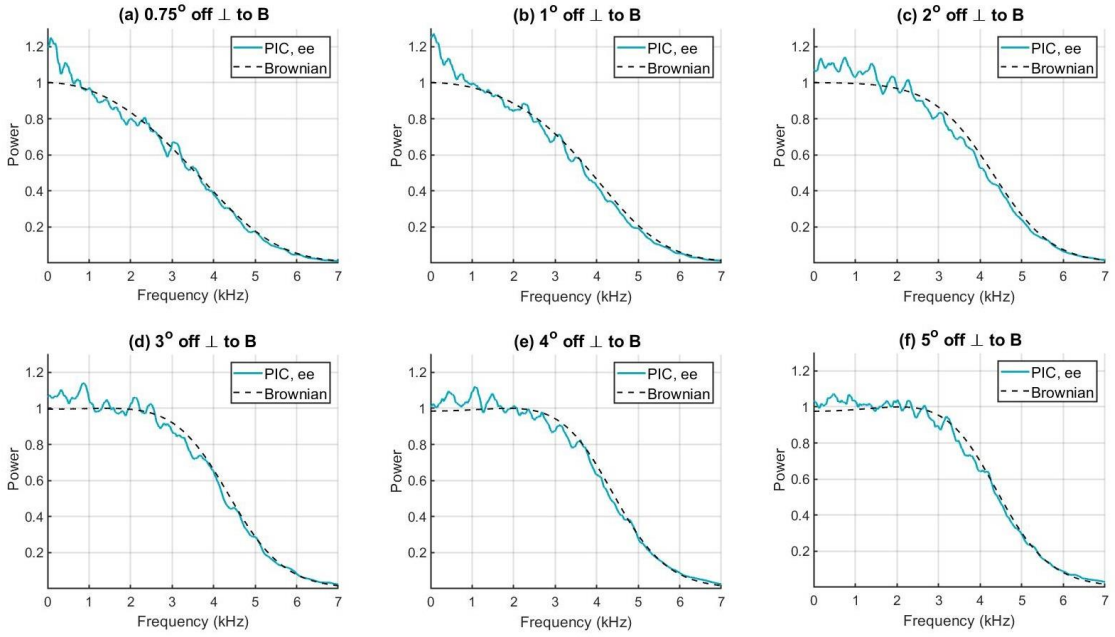

Figure 4.4 ISR spectra for a 440 MHz, normalized by total power. PIC simulations with only electron-electron collisions (orange) are narrower than Brownian collision theory (black) at aspect angles as large as 5°. In comparison with Figure 4.3, electron-electron collision effects are important at a wider range of aspect angles than electron-ion collisions. The PIC spectra are obtained by averaging 100 independent samples, and a 4th order Savitzky-Golay filter with a 21-bin span is used to smooth the simulated spectra.

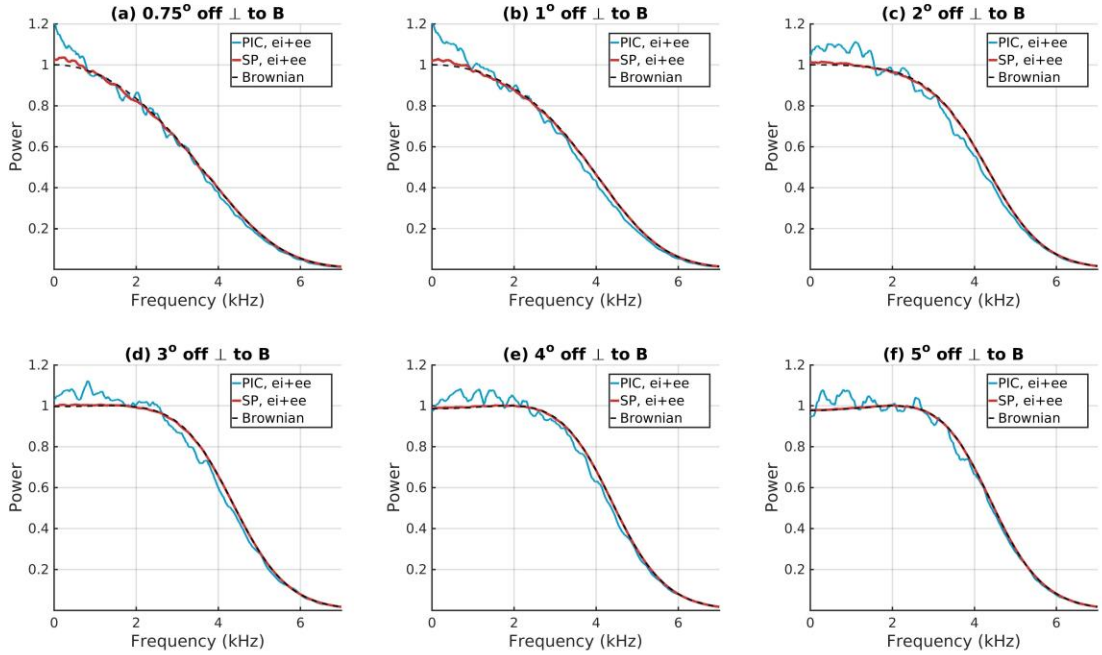

Figure 4.5 The normalized spectra of a 440 MHz radar with electron-ion and electron-electron collisions. The single particle simulations (red) use the method from *Kudeki and Milla* (2011) with the same plasma parameters as the PIC simulation (blue) given in Table 4.1. The Brownian collision theory (black) is shown for comparison. Both simulation methods are exactly fit by the Brownian theory for an aspect angle of 0° (see Figure 4.6). The PIC spectra are produced by averaging 200 independent samples.

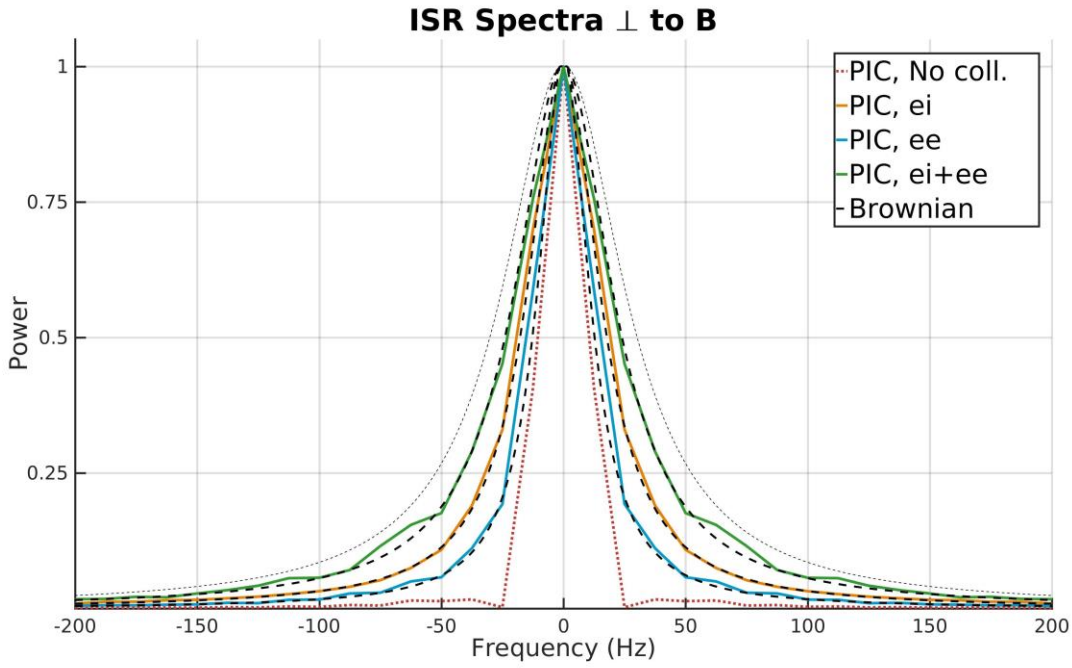

Figure 4.6 The spectra exactly perpendicular to *B* for a 440MHz radar. The frequency resolution is 25 Hz, so the collisionless PIC simulation (dashed-red) is effectively a discrete delta function. The spectra with only electron-ion collisions (orange) is fit exactly by the Brownian theory with a collision frequency of 370 Hz. The spectra with only electron-electron collisions (blue) is fit by the Brownian theory with a collision frequency of $370/\sqrt{2} = 262\ Hz$ as expected. The simulated spectra with both electron-ion and electron-electron collisions (green) is well fit by the Brownian theory, but the best fit collision frequency is 500 Hz, not the expected 632 Hz (shown as the widest dashed curve).

4.5 Discussion

4.5.1 Comparison of Simulation Methods

The combined effects of electron-ion and electron-electron collisions are shown in Figure 4.5 for both simulation methods using the parameters in Table 4.1. For these parameters the single-particle simulations are identical to the Brownian theory at 3° and larger, while the PIC simulations converge on the Brownian theory at 5° and larger. At all aspect angles the PIC simulations produce narrower spectra than the single particle

simulations. Figure 4.6 shows that the artificial electron mass in Table 4.1 does not affect the aspect angle at which the single particle simulations converge to the Brownian theory. This suggests temperature estimates using the libraries from *Sulzer and Gonzalez* (1999) and *Milla and Kudeki* (2011) will still underestimate the electron and ion temperatures. Figure 4.8 shows the electron temperatures needed for the Brownian theory and single-particle simulations to fit the narrower PIC spectra. The simulations are fit with Ti = 1000 K being held constant, and varying Te in 50 K increments. The error between the Brownian theory and the PIC simulations is 25% at 0.75° and decreases to 5% at 5°. Similarly, the error in the single particle simulations is 20% at 0.75° and matches the Brownian error at aspect angles of 2° and larger.

Table 4.2 summarizes the results for the different methods of calculating small aspect angle spectra. Included in Table 4.2 is the dressed particle theory, which solves the coupled electron and ion Boltzmann equations with a BGK collision operator (*Froula et al.*, 2011). The BGK and Brownian collision operators use a constant collision frequency *v*, and are (*Froula et al.*, 2011; *Woodman* 1967)

$$\frac{\partial f_e}{\partial t}_{BGK} = -\nu(f_e - f_0), \tag{4.20}$$

$$\frac{\partial f_e}{\partial t}_{Brownian} = \nu \frac{\partial}{\partial \vec{\boldsymbol{v}}} \cdot (\vec{\boldsymbol{v}} f_e) + \frac{1}{2} \nu \, v_{th}^2 \frac{\partial^2}{\partial \vec{\boldsymbol{v}} \partial \vec{\boldsymbol{v}}} (f_e). \tag{4.21}$$

The BGK operator models collisions as discrete events from a Poisson process (*Milla and Kudeki*, 2009), and therefore underestimates the effects of small angle ion-ion collisions which should kill off ion gyroresonances (*Farley,* 1964). The Brownian collision operator

is derived from the Fokker-Planck operator by assuming constant drag and diffusion coefficients, and better models Coulomb collisions as a series of small angle scatterings.

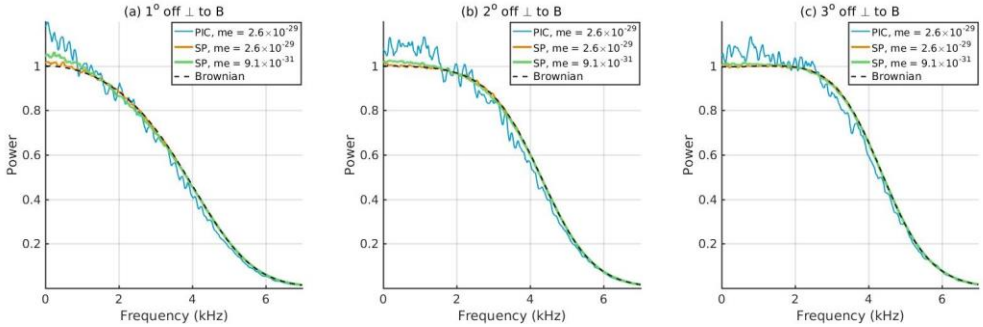

Figure 4.7 The normalized 440 MHz spectra showing the effect of a different electron mass. The PIC simulation (blue) uses an artificially large electron mass to shorten the simulation time. Single particle simulations with the artificial electron mass (orange) and the actual electron mass (green) differ slightly at low frequencies since $\nu_{ei,ee} \propto m_e^{1/2}$, but both simulations converge to the Brownian theory (black) at 3° off perpendicular to *B*.

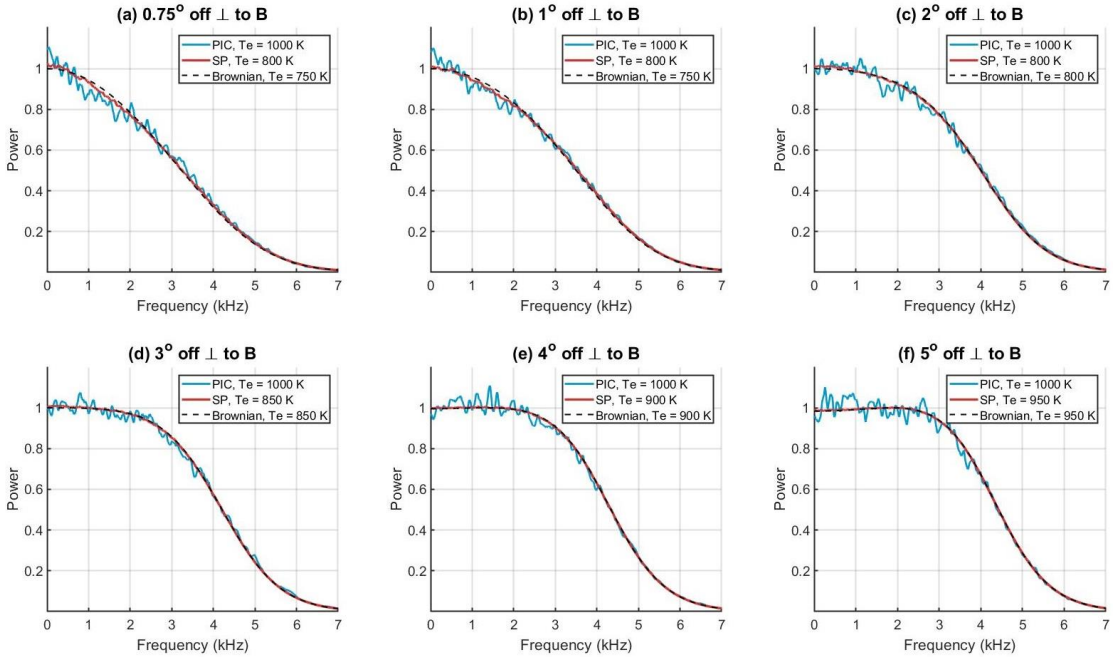

Figure 4.8 Same as Figure 4.5, except the electron temperature in the Brownian theory and single particle simulations is lowered in 50 K increments until the spectra best matches the PIC simulations. The ion temperature is 1000 K for all the spectra. The Brownian theory and single-particle simulations use the same parameters in Table 1 as the PIC code, aside from the change to electron temperature.

Table 4.2 Summary of different methods for calculating small aspect angle ISR spectra.

	Calculation of $\langle\lvert n_e\rvert^2\rangle$	Collision operator	Convergence to Theory (at 440 MHz)
Dressed Particle Theory	Solve e^- and ion Boltzmann equations for n_e	BGK, constant ν	Converges to collisionless theory at 0.5°. Fails to damp out ion gyroresonances for a 50 MHz radar.
Fluctuation-Dissipation Theory	Calculate ACFs and use *Kudeki and Milla* [2011] framework	Brownian, constant ν	Converges to collisionless theory at 0.5°.
Single-particle simulations	Calculate ACFs numerically and use *Kudeki and Milla* [2011] framework	Fokker-Planck, only e-i collisions	Model is not valid at small aspect angles, see Section 4.1.
		Fokker-Planck, only e-e collisions	Model exactly matches Brownian theory at angles > 0.35°. Converges to collisionless theory at 2°.
		Fokker-Planck, e-i and e-e collisions	Converges to collisionless theory at 3°.
PIC simulations	Direct calculation of n_e on a grid at every time step	Fokker-Planck, only e-i collisions	Converges to collisionless theory at 3°. Agrees well with single-particle simulations that include both e-i and e-e collisions
		Fokker-Planck, only e-e collisions	Converges to collisionless theory at 5°.
		Fokker-Planck, e-i and e-e collisions	Converges to collisionless theory at 5°.

4.5.2 Discrepancy Between Simulation Methods

When electron-electron collisions are included, the PIC simulations at small aspect angles produce spectra that are significantly narrower and more damped than the single particle simulations. For low frequency waves, same species collisions should only contribute to the damping of waves when considering particle dynamics near the Landau damping resonance (*Brambilla*, 1995). We hypothesize that the difference between the PIC and single particle simulations is due to the greater importance of nonlinear Landau damping at small aspect angles, leading to resonant electrons dissipating the wave through electron-electron collisions.

To understand the difference between the two simulation methods we look back to the equation for ISR spectra in its general form (*Kudeki and Milla*, 2011):

$$\langle \left| n_e\left(\omega, \vec{\boldsymbol{k}}\right) \right|^2 \rangle = \left| 1 - \frac{\sigma_e}{\epsilon} \right|^2 \langle \left| n_{th,e} \right|^2 \rangle + \left| \frac{\sigma_e}{\epsilon} \right|^2 \langle \left| n_{th,i} \right|^2 \rangle , \tag{4.22}$$

where the dielectric tensor $\epsilon = \sigma_e + \sigma_i + i\omega\epsilon_0$ describes the wave behavior of the system, and $\langle \left| n_{th,s} \right|^2 \rangle = 2N \ \mathrm{Re}[J_s]$ is the thermal scattering spectra of species *s* without collective interactions. For scattering in an unmagnetized plasma, or in the limit of large aspect angles, the scattered spectra is dominated by the ion term, $\left| \frac{\sigma_e}{\epsilon} \right|^2 \langle \left| n_{th,i} \right|^2 \rangle$, and there is unanimous agreement between experiment, theory, and simulations (*Diaz et al.*, 2008; *Milla and Kudeki*, 2011; *Longley et al.*, 2018). *Milla and Kudeki* (2011) shows that ion Gordeyev integrals are independent of aspect angle due to the low gyrofrequency of ions. In the unmagnetized limit the collision relaxation time (inverse of collision rate) is

significantly larger than the correlation time of any particle, so at large aspect angles the primary dissipative effect on the ion acoustic mode is linear Landau damping by both electrons and ions.

At the other limit, when scattering at an aspect angle exactly perpendicular to *B*, both single-particle and PIC simulations produce spectra that are exactly identical to the Brownian collision theory. In this limit, there is no low frequency wave behavior, so $\sigma_e/\epsilon \to 0$, and the spectra is dominated by the electron thermal scattering term, $\langle |n_{th,e}|^2 \rangle$. The thermal scattering term is calculated by considering the Thomson scattering of an electromagnetic wave off a collection of electrons, which yields (*Kudeki and Milla,* 2011)

$$\langle |n_{th,e}(\omega, \vec{k})|^2 \rangle = N \int_{-\infty}^{\infty} d\tau \, e^{-i\omega t} \, \langle e^{i\vec{k}\cdot\Delta\vec{r}} \rangle \, . \tag{4.23}$$

The Gordeyev integral, J_s, in equation (4.17) is then constructed as the one-sided transform of the integrand in equation (4.23). Thus, the agreement between the Brownian theory and all simulations at 0° aspect angle shows that the Gordeyev integral is calculated correctly using a Brownian collision model for the electron ACF. At small aspect angles the single particle simulations of *Sulzer and Gonzalez* (1999) and *Milla and Kudeki* (2011) improve the accuracy of the electron ACF, but the Gordeyev integral is still calculated in the same manner. Therefore, the difficulty in calculating spectra at small aspect angles between 0.35° and 5° must be due to inaccuracies in calculating the electron conductivity σ_e, which determines the electron wave behavior.

The electron conductivity for ISR scattering is calculated first by using the fluctuation-dissipation theorem to obtain the real part (*Kudeki and Milla*, 2011),

$$\mathrm{Re}[\sigma_e(\omega)] = \frac{\epsilon_0 \omega^2}{k^2 h^2} \mathrm{Re}[J_e(\omega)], \tag{4.245}$$

where *h* is the electron Debye length. The imaginary part of the conductivity is calculated from the Kramers-Kronig relations, which relate the imaginary and real parts of the conductivity by a Hilbert transform:

$$\mathrm{Im}[\sigma_e(\omega)] = \frac{1}{\pi} P \int_{-\infty}^{\infty} \frac{\mathrm{Re}[\sigma_e(\omega')]}{\omega' - \omega} d\omega' . \tag{4.25}$$

Substituting equation (4.24) into equation (4.25), and recognizing that the Gordeyev integral also obeys the Kramers-Kronig relations (*Kudeki and Milla*, 2011), we obtain

$$\mathrm{Im}[\sigma_e(\omega)] = \frac{\epsilon_0}{k^2 h^2} (\omega^2 \mathrm{Im}[J_e(\omega)] + \omega). \tag{4.26}$$

The Landau damping of the system is introduced by the poles of the Hilbert transform in equation (4.25), which evaluates the same complex residue as using the Plemelj theorem in the standard calculation of Landau damping in kinetic theory (*Nicholson*, 1983).

Equations (4.24) and (4.26) use both the fluctuation-dissipation theorem and the Kramers-Kronig relations to calculate the electron conductivity. Implicit in those theorems is an assumption that the system is stable and has a linear response to an electric field. The assumption of a linear response means Ohm's law can be written in the time domain as (*Jackson*, 1999)

$$J_e(t) = \int_0^t d\tau\, \sigma_e(t-\tau)E(\tau)\,, \tag{4.27}$$

with stability meaning $\sigma_e(\omega)$ is analytic in the complex lower half plane. (The sign choice in the Fourier transform in equation (4.17) identifies the lower half plane as the analytic region.) The long correlation times of electron ACFs at small aspect angles leads to a situation where (i) the collision relaxation time is on the same order of magnitude as the electron correlation time, and (ii) the bounce period of electrons near the Landau resonance is on the same order of magnitude as the correlation time. The statement of (i) is equivalent to the simple explanation provided by *Sulzer and Gonzalez* (1999) for the aspect angle dependence of Coulomb collisions. As the aspect angle decreases, electrons have to move farther along the magnetic field line in order to neutralize the ion acoustic mode, and therefore have a higher chance of collisions affecting their motion. This effect is well modeled by the Brownian theory and single particle simulations, which show collisions increase the ACF correlation times and narrow the spectra compared to collisionless theory.

The second statement means nonlinear Landau damping becomes important in modeling the ion acoustic wave. Nonlinear Landau damping occurs due to electrons moving with velocities near the wave's phase speed, which are trapped inside of the wave's electric potential well. Initially, electrons are accelerated or decelerated towards the wave's phase speed, which provides a net damping of the wave for a distribution with a negative velocity derivative (e.g. a Maxwellian). The inertia of electrons causes them to overshoot the potential minimum, which leads to energy being put back into the wave.

This process is repeated several times, alternating between damping and growth until the distribution is flattened near the phase velocity of the wave (*Nicholson,* 1983). The bounce frequency for particles oscillating near the bottom of the potential well of a monochromatic wave is

$$\omega_b = \sqrt{\frac{eE_0 k}{m}}. \tag{4.28}$$

The linear stage of Landau damping only occurs on time scales shorter than half the bounce period,

$$t_{hb} \approx \frac{\pi}{\omega_b}, \tag{4.29}$$

at which point the trapped electrons overshoot the potential minimum and return energy to the wave.

A full kinetic treatment of a broad spectrum of waves is needed to make an accurate calculation of the nonlinear Landau damping time scale in equation (29). A rough estimation of the electric field value used in equations (28) and (29) can be done using the PIC simulations with the parameters in Table 1. An RMS electric field is found by taking the discrete Fourier transform with unitary normalization, which for a 2D simulation is

$$\tilde{E}(k_x, k_y, t) = \frac{1}{\sqrt{N_x N_y}} \sum_{n=0}^{N_x-1} \sum_{m=0}^{N_y-1} E(x_n, y_m, t)\, e^{-i\left(\frac{k_x x_n}{N_x} + \frac{k_y y_m}{N_y}\right)}. \tag{4.30}$$

For a square domain, the unitary normalization simplifies to $1/\sqrt{N_x N_y} = 1/N$, where N is the number of grid points. This normalization was validated by two additional simulations that use the parameters from Table 1, but change the original 512x512 grid with $\Delta x = 1\ cm$ to a 1024x1024 grid that first uses the same $\Delta x = 1\ cm$, and then uses $\Delta x = 0.5\ cm$. The ~1 cm grid over resolves the 34 cm wavelength of interest from a 440 MHz radar, and thus the simulations should calculate the same value of the wave electric field value. The unitary normalization in equation (30) is the only normalization that keeps the electric field $E(\vec{k}, t)$ independent of the grid. Thus equation (30) provides the electric field strength of a plane wave as a function of wavelength and time. An RMS value of $E(\vec{k}, t)$, obtained by averaging over time and aspect angle, then provides an estimate of the electric field strength at the radar's wavelength. This approach does not separate the wave fields of the ion-acoustic mode and the high frequency Langmuir and gyro modes, but the latter two modes are a factor of $k^2\lambda_D^2$ weaker than the ion-acoustic mode (*Akbari et al.,* 2017). This approach to calculating E_0 also neglects the fact that in nonlinear Landau damping the particle trapping is done by the total electric field, and not just by the monochromatic component calculated in equation (30).

Using the procedure outlined above, the PIC simulations with the parameters in Table 1 have an RMS wave electric field of $E_0 \approx 0.25\ V/m$ for waves propagating with $k = 18.4$, corresponding to a radar frequency of 440 MHz. Using these values in equation (29), including the artificial electron mass from the PIC simulations, the linear stage of Landau damping lasts for $t_{hb} = 19\ \mu s$. Figure 9 shows the electron

autocorrelation functions produced from single particle simulations using the parameters in Table 1, including both electron-ion and electron-electron collisions. The correlation time at 5° is 15 μs, which is less than t_{hb}, so the nonlinear stage of Landau damping should not be reached. However, the correlation times at aspect angles of 4° and lower are longer than t_{hb}, so the ion acoustic mode reaches the nonlinear stages of Landau damping at these aspect angles. It is important to note that the ACF's calculated in Figure 9 use the parameters from Table 1, which includes the artificial electron mass of $m_e = m_{O+}/1024$. The gyroperiod using this artificial mass is adjusted to scale with simulation mass as $\omega_{ce}^{-1} \propto \sqrt{m_e}$, which also preserves the lower-hybrid frequency. The correlation time of any particle over the Bragg scattering wavelength, λ_B, without considering collisions is

$$\tau_{corr} = \frac{\lambda_B}{v_{th} \sin \alpha}, \tag{4.31}$$

where α is the aspect angle. This equation for correlation time will change if collisions are added, but the primary scaling will still be $\tau_{corr} \propto v_{th}^{-1}$. Thus, the correlation time, gyroperiod, and nonlinear Landau damping timescales in the PIC code all scale with the artificial electron mass as $\tau \propto \sqrt{m_e}$. Equation (31) also shows that the correlation time scales linearly with the radar's wavelength. Thus the 3 m Bragg wavelength at Jicamarca yields correlation times nearly an order of magnitude longer than the 0.34 cm Bragg wavelength at Millstone Hill, and therefore collisional and nonlinear Landau damping time scales are more easily reached at Jicamarca.

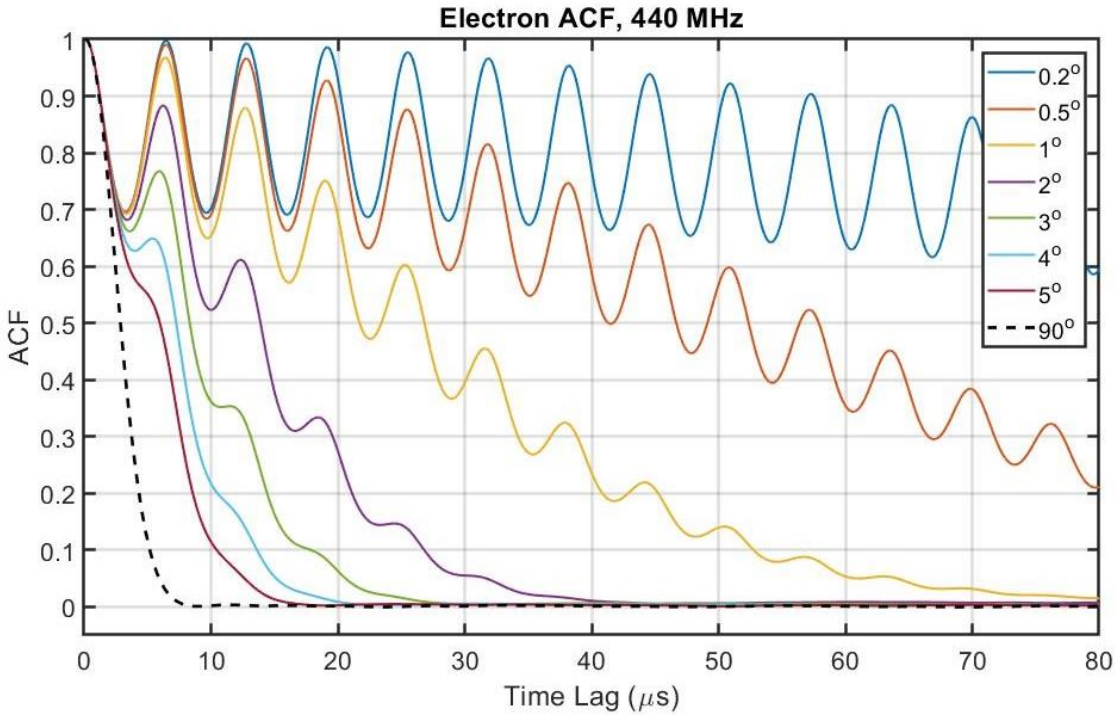

Figure 4.9 The electron autocorrelation functions for single particle simulations with both electron-ion and electron-electron collisions, calculated using the parameters in Table 4.1 (including the artificial electron mass). The correlation time is defined as the time it takes for the ACF to approach 0. With these parameters the ion acoustic mode reaches the non-linear stages of Landau damping after a time of $t_{hb} = 19\ \mu s$, which is shorter than the correlation times at aspect angles of 4° and smaller.

We suggest that the difference in small aspect angle spectra between the PIC simulations and the single particle simulations of *Milla and Kudeki* (2011) is due to nonlinear Landau damping violating the assumptions of the fluctuation-dissipation framework. The nonlinear stage of Landau damping involves wave growth, which places a pole in the lower half plane of $\sigma_e(\omega)$ and violates the assumptions of stability and linearity inherent in the Kramers-Kronig relations. Titchmarsh's theorem states that the Kramers-Kronig relations, the analyticity of $\sigma_e(\omega)$ in the lower half plane, and the causality of $\sigma_e(t)$ are all equivalent statements. Since causality cannot be violated in a

physical system, the only way to allow wave growth in the system is if the linear approach in equation (4.27) breaks down (*Baranov et al.,* 2015; *Markel* 2018). In contrast, the PIC simulations are fully kinetic and capture the nonlinear stages of Landau damping. At small aspect angles the long correlation times of electrons means electrons are trapped near the Landau resonance longer, which allows for electron-electron collisions to damp the wave (*Brambilla,* 1995).

The nonlinear stage of Landau damping also explains the different spectra from PIC simulations with only electron-ion collisions versus only electron-electron collisions. As the distribution flattens near the phase speed the first and second order velocity derivatives of the distribution in the Fokker-Planck collision operator (equations 4.1-4.4) change significantly, which provides the increased damping from electron-electron collisions. However, the mass difference in electron-ion collisions allows the Rosenbluth potentials to be simplified, and the Fokker-Planck collision operator becomes (*Brambilla,* 1995):

$$\frac{\partial f_e}{\partial t}_{e-i} = -\left(\frac{n_i e^4 \Lambda}{2\pi\epsilon_0^2 m_e^2}\right)\frac{f_e}{v^3}. \tag{4.32}$$

The electron-ion collision operator in equation (4.32) maintains the strong velocity dependence of Coulomb collisions, but the linearity in the electron distribution means the flattening of the distribution from nonlinear Landau damping has a smaller effect compared to electron-electron collisions for the same electron correlation time. At aspect angles less than 2° the correlation time is much longer than the nonlinear Landau damping time scale, which explains the PIC spectra with only electron-ion collisions

being significantly narrower than Brownian theory or single particle simulations at those aspect angles.

Modifying ISR theory to account for nonlinear Landau damping can be accomplished in two ways. First, the response function in equation (4.27) can be modified to include a nonlinear term, which will modify the derivation of the fluctuation-dissipation theorem and the Kramers-Kronig relations. This approach has the advantage of including velocity dependent collisions through single particle simulations of the electron ACF, and also opens the possibility of addressing nonequilibrium $T_e \neq T_i$ ISR spectra. The other way of modifying ISR theory is to use the dressed particle approach of solving the coupled Boltzmann equations (*Froula et al.,* 2011) to account for nonlinear Landau damping. Quasilinear diffusion theory solves for density perturbations on the assumption that the 0^{th} order distribution is time dependent, which allows for the flattening near the Landau resonance. Using the Boltzmann equation to solve for ISR spectra has the advantage of including all of the relevant kinetic physics, but the inclusion of a magnetic field and velocity dependent collisions can make the problem intractable.

4.5.3 Summary

Electron-electron collisions were implemented into a fully kinetic PIC code for use in modeling collisional, magnetized ISR spectra. The relaxation of an anisotropic Maxwellian distribution validated the use of simplified, analytical expressions for the Rosenbluth potentials. PIC simulations of ISR spectra show the effects of electron-electron collisions are important at magnetic aspect angles up to 5° away from perpendicular, whereas the electron-ion collisions are important at aspect angles up to 3°.

Single particle simulations using the method from *Milla and Kudeki* [2011] predict collision effects will become unimportant at aspect angles larger than 3°. Currently radars do not account for the narrowing of spectra at aspect angles between 3° and 5°, leading to an underestimate of electron and ion temperatures. The next chapter uses the Millstone Hill radar to measure small aspect angle spectra and compare the measurements to predicted spectra from the PIC code, single particle simulations, and Brownian theory.

The single-particle simulations with only electron-electron collisions are well described by a Brownian collision approximation at aspect angles larger than 0.35°. This is in stark contrast with the PIC simulations with only electron-electron collisions, which show spectra significantly narrower than the Brownian collision theory at aspect angles as large as 5°. The single particle and PIC simulation methods calculate the same drag and diffusion coefficients for use in the Langevin equation, the difference between the simulations is the PIC code solves for a self-consistent electric field at every time step and makes no assumptions about linear wave behavior. The narrowing of spectra in the PIC code due to electron-electron collisions suggests the calculation of the electron conductivity through the framework of *Kudeki and Milla* (2011) is not correct. We hypothesize that this is because the ion acoustic mode reaches the nonlinear stage of Landau damping, which involves wave growth that violates the assumption of stability inherent in the Kramers-Kronig relations and the fluctuation-dissipation theorem. The PIC simulation method is fully self-consistent and nonlinear, so future work on this subject will focus on using the PIC code to study and characterize the nonlinear Landau damping and its interplay with Coulomb collisions.

Chapter 5

Measurements of ISR Spectra Perpendicular to B

This chapter will be submitted with minor changes to J. Geophys. Res.: Space Physics as

Longley, William J., Philip J. Erickson, Meers M. Oppenheim, Juha Vierinen, Frank Lind, and Yakov S. Dimant (2019), Comparison of measured and simulated ISR spectra at small aspect angles.

Key points are:

- Millstone Hill ISR measured small aspect angle spectra in the F_1 region on four different days
- Collisions narrowed measured spectra at aspect angles less than 4.6° for high densities, and at angles less than 1.25° for low densities
- Comparison of measured spectra to simulated spectra show that current forward models underestimate the collisional narrowing

5.1 Small Aspect Angle ISR Measurements

Incoherent Scatter Radars (ISR) measure the plasma temperatures, density, and ion drift velocity in the ionosphere over a large range of altitudes, local times, seasons, and geomagnetic conditions. The decades of data produced by these radars are heavily utilized by researchers, including studies of short-term phenomena such as the onset of Equatorial Spread-F (*Hysell et al.*, 2015), and long-term solar cycle studies through assimilation into models such as IRI and MSIS (*Bilitza and Reinisch*, 2008; *Hedin*, 1991). While these data sets are generally robust, the electron and ion temperatures are

systematically underestimated when the radar line of sight is nearly perpendicular to the Earth's magnetic field. *Aponte et al*. (2001) gives a thorough review on the discovery and history of this "perpendicular to B" problem at the equatorially located Jicamarca Radio Observatory.

The ISR technique estimates temperatures by fitting a forward model of the heavily Landau damped ion-acoustic mode to the Doppler shift spectra measured by the radar, as discussed in Section 2.5.3. This fitting process is often done to the voltage autocorrelation function (ACF) of the radar, which is the Fourier transform of the Doppler spectra into the time domain. At magnetic aspect angles less than 5° from perpendicular to B, the ion-acoustic mode gains an additional source of damping as the magnetic field constrains electron motion in response to the wave's electric field. At these small aspect angles an electron has to move a longer distance along B in order to move one wavelength towards or away from the radar, and this increased transit time gives a higher probability that the electron will collide with another electron or an ion, thus changing its trajectory and contributing more damping to the acoustic mode. *Sulzer and Gonzalez* (1999) showed this physical explanation adds an additional damping source to the ion-acoustic mode at small aspect angles, which previous ISR theory neglected. This collisional narrowing of the spectra looks similar to the increased Landau damping which happens for smaller Te/Ti ratios, so fitting collisionless forward models to the collisionally narrowed spectra underestimates the plasma temperatures and can even calculate nonphysical $Te/Ti < 1$ ratios.

Sulzer and Gonzalez (1999) used single-particle simulations to develop a forward model of collisional ISR spectra, which was extended to aspect angles smaller than 0.1° by *Milla and Kudeki* (2011). This numerical model was validated against Jicamarca data in *Aponte et al.* (2001), showing electron Coulomb collisions were responsible for the nonphysical Te/Ti ratios measured by Jicamarca at small aspect angles. Recently, fully kinetic particle-in-cell (PIC) simulations from *Longley et al.* (2018, 2019), which are discussed in Chapters 3 and 4, showed that previously neglected kinetic effects from electron-electron collisions further narrow the small aspect angle spectra compared to the single particle simulations or the collisional theories developed in *Woodman* (2004) and *Kudeki and Milla* (2011). In this chapter, we use the 440 MHz Millstone Hill ISR to measure small aspect angle spectra and compare the spectra to PIC simulations in Chapter 4 from *Longley et al.* (2019), single-particle simulations from *Milla and Kudeki* (2011) and *Sulzer and Gonzalez* (1999), and to collisional theory from *Kudeki and Milla* (2011).

It is useful to summarize the experiments that *Aponte et al.* (2001) analyzed with the 50 MHz Jicamarca radar to validate the single-particle model. The first experiment occurred an hour after sunset and looked at aspect angles between 2° and 2.25° and altitudes of 330 km to 550 km. Fitting the measured ACFs from this experiment to collisionless ISR theory found nonphysical $Te/Ti < 1$ ratios at all altitudes, and refitting the ACFs to the collisional single-particle simulations of *Sulzer and Gonzalez* (1999) produced $Te/Ti \approx 1$ as expected at night. The same aspect angles were probed during the afternoon at altitudes of 200 to 550 km, showing that the Te/Ti ratio from collisionless

theory was significantly less than the ratio obtained by single-particle simulations. The next experiment analyzed aspect angles between 3° and 3.5° from 330 to 550 km at night. At this pointing direction the same results were found: Te/Ti was less than 1 when fit to collisionless theory, and fitting to single-particle simulations found Te/Ti ≈ 1 as expected. The last experiment analyzed by *Aponte et al.* (2001) was a daytime measurement of aspect angles between 4.5° and 5° at altitudes of 200 to 500 km. For these aspect angles the difference in Te/Ti between collisionless theory and single-particle simulations was minimal. In summary, *Aponte et al.* (2001) showed that fitting data to the collisional single-particle simulations of *Sulzer and Gonzalez* (1999) led to more accurate, and more physical Te/Ti ratios at nominal aspect angles of 2° and 3° but did not observe a significant difference between the two forward models at aspect angles of 4.5° or larger.

5.1.1 Millstone Hill ISR

The Millstone Hill Observatory in Westford, Massachusetts has a large UHF radar system used for Thomson or incoherent scatter since 1960. The Millstone Hill system is composed of a megawatt class UHF transmitter at 440 MHz and two Incoherent Scatter Radar (ISR) class antennas: the 68-meter zenith pointing antenna, and the fully steerable 46-meter MISA antenna. The MISA antenna is frequently used to make azimuth scans at low elevation angles that cover a large portion of North America. These scans are valuable due to their full view of the mid-latitude and sub-auroral ionosphere, containing such phenomena as storm enhanced density plumes and sub-auroral polarization stream fast velocity flows. Of particular interest for remote sensing, radar scans have good spatial overlap with a large number of GPS receivers concentrated in the U.S. and

Canada, which allows multi-point observations of mid-latitude phenomena such as SAPS, TIDs, or transient impacts such as those produced by solar eclipses (*Zhang et al.*, 2017).

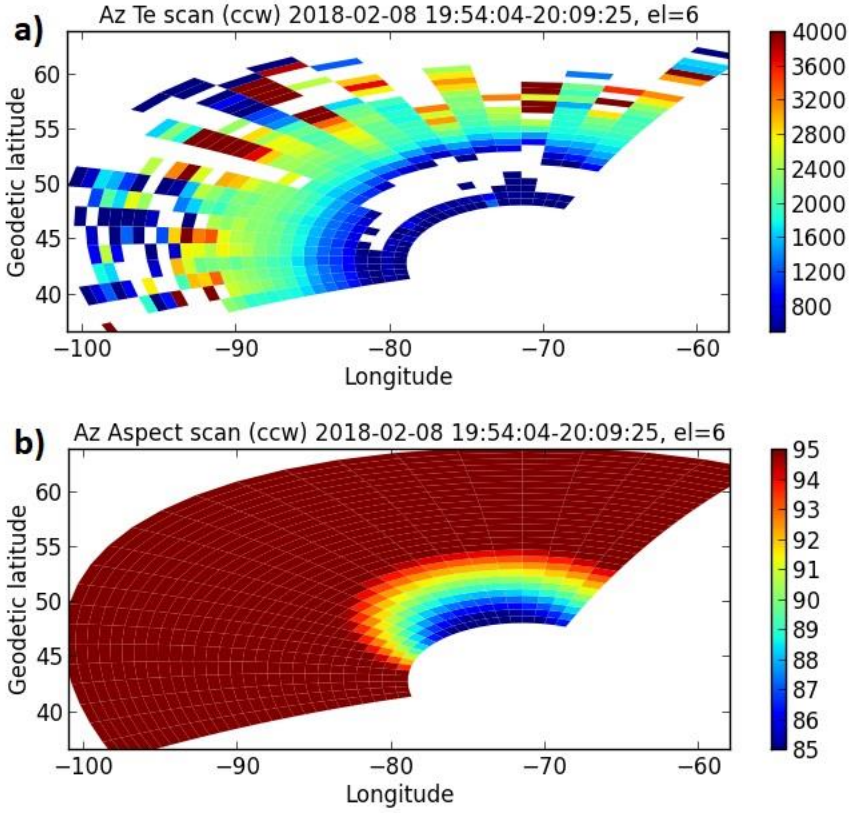

Figure 5.1 The steerable MISA antenna at Millstone Hill is frequently used to make azimuth scans across North America. In plot (a) the electron temperature from an azimuth scan at a 6° elevation angle is shown. The power returned to the radar decreases as the distance from the radar increases (located at -71 longitude, 43 latitude), which results in the data dropouts farthest from the radar. However, the data dropouts near the radar are due to the inversion routine failing to converge on a physical temperature solution. Plot (b) shows the data dropouts near the radar are precisely where the radar's line of sight is close to perpendicular to the magnetic field (90° in this figure) (*Erickson*, 2018).

At elevation angles less than 15° the MISA's line of sight can come within 5° of perpendicular to the Earth's magnetic field. Figure 5.1 shows how such small aspect angles can cause errors in temperature estimates. These errors are due to current ISR theory incorrectly accounting for the kinetic effects of electron-ion and electron-electron Coulomb collisions, which significantly change the shape of the spectra at small aspect angles by providing an additional source of damping to the measured ion-acoustic wave (*Milla and Kudeki,* 2011; *Longley et al.*, 2019).

5.1.2 Aspect Angle Geometry

Millstone Hill is located at a geomagnetic latitude of 51.5° as calculated by IGRF for the 2019 epoch, which allows the radar to look perpendicular to B in the F_1 region for a select combination of azimuth and elevation angles. Figure 5.2 shows the magnetic aspect angle as a function of elevation and range when the MISA antenna looks at -12° azimuth, which is direction of magnetic north. Similarly, Figure 5.3 shows how the aspect angle varies for an azimuth sweep with a 6° elevation angle. Figures 5.2 and 5.3 show that 202 km is the maximum altitude the radar can observe perpendicular to B, which corresponds to -12° azimuth and the lowest possible elevation angle of 4.4°. For a wide range of elevation angles at -12° azimuth, the MISA antenna is able to look at aspect angles of 5° and less in the F_2 region where the composition is nearly all O^+ ions.

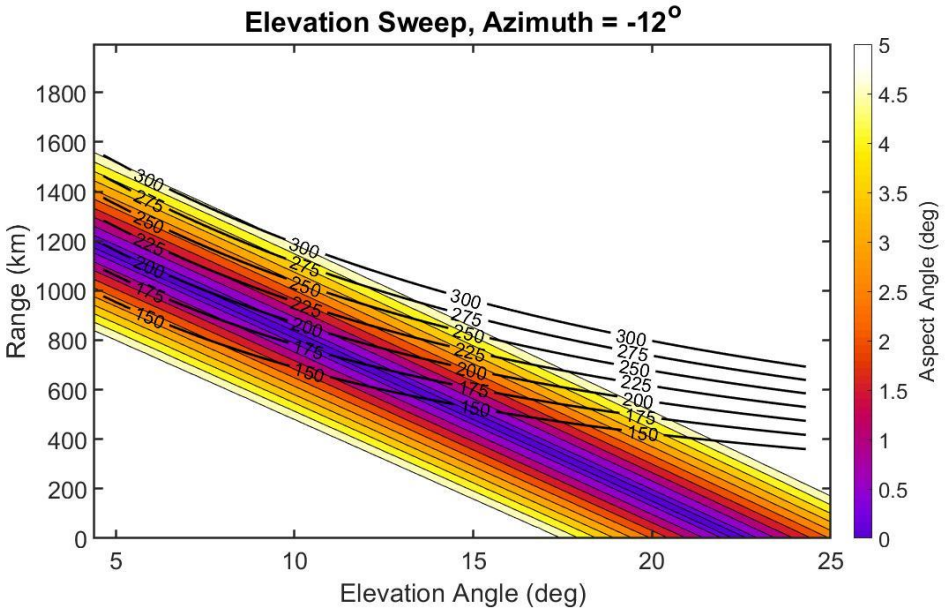

Figure 5.2 Magnetic aspect angle and altitude contours for Millstone Hill Observatory at different elevation angles with a -12° azimuth angle (magnetic north). At this azimuth angle the perpendicular to *B* direction is at an altitude of 200 km for elevation angles of 4° to 8°.

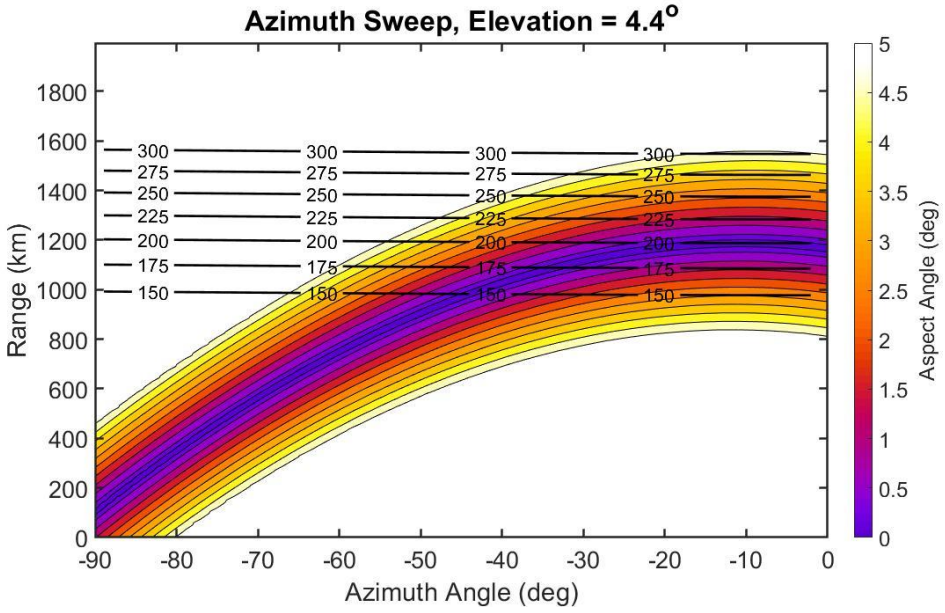

Figure 5.3 Magnetic aspect angle and altitude contours for Millstone Hill Observatory for an azimuth sweep at a 4.4° elevation angle. The perpendicular to *B* region is at altitudes of 200 km or less, but aspect angles within 5° of perpendicular are present in the F_2-region for a wide range of azimuth angles.

5.1.3 Pulse Coding

With the MISA antenna pointed at magnetic north, Figure 5.3 shows that a wide range of aspect angles can be placed in the O^+ dominated F_2 region at altitudes above 220 km. However, the range to these aspect angles of interest can be upwards of 1400 km from the radar, so a coded long pulse is needed to maintain high range resolution at the aspect angles of interest while preserving the high SNR (large energy on target) of a long pulse envelope. Two different pseudorandom pulse codes with 2 ms length were implemented to obtain high range and aspect angle resolution. The November 2013 experiment cycled between 32 different 100-baud pseudorandom codes, where the 20 μs baud length provided 3 km range resolution. To reduce the noise the ACFs were averaged over 5 consecutive range gates, giving an effective range resolution of 15 km. To improve the SNR while maintaining high range resolution, the experiments in February and April 2019 cycled between 50 different 50-baud pseudorandom codes, where the baud length of 40 μs gave a range resolution of 6 km. Due to the lower F-region density during those experiments the ACFs were averaged across 3 range gates to improve the SNR, giving an effective range resolution of 18 km in those experiments. Figure 5.4 shows an example of a 50-baud pseudorandom code and its matched filter response.

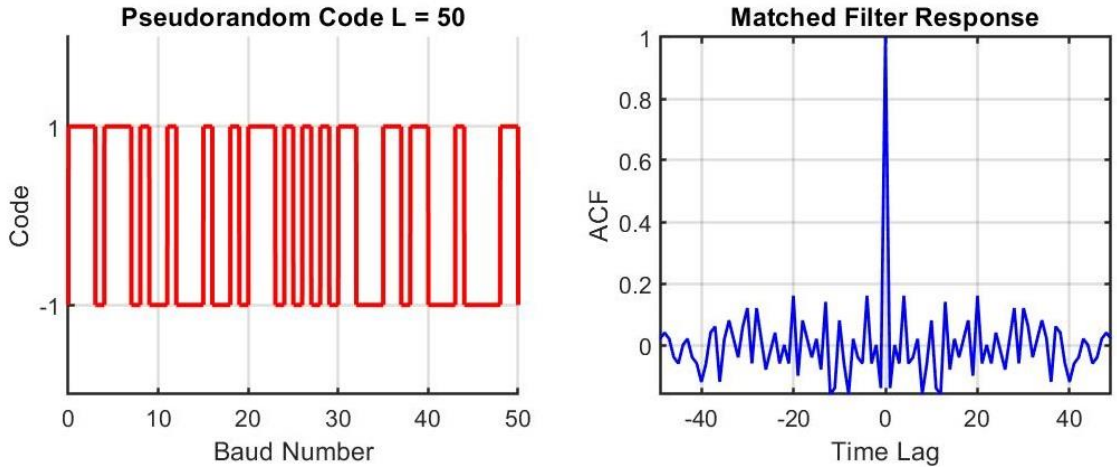

Figure 5.4 Plot of a 50-baud pseudorandom pulse code (a) and the matched filter response for the same code (b).

5.1.4 Experimental Setup

Four different experiments were performed with the Millstone Hill MISA antenna. The first experiment occurred on November 8th, 2013 with the antenna pointed at -12° azimuth and 4.4° elevation. A 100-baud pseudorandom code provided 15 km range resolution, and the ACFs were integrated from 15:20 to 16:43 local time. The second experiment occurred on April 20th, 2018 and also pointed in the -12° azimuth and 4.4° elevation direction. This experiment used a standard 480 μs uncoded pulse with 71.95 km range resolution and collected data from 16:20 to 18:30 local time at a 2-minute cadence. This pulse pattern is a standard mode at Millstone Hill and is used to generate F-region temperature and density plots at fixed range and time intervals. The mode's good SNR provides straightforward real-time processing and publication on the Madrigal database. For the purposes of this study, this mode allows for an analysis of collisional effects on the standard modes used by Millstone Hill.

On February 22nd, 2019 three sets of data were collected between 16:00 and 17:00 local time at different pointing positions. A 50-baud code provided 18 km range resolution, and the ACFs were integrated for approximately 15 minutes at each position. The first position pointed at -20° azimuth and 10° elevation to measure ACFs at aspect angles less than 3.5°, with the upper bound of this angle set by low SNR at this elevation position. The second position was at -55° azimuth and 10° elevation, measuring aspect angles in the F_1 region of 3-8°. The last position of the day was at -20° azimuth and 6° elevation but had poor SNR above 220 km (1° aspect angle) and therefore it is not used in this analysis.

The last experiment occurred on April 4, 2019 between 15:30 and 17:40 local daylight savings time. The same 50 baud pseudorandom code with 18 km range resolution from the February 2019 experiment was used to measure spectra at -12° azimuth with varying elevation angles. First, aspect angles between 0-2° were measured at an 8° elevation angle with 17 minutes of integration. The next two elevation angles integrated for over 30 minutes and were at 15° and 12° elevation, which probed aspect angles between 3-8° and 2-6° respectively. The last position of the day integrated over 10 minutes at a 45° elevation angle to provide a control set of spectra at large aspect angles. Table 5.1 summarizes all of the experiments at Millstone Hill.

Table 5.1 Summary of the different experiments at Millstone Hill. For each listed date and pointing direction, the ACFs are integrated over the listed local times to reduce noise.

Date	Range Resolution	(Azimuth, Elevation)	Integration Time
Nov. 8, 2013	15 km	(-12°, 4.4°)	15:20 to 16:43
Apr. 20, 2018	72 km	(-12°, 4.4°)	16:20 to 18:30
Feb. 22, 2019	18 km	(-20°, 10°)	16:02 to 16:18
		(-55°, 10°)	16:22 to 16:37
		(-20°, 6°)	16:38 to 16:55
Apr. 4, 2019	18 km	(-12°, 8°)	15:36 to 15:53
		(-12°, 15°)	15:55 to 16:32
		(-12°, 12°)	16:44 to 17:15
		(-12°, 45°)	17:29 to 17:39

5.2 ISR Temperature Fittings

5.2.1 Forward Models

ISR measures electron and ion temperatures through an inversion process where a forward model is fit to the data through a nonlinear least-squares technique. The ACFs measured by Millstone Hill are compared in this chapter to three forward models: Brownian collisional theory, Single-particle simulations, and PIC simulations. The Brownian theory and single-particle simulations both use the linear framework in *Kudeki and Milla* (2011) to calculate the ISR spectra. This framework uses the fluctuation-dissipation theory to relate the positional autocorrelation functions (ACF), $\langle e^{i\vec{k}\cdot\Delta\vec{r}}\rangle$, to the ISR spectra as (*Kudeki and Milla*, 2011)

$$\langle|n_e(\omega,k)|^2\rangle = \left|\frac{i\omega\epsilon_0+\sigma_i}{i\omega\epsilon_0+\sigma_e+\sigma_i}\right|^2\langle|n_{te}|^2\rangle + \left|\frac{\sigma_e}{i\omega\epsilon_0+\sigma_e+\sigma_i}\right|^2\langle|n_{ti}|^2\rangle. \qquad (5.1)$$

The conductivities, σ_s, and thermal scattering terms, $\langle|n_{ts}|^2\rangle$ are

$$\sigma_s(\omega,\vec{k}) = \frac{i\omega\epsilon_0}{k^2 h_d^2}(1 - i\omega J_s), \tag{5.2}$$

$$\langle\left|n_{ts}(\omega,\vec{k})\right|^2\rangle = 2N\mathrm{Re}[J_s]. \tag{5.3}$$

The Gordeyev integral, J_s, is simply the one-sided Fourier transform of the ACF (*Milla and Kudeki*, 2011):

$$J_s(\omega,\vec{k}) = \int_0^\infty d\tau e^{i\omega\tau}\langle e^{i\vec{k}\cdot\Delta\vec{r}}\rangle. \tag{5.4}$$

Equations (5.1) – (5.4) define the ISR spectra once the ACF of each species is known. For a magnetized plasma, with collisions approximated as a Brownian motion process, the ACF is (*Woodman*, 1967; see also *Kudeki and Milla*, 2011)

$$\langle e^{i\vec{k}\cdot\Delta\vec{r}}\rangle = \exp\left[-k_\parallel^2\frac{c_s^2}{\nu_{cs}^2}(\nu_{cs}\tau - 1 + e^{\nu_{cs}\tau})\right]$$
$$\times\exp\left[-k_\perp^2\frac{c_s^2}{\nu_{cs}^2+\Omega_s^2}(\cos(2\gamma) + \nu_{cs}\tau - e^{\nu_{cs}\tau}\cos(\Omega_s\tau - 2\gamma))\right]. \tag{5.5}$$

The first term describes how a given particle moves away from its initial position along B, over a time lag τ, while colliding at a constant rate ν_{cs}. The second term describes both the gyration around a magnetic field line and the collisional diffusion perpendicular to B. The parameter in the cosine functions is $\gamma \equiv \arctan(\nu_{cs}/\Omega_s)$. This Brownian theory is currently the most accurate analytic solution for collisional, magnetized ISR spectra, but the single-particle simulations in *Milla and Kudeki* (2011) and the PIC simulations in

Longley et al. (2018; 2019) all show that the Brownian theory is not an accurate forward model for temperature fittings at small aspect angles.

To improve on the Brownian theory, *Milla and Kudeki* (2011) extended the single-particle simulation method first presented in *Sulzer and Gonzalez* (1999). This forward model uses the same linear framework in equation (5.1) – (5.4) but calculates the ACFs numerically by simulating the motion of a particle subject to magnetic and collisional forces. The single-particle simulations use a Fokker-Planck collision operator for both electron-ion and electron-electron collisions, though only electron-ion collisions actually damp the ion-acoustic mode and narrow the spectra, and the electron-electron collisions serve to stabilize the simulation (*Longley et al.*, 2019). The last forward model this chapter will compare measured spectra to is the PIC simulations from *Longley et al.* (2018; 2019). PIC codes simulate the trajectory of ~10^9 individual particles and calculate the density on a grid at every time step to solve Poisson's equation for a self-consistent electric field. The density is then Fourier transformed to directly calculate the ISR spectra, $\langle |n_e(\omega, k)|^2 \rangle$, without needing the linear framework in equations (5.1) – (5.4). The PIC simulations use the same Fokker-Planck collision operators for electron-ion and electron-electron collisions as the single-particle simulations.

5.2.2 Inversion Methods

The Brownian theory has the advantage of being fast to compute, and therefore can be used for automatic fitting of measured data. Radars fundamentally measure the ACF of a voltage time series at the receiver terminals, which is a measure of the scattered

electric field that is directly related to the medium's electron density fluctuations, $\langle|n_e(t,k)|^2\rangle$. Subsequently, a Fourier transform of the voltage ACF is used to calculate the power spectra. Alternatively, using the Brownian theory in the time domain to fit the voltage ACF has the advantage of being able to weight each point in the time series according to how many measurements each point in the ACF has, and the results can be examined in either the time or frequency domain. There are many weighting schemes that can be employed (*Lehtinen and Huuskonen*, 1996), but we will use the framework where a voltage signal at discrete times $t = 0, \tau, 2\tau, \ldots, N\tau$ is weighted at each lag in the ACF as $W_t = \frac{1}{\sqrt{N}}, \frac{1}{\sqrt{N-1}}, \frac{1}{\sqrt{N-2}}, \ldots, 1$. The fitting is then accomplished using a Levenberg-Marquardt algorithm to search (Te, Ti) space while minimizing the cost function

$$\chi^2(T_e, T_i) = \sum_t \left(\langle\left|n_{Theory}(t,k)\right|^2\rangle - \langle|n_{Data}(t,k)|^2\rangle\right) \cdot W_t \,. \tag{5.6}$$

For each fitted ACF the error bars are then computed as the 95% confidence interval when assuming $\chi^2 = 1$.

The measured ACF depends on several plasma parameter values, not just on Te and Ti, but also on density and line of sight ion velocity. The density is proportional to the 0th lag of the ACF, which measures the total power of the system. To produce a density measurement this total power needs to be calibrated through the radar equation, and also corrected for temperature scaling as $1/(1 + T_e/T_i)$. Millstone Hill typically finds the calibration factor using either the plasma line frequency or the foF2 frequency from the UMass Lowell Digisonde. Since the total power is calibrated separately and

only effects the overall scaling of the ACF and spectra, it is not included in the fitting process. This is done by setting the first weight to $W_0 = 0$, and then normalizing the whole ACF by the value at the first time lag. The density is still needed in the Brownian theory to calculate the collision rates, which scale as $f_e \propto n_e$, so a 0th order density value taken from IRI is used as an approximation only for the collision rates. This does not introduce any significant errors when fitting ACFs at Millstone's wavelength since the Brownian theory becomes effectively collisionless at aspect angles larger than ~0.5° (*Longley et al.*, 2019). Similarly, the line of sight ion velocity is excluded from the fitting process since it only affects the mean Doppler shift of the spectra, which is typically much smaller than the width of the spectra. The ion velocity is excluded from the fitting process by calculating the theory with $v_{ion} = 0$, and fitting only the real part of the measured ACF. The magnetic field near Millstone Hill varies between 0.45 and 0.55 G depending on the altitude, latitude, and longitude. To simplify the fitting process a constant magnetic field of 0.5 G is used for all of the fits in this chapter. This primarily affects the ratio ν_{cs}/Ω_s, and thus collision rate, in the Brownian ACF from equation (5.5) since the electron motion remains tied to the field lines for the range of magnetic field values near Millstone.

Figures 5.5 to 5.7 show the measured spectra for the different experiments at Millstone Hill, and the spectra from the best fit ACFs calculated from Brownian theory. In the next section the temperatures and associated error bars for each fit are examined in detail. The data show a significant narrowing of the spectra at aspect angles below 1°, which indicates that the exactly perpendicular to B spectra is being measured within the

main lobe of the antenna. This is because the spectral width decreases from ~7 kHz for unmagnetized spectra to ~200 Hz for perpendicular spectra, while maintaining a roughly constant total power (*Milla and Kudeki*, 2011). Fitting spectra at these aspect angles therefore requires an accurate averaging of the forward model across the ~1.2° beam width, and also from the front to back of each range gate. This beam averaging is not included in the fittings shown below as the focus of this chapter is on aspect angles between about 2° to 6° where the spectra starts converging to collisionless theory. At aspect angles above 2° the shape of the spectra changes slowly with aspect angle, and the beam averaging is less important.

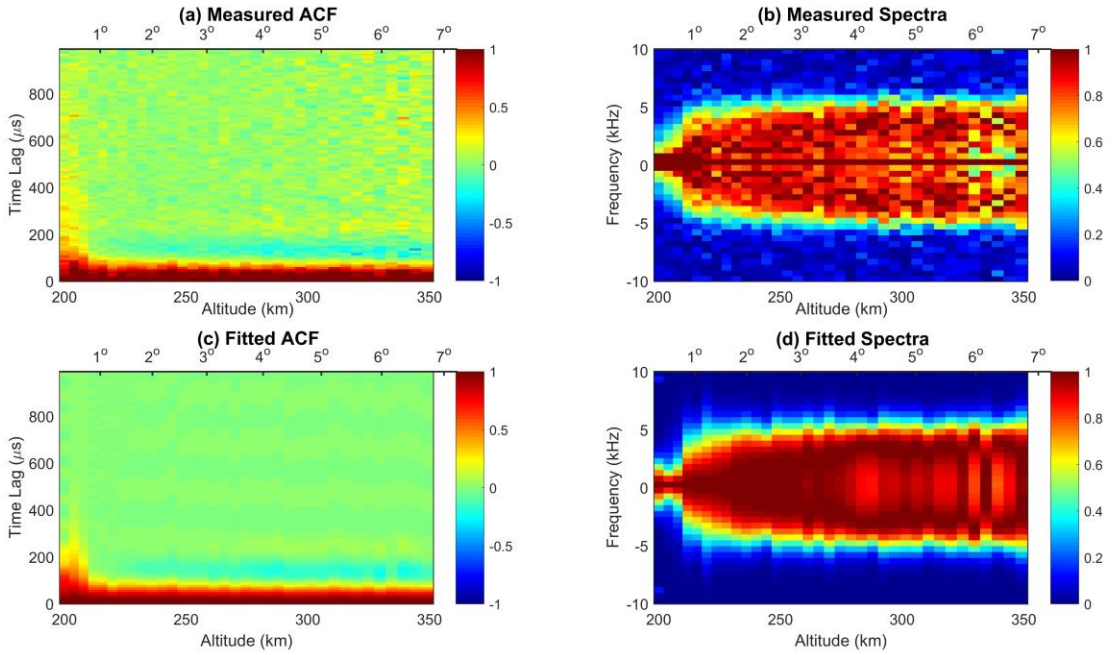

Figure 5.5 The normalized ACFs measured on November 8, 2013 are shown in plot (a). The ACFs are fit to the Brownian collisional model in plot (c). Plots (b) and (d) show the spectra corresponding to the data and fitted ACFs, respectively.

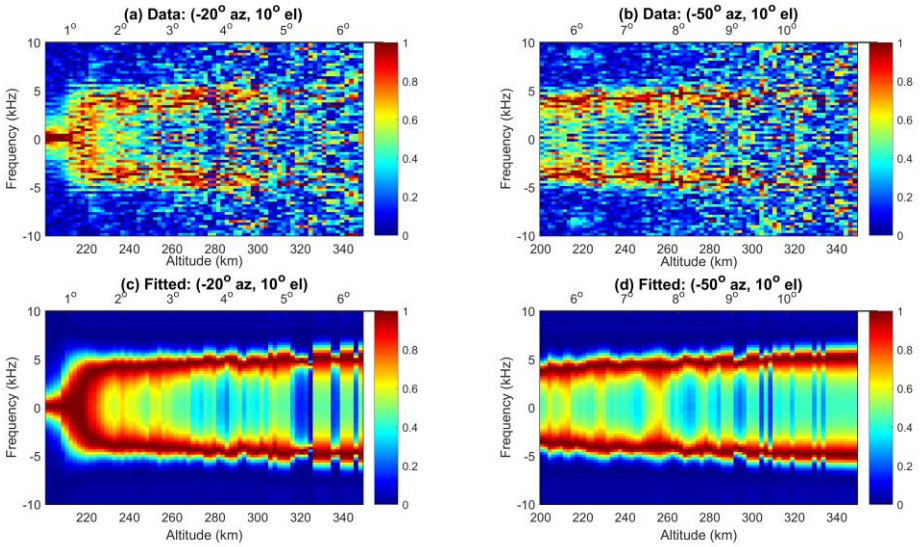

Figure 5.6 The spectra measured on February 22, 2019 are shown in plots (a) and (b). The ACFs are fit to the Brownian collisional model, and the spectra from the fits are shown in plots (c) and (d). For both pointing positions the SNR drops off dramatically at around 300 km and is not fit accurately.

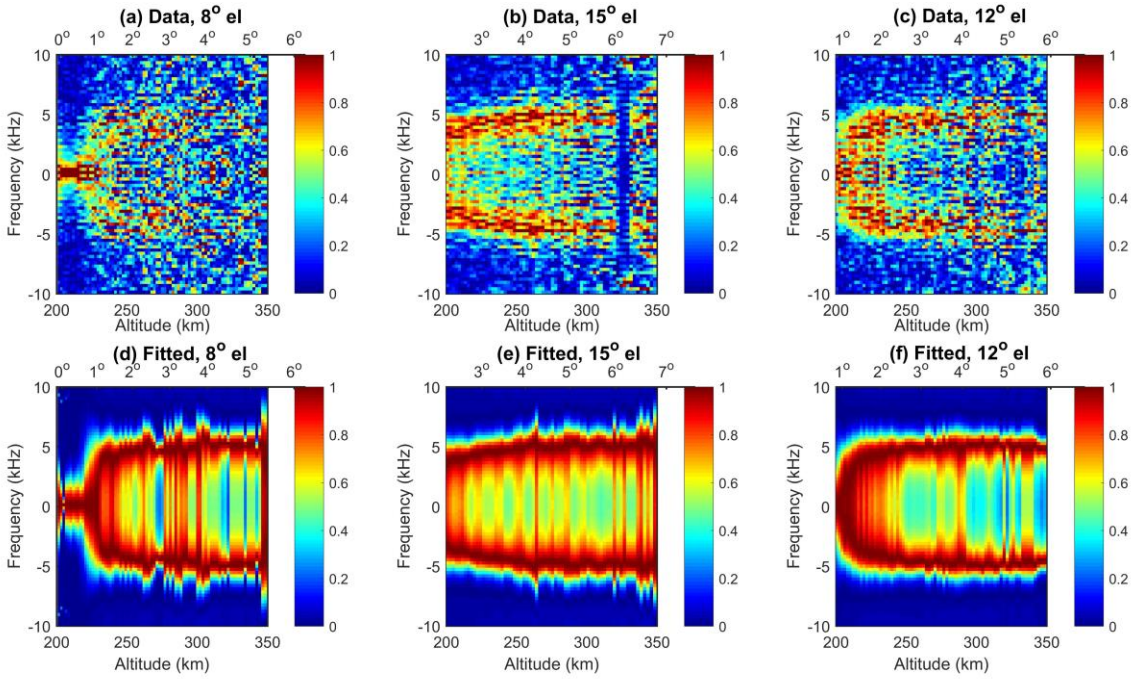

Figure 5.7 The spectra measured on April 4, 2019 are shown in plots (a), (b) and (c). The ACFs are fit to the Brownian collisional model, and the spectra from the fits are shown in plots (d), (e), and (f). For the first pointing position at 8° elevation the SNR drops off around 250 km in altitude, while the higher elevation angles are able to measure spectra out to 300 km.

5.3 Aspect Angles Where Collisions Matter

The experiment on April 20, 2018 measured spectra with a 71.95 km range resolution, which resolved aspect angle in approximately 1° increments. Figure 5.8 shows the plasma density obtained from Madrigal, which is obtained by fitting the spectra using the UMass Lowell Digisonde to calibrate total power. The density measurement is mostly influenced by the total spectral power, with a $1/(1 + T_e/T_i)$ temperature correction factor, and therefore is not as sensitive to the collisional effects at small aspect angles. This shows the regions where the radar is making measurements with a SNR > 0.1 and without any instabilities or clutter. Figure 5.8 also shows the Te/Ti ratio estimated by the standard Madrigal fitting routine, which uses collisionless ISR theory. The temperature ratio measurements show a large number of missing data points, which occur when the inversion routine fails to converge on a physically valid solution or returns error bars larger than 15%. Furthermore, at aspect angles of 3.6° and less the fitting routine converges to solutions of Te/Ti < 1 with small error bars, which is a nonphysical solution during the early afternoon when photoionization should preferentially heat electrons.

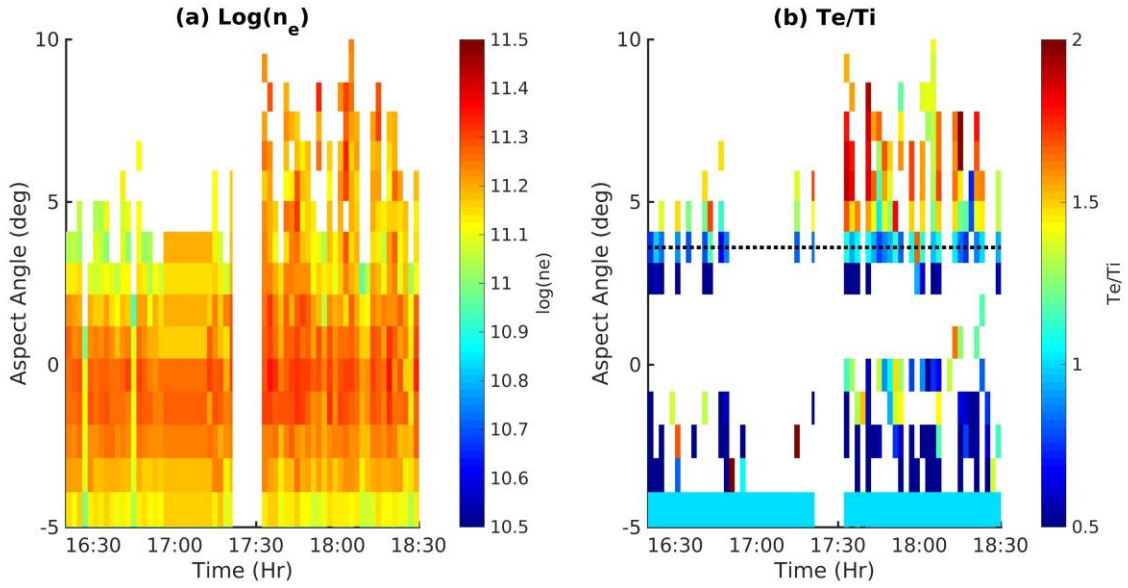

Figure 5.8 Density (left) and temperature ratio (right) measurements taken April 20, 2018 at Millstone Hill, plotted against magnetic aspect angle. Electron density measurements are less affected by spectral shape at small aspect angles. However, the Te/Ti ratio has data dropouts or nonphysical values at aspect angles as large as 3.6° (marked by horizontal dashed line), where collisions affect the inversion routine. The time axis is in UTC, which is 4 hours ahead of local time during the experiment.

The data shown in Figure 5.8 from the April 2018 experiment show non-physical Te/Ti fits at aspect angles as large as 3.6° when using a standard mode with 72 km range resolution. For this range resolution and pointing direction the aspect angle changes by approximately 1° from the front to the back of a range gate. To reduce any errors associated with this large of a spread in aspect angle at one range gate the experiments in February and April 2019 used a higher range resolution pulse code similar to the code first used in the November 2013 experiment. Figure 5.9 shows the measured and fitted temperature profiles from November 2013, with a 15 km range resolution providing ~0.2° aspect angle resolution. For aspect angles larger than ~1.5°, the fitted ion temperature follows the predicted temperature from IRI well, but the electron temperature

is significantly lower than the IRI prediction. The data show Te/Ti < 1 fits at aspect angles of 4.6° and less, showing that the Brownian theory underestimates the collisional effects at those aspect angles.

The fitted temperatures from the February 22, 2019 experiment with 18 km range resolution are plotted in Figure 5.10. For both positions only the data from 200 km to 300 km is shown to reduce complexity, as it restricts the analysis to the O^+ dominant region and altitudes with good SNR. Both the ion and electron temperatures are reasonably consistent with the IRI model predictions, especially compared to the fits in Figure 5.9 to the Nov. 2013 data. Plot (c) in Figure 5.10 shows physically valid Te/Ti ratios for data points that have error bars less than 25% and exit conditions that indicate convergence to a global minimum. A sharp increase in the temperature ratio from 1.5 to 3 occurs between 1-2° in aspect angle, which may indicate collisions affecting the spectra near 1°, but could also be due to the lack of beam averaging. The temperature profiles in Figure 5.11 show a similar trend occurred for the April 4, 2019 experiment. The fitted electron and ion temperatures follow the IRI model well at altitudes between 200 and 300 km and show therefore show physical and reasonable temperature ratios at aspect angles of 1.25° and above.

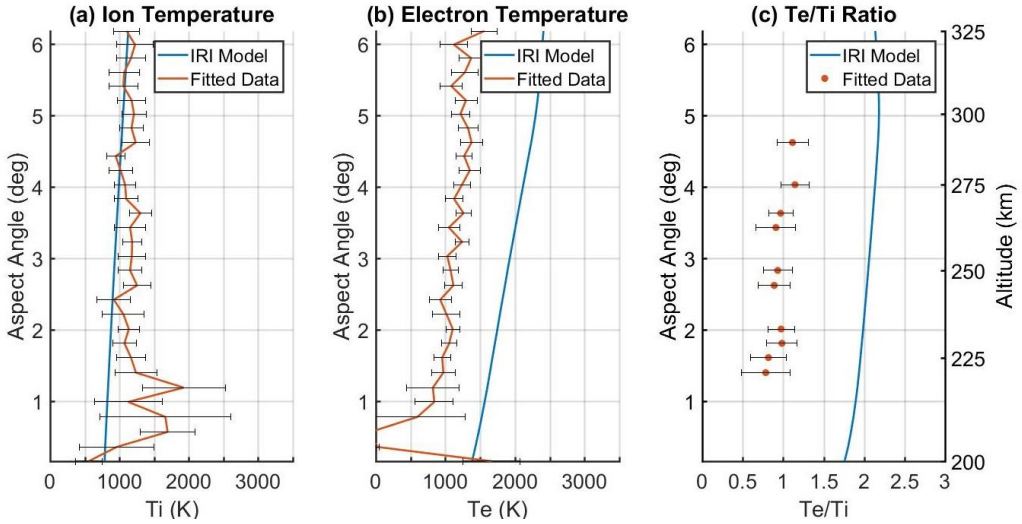

Figure 5.9 The fitted temperature (orange) to the ACFs measured on November 8, 2013. In plot (a) the ion temperatures generally follow the IRI model (blue), but in plot (b) the electron temperatures are much lower than IRI predicts. Plot (c) shows the Te/Ti ratio for data points that converged on a solution with errors less than 25%.

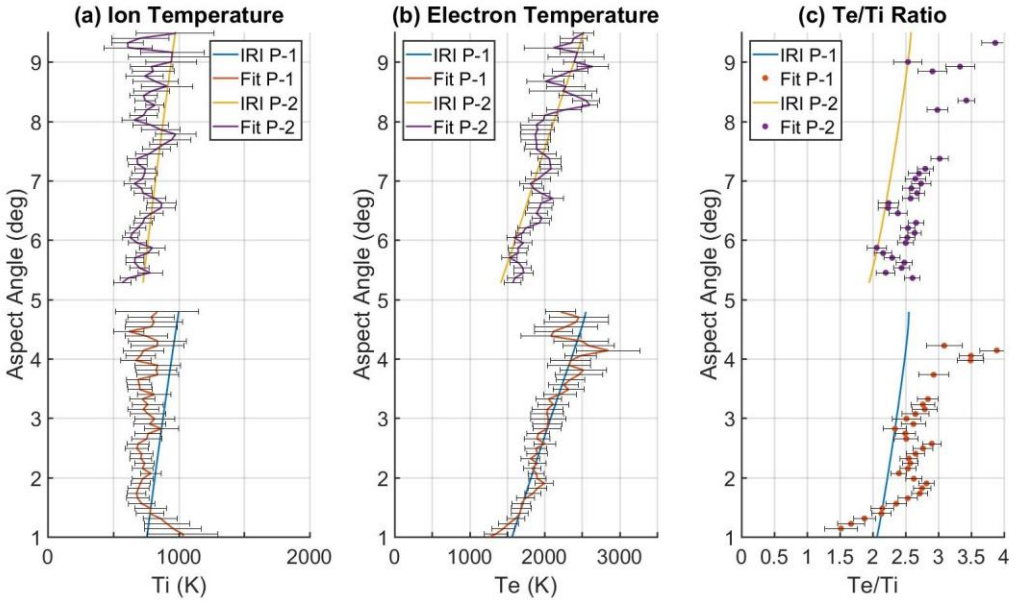

Figure 5.10 The fitted temperatures (orange and purple) compared to IRI predictions (blue and yellow) for ACFs measured on February 20, 2019. Both position 1 (-20° azimuth, orange and blue curves) and position 2 (-55° azimuth, purple and yellow curves) fit ion and electron temperatures near the IRI predictions. However, the good data points in plot (c) show temperature ratios larger than 1 at all plotted aspect angles, which is a physically valid solution. The data from each position are plotted from 200 km to 300 km, and the aspect angle increases monotonically with altitude.

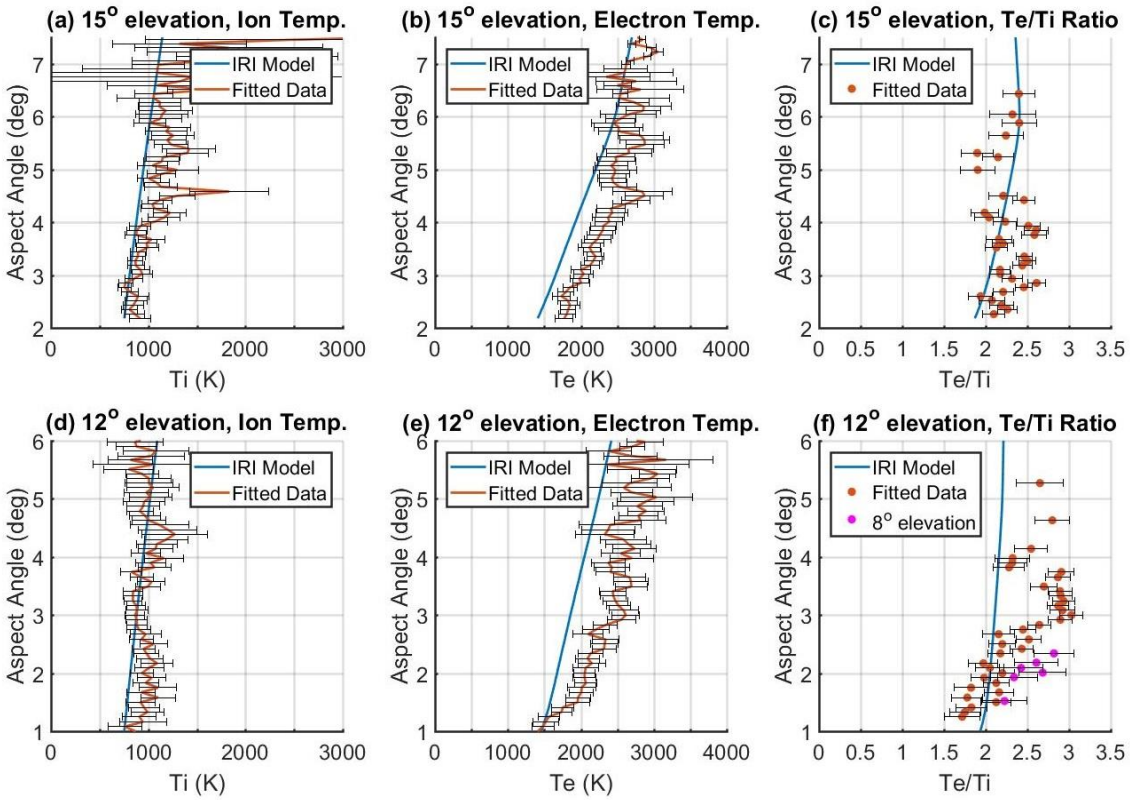

Figure 5.11 The fitted temperatures for ACFs measured on April 4th, 2019. The ion and electron temperatures (plots a, b, d, and e) all follow the general trend of IRI, and the temperature ratios for data points with good fits are physically valid at all aspect angles above 1°. In plot (f) the small number of points from the 8° elevation angle position with good fits are also shown in magenta.

The physical temperature ratios that follow IRI predictions well for both of the 2019 experiments are likely due to the overall lower collision rates. The UMass Lowell Digisondes show the 2013 experiment had a peak density at 275 km of 1.5×10^{12} m^{-3}, while the peak densities in the February and April 2019 experiments were both at 200 km and 3.8×10^{11} m^{-3} and 2.5×10^{11} m^{-3}, respectively. The average Coulomb collision rate varies as

$$\nu_e \propto \frac{n_e}{T^{3/2}}, \tag{5.7}$$

so the collision rate for November 2013 is 4 times higher than the collision rate in February 2019, and 6 times higher than the collision rate in April 2019. The *Sulzer and Gonzalez* (1999) explanation for Coulomb collisions narrowing ISR spectra is that as the aspect angle decreases, electrons have to move a longer distance along field lines to move one Bragg wavelength towards or away from the radar, which gives a higher chance of a collision occurring. This explanation more formally relates to the correlation time of an electron, which is how long the electron stays near its initial position. If this correlation time starts approaching the collisional timescale, $1/\nu_e$, then a collision will likely occur, which damps the ion-acoustic mode and causes the spectra to narrow.

The correlation time of an electron is

$$\tau = \frac{\lambda_B}{v_{th} \sin \alpha}, \tag{5.8}$$

where λ_B is the radar's Bragg scattering vector. The timescale argument from *Sulzer and Gonzalez* (1999) is then formalized: the spectra is narrower than collisionless theory if

$$\frac{\kappa}{\nu_e} \approx \tau = \frac{\lambda_B}{v_{th} \sin \alpha_c}, \tag{5.9}$$

where ν_e is an averaged collision rate, and κ is a scaling constant that accounts for the kinetic behavior of Coulomb collisions. Approximating the thermal speed as constant, equation (5.9) allows two densities to be compared to the critical aspect angle, α_c, where the spectra starts to narrow compared to collisionless theory:

$$\frac{\sin \alpha_{c1}}{n_{e1}} = \frac{\sin \alpha_{c2}}{n_{e2}} \tag{5.10}$$

Figure 5.9 shows for the November 2013 experiment that this critical angle is around 5°. Since the density, and thus collision rates, in February and April 2019 are respectively 4 and 6 times lower than in November 2013, equation (5.10) calculates the critical aspect angles as 1.25° for February 2019, and 0.8° for April 2019. Thus, at aspect angles larger than 1.25° and 0.8° collisions should not affect the spectra on those days. This is in agreement with Figures 5.10 and 5.11, which show physically valid Te/Ti ratios at these aspect angles, and a rapid decrease in Te/Ti at aspect angles below 1.5° in the February 2019 data in Figure 5.10, though the decrease could also be due to the lack of beam averaging.

The data from April 20, 2018 in Figure 5.8 show peak densities also around 3×10^{11} m^{-3}, and thus collisions should not affect the spectra at aspect angles larger than ~1° if the electron temperature is similar to November 2013. Therefore, the nonphysical temperature ratios in Figure 5.8 are likely the result of the poor 72 km range and 1° aspect angle resolution. Some of the fits in Figure 5.8 could likely be improved by averaging the forward model across the beam pattern, and fitting that beam averaged model to the measured spectra. The higher range resolution in the 2013 and 2019 experiments reduces the need for beam averaging the forward model in those fittings, but spectra at aspect angles less than about 1° measure the sharply peaked 0° aspect angle mode in the main lobe of the beam. Therefore, all temperature fits at aspect angles below 1° should not be trusted without beam averaging.

5.4 Analysis of Spectra

The spectra measured on November 11, 2013 show a distinct narrowing at aspect angles less than 5° compared to Brownian collisional theory from *Kudeki and Milla* (2011). The Brownian collisional model is the most accurate analytic theory and is useful for quickly inverting measured ACFs at Millstone Hill where aspect angles less than 5° are often not measured. The Jicamarca ISR only looks at aspect angles less than 5° due to its equatorial location and steering capabilities. As a result, Jicamarca uses the simulations from *Sulzer and Gonzalez* (1999), which was improved upon in *Milla and Kudeki* (2011), as the forward model for temperature fittings. In this section we compare the measured ACFs at Millstone Hill to the forward model from *Milla and Kudeki* (2011), and then compare the *Milla and Kudeki* (2011) forward model to the PIC simulations in *Longley et al.* (2018, 2019).

5.4.1 Comparison to Single Particle Simulations

We will first compare the measured ACFs to the single-particle simulations from *Kudeki and Milla* (2011), which are an extension of the *Sulzer and Gonzalez* (1999) model that is currently used for temperature fittings at Jicamarca (*Aponte et al.*, 2001). Figure 5.12 shows the measured ACFs from November 8, 2013 at aspect angles where the Brownian theory fits the data well (see plot (c) in Figure 5.9). The temperatures that best fit the data are listed in Table 5.2 and are used to run the single-particle simulations with a constant density of $n = 10^{12}$ m^{-3} for each range gate. The simulations are plotted

in Figure 5.12 and show that the single-particle ACFs look nearly identical to the Brownian theory.

To more quantitatively investigate the difference between the ACFs in Figure 5.12, the single-particles simulations are treated as data and then fit to the Brownian theory using the inversion process described in Section 5.3. The best fit temperatures to the single-particle ACFs are listed in Table 5.2 and have error bars of 1.5% or less on all of the fits. Ideally the single-particle simulations would be used to directly fit the data, but this is not feasible due to the computational time required to produce a single ACF. Thus, the fitting of the single-particle simulations to the Brownian theory (which provided the temperatures for the simulations) is a rough estimate of the improvement the single-particle simulations would have on fitting the data. The best metric for this improvement would be a scaling ratio for Te/Ti, similar to the ad hoc fix used at Jicamarca before the *Sulzer and Gonzalez* (1999) simulations. This scaling measure is listed in Table 5.2 and is calculated as

$$Scaling = \left(\frac{T_{e,Br}}{T_{i,Br}}\right) \cdot \left(\frac{T_{i,SP}}{T_{e,SP}}\right) \tag{5.11}$$

This scaling ratio has a significant drop off between 2.83° and 3.43° in aspect angle, showing that for this experiment the Brownian theory and single-particle simulations would produce nearly identical temperature estimates at aspect angles of 3.4° and higher. As shown in Section 5.3, this aspect angle of convergence between the two models will be dependent on the density and collision rate, but Figure 5.12 shows that the best fitting single-particle simulations at 3.43° and 3.63° still have a nonphysical Te/Ti < 1 ratio.

Table 5.2 The fitted temperatures (K) using the Brownian theory (labeled as Brwn Fit) for each aspect angle (α), from the November 8, 2013 experiment. The best fit temperatures are then used to run the single-particle simulations from *Milla and Kudeki* (2011). Those simulations are then fit with the Brownian theory (labeled as SP Fit) to show how the single-particle simulations will improve Te/Ti estimates at smaller aspect angles.

Altitude	226	230	234	246	251	264	268	277	290
α	1.61°	1.81°	2.01°	2.62°	2.83°	3.43°	3.63°	4.03°	4.62°
Brwn Fit, Ti	1167	1072	1136	1254	1154	1154	1302	1082	1235
Brwn Fit, Te	955	1056	1107	1115	1076	1050	1262	1239	1377
SP Fit, Ti	1254	1174	1170	1277	1178	1173	1318	1113	1248
SP Fit, Te	923	1079	1082	1081	1059	1062	1246	1240	1364
Scaling	1.11	1.07	1.05	1.05	1.04	1.01	1.02	1.03	1.02

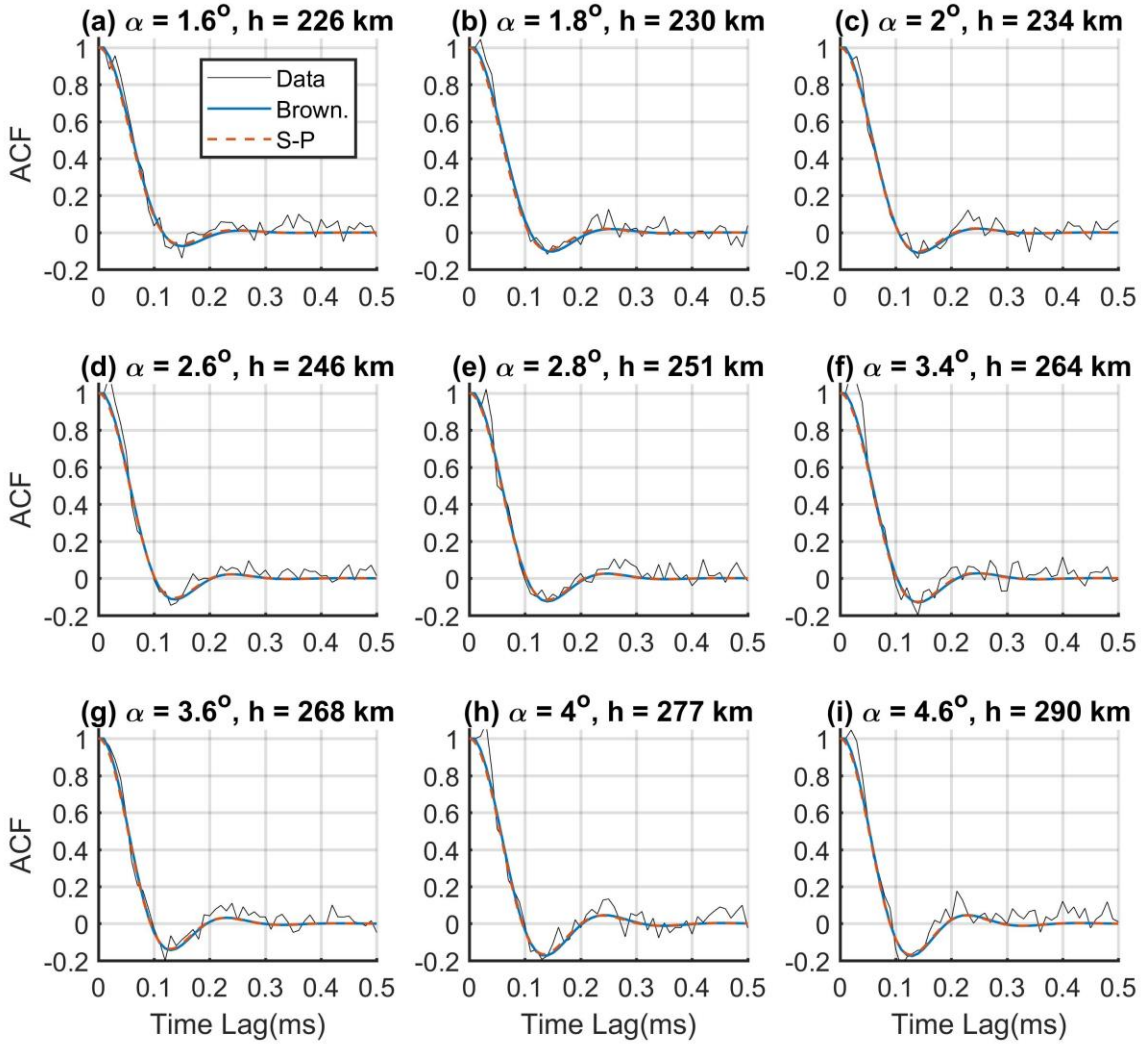

Figure 5.12 The observed ACFs (black) are compared to the Brownian theory fits (blue) and single-particle simulations (orange) that use Te and Ti from the Brownian fits. At aspect angles of 3.4° and larger the Brownian theory is identical to the single-particle simulations.

5.4.2 Comparison to PIC Simulations

The PIC simulations in Chapter 4 (*Longley et al.*, 2019) showed that nonlinear, kinetic effects from electron-electron collisions will cause a narrowing of the spectra at aspect angles as large as 5°. To compare this prediction to ISR measurements, a set of

PIC simulations is run for parameters similar to those found from the Brownian fits to the November 2013 data at 2.83° and 3.43°. The PIC code solves the electron and ion Bolzmann equations by discretizing the distribution function into macro-particles, which then evolve in time from the Lorentz force and the Fokker-Planck collision operator. Since the PIC code is solving the full nonlinear equations, the electron and ion distributions are coupled through the self-consistent electric field. This coupling tends to drive both distributions towards equilibrium, so a simulation with Te ≠ Ti will slowly evolve to one with Te = Ti. Properly simulating Te ≠ Ti in the PIC code requires an additional collision operator that acts to heat the electron distribution similar to photoionization, as well as including the ion-neutral collisions which keep the ion temperature lower than the electron temperature throughout the day. The Brownian theory and single-particle simulations can calculate Te ≠ Ti spectra by assuming the system is quasi-stationary and calculating the ACFs of each distribution separately (*Kudeki and Milla,* 2011). To avoid this difficulty, the PIC code is run in equilibrium with Te = Ti in this chapter.

The parameters used in the PIC simulation are shown in Table 5.3. The temperatures are chosen to be Te = Ti = 1150 K, which is the closest equilibrium temperature to the measured spectra at 2.83° and 3.43°. Those aspect angles correspond to altitudes above 250 km, so a 100% O^+ composition is appropriate. The grid is chosen such that the grid step $\Delta x = 0.5$ cm is significantly less than the Debye length of $\lambda_D = 1.1$ cm to avoid numerical heating (*Birdsall and Langdon,* 2004). Since the simulation needs to run for 20 ms to obtain 50 Hz resolution of the spectra, two artificial parameter

choices are made. First, the density is lowered to 5×10^{10} m^{-3} in order to increase the Debye length and avoid numerical heating. The collision operator is still calculated with a density of 10^{12} m^{-3} to make the simulations comparable to the data. Second, the electron mass in the simulation is 28.5 times heavier, which reduces the plasma frequency by a factor of $\sqrt{28.5} \approx 5.4$. The Courant condition for PIC codes simplifies to $\Delta t = C/\omega_p$, where *C* is a constant specific to the problem. Thus, raising the electron mass by a factor of 28.5 reduces the runtime of the simulation by a factor of 5.4. This mass adjustment requires raising the electron gyrofrequency by a factor of 5.4 to keep the ratio ν_e/Ω_e in equation (5.5) constant (*Longley et al.*, 2018). With these parameters, the grid scale size gives an aspect angle resolution of 0.71°. For aspect angles larger than 0.71° the spectra can be interpolated in (k_x, k_y) space with good accuracy, but at smaller angles this interpolation includes the exactly perpendicular to B grid point which dominates the spectra with a sharp spike at low frequencies (*Longley et al.*, 2019). Since ISR measurements require an averaging over many samples, the PIC code is run 100 times with different random seeds to give different initial particle positions and different random number draws during the collision step.

Figure 5.13 shows the results of the PIC simulation at small aspect angles. The single-particle simulations are run with the same parameters in Table 5.3 for comparison. At all of the shown aspect angles the ACFs from the PIC code are the same width as those from the single-particle simulations, indicating that both models will reproduce the same Ti measurement. However, all of the ACFs from the PIC code have a shallower minimum around 150 μs compared to the single-particle ACFs. Since the ACF is

effectively measuring a position (electron correlation across a wavelength) over time, the depth of the minimum can be interpreted as the damping strength of an oscillator. Without any damping of the ion-acoustic mode the ACF would be a sine function, so therefore the shallower minimums in the PIC code ACFs indicate a more heavily damped wave than what the single-particle simulations predict. The total damping is due to collisions, geometrical constraints of the magnetic field, and Landau damping. Fitting the measured ACFs from Millstone to a forward model that underestimates collisional damping will cause the fitting routine to compensate by lowering Te/Ti, which in turn increases the Landau damping in the forward model.

To qualitatively investigate the difference between the PIC simulations and the single-particle simulations, the ACFs from each are run through the same fitting routine as the data were in Section 5.3, with the Brownian theory as the forward model. The best fit temperatures are listed in Table 5.4, and for all of the plotted aspect angles, 1.2° to 5°, the PIC simulations are best fit by Te/Ti < 1. From Figure 5.12 we see that the Brownian theory used in the fitting routine is identical to the single-particle simulations for aspect angles of 3.4° and larger, and at smaller aspect angles the single-particle simulations produce narrower spectra. This is confirmed in Table 5.4, which shows at 1.2° in aspect angle the single-particle simulations are best fit by the Brownian theory with Te/Ti = 0.97, but at larger aspect angles Te/Ti ranges from 0.98 to 1. This means using the single-particle simulations as the forward model should provide minor improvements to the temperature fits to the PIC spectra aspect angles of 1.2°, but not at larger aspect angles.

Table 5.3 Parameters used in the PIC simulation

Grid Size	1024 x 1024	Electron mass	$m_e = 2.594 \times 10^{-29}$ kg
Grid Step	$\Delta x = \Delta y = 5$ mm	Ion mass (O+)	$m_i = 2.657 \times 10^{-26}$ kg
Total Time Steps	500,000	Temperature	$T_e = T_i = 1150$ K
Time Step Size	$\Delta t = 40$ ns	B field for electrons	$B_e = 2.7$ G
Particles per grid cell	128	B field for Ions	$B_i = 0.5$ G
Average density	$n = 5 \times 10^{10}$ m^{-3}	Collision density	$n_{coll} = 10^{12}$ m^{-3}

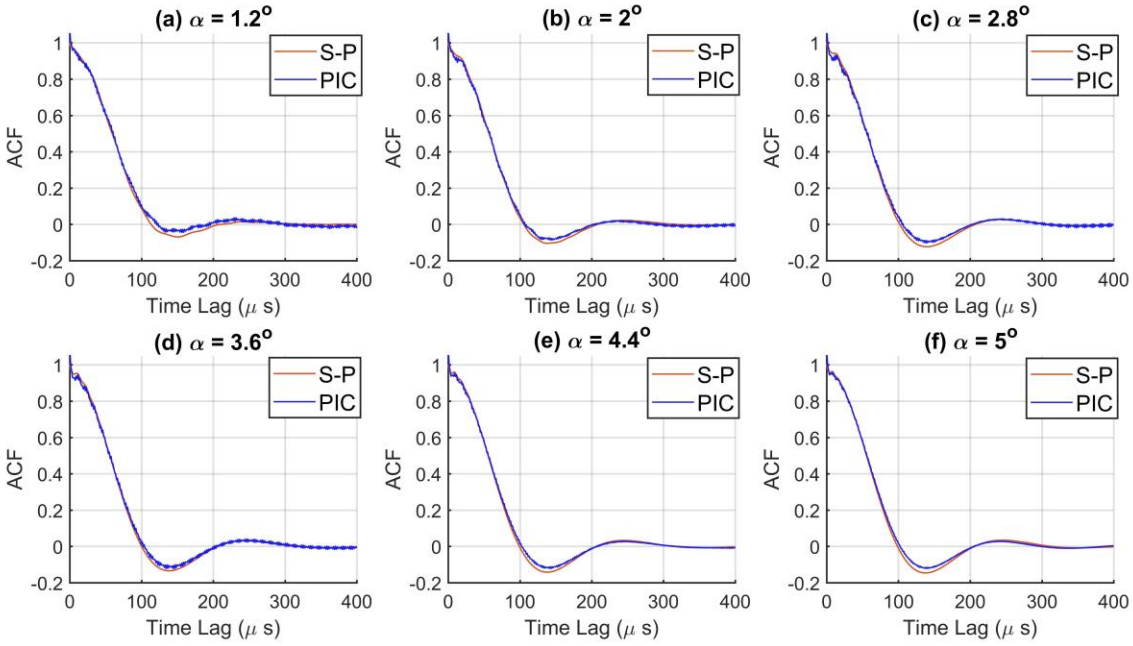

Figure 5.13 The PIC simulations (blue) and the single-particle simulations (orange) using the parameters in Table 5.3 are shown at different aspect angles. Table 5.3 shows the temperatures one would obtain when fitting the simulations to the Brownian theory.

Table 5.4 The temperature ratios obtained from fitting the PIC and single-particle (S-P) simulations shown in Figure 5.12 to the Brownian collisional theory. The errors in Te and Ti for all fits are less than 2% (approximately 20K).

Aspect Angle	1.2°	2°	2.8°	3.6°	4.4°	5°
PIC Te/Ti	0.61	0.78	0.77	0.94	0.86	0.96
S-P Te/Ti	0.97	0.98	0.99	0.98	1.00	0.99

5.5 Discussion

In this chapter the ACFs measured by a 440 MHz radar were fit to collisional ISR theory, and then compared to ACFs from single-particle and PIC simulations. The comparison of 440 MHz ACFs to collisional forward models has shown the importance of collisions depends both on the aspect angle and on the collision rate – which is controlled by the density and temperature. The experiment on November 8, 2013 was near solar maximum, with an average F10.7 value of 150 producing a peak density of 1.5×10^{12} m^{-3} in the F_2 region. The measured ACFs show collisions are responsible for Te/Ti < 1 fits at aspect angles of 3.6° and below. The ACFs at 4° and 4.6° also look collisionally narrowed, but the fitting routine obtained a physically valid Te/Ti > 1 ratio. The experiments in February and April 2019 took place closer to solar minimum where the average F10.7 was 70, and the peak densities of 3.8×10^{11} m^{-3} and 2.5×10^{11} m^{-3} occurred at lower altitudes in the F_1 region. The lower densities dropped the collision rates, and the data showed no significant drop in Te/Ti compared to the IRI model at aspect angles less than 1.5°. Below 1° beam averaging the forward model becomes important, so we were not able to definitively see if equation (5.10) correctly predicts that collisional effects become important at 1.25° and 0.8° for the February and April measurements respectively.

The ACFs measured on November 8, 2013 were further compared to the single-particle simulations from *Milla and Kudeki* (2011) and the PIC simulations from *Longley et al.* (2019) to investigate the validity of those two models. At aspect angles of 3.4° and larger the single-particle simulations were shown to be nearly identical to the Brownian

theory for the same temperatures. This means using the single-particle simulations as the forward model in the fitting process would still reproduce the Te/Ti < 1 fits to the November 2013 data at 3.4° and 3.6°. Comparing the single-particle simulations to the PIC simulations for a set Te = Ti = 1150 K run showed that at all aspect angles of 5° and less the PIC simulations produce more heavily damped ACFs than the single-particle simulations. This suggests that using the PIC simulations as a forward model in the fitting routine would lead to more accurate Te/Ti ratios for the data measured on November 8, 2013, but not for the measurements in February and April 2019 where the density remained low.

Lastly, the results from the February and April 2019 experiments are in slight contrast with those in *Aponte et al.* (2001). The data set analyzed by Aponte was taken at the equatorially located 50 MHz Jicamarca radar. At aspect angles of 3.5° and less, and for a wide range of densities and temperatures, they found that collisions narrowed the spectra and produced nonphysical Te/Ti ratios. Furthermore, fitting the spectra to the single-particle simulations from *Sulzer and Gonzalez* (1999) showed that all of the Te/Ti ratios were being underestimated at aspect angles of 3.5° or less. This higher sensitivity to collisions even at low densities is due to the lower transmission frequency of Jicamarca. The Bragg scattering wavelength of 3 m at Jicamarca is about 9 times longer than the 0.34 cm Bragg wavelength of Millstone Hill, so according to equation 5.8 the electron correlation time is 9 times longer at Jicamarca. Therefore, when the density drops by a factor of 5 as it did for the February and April 2019 experiments, Jicamarca would still see collisional effects at a wider range of aspect angles since the correlation

time is 9 times longer than at Millstone Hill. This means one would expect to always see collisions affecting Te/Ti measurements at Jicamarca, whereas Millstone Hill is only affected when the density is high (~10^{12} m^{-3}). This can occur frequently at Millstone Hill during solar maximum, as the November 8, 2013 experiment showed, or during an extreme storm time event where densities are increased due to particle precipitation or electron heating.

Chapter 6

Conclusions

6.1 Summary of the Dissertation

When a radar looks within 5° of perpendicular to the Earth's magnetic field current ISR techniques underestimate the plasma temperature by up to 30%. The prevalence of ISR data in current space physics research requires data products of the highest accuracy. To understand and correct the systematic errors in ISR temperature measurements this dissertation answered the following questions:

1) Do Coulomb collisions effect temperature and density measurements of the Earth's ionosphere?

In Chapters 3 and 4, I implemented both electron-ion and electron-electron Coulomb collisions into EPPIC, a fully kinetic PIC code. Simulations with either collision type produced spectra that were narrower than both collisionless theory and a collisional theory that approximates Coulomb collisions as a Brownian motion process. Using these theories as a forward model for ISR inversions will lead to underestimates in the electron and ion temperatures compared to the PIC simulations. From Chapter 2 the density measured from ISR is related to the total measured power by the ratio $1/(1+\frac{Te}{Ti})$, so underestimates in temperature also affect the accuracy of density measurements. This confirms the hypothesis of *Sulzer and Gonzalez* (1999) that electron Coulomb collisions are responsible for the systematic underestimation of temperatures that have plagued

Jicamarca since the facility became operational (*Carlson and Sayers,* 1970; *McClure et al.,* 1973, *Aponte et al.,* 2001).

2) Do electron-electron collisions damp a plasma wave differently than electron-ion collisions?

In Chapter 4, I examined the effects of electron-electron collisions on ISR spectra in detail. Analytic theories treat all collisions with either a BGK collision operator or a Brownian collision operator, and therefore cannot distinguish between an electron-ion collision and an electron-electron collision as both collision types are approximated the same way. The first set of single-particle simulations by *Sulzer and Gonzalez* (1999) implemented velocity dependent electron-electron collisions and found that their primary effect was to reduce the effects of electron-ion collisions at aspect angles larger than 3°. *Milla and Kudeki* (2011) extended the single-particle simulation technique to 3D and modeled both collision types with the velocity dependent Fokker-Planck operator, but did not specifically examine the effects of electron-ion collisions versus electron-electron collisions. In Chapter 4 I wrote a single-particle code following the methodology in *Milla and Kudeki* (2011) to do this examination. Single-particle simulations with only electron-ion collisions are not numerically stable and therefore cannot be analyzed on their own. The single-particle simulations with only electron-electron collisions exactly matched the Brownian collisional theory at aspect angles of 0.35° and larger, where the ion-acoustic mode is able to propagate. This shows that in the single-particle simulation method electron-electron collisions do not contribute to the damping of the ion-acoustic mode. However, the PIC simulations in Chapter 4 with only electron-electron collisions show

significant damping of the ion-acoustic mode and narrowing of the spectra at aspect angles up to 5°.

The discrepancy between these two results is due to the PIC code simulating the full nonlinear system, whereas single-particle simulations still rely on the linear ISR framework in *Kudeki and Milla* (2011) to calculate spectra from the particle displacement statistics. Using the output wave electric field from the PIC code the nonlinear Landau damping timescale is calculated to be very close to the electron correlation times at aspect angles of 4° and less. The ion-acoustic mode propagating at these small aspect angles will then Landau damp for long enough that the electron distribution starts to flatten out near the wave's phase speed. This flattening of the distribution then changes the collision operators and therefore the collisional damping. Electron-electron collisions are described by the full Fokker-Planck collision operator, which has first and second order derivatives of the distribution and is sensitive to the distribution flattening during nonlinear Landau damping. For electron-ion collisions the Fokker-Planck operator can be reduced to a single term that is linear in the distribution, and therefore the collision operator changes slowly as nonlinear Landau damping progresses. The change to the collision operators during nonlinear Landau damping is the reason why the PIC simulations do not match single-particle simulations, despite both approaches using the exact same collision operators.

3) Do particle-in-cell (PIC) simulations provide a more accurate forward model than current theories for ISR temperature estimates?

To understand how the different forward models compare for temperature fittings I examined small aspect angle spectra measured by Millstone Hill in Chapter 5. Inverting the spectra with the Brownian collisional theory as the forward model showed nonphysical Te/Ti ratios at aspect angles as large as 3.6°, and underestimates of Te/Ti up to the largest measured aspect angle of 4.6°. This confirms the conclusion in *Milla and Kudeki* (2011) that the Brownian theory is inadequate for ISR temperature fittings. For select aspect angles and temperatures, the measured spectra were compared to the single-particle simulations from Chapter 4, showing that the kinetic treatment of Coulomb collisions does slightly improve temperature fits at small aspect angles. However, a set of PIC simulations with parameters taken from the data, including Te = Ti = 1150 K, showed that the PIC simulations produce narrower spectra than the single-particle simulations at aspect angles of 5° and less. This indicates that the PIC code, with kinetic collisions and nonlinear Landau damping, is a better forward model for temperature fittings than the collisional theories and single-particle simulations currently in use.

6.2 Future Work

The main path forward from this dissertation is to take what we learned about nonlinear damping of the ion-acoustic mode at small aspect angles and translate that knowledge into a forward model that can be used at Jicamarca, Millstone Hill, ALTAIR, and any future ISR deployed at mid or low latitudes. In principle the PIC code can

accurately provide this forward model by calculating a database spanning many electron and ion temperatures. While the PIC simulations in this dissertation were relatively cheap at approximately 50,000 CPU hours for each set of parameters, computing spectra at many different parameter sets is narrowly out of reach with current supercomputer hour allocations. Such a library of PIC spectra can likely be obtained on the next generation of supercomputers, or through an allocation on the order of 10 million hours for this specific task.

The parameters this dissertation used for PIC simulations were chosen and validated in excruciating detail to minimize numerical instabilities, nonphysical results, or other inaccuracies. However, a few compromises had to be made which warrant further analysis if the PIC code is used for building a library of spectra. First, the electron mass dictates the time step necessary from the Courant condition, and a typical trick in PIC simulations is to artificially increase the electron mass to bring ion and electron time scales closer together. Chapter 3 discusses this approximation in detail. The simulations in this dissertation were all 2D in space, and 3D in particle velocity. No analysis has been done on the accuracy of this approximation, and it is possible that constraining the spatial system to 2D has adverse effects on the wave propagation and energy exchange. *Oppenheim et al.* (2013) discusses the effects of constraining EPPIC to 2D, though the application is for the Farley-Buneman instability and the 2D space is all perpendicular to B, whereas the 2D plane for ISR simulations has a parallel and perpendicular to B direction. The last issue with the PIC simulations is the grid used. The 512 by 512 grid used in Chapters 3 and 4 resolved 0.7° increments in aspect angle for the 1024 m_i/m_e

mass ratio. Overcoming this grid discretization requires larger, more expensive simulations by either increasing the grid size or using a more realistic electron mass.

A possibly faster and less computationally reliant solution for producing an operational forward model is to modify ISR theory to account for nonlinear Landau damping. This can be accomplished in two ways. First, the response function in equation (4.27) can be modified to include a nonlinear term, which will modify the derivation of the fluctuation-dissipation theorem and the Kramers-Kronig relations. This approach has the advantage of including velocity dependent collisions through single particle simulations of the electron ACF. The other way of modifying ISR theory is to use the dressed particle approach to account for nonlinear Landau damping. Quasilinear diffusion theory solves for density perturbations on the assumption that the 0^{th} order distribution is time dependent, which allows for the flattening near the Landau resonance. Using the Boltzmann equation to solve for ISR spectra has the advantage of including all of the relevant kinetic physics, but the inclusion of a magnetic field and velocity dependent collisions can make the problem intractable. Both of these approaches also open the possibility of addressing the assumptions of stationarity and quasi-equilibrium that are currently used to derive nonequilibrium $T_e \neq T_i$ ISR spectra.

This dissertation focused on the effects of Coulomb collisions on ISR spectra for 440 MHz radars. The PIC code outputs a wide range of radar wavelengths, and the 440 MHz frequency was chosen since it represents a large number of radars: Millstone Hill operates at 440 MHz, Arecibo operates at 430 MHz, the AMISR systems operate at 450 MHz, and one of ALTAIR's bands is 422 MHz. Thus, the results in this dissertation

apply to all of those radars, even though only Millstone Hill and ALTAIR can actually look at aspect angles less than 10°. Analysis of PIC spectra at frequencies ranging from 350 MHz to 700 MHz showed similar results to the 440 MHz case. Ideally this dissertation would also look at 50 MHz simulations since Jicamarca is always looking within 6° of perpendicular to B. This was not done simply due to the computational time needed; the 440 MHz frequency is simulated by resolving many 0.34 cm Bragg scattering wavelengths across the domain, whereas 50 MHz corresponds to a 3 m Bragg wavelength. Thus, for a 2D simulation with the same resolution it is 80 times more expensive to simulate a 50 MHz radar compared to a 440 MHz radar since the simulation cost increases linearly with the number of grid points. Therefore, future work will also address the nonlinear damping physics for the 50 MHz Jicamarca radar, either through an increase in computing budget or through deriving a new analytic theory as described above.

List of Journal Abbreviations

The doi string in each reference can be Googled to find the journal each article came from. For those who are technologically backwards the following is a list of the journal abbreviations that you can use to request mail order copies of the articles.

Ann. Geophys.	Annales Geophysicae
Ap. J.	Astrophysical Journal
Geophys. Res. Lett.	Geophysical Research Letters
IEEE Trans. Plas. Sci.	IEEE Transactions of Plasma Science
IEEE Trans. Geosci. Remote Sens.	IEEE Transactions of Geoscience Remote Sensing
J. Adv. Space Res.	Journal of Advanced Space Research
J. Atmos. Solar-Terr. Phys.	Journal of Atmospheric and Solar-Terrestrial Physics
J. Comp. Phys.	Journal of Computational Physics
J. Geophys. Res.	Journal of Geophysical Research
J. Opt. Soc. Am.	Journal of the Optical Society of America
Phys. Plasmas	Physics of Plasma
Phys. Rev.	Physical Review
Phys. Rev. Lett.	Physical Review Letters
Radio Sci.	Radio Science
Space Sci. Rev.	Space Science Reviews

References

Abdu, M. A. (2012), Equatorial spread F/plasma bubble irregularities under storm time disturbance electric fields, J. Atmos. Solar-Terr. Phys, 75-76. doi: 10.1016/j.jastp.2011.04.024.

Abel, B., and R. M. Thorne (1998), Electron scattering loss in Earth's inner magnetosphere: 1. Dominant physical processes, J. Geophys. Res., 103(A2), 2385–2396, doi:10.1029/97JA02919.

Akbari, H., A. Bhatt, C. La Hoz, and J. L. Semeter (2017). Incoherent Scatter Plasma Lines: Observations and Applications, Space Sci. Rev., 212: 249. doi:10.1007/s11214-017-0355-7

Aponte, N., M. P. Sulzer, and S. A. González (2001), Correction of the Jicamarca electron-ion temperature ratio problem: Verifying the effect of electron Coulomb collisions on the incoherent scatter spectrum, J. Geophys. Res., 106(A11), 24785–24793, doi:10.1029/2001JA000103.

Baranov, D. G., A. A. Zyablovsky, A. V. Dorofeenko, A. P. Vinogradov, and A. A. Lisyansky (2015), Comment on “Counterintuitive Dispersion Violating Kramers-Kronig Relations in Gain Slabs”, Phys. Rev. Lett., 114, 089301. doi: 10.1103/PhysRevLett.114.089301.

Bellan, P. M. (2006) Fundamentals of Plasma Physics, Cambridge University Press.

Bhatt, A. N., E. A. Gerken Kendall, M. C. Kelley, M. P. Sulzer, and E. B. Shume (2006), Observations of strong gyro line spectra at Arecibo near dawn, Geophys. Res. Lett., 33, L14105, doi:10.1029/2006GL026139.

Birdsall, C. K. and A. B. Langdon (2004) Plasma Physics via Computer Simulation, CRC Press.

Bhatnagar, P.L., E. P. Gross, and M. Krook (1954), A Model for Collision Processes in Gases. I. Small Amplitude Processes in Charged and Neutral One-Component Systems, Phys. Rev. 94, 511. doi:10.1103/PhysRev.94.511

Bilitza, D., and B. W. Reinisch (2008), International Reference Ionosphere 2007: Improvements and new parameters. J. Adv. Space Res., Vol. 42, Issue 4, doi: 10.1016/j.asr.2007.07.048.

Brambilla, M. (1995), The effects of Coulomb collisions on the propagation of cold-plasma waves, Phys. Plasmas, 2(4), 1094, doi:10.1063/1.871388.

Bowles, K. L. (1958), Observations of vertical incidence scatter from the ionosphere at 41 mc/s., Phys. Rev. Lett., 1, 454–455. doi: 10.1103/PhysRevLett.1.454

Carlson, H. C., and J. Sayers (1970), Discrepancy in electron temperatures deduced from Langmuir Probes and from incoherent scatter radars, J. Geophys. Res., 75(25), 4883–4886. doi:10.1029/JA075i025p04883.

Chaniotis, A. K. and D. Poulikakos (2004), High order interpolation and differentiation using B-splines. J. Comp. Phys. 197, 253-274, doi:10.1016/j.jcp.2003.11.026

Chen, F. F. (2016), Introduction to Plasma Physics and Controlled Fusion. Heidelberg, NY: Springer.

Cohen, B. I., A. M. Dimits, A. Friedman, and R. E. Caflisch (2010), Time-step considerations in particle simulation algorithms for Coulomb collisions in plasmas. IEEE Trans Plas Sci 38, 2394. doi: 10.1109/TPS.2010.2049589

Diaz, M. A., J. L. Semeter, M. Oppenheim, and M. Zettergren (2008), Particle-in-cell simulation of the incoherent scatter radar spectrum, Radio Sci., 43, RS1007, doi:10.1029/2007RS003722.

Dimant, Y. S., and M. M. Oppenheim (2011a), Magnetosphere-ionosphere coupling through E region turbulence: 1. Energy budget, J. Geophys. Res., 116, A09303, doi:10.1029/2011JA016648.

Dimant, Y. S., and M. M. Oppenheim (2011b), Magnetosphere-ionosphere coupling through E region turbulence: 2. Anomalous conductivities and frictional heating. J. Geophys. Res., 116, A09304, doi:10.1029/2011JA016649.

Dougherty, J. P., & Farley, D. T. (1960). A theory of incoherent scattering of radio waves by a plasma. Proceedings of the Royal Society of London Series A-Mathematical and Physical Sciences, 259(1296), 79–99, doi:10.1098/rspa.1960.0212

Dougherty, J. P. (1963). The conductivity of a partially ionized gas in alternating electric fields. Journal of Fluid Mechanics, 16(1), 126–137. doi:10.1017/S002211206300063X

Dougherty, J. P., and Farley, D. T. (1963). A theory of incoherent scattering of radio waves by a plasma: 3. Scattering in a partly ionized gas. Journal of Geophysical Research, 68(19), 5473. doi:10.1029/JZ068i019p05473.

Dungey, J. W. (1961), Interplanetary Magnetic Field and the Auroral Zones. Phys. Rev. Lett. 6, 47. doi:10.1103/PhysRevLett.6.47

Epperlein, E. M., R. W. Short, and A. Simon (1992), Damping of ion-acoustic waves in the presence of electron-ion collisions. Phys. Rev. Lett. 69, 1765, doi:10.1103/PhysRevLett.69.1765

Erickson, P., MIT/Haystack Observatory. (2018) Data from the CEDAR Madrigal database. Available from https://w3id.org/cedar?experiment_list= experiments/2018/mlh/08feb18&file_list=mlh180208g.001.hdf5

Farley, D. T., Dougherty, J. P., & Barron, D. W. (1961). A theory of incoherent scattering of radio waves by a plasma: 2. Scattering in a magnetic field. Proceedings of the Royal Society of London Series A-Mathematical and Physical Sciences, 263(131), 238. doi:10.1098/rspa.1961.0158

Farley Jr., D. T. (1964), The effect of Coulomb collisions on incoherent scattering of radio waves by a plasma, J. Geophys. Res., 69(1), 197–200, doi:10.1029/JZ069i001p00197.

Farley, D. T. (1966), A theory of incoherent scattering of radio waves by a plasma: 4. The effect of unequal ion and electron temperatures, J. Geophys. Res., 71(17), 4091– 4098, doi:10.1029/JZ071i017p04091.

Farley, D. T. (1969), Faraday Rotation Measurements Using Incoherent Scatter, Radio Sci., 4(2), 143– 152, doi:10.1029/RS004i002p00143.

Fejer, J. A. (1960). Scattering of radio waves by an ionized gas in thermal equilibrium. Canadian Journal of Physics, 38(8), 1114–1133.

Fejer, J. A. (1961). Scattering of radio waves by an ionized gas in thermal equilibrium in presence of a uniform magnetic field. Canadian Journal of Physics, 39(5), 716.

Fetter, A. F., and J. D. Walecka (2003), Theoretical Mechanics of Particles and Continua. Mineola, N. Y.: Dover Publications, Inc.

Fletcher, A. C, and S. Close (2017), Particle-in-cell simulations of an RF emission mechanism associated with hypervelocity impact plasmas. Phys. Plasmas 24, 053102, doi:10.1063/1.4980833

Froula, D. H., S. H. Glenzer, N. C. Luhmann Jr., and J. Sheffield (2011), Plasma Scattering of Electromagnetic Radiation: Theory and Measurement Techniques. Burlington, MA: Academic Press. doi:10.1016/B978-0-12-374877-5.00001-4

González, S. A., Sulzer, M. P., Nicolls, M. J., and Kerr, R. B. (2004), Solar cycle variability of nighttime topside helium ion concentrations over Arecibo, J. Geophys. Res., 109, A07302, doi:10.1029/2003JA010100.

Goodwin L.V., J.-P. St.-Maurice, H. Akbari, and R.J Spiteri (2018), Incoherent scatter spectra based on Monte-Carlo simulations of ion velocity distributions under strong ion frictional heating, Radio Sci., 53, doi:10.1002/2017RS006468.

Gordon, W. E. (1958), Incoherent scattering of radio waves by free electrons with application to space exploration by radar, Proc. of the IRE, pp. 1824–1829. doi:10.1109/JRPROC.1958.286852

Hagfors, I. (1961). Density fluctuations in a plasma in a magnetic field, with applications to ionosphere. Journal of Geophysical Research, 66(6), 1699. doi:10.1029/JZ066i006p01699.

Hedin, A. E. (1991), Extension of the MSIS Thermosphere Model into the middle and lower atmosphere, J. Geophys. Res., 96(A2), 1159–1172, doi:10.1029/90JA02125.

Hellinger, P., and P. M. Trávnícek (2009), On Coulomb collisions in bi-Maxwellian plasmas, Phys. Plasmas, 16, 054501. doi: 10.1063/1.3139253

Hysell, D. L., Chau, J. L., and Huba, J. D. (2009) Topside measurements at Jicamarca during solar minimum, Ann. Geophys., 27, 427-439, doi:10.5194/angeo-27-427-2009

Hysell, D. L., R. Jafari, M. A. Milla, and J. W. Meriwether (2014), Data-driven numerical simulations of equatorial spread F in the Peruvian sector, J. Geophys. Res. Space Physics, 119, 3815–3827, doi:10.1002/2014JA019889.

Hysell, D. L., M. A. Milla, L. Condori, and J. Vierinen (2015), Data-driven numerical simulations of equatorial spread F in the Peruvian sector 3: Solstice, J. Geophys. Res. Space Physics, 120, 10,809–10,822, doi:10.1002/2015JA021877.

Hysell, D. L., M. A. Milla, F. S. Rodrigues, R. H. Varney, and J. D. Huba (2015), Topside equatorial ionospheric density, temperature, and composition under equinox, low solar flux conditions. J. Geophys. Res. Space Physics, 120, 3899–3912. doi: 10.1002/2015JA021168.

Hysell, D. L., J. Vierinen, and M. P. Sultzer (2017), On the theory of the incoherent scatter gyrolines, Radio Sci., 52, 723–730, doi:10.1002/2017RS006283.

Hysell, D. L., (2018), Antennas and radars for environmental scientists and engineers. New York, NY: Cambridge University Press.

Jackson, J. D. (1999). Classical electrodynamics. New York, NY: Wiley.

Jones, M. E., D. S. Lemons, R. J. Mason, V. A. Thomas, and D. Winske (1996), A grid-based Coulomb collision model for PIC codes. J. Comp. Phys., 123, 169-181. doi:10.1006/jcph.1996.0014

Kelley, M. C. (2009), The Earth's Ionosphere. Burlington, MA: Academic Press.

Kudeki, E., Woodman, R. F., and Feng, Z. (2003), Incoherent scatter radar plasma density measurements at Jicamarca using a transverse-mode differential-phase method, Geophys. Res. Lett., 30, 1255, doi:10.1029/2002GL015496, 5.

Kudeki, E., and M. Milla (2011), Incoherent scatter spectral theories part I: A general framework and results for small magnetic aspect angles. IEEE Trans. Geosci. Remote Sens., 49(1), 315–328. doi: 10.1109/TGRS.2010.2057252

Lehtinen, M. S., and A. Huuskonen (1996), General incoherent scatter analysis and GUISDAP, J. Atmos. Solar-Terr. Phys., 58, 435. doi: 10.1016/0021-9169(95)00047-X

Lemons, D. S., D. Winske, W. Daughton, and B. Albright (2009), Small-angle Coulomb collision model for particle-in-ell simulations. J. Comp. Phys., 228, 1391-1403. doi: 10.1016/j.jcp.2008.10.025

Longley, W. J., M. M. Oppenheim, A. C. Fletcher, Y. S. Dimant, Y. S. (2018). ISR spectra simulations with electron-ion Coulomb collisions. J. Geophys. Res. Space Physics, 123. doi: 10.1002/2017JA025015

Longley, W. J., Meers M. Oppenheim, Yakov S. Dimant, (2019). Nonlinear effects of electron-electron collisions on ISR temperature measurements. J. Geophys. Res. Space Physics, doi:10.1002/2019JA026753

Lyon, J.G., J.A. Fedder, and C.M. Mobarry (2004), The Lyon-Fedder-Mobarry (LFM) global MHD magnetospheric simulation code, J. Atmos. Solar-Terr. Phys., 66, 1333. doi:10.1016/j.jastp.2004.03.020

Madsen, C. A., Y. S. Dimant, M. M. Oppenheim, and J. M. Fontenla (2014), The multi-species Farley-Buneman instability in the solar chromosphere. Ap. J., 783:128. doi: 10.1088/0004-637X/783/2/128

Malnes, E., and N. Bjørna (1993), Enhancement of incoherent scatter gyro lines by suprathermal electrons, J. Atmos. Terr. Phys.,55, 667–674. doi:10.1016/0021-9169(93)90012-N

Manheimer, W. M., M. Lampe, and G. Joyce, (1997), Langevin representation of Coulomb collisions in PIC simulations. J. Comp. Phys., 138, 563-584. doi:10.1006/jcph.1997.5834

Markel, V. A., (2018), Two-stream theory of light propagation in amplifying media. J. Opt. Soc. Am. B 35, 533-544. doi:10.1364/JOSAB.35.000533.

Martínez-Ledesma, M., & Díaz Quezada, M. A. (2019). Determination of the Signal Fluctuation Threshold of the Temperature-Ion Composition Ambiguity Problem Using Monte Carlo Simulations. J. Geophys. Res. Space Physics, 124. doi:10.1029/2018JA026217

McClure, J. P., et al. (1973), Comparison of Te and Ti from Ogo 6 and from various incoherent scatter radars, J. Geophys. Res., 78(1), 197–205, doi:10.1029/JA078i001p00197.

Merkin, V. G., and J. G. Lyon (2010), Effects of the low-latitude ionospheric boundary condition on the global magnetosphere, J. Geophys. Res., 115, A10202, doi:10.1029/2010JA015461.

Milla, M., and E. Kudeki (2006), F-region electron density and Te/Ti measurements using incoherent scatter power data collected at ALTAIR. Ann. Geophys., 24, 1333–1343. doi:10.5194/angeo-24-1333-2006

Milla, M., and E. Kudeki (2009), Particle dynamics description of "BGK collisions" as a Poisson process, J. Geophys. Res., 114, A07302, doi:10.1029/2009JA014200.

Milla, M., and E. Kudeki (2011), Incoherent scatter spectral theories part II: Modeling the spectrum for modes propagating perpendicular to B. IEEE Trans. Geosci. Remote Sens., 49(1), 329–345. doi:10.1109/TGRS.2010.2057253

Nanbu, K., (1997), Theory of cumulative small-angle collisions in plasmas. Phys. Rev. E 55, doi:10.1103/PhysRevE.55.4642

Nicholson, D. R. (1983), Introduction to Plasma Theory. New York, NY: Wiley.

Oppenheim, M. M., Y. S. Dimant, and L. P. Dyrud (2008), Large-scale simulations of 2D fully kinetic Farley-Buneman turbulence. Ann Geophy., 26, 453-553. doi:10.5194/angeo-26-543-2008

Oppenheim, M. M., and Y. S. Dimant (2013), Kinetic simulations of 3-D Farley-Buneman turbulence and anomalous electron heating, J. Geophys. Res. Space Physics, 118, 1306–1318, doi:10.1002/jgra.50196.

Oppenheim, M. M., and Y. S. Dimant (2016), Photoelectron-induced waves: A likely source of 150 km radar echoes and enhanced electron modes, Geophys. Res. Lett., 43, 3637–3644, doi:10.1002/2016GL068179.

Rodrigues, F. S., M. J. Nicolls, and D. L. Hysell (2007), Improved electron density measurements at Jicamarca, J. Geophys. Res., 112, A11315, doi:10.1029/2007JA012598.

Rodrigues, F. S., M. J. Nicolls, R. Woodman, D. L. Hysell, J. L. Chau, and S. A. González (2007), Ion gyroresonance observations at Jicamarca revisited, Geophys. Res. Lett., 34, L13107, doi:10.1029/2007GL029680.

Rosenbluth, M. N., W. M. MacDonald, and D. L. Judd (1957), Fokker-Planck equation for an inverse square force. Phys. Rev., Vol 107, No 1. doi:10.1103/PhysRev.107.1

Rosin, M. S., L. F. Ricketson, A. M. Dimits, R. E. Caflisch, and B. I. Cohen (2014), Multilevel Monte Carlo simulation of Coulomb collisions. J. Comp. Phys., 274, 140-157. doi:10.1016/j.jcp.2014.05.030

Rybicki, G. B., and A. P. Lightman (1979) Radiative Processes in Astrophysics. Weinheim, Germany: Wiley-VCH.

Salpeter, E. E. (1960). Electron density fluctuations in a plasma. Physical Review, 120(5), 1528–1535. doi:10.1103/PhysRev.120.1528

Salpeter, E. E. (1961a). Effect of magnetic field in ionospheric backscatter. Journal of Geophysical Research, 66(3), 982. doi:10.1029/JZ066i003p00982.

Salpeter, E. E. (1961b). Plasma density fluctuations in a magnetic field. Physical Review, 122(6), 1663. doi:10.1103/PhysRev.122.1663

Schunk, R. W., and A. F. Nagy (2009), Ionospheres: Physics, Plasma Physics, and Chemistry. Cambridge, UK: Cambridge University Press.

Shkarofsky, I. P., T. W. Johnston, and M. P. Bachynski (1966), The Particle Kinetics of Plasmas. Reading, MA: Addison-Wesley.

Sulzer, M. P., and S. González (1999), The effect of electron Coulomb collisions on the incoherent scatter spectrum in the F region at Jicamarca. J. Geophys. Res., 104(A10), 22535–22551, doi:10.1029/1999JA900288.

Swoboda, J. P. (2017) Space-time sampling strategies for electronically steerable incoherent scatter radar, Ph.D. dissertation, Boston Univ., Boston, MA

Takizuka, T., and H. Abe (1977). A binary collision model for plasma simulation with a particle code. J. Comp. Phys., 25, 205-219. doi:10.1016/0021-9991(77)90099-7

Vierinen, J., Gustavsson, B., Hysell, D. L., Sulzer, M. P., Perillat, P., and Kudeki, E. (2017), Radar observations of thermal plasma oscillations in the ionosphere, Geophys. Res. Lett., 44, 5301– 5307, doi:10.1002/2017GL073141.

Woodman, R. F. (1967), Incoherent scattering of electromagnetic waves by a plasma, Ph.D. dissertation, Harvard Univ., Cambridge, MA, Mar. 1967.

Woodman, R. F. (2004), On a proper electron collision frequency for a Fokker-Planck collision model with Jicamarca applications. J. Atmos. Sol. Terr. Phys., 66.17, 1521–1541. doi: 10.1016/j.jastp.2004.07.001

Zheng, L., A. A. Chan, J. M. Albert, S. R. Elkington, J. Koller, R. B. Horne, S. A. Glauert, and N. P. Meredith (2014), Three-dimensional stochastic modeling of radiation belts in adiabatic invariant coordinates, J. Geophys. Res. Space Physics, 119, 7615–7635, doi:10.1002/2014JA020127.